université
PARIS-SACLAY

Non-compact conformal field theory and lattice models - the open case

Thèse de doctorat de l'Université Paris-Saclay

École doctorale n° 564, Ecole Doctorale Physique en Ile-de-France (EDPIF)
Spécialité de doctorat: Physique
Unité de recherche: Université Paris-Saclay, CNRS, CEA, Institut de physique théorique, 91191, Gif-sur-Yvette, France.
Référent: : Faculté des sciences,

Thèse présentée et soutenue en visioconférence totale, le 16 juin 2020, par

Niall Robertson

Composition du jury

Vincent Pasquier Directeur de recherche, IPhT Saclay	Président
Olalla Castro-Alvaredo Associate Professor, City, University of London	Rapporteur
Rafael Nepomechie Professeur des Universités, University of Miami	Rapporteur
Clare Dunning Associate Professor, University of Kent	Examinatrice
Hubert Saleur Directeur de recherche, IPhT Saclay	Directeur de thèse
Jesper Jacobsen Professeur des Universités, ENS Paris	Codirecteur de thèse

Thèse de doctorat

NNT: 2020UPASS099

Is fada an bóthar nach mbíonn casadh ann

Abstract

The description of critical lattice models by Conformal Field Theories (CFTs) has been studied in detail for several decades. Recent years have seen a growing interest in the study of a particular class of critical models with continuum limits that are described by so-called *non-compact* CFTs, identified by the appearance of a continuum of critical exponents. A striking feature of a number of such models is that this "non-compactness" appears despite their lattice descriptions admitting only a *finite* number of degrees of freedom - hence classified as so-called "compact" lattice models. The connection between critical, compact lattice models and non-compact CFT has not yet been brought under sufficient control and leaves open a number of questions. This thesis addresses these and related questions by turning to the corresponding *open* critical lattice models and uses tools from integrability, boundary conformal field theory and lattice algebra representation theory.

The early parts of this thesis deal with the antiferromagnetic Potts model, known to be closely related to the non-compact CFT referred to as the Euclidean Black Hole theory. The representation theory of the underlying lattice algebra of the Potts model is related to the representation theory of the Virasoro algebra, resulting in a set of new identities relating the Black Hole Theory to the Parafermion CFT - a *compact* theory. Other aspects of these CFTs - such as fusion, normalisability and disorder operators - are understood from a lattice point of view.

The middle part of this thesis turns to boundary integrability and in particular the Bethe Ansatz technique. An exact mapping is presented between the antiferromagnetic Potts model and an integrable model constructed from the twisted affine D_2^2 Lie algebra. The known integrable boundary conditions of this D_2^2 model are then interpreted in the context of the antiferromagnetic Potts model and the Black Hole theory.

The final part looks at a different boundary condition in the D_2^2 model and finds that it admits a simple geometrical interpretation in the Potts model, resulting in an exact solution which had, until now, been lacking. This exact solution is used to study the continuum limit of the model and is found to result in a non-compact boundary CFT. This lattice boundary condition is observed to correspond to a repulsive fixed point under RG, and flows towards free boundary conditions in the antiferromagnetic Potts model.

Acknowledgements

I would firstly like to express my sincere gratitude to my supervisors Hubert and Jesper for their advice and guidance throughout this PhD. It was a privilege and a pleasure to work with both of you and to have got to know you over many discussions about a range of interesting topics.

I would like to thank the rapporteurs, Rafael Nepomechie and Olalla Castro-Alvaredo, for their thorough reading of the thesis and for their detailed and insightful comments. I would furthermore like to thank the examiners Clare Dunning and Vincent Pasquier for reading the thesis and for agreeing to be on my thesis committee - particular thanks to Vincent for being the President of the jury.

I would like to thank everyone at Université Paris-Sud and at École Doctorale en Ile-de-France as well as all of the administrative staff at IPhT, ENS and CEA, in particular Laure Sauboy, Sylvie Zaffanella, Loic Bervas and Emmanuelle de Laborderie.

I would like to express my gratitude to all of my lecturers at Trinity College Dublin and at the University of Cambridge whose teaching at undergraduate and master's level provided me with a great passion for physics and inspired me to undertake a PhD. I am particularly grateful to Tristan McLoughlin, Dmytro Volin and Mauro Ferreira.

Quand je suis arrivé en France, j'ai eu la chance d'être chaleureusement accueilli par mes collègues Romain et Etienne avec qui je partageais un bureau pendant ces années de thèse, merci pour tout - en particulier pour avoir été très patient avec mon français.

I would like to furthermore thank all the other members of our research group: Jonathan, Michal, Yifei, Thiago and Linnea for the rewarding years of working together. Thank you Jonathan for your patience in answering my (many) questions, particularly in my first year.

I am grateful to all of the friends that I made during these years at IPhT - particular thanks to the "Chouffe" crew - Santi, Luca, Christian, Severin and Pierre - for the pints, debates and general good times. Thank you also to Santi for the discussions along the RER B which were of crucial importance to this thesis.

I am very grateful to all of the postdocs and PhD students that I have had the pleasure to have lunch and drink coffee with at IPhT: thank you to Federico, Elba, Ben, Orazio, Kemal, Benoit, Lilian, Ingrid, Sebastian and Sarah. Je voudrais aussi remercier mes professeurs de français à IPhT: Henriette et Sandrina.

To the Trinity TPs - Brian, Evan, Frank, Conor, Eamonn and Manya - thank you for making those years studying together such an enjoyable and memorable time. Long may the TP reunions continue, wherever we are in the world.

To all my friends in Dublin with whom it is always a pleasure to catch up with and have pints together, thank you for being there for all of these years - particular thanks to Rebecca, Neil, Rob, Donal and Rory.

I am also extremely grateful to the friends I have made in Paris in perhaps the most unlikely circumstances: Cianan, Helene, Anastasia and James - I am very happy to have become friends with all of you entirely as a result of exploring the same part of this wonderful city at the same time.

I would like to thank the Cité Internationale Universitaire de Paris for hosting me and for the welcoming environment and warm atmosphere I encountered upon my arrival in France. The opportunity to live with and to become friends with hundreds of other young people from all around the world was one that I relished and will be forever grateful. Thank you to the floor 2 residents at the FEU: Deanna, Elisa, Alex, Melanie, Hannah and Zach - discovering Paris with all of you during my first year was an exciting adventure. I am also extremely grateful to have later been adopted by the Greek house at Cité Universitaire and for the many enjoyable evenings spent in the salon of the Fondation Hellénique: particular thanks to Chris, Revekka, Zitania, Gianluca and Melina. Chris - I hope you will one day be able to beat me at FIFA. Gianluca - thank you for all the delicious pizza and Focaccia!

Μελίνα - Σε ευχαριστώ για όλη αυτή την στήριξη και ιδιαιτέρως, για το ότι με ξυπνούσες συνεχώς στην ώρα μου για να γράψω αυτό το διδακτορικό - καλημέρα τραχανα!

Finally to my family: to Nana and Papa - I am thinking of you, this thesis would literally never even have begun without you. To Granny - I finished my big sum on the computer! Ruairi - I am looking forward to our next kayak adventure to Lerici! De - I hope you get to meet Damo soon. Donagh aka “The Don” - congratulations on being possibly the youngest ever participant of a PhD defence! Brian and Aedeen - thank you for the molkky sessions, I look forward to the next big tournament in Tellaro. Mum and Dad, thank you for everything - I can’t describe how much I mean that. I look forward to a day in the near future when we will all be catching up and celebrating in Finnegan’s!

Contents

1 Introduction **9**

2 Bulk and Boundary CFT **13**
2.1 Conformal Transformations 13
2.2 Conformal Invariance in Field Theories 14
2.2.1 The classical case 14
2.2.2 Quantum Conformal Field Theories 15
2.3 The Hilbert Space 17
2.4 Boundary CFT 18
2.5 Statistical Mechanics 19

3 The Potts model **23**
3.1 The lattice model 24
3.1.1 Loop Model Formulation 25
3.1.2 The Temperley-Lieb algebra 27
3.1.3 The vertex representation 29
3.1.4 The blob algebra 31
3.1.5 RSOS models 34
3.1.6 Blobbed boundary conditions in the RSOS model 36
3.2 The critical ferromagnetic Potts model 37
3.3 The critical antiferromagnetic Potts model 41
3.4 New boundary conditions in the antiferromagnetic Potts model 44
3.4.1 The alt boundary conditions in the loop model 44
3.4.2 The alt boundary conditions in the RSOS model 49
3.4.3 Missing string functions and alt boundary conditions 50
3.5 Normalisability issues 52
3.5.1 A first-order boundary phase transition 54
3.6 Combining alt boundary conditions in the loop model 55
3.7 Combining alt boundary conditions in the RSOS model 57
3.7.1 Numerics 57
3.7.2 2BTL representation theory 59
3.8 Special cases: the two and three state Potts model 62
3.8.1 The alt boundary conditions in terms of Potts spins 62
3.8.2 Relationship to the six-vertex model 66
3.9 Odd number of sites and disorder operators 70

4 The Bethe Ansatz **73**
4.1 Some general properties . . . 75
4.2 Integrability: bulk and boundary . . . 76
4.3 The Analytical Bethe Ansatz . . . 77
4.4 The Hamiltonian Limit . . . 79
4.5 The CFT limit: examples . . . 80

5 Integrable boundary conditions in the Potts model **81**
5.1 The staggered six-vertex model and the D_2^2 model . . . 82
5.1.1 Background . . . 82
5.1.2 Review of the staggered six-vertex model . . . 82
5.1.3 Mapping between the two models: General strategy . . . 85
5.1.4 Deriving the Boltzmann weights . . . 86
5.2 The open D_2^2 model . . . 92
5.2.1 Hamiltonian limit . . . 93
5.2.2 Additional symmetries . . . 95
5.2.3 The $\gamma \to 0$ limit . . . 95
5.2.4 Non-zero γ . . . 96
5.3 The Bethe Ansatz solution . . . 98
5.3.1 The XXZ subset . . . 99
5.3.2 Other solutions of Bethe Ansatz equations . . . 102
5.4 Other Temperley-Lieb representations . . . 106
5.4.1 Loop representation . . . 106
5.4.2 RSOS representation . . . 106

6 A Non-Compact Boundary Conformal Field Theory **109**
6.1 New Boundary Conditions . . . 110
6.1.1 The Hamiltonian limit . . . 110
6.1.2 Geometry change . . . 111
6.1.3 The Transfer Matrix . . . 112
6.2 Finding an Exact Solution . . . 116
6.2.1 The complete solution . . . 118
6.2.2 Correspondence with the XXX model . . . 119
6.3 The Continuum Limit . . . 122
6.3.1 The Loop model . . . 123
6.3.2 Back to the Bethe Ansatz . . . 125
6.3.3 Discrete States . . . 127
6.3.4 XXZ Subset . . . 127
6.3.5 RSOS model . . . 129
6.4 A Boundary RG Flow . . . 130

7 Discussion **133**

A Résumé **137**

Chapter 1

Introduction

Since its birth in the first half of the 20^{th} century, its later evolution and final acceptance as a viable descriptor of nature in the second half of the century, Quantum Field Theory (QFT) has become an immensely powerful tool in a variety of contexts ranging from the study of fundamental particles to quantum many-body physics and condensed matter theory. Any situation that calls on QFT to tackle it is invariably reduced to the problem of calculating its correlation functions - a concept that is most intuitively understood in the path integral approach, most easily compared with ordinary quantum mechanics in the operator formalism and has what could be described as the most mathematically rigorous definition in the bootstrap approach to QFT [1].

A significant part of late 20^{th} and early 21^{st} century research in theoretical physics has been and continues to be dedicated to calculating the contributions to QFT correlation functions from Feynman diagrams at higher and higher orders. Such an approach necessarily involves perturbation theory - and hence approximations - thus putting aside any attempt at an exact solution. For any given QFT, one could hope to enhance this approach by appealing to the symmetries of the field theory under study. Indeed, it has been known for several decades that, while the correlation functions of most physical QFTs depend strongly on some length scale - the so-called correlation length - there also exist "scale-invariant" theories where this length scale diverges. Furthermore, it is known that under certain constraints, this scale invariance is in fact enhanced to conformal invariance [2] - leading us to label such theories as Conformal Field Theories (CFTs).

Conformal Field Theories in fact occupy particularly special points in the space of all possible QFTs. A generic QFT comes equipped with a characteristic length or energy scale below which - or above respectively - the theory is no longer valid in the sense that the resulting calculations should no longer be expected to correspond to the physical phenomenon under study - the famous "cut-off" of the energy scale in the path integral. One can reduce this energy cut-off and at the same time change the coupling constants of the theory in such a way as to compensate for the change in the cut-off and hence end up with the same result for the correlation function with either energy scale. Doing so continuously leads to a flow in the space of coupling constants - the so-called "Renormalisation Group" (RG) flow [3]. This leads to the concept of "universality" - whereby two quantum field theories with different coupling constants can be described by the same theory in the long distance/low energy limit - and are hence referred to as being in the same "universality class". Conformal Field Theories are the theories at the fixed points of these RG flows.

Conformal invariance however is not generally enough to calculate exactly the correlation functions of a QFT. Indeed, it is remarked in [4] that in D spatial dimensions, conformal invariance amounts to just "slightly more than rotation or scale invariance" and hence one should not necessarily expect all conformally invariant field theories to admit an exact solution just by the observation of this symmetry alone. The power of CFT becomes apparent however when we consider $D = 2$ spatial dimensions, where after allowing for *local* conformal transformations (discussed in more detail in chapter 2) one observes that there are an infinite number of independent such transformations under which the theory is invariant. This observation allowed the authors of [5] to find an exact solution of an infinite family of CFTs - now referred to as the minimal models - thus giving rise to the modern study of two dimensional CFT. These minimal models were found by studying irreducible representations of the celebrated Virasoro algebra:

$$[L_n, L_m] = (n-m)L_{n+m} + \frac{c}{12}n(n^2-1)\delta_{n+m,0} \tag{1.1}$$

which will be discussed in more detail in chapter 2. More exotic CFTs (such as those that are logarithmic - see e.g. [6, 7, 8, 9]) can be found by allowing for indecomposable, reducible representations of the Virasoro algebra. In any case, the problem of classifying two dimensional CFTs is equivalent to classifying the representations of the Virasoro algebra.

While providing a set of non-perturbative tools to solve certain strongly interacting QFTs is a valuable achievement, two dimensional CFT becomes even more exciting when applied to statistical mechanics and critical phenomena. It has long been known that lattice models undergoing a second-order phase transition have no characteristic length scale - (see for example the discussion in [10]) - and as discussed above, scale invariance typically leads to conformal invariance. One would therefore expect the long distance limit of critical lattice models to be described by CFTs, and indeed this is invariably observed to be the case. Furthermore, critical lattice models can also be categorised into universality classes in the sense that very often, two models that are described by different classical Hamiltonians (and hence different Boltzmann weights) can belong to the same universality class and hence be described by the same CFT in the long distance limit.

Modern research in CFT can be broadly classed into two main categories. The first category involves trying to gain a better understanding of CFT in dimensions higher than $D = 2$, and therefore map out new RG fixed points in the space of all QFTs. An important aspect of this is the conformal bootstrap [11, 12, 13, 14, 15] - a technique that aims to build and map out the space of conformal field theories just by using conformal symmetry and constraints that arise from consistency conditions. The second category involves taking advantage of the spectacular success of CFT in two dimensions in order to understand more complicated and physically relevant CFTs (such as those that are non-compact, logarithmic or non-unitary) that describe systems in quantum many body physics and statistical mechanics [16, 17].

This thesis will focus on the second category and will revolve around the CFT description of various critical systems defined on the lattice to find out a) what this can tell us about the thermodynamic properties of these lattice systems and b) what these

lattice systems can tell us about certain interesting CFTs.

However, phase transitions only exist in the thermodynamic limit - one should not therefore necessarily expect to be able to observe properties of a CFT directly on the finite lattice, even when the coupling constants are tuned to their critical values. Thankfully however, the CFT does leave a trace of its existence even in finite size and we can observe it by studying the finite size scaling behaviour of the eigenvalues of either the transfer matrix or Hamiltonian describing the lattice system [18, 19, 20] - this is discussed in detail in chapter 2.

Interestingly, there are situations where certain properties of the CFT *can* in fact be observed directly on the finite lattice. In particular, the structure of certain representations of the Virasoro algebra is precisely the same as the structure of certain representations of a lattice algebra known as the Temperley-Lieb algebra [21, 22, 23] and its extension - the so-called blob algebra [24, 25] - a result that is taken advantage of in chapter 3 to understand the connection between two different CFTs - the "Euclidean Black Hole CFT" and the "Parafermion CFT".

While finding the CFT that describes the thermodynamic behaviour of a given critical lattice model is often referred to as having "solved" the model, this "solution" is only exact when the lattice size is infinite. In this thesis the word "solved" will be used in this sense, and the expression "exactly solved" will be used to refer to a model that is solved in finite size - i.e. having found the eigenvalues and eigenvectors of the corresponding Hamiltonian/Transfer Matrix for all finite sizes or, as is more commonly the case, having found a method to obtain the eigenvalues and eigenvectors that is more numerically efficient than directly diagonalising the Hamiltonian/Transfer Matrix.

An exact solution in finite size is in fact very often used to find the CFT solution in the thermodynamic limit. Precisely this procedure is carried out in chapters 5 and 6 by using the Bethe Ansatz - a tool that can be applied to integrable models (see chapter 4). Integrability, and in particular the Bethe Ansatz technique, typically allows us to reduce the problem of diagonalising a transfer matrix or Hamiltonian to solving a set of coupled non-linear equations - a problem which is vastly easier to tackle numerically for Hamiltonians acting on large Hilbert spaces.

This thesis "solves" and "exactly solves" - in the sense defined above - a number of models that are listed here and explained in more detail in the main text. A central result of chapter 3 is the solution to an open boundary loop model described by a transfer matrix written entirely in terms of Temperley Lieb algebra generators e_i and blob algebra generators b:

$$T = t_1 t_2 \,, \tag{1.2}$$

where

$$t_1 = b(e_1)(x+e_3)(x+e_5)\cdots(x+e_{2L-1})(1+xe_2)(1+xe_4)\cdots(1+xe_{2L-2}) \tag{1.3}$$

$$t_2 = (1-b)(e_1)(x+e_3)(x+e_5)\cdots(x+e_{2L-1})(1+xe_2)(1+xe_4)\cdots(1+xe_{2L-2}) \tag{1.4}$$

where x is related to the Potts model coupling constant, defined in chapter 3. Chapter 5 both solves *and* exactly solves a Hamiltonian written entirely in terms of Temperley

Lieb generators e_i:

$$\mathcal{H} = -\frac{1}{\cos\gamma}(e_1 + e_{2L-1}) + 2\cos\gamma \sum_{m=1}^{2L-1} e_m - \sum_{m=1}^{2L-2}(e_m e_{m+1} + e_{m+1}e_m)\,. \tag{1.5}$$

Chapter 6 both solves and exactly solves another Hamiltonian written in terms of e_i:

$$\mathcal{H} = 2\cos\gamma \sum_{j=1}^{2L-1} e_j - \sum_{j=1}^{2L-2}(e_j e_{j+1} + e_{j+1}e_j) \tag{1.6}$$

Chapter 6 also finds that the Hamiltonian in (1.6) flows under RG to the Hamiltonian in (1.5).

This thesis is structured as follows: chapter 2 provides a brief review of conformal field theory, boundary conformal field theory and its connection to critical models in statistical mechanics. Chapter 3 considers the antiferromagnetic Potts model - the starting point of the analysis is the solution to the transfer matrix written in (3.68). This paves the way to interpreting various aspects of the CFT on the lattice such as non-normalisable states, fusion and the appearance of disorder operators. Chapter 4 provides a brief review of integrability and the Bethe Ansatz, with a particular focus on open integrable models. Chapter 5 presents an exact mapping between the vertex representation of the antiferromagnetic Potts model and an integrable model constructed from the twisted affine D_2^2 Lie algebra. This leads to the interpretation of a particular set of integrable boundary conditions (i.e. K-matrices) in terms of Temperley-Lieb generators so that the full Hamiltonian of the model with these boundary conditions becomes that written in (1.5). The exact solution of the model then leads to the solution of the corresponding CFT. A similar procedure is carried out in chapter 6, where a different D_2^2 boundary condition is considered and this time it is shown to correspond to the Hamiltonian in equation (1.6)- in this case the transfer matrix also permits an interpretation in terms of Temperley Lieb generators (see equation (6.22)). A complete Bethe Ansatz solution to the Hamiltonian in (1.6) is found and used to show that the corresponding boundary CFT is non-compact and is interpreted in terms of the Euclidean Black Hole CFT with $w = 1$. Finally, an RG flow is observed from the Hamiltonian in 1.6 to the Hamiltonian in (1.5), corresponding to an RG flow from a non-compact boundary CFT to a compact one.

Chapter 2

Bulk and Boundary CFT

The following chapter will provide a brief overview of conformal field theory (CFT) and will introduce the main objects of interest. Its main purpose is to define the notation and to introduce the tools that will be used extensively throughout this thesis. We will briefly discuss how we can use CFT to describe critical lattice models, and in particular, how we can use *boundary* CFT to describe *open* critical lattice models. We will start with a brief review of conformal transformations, followed by a concise discussion of the consequences of conformal symmetry in two-dimensional quantum field theories. We will introduce boundary conformal field theory before discussing the tools that will be used to relate statistical mechanics and CFT.

2.1 Conformal Transformations

A conformal transformation of spacetime coordinates $\mathbf{x}$ is an invertible mapping $\mathbf{x} \to \mathbf{x}'$ such that the induced change in the metric:

$$g'_{\mu\nu}(\mathbf{x}') = \frac{\partial x^\alpha}{\partial x'^\mu}\frac{\partial x^\beta}{\partial x'^\nu} g_{\alpha\beta}(\mathbf{x}) \tag{2.1}$$

is reduced to a rescaling:

$$g'_{\mu\nu}(\mathbf{x}') = \Lambda(\mathbf{x}) g_{\mu\nu}(\mathbf{x}) \tag{2.2}$$

That the transformation is invertible and defined everywhere will turn out to be a strong constraint, allowing only for so-called global conformal transformations. Local conformal transformations obey (2.2) but are not necessarily invertible or defined everywhere. Global conformal transformations are of four possible types: translations, rotations, dilations and so-called special conformal transformations (this result is derived in many places, see e.g. [26, 4]). An infinitesial translation is of the form:

$$x'^\mu = x^\mu + \epsilon^\mu \tag{2.3}$$

with ϵ^μ an infinitesimal vector. An infinitesimal rotation is of the form:

$$x'^\mu = x^\mu + \epsilon^{\mu\nu} x_\nu \tag{2.4}$$

with $\epsilon^{\mu\nu}$ an infinitesimal antisymmetric tensor. Infinitesimal dilations (i.e. scalings) are of the form:

$$\mathbf{x}' = \mathbf{x} + \epsilon\mathbf{x} \tag{2.5}$$

with ϵ an infinitesimal scalar. Finally, infinitesimal special conformal transformations are given by:

$$x'^{\mu} = x^{\mu} + 2(\boldsymbol{\epsilon}.\mathbf{x})x^{\mu} - \epsilon^{\mu}\mathbf{x}.\mathbf{x} \tag{2.6}$$

with ϵ^u an infinitesimal vector. In two dimensions we observe that the conformal group is six dimensional: two from translational symmetry, one from rotational symmetry, one from scaling and two from special conformal transformations. In what follows, we will exclusively consider two dimensions.

When we relax the constraint that the transformation $\mathbf{x} \to \mathbf{x}'$ is invertible and defined everywhere, we are left only with the constraint in equation (2.2) and it can be shown [4] that, in two dimensions, this constraint becomes just the Cauchy-Riemann equations, implying that the function $\mathbf{x}'(\mathbf{x})$ can be reformulated in terms of complex variables and is holomorphic. To do this, we introduce the complex variables:

$$\begin{aligned} z &= x^0 + ix^1 \\ \bar{z} &= x^0 - ix^1 \end{aligned} \tag{2.7}$$

The transformation $\mathbf{x} \to \mathbf{x}'$ can then be reformulated as a function $z \to f(z)$ and the constraint (2.2) requires that the function $f(z)$ be holomorphic. Since the set of holomorphic functions is infinite dimensional, so too is the set of local conformal transformations in two dimensions. This result has profound consequences in the context of field theories, both classical and quantum.

2.2 Conformal Invariance in Field Theories

2.2.1 The classical case

Conformal invariance of a classical field theory amounts to invariance of the action under conformal transformations; the constraint that the action be invariant under *local* conformal transformations therefore results in an infinite number of conserved currents/charges via Noëther's theorem, rendering the theory exactly solvable.

One of these conserved currents is the stress-energy tensor, corresponding to translational symmetry. We can simplify the relevant notation greatly by sticking with complex coordinates z and $\bar{z}$ and then making use of the notions of holomorphic and anti-holomorphic functions. The components of the stress energy tensor in this coordinate system become:

$$\begin{aligned} T_{zz} &= \frac{1}{4}(T_{11} - T_{22} + 2iT_{12}) \\ T_{\bar{z}\bar{z}} &= \frac{1}{4}(T_{11} - T_{22} - 2iT_{12}) \\ T_{z\bar{z}} &= T_{\bar{z}z} = \frac{1}{4}(T_{11} + T_{22}) \end{aligned} \tag{2.8}$$

Scale invariance causes the trace of the stress energy tensor $T_{11} + T_{22}$ to vanish so we are only left with the terms T_{zz} and $T_{\bar{z}\bar{z}}$. (Note that the vanishing trace holds also at the level of operators in the quantum theory.) The conservation law from Noëther's theorem:

$$\partial_\mu T^{\mu\nu} = 0 \tag{2.9}$$

becomes in complex coordinates:

$$\begin{aligned} \partial_{\bar{z}} T_{zz} + \partial_z T_{z\bar{z}} &= 0 \\ \partial_z T_{\bar{z}\bar{z}} + \partial_{\bar{z}} T_{\bar{z}z} &= 0 \end{aligned} \tag{2.10}$$

But since $T_{z\bar{z}}$ and $T_{\bar{z}z}$ vanish due to the disappearing trace, we have just:

$$\begin{aligned} \partial_{\bar{z}} T_{zz} &= 0 \\ \partial_z T_{\bar{z}\bar{z}} &= 0 \end{aligned} \tag{2.11}$$

If we define $T(z,\bar{z}) \equiv T_{zz}$ and $\bar{T}(z,\bar{z}) \equiv T_{\bar{z}\bar{z}}$ then (2.11) tells us that T is functionally independent from $\bar{z}$ and that $\bar{T}$ is functionally independent from z and we can write $T(z,\bar{z}) = T(z)$ and $\bar{T}(z,\bar{z}) = \bar{T}(\bar{z})$. In other words, $T(z)$ is holomorphic and $\bar{T}(\bar{z})$ is anti-holomorphic. We can therefore expand $T(z)$ as:

$$T(z) = \sum_{n\in\mathbb{Z}} z^{-n-2} L_n \tag{2.12}$$

with the L_n given by:

$$L_n = \frac{1}{2\pi i} \oint dz T(z) z^{n+1} \tag{2.13}$$

This definition of L_n actually coincides with the conserved Noëther charge resulting from a holomorphic (i.e. locally conformal) transformation given by $z \to z + \epsilon z^{n+1}$. Similarly we can write:

$$\bar{T}(\bar{z}) = \sum_{n\in\mathbb{Z}} \bar{z}^{-n-2} \bar{L}_n \tag{2.14}$$

with the $\bar{L}_n$ given by:

$$\bar{L}_n = \frac{1}{2\pi i} \oint dz \bar{T}(\bar{z}) \bar{z}^{n+1} \tag{2.15}$$

2.2.2 Quantum Conformal Field Theories

We will now consider the consequences of conformal invariance in quantum field theories. In the context of the discussion of the stress energy tensor in section 2.2.1, promoting a classical theory to a quantum theory makes the operators $T(z)$ and $\bar{T}(\bar{z})$ independent operators and hence the L_n and $\bar{L}_n$ are independent also. One can show (see e.g. [4]) that in the quantum theory, the L_n operators satisfy:

$$[L_n, L_m] = (n-m)L_{n+m} + \frac{c}{12} n(n^2-1)\delta_{n+m,0} \tag{2.16}$$

where c is the so-called central charge, one of the defining parameters of any particular conformal field theory. Equation (2.16) is the defining relation of the celebrated Virasoro algebra. The $\bar{L}_n$ satisfy the same commutation relation as (2.16) and commute with L_n. We have arrived at one of the central results of two dimensional bulk quantum conformal field theory: the full symmetry algebra is given by *two* copies of the Virasoro algebra defined in (2.16).

More generally, conformal invariance in a quantum theory amounts to invariance of the correlation functions under conformal transformations, leading to certain constraints that these correlation functions must satisfy. There is a certain class of fields in the quantum theory known as *quasi-primary* fields, an important subset of which are the *primary* fields. A spinless *quasi-primary* field $\phi(x)$ transforms under a scaling transformation as:

$$\phi(x) \to \phi'(x') = \lambda^{-\Delta_\phi}\phi(x) \tag{2.17}$$

where we have introduced Δ_ϕ, known as the scaling dimension of the field $\phi(x)$. More generally, under any *global* conformal transformation a quasi-primary field transforms as:

$$\phi(x) \to \phi'(x') = \left|\frac{\partial x'}{\partial x}\right|^{-\frac{\Delta_\phi}{2}} \phi(x) \tag{2.18}$$

It can then be shown [4] that the two point correlation function of quasi-primary fields has the following form:

$$\langle\phi(x_1)\phi(x_2)\rangle = \frac{A}{|x-y|^{2\Delta_\phi}} \tag{2.19}$$

for some constant A. A spinless *primary* field, as distinct from a quasi-primary field, transforms as (2.18) for all *local* conformal transformations, not just the global subset. The scale invariance of the quantum field theory imposes the following constraint on the n point function of a spinless quasi-primary field:

$$\langle\phi(\lambda x_1)...\phi(\lambda x_n)\rangle = \lambda^{-n\Delta_\phi}\langle\phi(x_1)...\phi(x_n)\rangle \tag{2.20}$$

It is clear that the two point correlation function in (2.19) satisfies (2.20). An example of a field that is quasi-primary but not primary is provided by the stress energy tensor. We can see this more clearly by returning to complex coordinates z. One can define a map from the plane to the cylinder by:

$$w = \frac{L}{2\pi}\log z \tag{2.21}$$

so that the “space" direction becomes the periodic axis of the cylinder and time flows along the other axis. Under such a local conformal transformation, the stress energy tensor transforms in the following way:

$$T_{cyl}(w) = \left(\frac{2\pi}{L}\right)^2\left[T_{pl}(z)z^2 - \frac{c}{24}\right] \tag{2.22}$$

One observes the appearance of the central charge c which ensures that the stress energy tensor does not obey (2.18) under this transformation, and hence is not primary. Interestingly, we can see that even when we impose that the vacuum expectation value of the stress energy tensor on the plane vanishes, it does not vanish on the cylinder and is instead given by:

$$\langle T_{cyl}(w)\rangle = -\frac{\pi^2 c}{6L^2} \tag{2.23}$$

This will prove to be an important result when we formulate the CFT as a Hamiltonian acting on some Hilbert space in the next section.

2.3 The Hilbert Space

The Hilbert space of a CFT must form a representation space of a direct sum of two copies of the Virasoro algebra. We can take advantage of this setup by defining concentric circles around the origin as the surfaces of equal time, then the dilation operator:

$$D = L_0 + \bar{L}_0 \tag{2.24}$$

generates "time" translations and can be used to define the Hamiltonian of the theory. It is natural in this set up to consider the mapping from the plane to the infinite cylinder of length L, using the transformation in (2.21). The dilation operator in (2.24) now generates translations along the "time" axis of the cylinder and we define the Hamiltonian with the following normalisations:

$$H = \frac{2\pi}{L}(L_0 + \bar{L}_0 - \frac{c}{12}) \tag{2.25}$$

The constant term can be seen to arise from (2.23), where the extra factor of L in (2.23) comes from the fact that $T(w)$ is an energy *density*. A central result of CFT is that there is a one to one mapping between the primary fields introduced in section 2.2.2 and between so-called "primary states" in the Hilbert space which obey:

$$\begin{aligned} L_n|h,\bar{h}\rangle &= 0 \ , \ n > 0 \\ \bar{L}_n|h,\bar{h}\rangle &= 0 \ , \ n > 0 \\ L_0|h,\bar{h}\rangle &= h|h,\bar{h}\rangle \\ \bar{L}_0|h,\bar{h}\rangle &= \bar{h}|h,\bar{h}\rangle \end{aligned} \tag{2.26}$$

The whole Hilbert space is spanned by these primary states and by the "descendant states" which are obtained by acting on the primaries $|h,\bar{h}\rangle$ with L_n and $\bar{L}_n$. We have introduced the quantities h and $\bar{h}$ as eigenvalues of the operators L_0 and $\bar{L}_0$ and they are connected with the scaling dimension Δ of a primary field and with the spin s in the following way:

$$\begin{aligned} \Delta &= h + \bar{h} \\ s &= h - \bar{h} \end{aligned} \tag{2.27}$$

The full Hilbert space can be divided into a series of conformal "families"; each family is constructed by starting with a primary state $|h,\bar{h}\rangle$ and acting with L_n and $\bar{L}_n$. Note that one cannot move from one conformal family to another just by acting with L_n or $\bar{L}_n$. Since L_n and $\bar{L}_n$ commute, we can consider separately the states that they generate, referred to as the "holomorphic" sector and the "anti-holomorphic" sector respectively. An important object defined for each of these sectors in any given conformal family is the "generating function" or "character" of the representation, given by:

$$\mathcal{X}_{c,h}(q) = \mathrm{Tr}\, q^{L_0 - \frac{c}{24}} \tag{2.28}$$

where q is referred to as the "modular parameter". This thesis will make regular use of the generating function and very often the aim will be to observe it on the lattice. Note that only in some special cases will a CFT have a finite number of conformal families. This thesis will be particular interested in theories with not only an infinite number of primaries and hence of conformal families, but a *continuum* of them, a key feature of so-called "non-compact" conformal field theories.

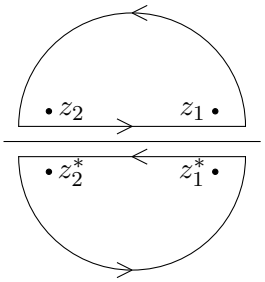


Figure 2.1: The contour integral in equation (2.30) for a boundary CFT. Boundary CFTs are only defined in the upper half plane but by using the so-called method of images [18] one can extend it to the whole plane such that the boundary CFT correlation functions are identified with those of a bulk CFT with twice as many insertions.

2.4 Boundary CFT

We have so far been working in the entire complex plane and therefore considering "bulk" conformal field theories. The most convenient way to introduce a boundary into the system is to consider the field theory to exist only in the upper half plane and to impose that there is no "momentum transfer" across the imposed boundary. This amounts to the condition: $T_{12} = T_{21} = 0$ along the real line which in complex coordinates gives $T_{zz} = T_{\bar{z}\bar{z}}$ along the real line. We can implement this constraint by imposing:

$$T(z) = \bar{T}(\bar{z}) \tag{2.29}$$

which means that T and $\bar{T}$ are no longer independent operators. From (2.13) and (2.15) we see that L_n and $\bar{L}_n$ are no longer independent either and hence the symmetry algebra of a *boundary* conformal field theory is just *one* copy of the Virasoro algebra.

The dependence of $\bar{T}$ on T (and of $\bar{L}_n$ on L_n) has far reaching consequences which will now be briefly outlined. The invariance of a QFT under a continuous symmetry leads to a set of constraints - the Ward identities - that the correlation functions of the theory must satisfy and conformal symmetry is no exception. The derivation of the conformal Ward identity for a bulk CFT can be found in many places, see for example [4, 27, 28]. The main result is that for a local conformal transformation parameterised by $\epsilon(z)$, (where we note that it is of crucial importance that ϵ is a function of z), the variation of the correlation function $X \equiv \langle \phi(x_1)...\phi(x_n) \rangle$ due to the variation of the fields is given by:

$$\delta_\epsilon \langle X \rangle = \frac{1}{2\pi i} \oint_C \mathrm{d}z \epsilon(z) \langle T(z) X \rangle - \frac{1}{2\pi i} \oint_C \mathrm{d}\bar{z} \bar{\epsilon}(\bar{z}) \langle \bar{T}(\bar{z}) X \rangle \tag{2.30}$$

where the contour C must surround all of the points x_i. In the case of a boundary CFT however, the contour is constrained to be in the upper half plane and furthermore, the two terms on the right hand side of (2.30) are not independent due to equation (2.29). The sum of the two terms then become the contour integrals in Figure 2.1, where the horizontal parts of both contours can be seen to cancel out - leaving us with a full circular contour that enters the lower half plane, now with twice the number of insertions as before. This is the "method of images" presented in [29] - the key result of which is the following: the correlation function $\langle \phi(z_1, \bar{z}_1)...\phi(z_n, \bar{z}_n) \rangle$ in a boundary CFT, defined in the upper half plane, can be written as the holomorphic correlation

function $\langle\phi(z_1)...\phi(z_n)\phi(z_1^*)...\phi(z_n^*)\rangle$ of the bulk CFT - which we see has twice as many operator insertions.

The Hilbert space of a boundary CFT is spanned by the primary states and the states created by acting with L_n. Acting on the primaries with $\bar{L}_n$ does not create states that are independent from those created by L_n. In the bulk case we mapped the plane to the infinite cylinder and defined the Hamiltonian as the generator of translations along the "time" direction of the cylinder. In the boundary case we will map the upper half plane to the infinite strip of width L, again via the map (2.21). The generator of translations along the infinite time axis is now given by the Hamiltonian:

$$H = \frac{\pi}{L}(L_0 - \frac{c}{24}) \tag{2.31}$$

The infinite strip is not however required to have the same boundary condition on both sides. One could impose a boundary condition labelled by a on the left side of the strip, and a boundary condition labelled by b on the right side. On the plane, this corresponds to having a different boundary condition on the negative real axis to the positive real axis. We can implement this by inserting a "boundary changing operator" ϕ_{ab} at the origin. Correlation functions in the theory are then calculated with ϕ_{ab} inserted at the origin, or equivalently, the "vacuum" of the boundary conformal field theory is obtained by acting on the vacuum of the bulk theory by ϕ_{ab}.

2.5 Statistical Mechanics

A large part of this thesis will be concerned with calculating CFT quantities from finite size lattice models. We briefly review here the techniques to do so, and in particular how we can use tools from statistical mechanics to study CFT. We will be particularly interested in models that can be described by a transfer matrix. Very generally speaking, the transfer matrix is an object that encodes the Boltzmann weights of one full row of the lattice under consideration, including the contribution from the interaction with the row beneath it. The full partition function of the model (i.e. the sum of the Boltzmann weights) is then typically given by

$$Z = \mathrm{Tr}\, T^m \tag{2.32}$$

where m is the number of rows in the lattice and where we must be careful by what we mean by Tr. For models with Boltzmann weights defined locally, Tr is just the usual matrix trace. However for models with non-local Boltzmann weights, e.g. loop models, this trace must be modified to become the "Markov Trace", a topic which we will not be too concerned with here. For lattice models with periodic boundary conditions, it is sometimes useful to decompose the transfer matrix into a product of "R-matrices":

$$T = \mathrm{Tr}_a(R_{a1}...R_{aL}) \tag{2.33}$$

It will be discussed in chapter 4 that when the R-matrix satisfies the Yang-Baxter equation the transfer matrix in (2.33) is integrable.

To understand how this discussion of statistical mechanics quantities is related to CFT consider the example of a lattice model living on the cylinder with local degrees of freedom $\sigma_{t,j}$ where t and j label the rows and columns of the lattice respectively. We will consider m rows and n columns and take the periodic direction to be the horizontal

direction, hence $\sigma_{t,j} = \sigma_{t,j+n}$. We will for now consider the variables σ to be the spins of the Ising model [30] but the discussion also applies to other models with locally defined Boltzmann weights. It is a well known and easily proved result [4] that the two point correlation function is given by:

$$\langle \sigma_{t,j}\sigma_{t+r,k}\rangle = \frac{\mathrm{Tr}(T^{m-r}\hat{\sigma}_j T^r \hat{\sigma}_k)}{\mathrm{Tr}\, T^m} \tag{2.34}$$

We have introduced here the lattice operators $\hat{\sigma}_j$ that act on the Hilbert space upon which the transfer matrix acts and whose eigenvalues are given by σ_j. Using the result in (2.34), and taking an infinite cylinder, i.e. $m \to \infty$, we find:

$$\langle \sigma_{t,j}\sigma_{t+r,k}\rangle \approx \langle 0|\hat{\sigma}_j \left(\frac{T}{\Lambda_0}\right)^r \hat{\sigma}_k|0\rangle \tag{2.35}$$

where $|0\rangle$ is the eigenstate of the transfer matrix with the largest eigenvalue Λ_0. Inserting now a complete set of eigenstates $|n\rangle\langle n|$ into the expression in (2.35), and using the fact that the expectation value of $\hat{\sigma}$ is vanishing, we find that it reduces to:

$$\frac{\langle 0|\hat{\sigma}_j T^r|1\rangle\langle 1|\hat{\sigma}_k|0\rangle}{\Lambda_0^r} \propto \left(\frac{\Lambda_1}{\Lambda_0}\right)^r \tag{2.36}$$

We have shown therefore that the two point correlation function on the infinite cylinder scales with the ratio of the first two eigenvalues of the transfer matrix, a result which will prove to be useful when calculating the CFT data. Consider now the CFT two point correlation function on the plane in (2.19), where fields can be normalised such that the constant A becomes 1. Under the transformation $z \to w$ from the plane to the cylinder in (2.21), this correlation function becomes:

$$\langle \phi(r,x_1)\phi(0,x_2)\rangle = \left(\frac{2\pi}{L}\right)^{2\Delta_\phi}\left[2\cosh\left(\frac{2\pi r}{L}\right) - 2\cos\left(\frac{2\pi x_{12}}{L}\right)\right]^{-\Delta_\phi} \tag{2.37}$$

where we have $w = r + ix$ and:

$$x_{12} = x_1 - x_2 \tag{2.38}$$

Taking the large r limit, we observe that the correlation function decays as:

$$\langle \phi(r,x_1)\phi(0,x_2)\rangle \propto e^{-\frac{r}{\xi}} \tag{2.39}$$

where the correlation length ξ is given by:

$$\xi = \frac{L}{2\pi\Delta_\phi} \tag{2.40}$$

Equating the scaling behaviour of the lattice two point correlation with that of the CFT, we have then:

$$\left(\frac{\Lambda_1}{\Lambda_0}\right)^r \propto e^{-\frac{r2\pi\Delta_\phi}{L}} \tag{2.41}$$

which allows us to write:

$$\log\left(\frac{\Lambda_1}{\Lambda_0}\right) = -\frac{2\pi\Delta_\phi}{L} + o\left(\frac{1}{L}\right) \tag{2.42}$$

and we recall that we have quite generally:

$$\Delta = h + \bar{h} \tag{2.43}$$

Equation (2.42) provides us with a practical way to observe the scaling dimension Δ_ϕ on the lattice by observing the scaling behaviour of the transfer matrix eigenvalues for sufficiently large L. We can in fact observe all of the scaling dimensions in the theory this way by the following more general result [26, 19, 18]:

$$\frac{\log \Lambda_i}{L} = f_0 - \frac{2\pi}{L^2}\left(\frac{c}{12} - h_i - \bar{h_i}\right) + o\left(\frac{1}{L^2}\right) \tag{2.44}$$

where Λ_i is the i-th largest transfer matrix eigenvalue and h_i and $\bar{h}_i$ are the conformal dimensions of the primary operator corresponding to that eigenvalue. Comparing equation (2.44) with (2.25) we see that after subtracting the non-universal bulk energy term term f_0, the log of the transfer matrix of the closed model corresponds to the bulk CFT Hamiltonian on the cylinder. One therefore expects a similar relationship to hold between the transfer matrix of open critical models with the Hamiltonian of a boundary CFT on the strip. The scaling behaviour of the eigenvalues of the open transfer matrix is [26, 31]:

$$\frac{\log \Lambda_i}{L} = f_0 + \frac{f_s}{L} - \frac{\pi}{L^2}\left(\frac{c}{24} - h_i\right) + o\left(\frac{1}{L^2}\right) \tag{2.45}$$

where f_s is a non-universal quantity corresponding to the surface energy, h_0 is the conformal dimension of the corresponding boundary changing operator inserted at the origin, and the other h_i are the conformal dimensions of its descendants. Comparing (2.45) with (2.31) one observes that the Hamiltonian of a boundary CFT on the infinite strip is given by the log of the open transfer matrix after subtracting the non-universal terms $f_0 L$ and f_s.

Chapter 3

The Potts model

This chapter will discuss a particular critical lattice model in the context of the discussion of bulk and boundary CFTs in chapter 2. The model of interest is the Potts model on the square lattice which has two distinct critical points, one where the model is "ferromagnetic" and one where it is "antiferromagnetic", labels which stem from the sign of the nearest neighbour coupling constant appearing in the classical Hamiltonian at each of these critical points. The ferromagnetic region has been well studied and its critical properties well established, see for instance [32, 33] as well similar work applied to Potts spin chain in [34, 35]. The antiferromagnetic region however is less well understood despite a large amount of literature on the topic [36, 32, 37, 38, 39]. Its most striking property, when studied with periodic boundary conditions, is the appearance of a continuum of critical exponents and its subsequent description, in the continuum limit, by a non-compact CFT. The remarkable nature of this result should be emphasised: the lattice model has a finite number of degrees of freedom and is compact, yet produces a non-compact field theory in the continuum limit. This continuum limit is known to be closely related to the $SL(2,\mathbb{R})_k/U(1)$ coset model [40, 41, 42], also known as the "Euclidean Black Hole CFT" as a result of its origins in string theory.

This leads us to ask questions surrounding the nature of the corresponding boundary CFT. While there are a number of examples of lattice models with a finite number of degrees of freedom that are described by non-compact continuum limits [43, 44, 45, 46], these examples only consider the periodic case. As was discussed in chapter 2, boundary conformal field theories are in some sense "simpler" than their bulk counterparts due to the appearance of just one copy of the Virasoro algebra. One would therefore hope that a more intricate understanding of the field theory limit could be reached when studied in the "simpler" case with open boundaries. The price to be paid is that one must search for lattice boundary conditions that do indeed correspond to conformal boundary conditions [47, 48, 49]; it is no guarantee that any particular boundary condition will do the trick and we will in fact present here a boundary condition that is conformal in the ferromagnetic model but seemingly *not conformal* in the antiferromagnetic case.

The point of this chapter is to elucidate the results of this search and to explore their consequences. New boundary conditions in the antiferromagnetic model are indeed found and the corresponding spectrum generating functions in the continuum limit are identified with the discrete characters of the $SL(2,\mathbb{R})_k/U(1)$ coset, hence confirming the close relationship between the antiferromagnetic Potts model and the Euclidean black hole. A number of other new results are obtained along the way. In particular, it is well

known that the Potts model can be reformulated as a RSOS height model, when the new boundary conditions are interpreted in this language one finds that the spectrum generating functions in this context are identified with the "string functions" of the $SU(2)_{k-2}/U(1)$ parafermion theory [50], a compact CFT. By using the representation theory of the lattice algebra, the Temperley Lieb algebra and its extension known as the blob algebra, the connection between the compact and non-compact models (i.e. the parafermion theory and the black hole theory) is made more precise by an expression identifying the string functions with an alternating infinite sum of discrete black hole characters.

We will begin in section 3.1 with a review of the Potts model on the square lattice and its formulation as a loop, height and vertex model. The algebraic structures required for the remainder of the chapter, namely the Temperley Lieb algebra and the blob algebra, will be reviewed. Section 3.2 will then review the Potts model at its ferromagnetic critical point. We will then consider the antiferromagnetic Potts model in section 3.3 where we will study the continuum limit of the model with free boundary conditions. The new boundary conditions mentioned above and the corresponding continuum limit will be presented in section 3.4. This section will also consider the RSOS version of the model and study the new boundary conditions in this context. Section 3.5 will consider the issues of normalisability in the black hole theory and discuss its interpretation on the lattice. Sections 3.6 and 3.7 will consider the antiferromagnetic Potts model with the new boundary conditions on *both* sides of the lattice and relate this to the fusion rules in the CFT. In fact, the fusion rules in the parafermion theory will be both observed numerically and derived analytically from the lattice results. Section 3.8 will specialise to the case of the two and three state Potts model and section 3.9 will discuss the disorder operators of the parafermion theory and their appearance on the lattice.

3.1 The lattice model

We will consider here the Q-state Potts model on the square lattice defined by the classical Hamiltonian:

$$\mathcal{H} = -K_1 \sum_{\langle ij\rangle_1} \delta_{\sigma_i,\sigma_j} - K_2 \sum_{\langle ij\rangle_2} \delta_{\sigma_i,\sigma_j} \,, \tag{3.1}$$

where $\langle ij\rangle_1$ and $\langle ij\rangle_2$ denote respectively the set of horizontal and vertical nearest neighbours, while K_1 and K_2 are the corresponding coupling constants. Eq. (3.1) gives the partition function

$$\mathcal{Z} = \sum_{\{\sigma\}} \prod_{\langle ij\rangle_1} \exp(K_1 \delta_{\sigma_i,\sigma_j}) \prod_{\langle ij\rangle_2} \exp(K_2 \delta_{\sigma_i,\sigma_j}) \,, \tag{3.2}$$

where the sum is over all configurations of the Potts spins σ. Here each spin can take the integer values $\sigma_i = 1, 2, \ldots, Q$, and $\{\sigma\}$ denotes the collection of all spins. We will be particularly interested in the isotropic model, i.e. $K_1 = K_2 = K$. In this case, eqs. (3.1)–(3.2) become

$$\mathcal{H} = -K \sum_{\langle ij\rangle} \delta_{\sigma_i,\sigma_j} \tag{3.3}$$

and

$$\mathcal{Z} = \sum_{\{\sigma\}} \exp(-\mathcal{H}) = \sum_{\{\sigma\}} \prod_{\langle ij\rangle} \exp(K \delta_{\sigma_i,\sigma_j}) \tag{3.4}$$

respectively. It is known that the model admits a duality transformation. Recall that the dual lattice can be defined by placing a lattice site at each face of the original lattice. A duality transformation then is one which defines the model on this new lattice with new coupling constants such that the new partition function only differs from the old one by a multiplicative normalisation factor. Under such a transformation the variable $v \equiv e^K - 1$ is replaced by its dual value $v^* \equiv Q/v$. It turns out that the "self-dual" point, i.e. $v_c = \sqrt{Q}$, corresponds to the ferromagnetic critical point [51]. Notice that under duality, a horizontal pair of nearest neighbours is replaced by a dual vertical pair, and vice versa. The isotropic square-lattice Potts model is also critical at another value, $v_{AF} = -2 + \sqrt{4-Q}$, the antiferromagnetic critical point [36]. Note that this point is clearly not self-dual, hence the dual value of the antiferromagnetic critical coupling $v^*_{AF} \equiv Q/v_{AF} = -2 - \sqrt{4-Q}$ provides a second AF critical point in the same universality class as v_{AF}.

3.1.1 Loop Model Formulation

The partition function in (3.2) is written as a sum over spin configurations $\{\sigma\}$. We will now proceed to formulate the Potts model as a loop model, i.e. to write $\mathcal{Z}$ in (3.2) as a sum over loop configurations. Consider again the anisotropic model where we can write

$$\begin{aligned} \exp(K_1\delta_{\sigma_i,\sigma_j}) &= 1 + v_1\delta_{\sigma_i,\sigma_j} \\ \exp(K_2\delta_{\sigma_i,\sigma_j}) &= 1 + v_2\delta_{\sigma_i,\sigma_j} \end{aligned} \tag{3.5}$$

and evaluating these identities for $\delta_{\sigma_i,\sigma_j} = 0$ or 1, we see that they are satisfied provided we set

$$\begin{aligned} v_1 &= e^{K_1} - 1 \\ v_2 &= e^{K_2} - 1\,. \end{aligned} \tag{3.6}$$

Following the strategy of Fortuin and Kasteleyn [52], we insert (3.5) into (3.2) and expand out the products. For each term in the expansion, we draw a line between neighbouring Potts spins i and j provided it corresponds to picking the second term $v_k\delta_{\sigma_i,\sigma_j}$ in (3.5), and no line if the first term, 1, is taken. Making this choice for each nearest neighbour pair defines a graph G of clusters (connected components) containing $|G_1|$ horizontal and $|G_2|$ vertical lines. We can then write the partition function as a sum over all possible clusters:

$$\mathcal{Z} = \sum_G v_1^{|G_1|} v_2^{|G_2|} \sum_{\{\sigma\}} \prod_{\langle ij\rangle \in G} \delta_{\sigma_i,\sigma_j}\,, \tag{3.7}$$

where $\sum_G$ is a sum over all clusters. We denote the total number of lines in G as

$$|G| = |G_1| + |G_2|\,. \tag{3.8}$$

If we define the quantity $C(G)$ as the number of connected components in G, the partition function (3.2) can be rewritten as [52]

$$\mathcal{Z} = \sum_G v_1^{|G_1|} v_2^{|G_2|} Q^{C(G)}\,. \tag{3.9}$$

Following Baxter, Kelland and Wu [53], we can next transform this cluster model into a loop model, i.e., rewrite the partition function as a sum over loops. The graph

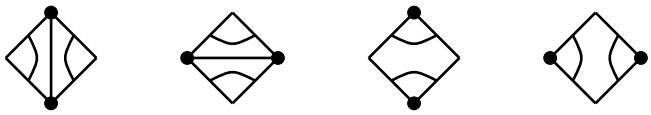


Figure 3.1: Each tile on the lattice will take one of the forms shown in panels (a), (b), (c) and (d). The black circles represent the points where the Potts spins lie. The vertices with no black circles are points on the dual lattice.

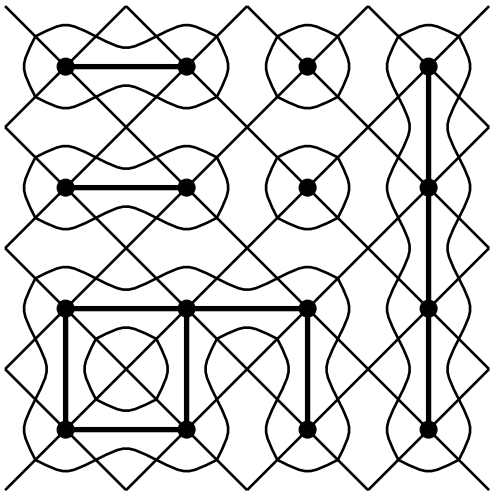


Figure 3.2: The one-to-one mapping between cluster configurations and loop configurations.

of clusters G is made up of four different types of tiles, shown in Figure 3.1, defined by the following two binary choices: 1) For tiles of type (a) and (c), the Potts spins (resp. dual Potts spins) stand at the top and bottom vertices (resp. at the left and right vertices) of the tile, while it is the other way around for tiles of type (b) and (d). 2) For tiles of type (a) and (b), the FK expansion contains a line between the two Potts spins, while for tiles of type (c) and (d) there is no such line. A loop representation equivalent to the FK one is now defined by assigning to each tile two quarter-turn loop segments, as shown in Figure 3.1. Doing this for each tile of the lattice (with appropriate boundary conditions), we obtain an ensemble of closed loops, as shown in Figure 3.2.

It follows from this property of surrounding that the number of loops ℓ in any given configuration is the sum of the number of connected components C and the number of independent cycles S in the corresponding FK cluster configuration:

$$\ell = C + S \tag{3.10}$$

We furthermore have another easily verified topological identity for each cluster configuration:

$$C = |V| - |G| + S\,, \tag{3.11}$$

where $|V|$ is the number of vertices on the lattice. Combining eqs. (3.10)–(3.11) gives us

$$C = \frac{1}{2}(|V| - |G| + \ell)\,, \tag{3.12}$$

and inserting this into (3.9) gives us the partition function expressed as a sum over loop configurations[53]

$$\mathcal{Z} = Q^{\frac{|V|}{2}} \sum_{\text{loops}} x_1^{|G_1|} x_2^{|G_2|} Q^{\frac{\ell}{2}}\,, \tag{3.13}$$

where we have defined $x_1 \equiv \frac{e^{K_1}-1}{\sqrt{Q}}$ and $x_2 \equiv \frac{e^{K_2}-1}{\sqrt{Q}}$. The isotropic case corresponds to $x_1 = x_2 = x$. In other words, apart from an unimportant overall factor, $\mathcal{Z}$ consists of local weights x_1, x_2 depending on the choice of tiles, and a non-local weight of $\sqrt{Q}$ per loop.

3.1.2 The Temperley-Lieb algebra

It will be convenient to describe the model within an algebraic framework that we now define. It will turn out that by writing the transfer matrix in terms of generators of a particular algebra, we can use some powerful tools from the representation theory of that algebra to understand aspects of the model both at the level of the lattice in finite size and of the underlying CFT itself.

In the open case with "free" boundary conditions the cluster and loop expansions described previously work in the same way. If we consider the Potts model on a strip of the square lattice of width L, the loop model defined in(3.13) can be described by a transfer matrix "propagating" in the vertical direction, given by:

$$T = (x_1 + e_1)(x_1 + e_3)\cdots(x_1 + e_{2L-1})(1 + x_2 e_2)(1 + x_2 e_4)\cdots(1 + x_2 e_{2L-2})\,. \tag{3.14}$$

Equation (3.14) and the operators e_i can be most easily understood using a graphical representation. In the factors of the form $(x_1 + e_{2k-1})$ the first term corresponds to a

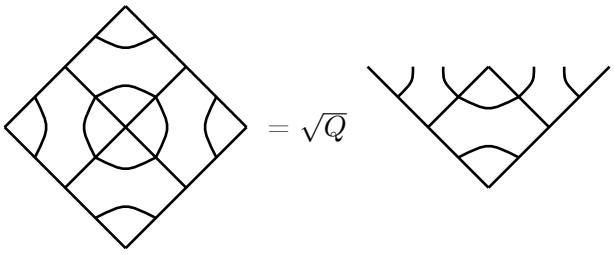


Figure 3.3: Graphical interpretation of the Temperley Lieb algebra $e_i^2 = \sqrt{Q}e_i$. Multiplying Temperley Lieb operators corresponds to stacking tiles vertically. Stacking the tiles in the left-hand part of the figure corresponds to the following string of Temperley Lieb operators: $e_i I_{i-1} I_{i+1} e_i = e_i e_i = \sqrt{Q}e_i$.

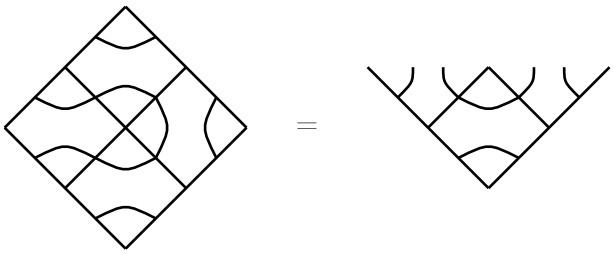


Figure 3.4: Graphical interpretation of the Temperley Lieb algebra $e_i e_{i-1} e_i = e_i$. Stacking the tiles in the left-hand part of the figure corresponds to the following string of Temperley Lieb operators: $e_i I_{i+1} e_{i-1} e_i = e_i e_{i-1} e_i$

tile of type (a) in Figure 3.1, while the second term corresponds to a tile of type (c). Similarly, in the factors of the form $(1 + x_2 e_{2k})$ the first term corresponds to a tile of type (d), while the second term corresponds to a tile of type (b). In other words, the former factors add a row of vertical edges between the Potts spins, while the latter ones add a row of horizontal edges. The action of the transfer matrix can then be seen to build all of the possible configurations of loops, with the appropriate factors of x_1 and x_2. To ensure that the transfer matrix (3.14) correctly assigns the Boltzmann weight $\sqrt{Q}$ to each loop, one imposes that the e_i satisfy the defining relations of the Temperely Lieb algebra [21]:

$$\begin{aligned} e_i^2 &= \sqrt{Q}e_i\,, \\ e_i e_{i\pm1} e_i &= e_i\,, \\ e_i e_j &= e_j e_i \text{ for } |i-j| \geq 2\,. \end{aligned} \tag{3.15}$$

In the loop language, we can interpret the TL relations graphically by associating a tile with the loop configurations shown in Figure 3.1(d) to the identity operator, and the tile in Figure 3.1(c) to the TL operator e_i. The corresponding tiles (a) and (b) have the same interpretation, except that they include the factors $x_{1,2}$ in order to account for the weighting of the lines in the expansion.

Multiplying TL generators then corresponds to stacking tiles vertically. The graphical interpretation of the relation $e_i^2 = \sqrt{Q}e_i$ is shown in Figure 3.3. We see that stacking an e_i tile on top of another e_i tile creates a loop, and this loop gets the Boltzmann weight $\sqrt{Q}$. Similarly, the relation $e_i e_{i-1} e_i$ is illustrated in Figure 3.4.

While the particular graphical description of the TL generators in Figures 3.1, 3.3

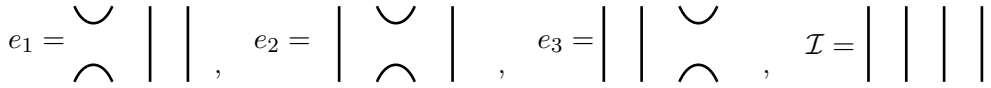


Figure 3.5: The graphical interpretation of the Temperley-Lieb loop representation.

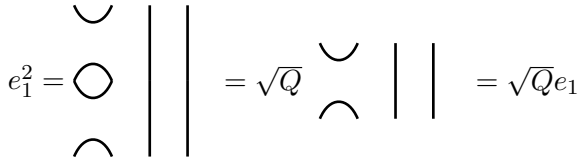


Figure 3.6: Graphical interpretation of $e_i^2 = \sqrt{Q} e_i$.

and 3.4 is convenient to illustrate the connection to the Potts model on the square lattice in Figure 3.2, slightly different notation should be used if the full power of the algebra representation theory is to be utilised. Consider the action of e_i on $N = 2L = 4$ strands. The graphical description of each of the generators for $N = 4$ is displayed in Figure 3.5. Then the graphical interpretation of the algebraic relations in (3.15) are shown in Figures 3.6 and 3.7. We can consider the transfer matrix to act on the representation spaces defined in Figure 3.8. The full space is divided into sectors $\mathcal{W}_0$, $\mathcal{W}_1$ and $\mathcal{W}_2$ where $\mathcal{W}_j$ is the sector with $2j$ through lines.

3.1.3 The vertex representation

The loop model can be reformulated as a vertex model by assigning an orientation to each of the loops. An example of a configuration of such an oriented loop model is shown in Figure 3.9. Observe that each of the tiles on the lattice now take the form of one of the vertices in Figure 3.10 instead of one of the tiles in Figure 3.1 (c) and (d). The Boltzmann weights of a vertex on a tile corresponding to a horizontal coupling of Potts spins are displayed below the vertices, and the Boltzmann weights for vertical couplings are displayed above the vertices. These weights ensure that loops oriented in an anti-clockwise direction get a Boltzmann weight of $e^{-i\gamma}$, and that loops oriented in a clockwise direction get a Boltzmann weight of $e^{i\gamma}$, hence their sum gives $\sqrt{Q} = 2\cos\gamma = e^{i\gamma} + e^{-i\gamma}$. The factors of x in Figure 3.10 then ensure that the corresponding partition function of the vertex model is equal to that of the loop model in equation (3.13). The vertex representation of the Tempereley Lieb algebra is given by:

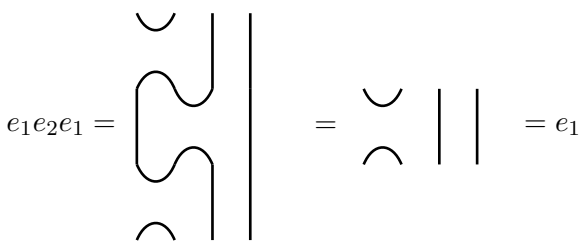


Figure 3.7: Graphical interpretation of $e_1 e_2 e_1 = e_1$.

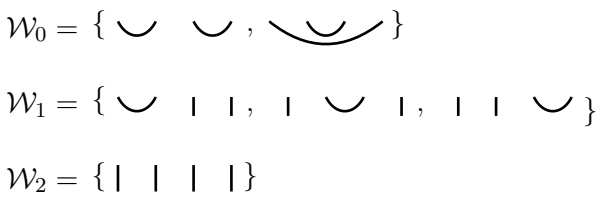


Figure 3.8: The representation spaces of the Temperley-Lieb algebra acting on $N = 4$ strands.

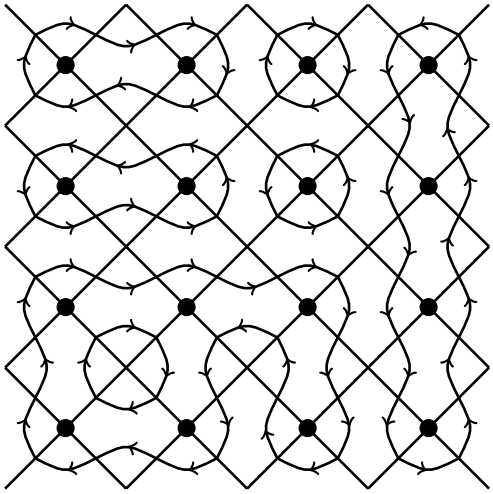


Figure 3.9: A configuration of oriented loops. The oriented loop model becomes a vertex model.

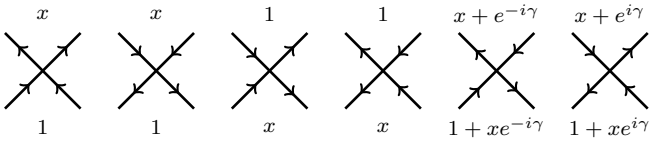


Figure 3.10: The vertices and their Boltzmann weights

$$e_n = I^{\otimes n-1} \otimes \begin{bmatrix} 0 & 0 & 0 & 0 \\ 0 & e^{-i\gamma} & 1 & 0 \\ 0 & 1 & e^{i\gamma} & 0 \\ 0 & 0 & 0 & 0 \end{bmatrix} \otimes I^{\otimes 2L-n-1} . \tag{3.16}$$

The operator e_n can also be written in terms of Pauli matrices

$$e_n = \frac{1}{2}\left[\sigma_n^x\sigma_{n+1}^x + \sigma_n^y\sigma_{n+1}^y - \cos\gamma(\sigma_n^z\sigma_{n+1}^z - I) - i\sin\gamma(\sigma_n^z - \sigma_{n+1}^z)\right] . \tag{3.17}$$

This vertex model was studied with periodic boundary conditions in [54] where one can describe it using a transfer matrix written in terms of R-matrices which at the isotropic point $x_1 = x_2 = x$ are written as:

$$R_{i,i+1} = (x + e_{2i})(1 + xe_{2i-1})(1 + xe_{2i+1})(x + e_{2i}) \tag{3.18}$$

Then the transfer matrix of the periodic model is given by:

$$T = \mathrm{Tr}_a(R_{a1}...R_{aL}) \tag{3.19}$$

It was in this representation of the Potts model that the continuum limit was found to be given by the Euclidean Black Hole CFT, discussed in section 3.3.

3.1.4 The blob algebra

The only open boundary conditions that we have so far considered are "free" boundary conditions and the corresponding transfer matrix was written in equation (3.14). Free boundary conditions turn out to be conformally invariant in the continuum limit for both the ferromagnetic and antiferromagnetic models, as will be discussed below. The ferromagnetic model admits another type of conformally invariant boundary conditions referred to as "blob" boundary conditions for reasons that will now be discussed.

Consider the open Q-state Potts model where the Potts spins on one of the boundaries (say the left boundary for now) are restricted to take values in $\{1, 2, \ldots, Q_1\}$ with $Q_1 \leq Q$. By carrying out the mapping from the Potts model to the loop model outlined in section 3.1.1, but this time with the new restricted boundary conditions, one arrives at the following loop model partition function:

$$\mathcal{Z}_{\text{blob}} = Q^{\frac{|V|}{2}} \sum_{\text{loops}} x^{|G|} Q^{\frac{\ell}{2}} \left(\frac{Q_1}{Q}\right)^{l_1} \tag{3.20}$$

where l_1 is the number of loops that touch the left boundary, l is still the *total* number of loops and we have set $x_1 = x_2 = x$. By setting:

$$y = \frac{Q_1}{\sqrt{Q}} \tag{3.21}$$

we can rewrite equation (3.20) as:

$$\mathcal{Z}_{\text{blob}} = Q^{\frac{|V|}{2}} \sum_{\text{loops}} x^{|G|} (\sqrt{Q})^{l-l_1} y^{l_1} \tag{3.22}$$

where we see that the "blob" partition function is a sum over loop configurations where, as in the periodic and free case, loops in the bulk get a Boltzmann weight $\sqrt{Q}$ but now

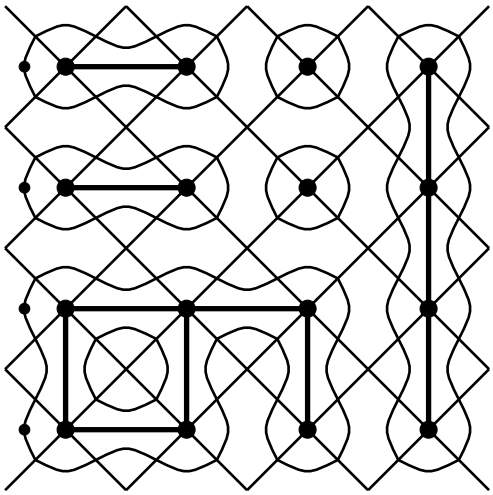


Figure 3.11: The blobbed loop model where loops that touch the left boundary at least once (blobbed loops) get a modified Boltzmann weight.

loops that touch the left boundary at least once get a Boltzmann weight $y = \frac{Q_1}{Q}$. We mark these boundary loops with a "blob", as is shown in a typical configuration of loops with these boundary conditions in Figure 3.11. Note that for the original Q-state Potts model where Q must be an integer, this boundary condition only makes sense if $Q_1 \leq Q$ is also integer. However, once the definition of the model has been extended to all real values of Q in the loop model, it is no longer necessary to impose this restriction on Q_1, which can hence take arbitrary real values as well. The blobbed loop Boltzmann weight y is normally parameterised in the following way:

$$y = \frac{\sin((r+1)\gamma)}{\sin(r\gamma)} \tag{3.23}$$

While the Temperley Lieb algebra was used to describe free boundary conditions, we will turn to an extension of this algebra, the blob algebra [55, 56, 57], to describe the "blobbed" boundary conditions. The blob algebra is defined by supplementing (3.15) by an extra generator b subject to the new relations:

$$\begin{aligned} e_1 b e_1 &= y e_1 \,, \\ b^2 &= b \,, \\ e_i b &= b e_i \text{ for } i > 1 \,. \end{aligned} \tag{3.24}$$

The graphical interpretation of the first of these relations is illustrated in Figure 3.12. The blob operator b adds a "blob" to the left most loop strand and closed "blobbed loops" then get the modified Boltzmann weight y. The relation $b^2 = b$ describes the property that loops which touch the left boundary more than once get the same weight as loops that touch the left boundary exactly once. Note that the general blob boundary conditions include the case of free boundary conditions ($Q_1 = Q$), as well as, for $Q \in \{1, 2, 3, 4\}$ integer, the case of fixed ($Q_1 = 1$) or "mixed" ($1 < Q_1 < Q$ integer) boundary conditions [58]. Just as in Figure 3.5 we introduced an explicit representation of each Temperley Lieb algebra generator, we will do the same for the blob algebra - its graphical representation when acting on $N = 4$ strands is shown in Figure 3.13. Staying with this notation, the first identity in equation (3.24) is depicted graphically in Figure 3.14.

Now consider the representation spaces that the blob algebra acts on. We must distinguish between spaces $\mathcal{W}_j^b$ and $\mathcal{W}_j^u$ corresponding to sectors with $2j$ "through lines"

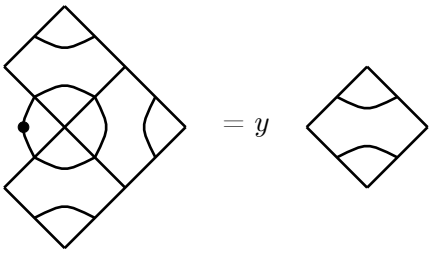


Figure 3.12: Graphical interpretation of the blob algebra relation $e_1be_1 = ye_1$

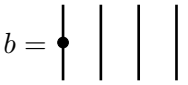


Figure 3.13: The graphical interpretation of the blob generator b.

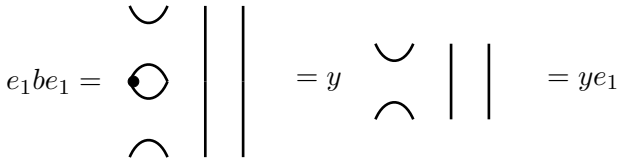


Figure 3.14: Graphical interpretation of $e_1be_1 = ye_1$

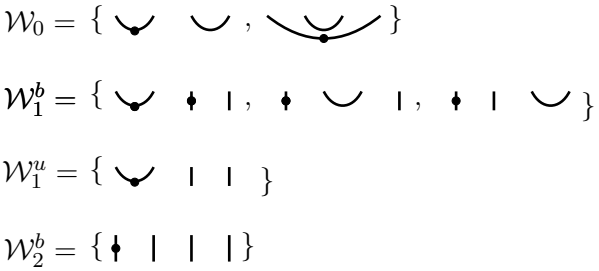


Figure 3.15: The representation spaces of the blob algebra acting on $N = 4$ strands.

where the leftmost through line is "blobbed" and "unblobbed" respectively. The spaces for $N = 4$ are shown in Figure 3.15. Clearly there is no notion of "blobbed" and "unblobbed" sectors when $j = 0$ since there is no line to blob in that case. Similarly, when $2j = N$ we do not consider the "unblobbed" sector since we are imposing that loops that touch the left boundary must take a blob. Both of these points are illustrated in Figure 3.15.

3.1.5 RSOS models

RSOS models are defined by assigning integer heights both to the vertices where the Potts spins lie and to their duals. More precisely, the RSOS heights live on all of the vertices of the tilted square lattice shown in Figure 3.2. In the models of interest here, the heights are constrained such that nearest neighbours must differ by ± 1. More generally however, RSOS models can be built from a Dynkin diagram [59, 60, 61] and obey the more general constraint that nearest neighbour heights on the lattice must also be nearest neighbours in the Dynkin diagram. We are considering here the "A-series" RSOS models, hence the particular constraint that the heights differ by ± 1.

We should also clarify here that the RSOS models of interest are *not* the same models as the RSOS models introduced by Andrews, Baxter and Forrester (ABF) [62]. The RSOS models that we are interested in, henceforth referred to as the AF Potts RSOS models, have Boltzmann weights assigned to each tile, and these weights are "staggered", i.e., even and odd numbered tiles will have different Boltzmann weights. These staggered weights ultimately stem from the alternating local weights x_1 and x_2 defined in (3.13).

To understand this in detail, consider the lattice in Figure 3.16. The degrees of freedom which live on the vertices of the lattice are integer heights from the set $\{1, 2, \ldots, k-1\}$—i.e., the Dynkin diagram A_{k-1}—where the parameter k will be related to the loop weight $\ell = 2\cos\gamma$ via the relation $\gamma = \frac{\pi}{k}$. Boltzmann weights are then associated to each tile and depend on the heights at each of the tile's vertices; see Figure 3.17. Each tile in the lattice is labelled by an integer giving its position along the horizontal axis, as shown in Figure 3.16. The staggering comes about by allowing the Boltzmann weights to depend on the parity of the tile label. Specifically, to tiles with an even label we give the weight

$$W(a,b,c,d) = \delta(a,c) + x_2 \frac{\sqrt{S_a S_c}}{\sqrt{S_b S_d}} \delta(b,d)\,, \tag{3.25}$$

whereas tiles with an odd label get the weight

$$W(a,b,c,d) = x_1 \delta(a,c) + \frac{\sqrt{S_a S_c}}{\sqrt{S_b S_d}} \delta(b,d)\,. \tag{3.26}$$

In these expressions, the height values a, b, c, d are associated with the vertices bordering the tile as shown in Figure 3.17, and we have defined

$$S_a = \frac{\sin(\frac{a\pi}{k})}{\sin(\frac{\pi}{k})}\,. \tag{3.27}$$

It is easy to see that the weights x_1 and x_2 are analogous to those appearing in Figure 3.1. Moreover, the Kronecker deltas are related with the line expansion in Figure 3.2.

We can describe the AF Potts RSOS model using the transfer matrix defined in (3.14), but using a new "RSOS representation" of the Temperley Lieb generators e_i

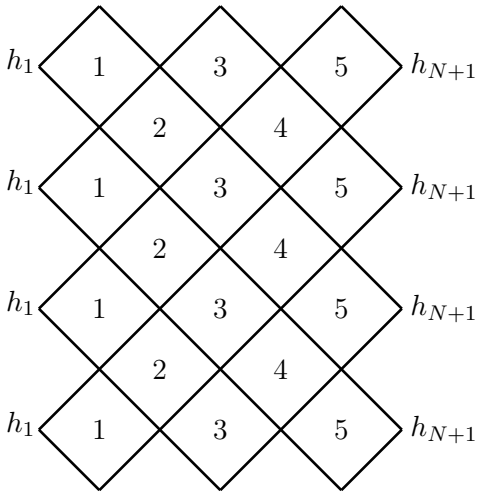


Figure 3.16: The staggered RSOS model. An integer heights lives on each vertex, here shown for a lattice of width $N = 2L = 6$. The numbers on the centre of the tiles are labels; in the staggered model, even and odd numbered tiles get different Boltzmann weights. When we fix the boundary heights h_1 and h_{N+1}, the model corresponds to "free" boundary conditions in the original formulation of the Q-state Potts model.

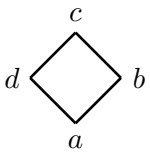


Figure 3.17: Four heights around a tile in the RSOS model

[59], given explicitly by

$$e_i \left|h_1, \ldots, h_{i-1}, h_i, h_{i+1}, \ldots, h_{N+1}\right\rangle = \delta(h_{i-1}, h_{i+1}) \sum_{h_i'} \frac{\sqrt{S_{h_i} S_{h_i'}}}{S_{h_{i-1}}} \left|h_1, \ldots, h_{i-1}, h_i', h_{i+1}, \ldots, h_{N+1}\right\rangle , \tag{3.28}$$

where $|h_1, \ldots, h_{i-1}, h_i, h_{i+1}, \ldots, h_{N+1}\rangle$ is a state specifying the heights on the $N+1$ consecutive sites along one row of the lattice (see Figure 3.18). This representation of e_i recovers the Boltzmann weights defined in equations (3.25) and (3.26).

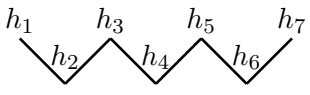


Figure 3.18: The state $|h_1 h_2 h_3 h_4 h_5 h_6 h_7\rangle$.

Note that the transfer matrix in (3.14) corresponds to "free" boundary conditions in the Q-state Potts model but in the RSOS formulation of the model that we have just described we must fix the heights at the two boundaries. Section 3.1.6 will discuss in more detail the mapping between the Potts/loop version of the model with the RSOS version, and in particular, the interpretation of blobbed boundary conditions in the RSOS model.

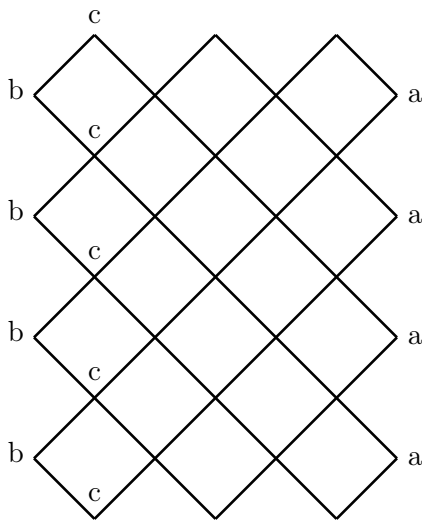


Figure 3.19: The RSOS model: heights live on the all vertices. In the ferromagnetic model, fixing the heights at a,b and c is a conformal boundary condition.

3.1.6 Blobbed boundary conditions in the RSOS model

In section 3.1.5 it was shown that the RSOS model with the outermost heights fixed to constant values could be described by the same transfer matrix (3.14) as the loop model with free boundary conditions, but with the loop representation of e_i replaced with the RSOS representation written in equation (3.28). To understand how we can interpret the blobbed boundary conditions of section 3.1.4 we will briefly review the link between the loop and RSOS versions of the model. In particular, we will show that the partition functions of the two models can be identified.

Consider again the transfer matrix of the RSOS model (equations (3.14) and (3.28)) and decorate each tile with either a vertical line or a horizontal line corresponding to the identity operator and the Temperley Lieb operator respectively. We also need to include a factor of $x = \frac{e^K - 1}{\sqrt{Q}}$ on the vertical lines for odd numbered tiles, and on the horizontal lines for even numbered tiles, (corresponding to the position of the factors of x in (3.47)). Due to the presence of the delta function on the right hand side of equation (3.28), these lines form configurations of clusters that join equal heights. To each of these cluster configurations we can associate a loop configuration by decorating each tile as in Figure 3.20.

The Boltzmann weights defined in equations (3.26) and (3.25) of the RSOS model result in the same partition function as the loop model defined by the transfer matrix in equation (3.47). (This statement is true only when one is careful with the boundary conditions in both models; as emphasised previously, free boundary conditions in the loop model are mapped to a boundary condition in the RSOS model where the outermost heights are fixed). There is a long discussion of this identity of loop model/RSOS model partition functions in [57]. The main idea of the mapping is that since heights in the RSOS model must differ by ± 1, once we fix a particular height to be b say, each neighbouring interaction contributes $\frac{S_{b+1}}{S_b} + \frac{S_{b-1}}{S_b}$ to the partition function. From

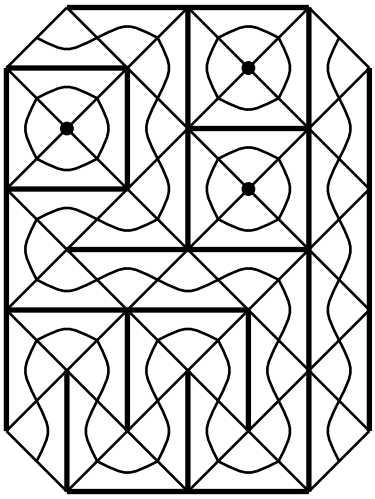


Figure 3.20: The RSOS and loop models: the lines join vertices with equal heights. Vertical lines correspond to the identity operator and horizontal lines correspond to the Temperley Lieb operator. Periodic boundary conditions in the vertical direction are imposed.

equation (3.27) then we have:

$$\frac{S_{b+1}+S_{b-1}}{S_b} = \frac{\sin(\frac{(b+1)\pi}{k}) + \sin(\frac{(b-1)\pi}{k})}{\sin\left(\frac{b\pi}{k}\right)} = 2\cos\left(\frac{\pi}{k}\right) = \sqrt{Q}. \tag{3.29}$$

where we recall that $\sqrt{Q}$ is the Boltzmann weight of a loop in the loop model. Equation (3.29) is the crucial relationship that leads to the identification of the loop model and RSOS partition function in [57]. Consider then the RSOS boundary conditions in Figure 3.19 where the outermost heights have been fixed to b and a and the the second height from the left has been fixed to $c = b \pm 1$. The analogy to equation (3.29) for the boundary then is

$$\frac{S_{b+1}}{S_b} = \frac{\sin(\frac{(b+1)\pi}{k})}{\sin\left(\frac{b\pi}{k}\right)} = y \tag{3.30}$$

if c is fixed to $c = b + 1$ and if we take $r = b$ in equation (3.23). Therefore, the interpretation of blobbed boundary conditions defined in section 3.1.4 in the RSOS model is those defined in Figure 3.19 with $c = b + 1$.

3.2 The critical ferromagnetic Potts model

There are two well-known critical lines of physical interest for the Q-state Potts model on the square lattice. The ferromagnetic self-dual line is obtained for $x_1x_2 = 1$, with $x_i > 0$. The isotropic case corresponds to $x_1 = x_2 = 1$ and thus

$$e^{K_1} = e^{K_2} = 1 + \sqrt{Q} \tag{3.31}$$

The continuum limit of the ferromagnetic loop model is reviewed in many places (see e.g. [32, 33]). The isotropic ferromagnetic model with free boundary conditions is described by the transfer matrix:

$$T = (1 + e_1) \cdots (1 + e_{2L-1})(1 + e_2) \cdots (1 + e_{2L-2}) \tag{3.32}$$

When we take the continuum limit, the space that the transfer matrix acts on should become the Hilbert space of the corresponding CFT. We will be interested in calculating the CFT generating function, which is defined by the trace of the operator $q^{L_0-c/24}$ over the CFT Hilbert space. We will study separately the action of the transfer matrix on the modules $\mathcal{W}_j$ and each of these modules will produce a different CFT generating function. Note that taking each $\mathcal{W}_j$ separately only makes sense when we impose that e_i acting on two "defect lines" at positions i and $i+1$ gives zero - otherwise the space $\mathcal{W}_j$ would interact with $\mathcal{W}_{j-1}$ under the action of e_i. We will then use the notation $\mathrm{Tr}_{\mathcal{W}_j}$ to mean the trace over the modules of the Temperely-Lieb algebra in the sector with $2j$ through lines and this trace should become a CFT generating function when we take the continuum limit. In particular, we will write $\mathrm{Tr}_{\mathcal{W}_j} q^{L_0-c/24}$ to mean the CFT generating function obtained in the continuum limit by acting on the TL module $\mathcal{W}_j$. One then obtains these generating functions by studying the finite size scaling behaviour of the free energy density f_L:

$$f_L = f_0 + \frac{f_s}{L} - \frac{\pi(\frac{c}{24} - h)}{L^2} + o\left(\frac{1}{L^2}\right) , \tag{3.33}$$

where f_L is related to the leading transfer matrix eigenvalue λ_0 by [1]

$$f_L = \frac{\log \lambda_0}{2L} . \tag{3.34}$$

We compute f_L explicitly by exact numerical diagonalisation methods, then extract h and c by studying the scaling of f_L and comparing with (3.33). We find the remaining exponents in the model by extrapolating to the limit $\frac{1}{L} \to 0$ the quantities

$$h^{(L)} = -\frac{L}{\pi} \log \left| \frac{\lambda^i}{\lambda_0} \right| , \tag{3.35}$$

where λ^i denotes the i-th leading transfer matrix eigenvalue. It is found that, by applying this procedure to the transfer matrix in equation (3.32), one arrives at the generating function Z_j of levels corresponding to a Kac module:

$$Z_j = \mathrm{Tr}_{\mathcal{W}_j} q^{L_0-c/24} = q^{-\frac{c}{24}} \frac{q^{h_{1,1+2j}} - q^{h_{1,-1-2j}}}{\prod_{n=1}^{\infty}(1-q^n)} \tag{3.36}$$

where

$$h_{r,s} = \frac{(kr-(k-1)s)^2 - 1}{4k(k-1)} \tag{3.37}$$

and

$$c = 1 - \frac{6}{k(k-1)} . \tag{3.38}$$

where we have used the parametrisation $\sqrt{Q} = 2\cos\gamma$, with $\gamma = \frac{\pi}{k}$ and $k \geq 2$.

The ferromagnetic loop model with blobbed boundary conditions is described by the transfer matrix:

[1] The factor of 2 appearing here comes from the fact that (3.47) is a double-row transfer matrix. We will later consider an example of a four-row transfer matrix—see eq. (3.68)—where this factor of 2 will be replaced by 4 when computing the exponents.

$$T = b(1+e_1)\cdots(1+e_{2L-1})(1+e_2)\cdots(1+e_{2L-2})\,, \tag{3.39}$$

When the blob transfer matrix in equation (3.39) acts on the $\mathcal{W}_j^b$ module, the generating function of levels in the continuum limit is that of a Verma module:

$$Z_j^b = \mathrm{Tr}_{\mathcal{W}_j^b} q^{L_0 - c/24} = q^{-\frac{c}{24}} \frac{q^{h_{r,r+2j}}}{\prod_{n=1}^{\infty}(1-q^n)} \tag{3.40}$$

where r is the parameter appearing in the weights of the blobbed loops, defined in (3.23). Similarly, when the transfer matrix in (3.39) acts on the $\mathcal{W}_j^u$ module the Verma module generating function that we get in the continuum limit is:

$$Z_j^u = \mathrm{Tr}_{\mathcal{W}_j^u} q^{L_0 - c/24} = q^{-\frac{c}{24}} \frac{q^{h_{r,r-2j}}}{\prod_{n=1}^{\infty}(1-q^n)} \tag{3.41}$$

We see then that the representation spaces of the Temperley Lieb algebra and the blob algebra become, in the continuum limit, representation spaces of the Virasoro algebra. In the case of the Temperley Lieb transfer matrix in equation (3.32), we get a Kac module and for the blob transfer matrix in (3.39) we get a full Verma module. However, when the parameters k, r and s take integer values, it is well known that the Verma modules are reducible. As we will now see, this property of reducibility in the continuum limit can actually be seen in finite size by studying the representation theory of the blob algebra.

Let's first consider how this works for the Temperley Lieb algebra and the corresponding Kac module in the continuum limit (see equation (3.36)). Consider the representation spaces of the Temperley Lieb algebra with $N = 4$ strands as in Figure (3.8), and let's take the simple case of $\sqrt{Q} = 1$. In this case, the space shown in Figure 3.21 is annihilated by e_1, e_2 and e_3. The space $\mathcal{W}_2$ in Figure (3.8) is also annihilated by e_1,

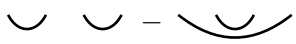


Figure 3.21: A state in $\mathcal{W}_0$ with $N = 4$ strands that is annihilated under the action of the Temperley Lieb algebra for $\sqrt{Q} = 1$ and is isomorphic to $\mathcal{W}_2$.

e_2 and e_3 since, as before, we impose that e_i acting on two through lines at sites i and $i+1$ gives zero. Hence, the space $\mathcal{W}_2$ is isomorphic to the space in $\mathcal{W}_0$ that is displayed in Figure 3.21. The fact that $\mathcal{W}_0$ contains an invariant subspace at all means that it is a reducible representation, but we can make an irreducible representation by taking the quotient of $\mathcal{W}_0$ with respect to its invariant subspace - that which is isomorphic to $\mathcal{W}_2$. We write this quotient as $\frac{\mathcal{W}_0}{\mathcal{W}_2}$. One can perform the same calculation for $N = 6$ (see e.g. appendix A of [63]) to find the exact sequence shown in Figure 3.22, (and in fact, Figure 3.22 is an example of a short exact sequence). Setting, as before, $\sqrt{Q} = 2\cos\gamma$ and $\gamma = \frac{\pi}{k}$, the exact sequence for general N and k is shown in Figure 3.23. Moving now to the blob algebra, we recall from Figure 3.15 that representations come in two forms, $\mathcal{W}_j^b$ and $\mathcal{W}_j^u$. Performing the same calculation as for the Temperley Lieb algebra leads to an exact sequence in terms of quotients of $\mathcal{W}_j^b$ and $\mathcal{W}_j^u$. The details of the calculation can be found in the appendix of [63] and the result is presented in Figure 3.24. There is a more intricate structure to the representation theory of the blob algebra than is

$$0 \longleftarrow \mathcal{W}_0 \longleftarrow \mathcal{W}_2 \longleftarrow \mathcal{W}_3 \longleftarrow 0$$

Figure 3.22: A short exact sequence of Temperley Lieb algebra representations for $N = 6$ and $\sqrt{Q}$=1.

$$\mathcal{W}_j \longleftarrow \mathcal{W}_{k-1-j} \longleftarrow \mathcal{W}_{k+j} \longleftarrow \mathcal{W}_{2k-1-j} \longleftarrow \dots$$

Figure 3.23: An exact sequence of Temperley Lieb algebra representations for general N and k.

captured by Figure 3.24. In particular, it is known (see e.g. [64]) that for r and k integer the module $\mathcal{W}^b_{k-r-j}$ is an invariant subspace (under the action of the blob algebra) of $\mathcal{W}^b_j$. To create an irreducible representation of the blob algebra on the lattice, and indeed an irreducible representation of the Virasoro algebra in the continuum limit one should consider the full diagram of inclusions of the blob algebra which is shown in Figure 3.25. In this case an arrow from one space to another means that the first space is isomorphic to an invariant subspace of the second. For example, $\mathcal{W}^b_j \leftarrow \mathcal{W}^u_{r+j}$ means that $\mathcal{W}^u_{r+j}$ is an invariant subspace of $\mathcal{W}^b_j$.

As before, to create an irreducible representation one must quotient out all of the invariant subspaces. Using the diagram in Figure 3.25, the irreducible representation is formally obtained via

$$\mathcal{X}^b_{r,j} = \bigoplus_{n=0}^{\infty} \frac{\mathcal{W}^b_{j+nk}/\mathcal{W}^u_{j+r+nk}}{\mathcal{W}^b_{k-j-r+nk}/\mathcal{W}^u_{k-j+nk}} \tag{3.42}$$

The quantity $\mathcal{X}^b_{r,j}$ is the irreducible module. Calculating then the corresponding generating function in the continuum limit of the irreducible representation, one arrives at the infinite alternating sum:

$$\mathrm{Tr}_{\mathcal{X}^b_{r,j}}\, q^{L_0-c/24} = \sum_{n=0}^{\infty}(Z^b_{j+nk} - Z^b_{k-r-j+nk}) - \sum_{n=0}^{\infty}(Z^u_{j+r+nk} - Z^u_{k-j+nk}) \tag{3.43}$$

This irreducible representation of the lattice algebra in fact corresponds to the RSOS representation and predicts that the expression in (3.43) is the generating function of the RSOS model with blobbed boundary conditions as defined in 3.1.6. Recall now the well studied (see e.g. [4]) method to construct an irreducible representation starting from a Verma module, i.e. the construction of CFT minimal models. One starts with a Verma module $V_{r,s}$, that is a highest weight representation of the Virasoro algebra and quotients out the singular vectors to build an irreducible representation. The inclusion diagram for the Verma module is shown in Figure 3.26. One observes that it is in exact correspondence with the inclusion diagram of the blob algebra in Figure 3.25 when the following correspondences are made:

$$\begin{aligned} \mathcal{W}^b_j &\leftrightarrow \mathcal{V}_{r,r+2j} \\ \mathcal{W}^u_j &\leftrightarrow \mathcal{V}_{r,r-2j} \end{aligned} \tag{3.44}$$

The character of the minimal models is then given by an infinite alternating sum of Verma module characters, and this expression must then coincide with the expression in (3.43).

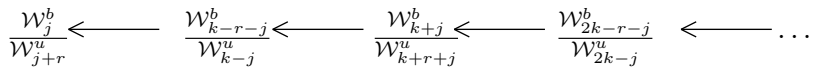


Figure 3.24: An exact sequence of blob algebra representations for general N and k.

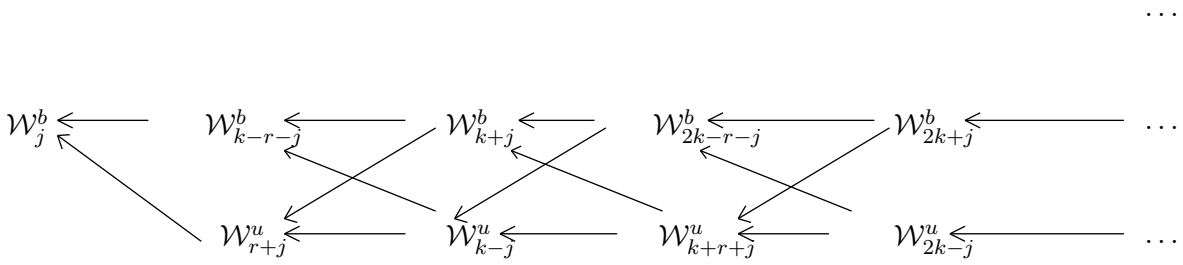


Figure 3.25: The inclusion diagram of the blob algebra module $\mathcal{W}_j^b$

While the expression in (3.43) relating the generating function of minimal models to an infinite alternating sum of Verma module generating functions was known before the representation theory of the blob algebra was worked out, the above analysis provides us with some useful insights for how to understand the Virasoro algebra on the lattice. In particular, later sections will apply the same techniques from the above analysis to the *antiferromagnetic* model and in so doing will derive a new identity relating the generating functions of the parafermion CFT (so-called "string functions") to the discrete character of the Euclidean Black Hole CFT.

3.3 The critical antiferromagnetic Potts model

The antiferromagnetic (AF) critical line is given by

$$\left(e^{K_1}+1\right)\left(e^{K_2}+1\right)=4-Q \tag{3.45}$$

and at the isotropic point corresponds to

$$e^{K_1}=e^{K_2}=-1+\sqrt{4-Q}\,. \tag{3.46}$$

Note that the corresponding loop model has weights that depend also on $|G|$, the number of lines in the graphical expansion. Free boundary conditions are known to be conformally invariant for the antiferromagnetic Potts model, just like they were for the ferromagnetic one. The transfer matrix is given by equation (3.14), which reads in the isotropic case

$$T=(x+e_1)\cdots(x+e_{2L-1})(1+xe_2)\cdots(1+xe_{2L-2})\,, \tag{3.47}$$

but now with the AF choice (3.46) of the coupling constants:

$$x=\frac{e^K-1}{\sqrt{Q}}=\frac{-2+\sqrt{4-Q}}{\sqrt{Q}} \tag{3.48}$$

This corresponds, in the six-vertex model representation of the TL algebra, to a staggered six-vertex model (see Figure 3.10) with full $U_{\mathfrak{q}}sl(2)$ symmetry: the transfer matrix

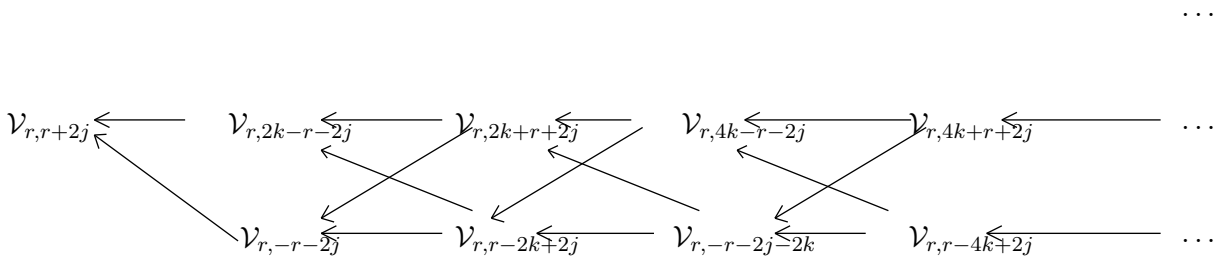


Figure 3.26: The inclusion diagram of the Verma module $\mathcal{V}_{r,r+2j}$

(3.47) commutes with the generators of the quantum group [22]. The central charge along the AF line is well established to be [32, 37]

$$c_{\rm PF} = 2 - \frac{6}{k}\,, \tag{3.49}$$

where the subscript PF abbreviates "parafermion" for reasons that will be exposed in detail below. This can be observed by studying the finite size scaling behaviour of the largest eigenvalue of the transfer matrix using (3.33). The full CFT describing the continuum limit of the AF Potts model with these boundary conditions was elucidated as early as [32], and further studied and confirmed in [65, 66, 37]. In the sector with $l = 2j$ through lines the leading critical exponent is given by:

$$\Delta_l = \frac{l(l+2)}{4k}\,, \tag{3.50}$$

which can be identified [32, 37] as one of a more general family of exponents for the $SU(2)_{k-2}/U(1)$ compact parafermion theory

$$\Delta_l^m = \frac{l(l+2)}{4k} - \frac{m^2}{4(k-2)}\,. \tag{3.51}$$

In particular, we have $\Delta_l = \Delta_l^0$. The full generating function of conformal levels was proposed to be [32]

$$K_l = {\rm Tr}_{\mathcal{W}_{j=l/2}} q^{L_0 - c/24} = \frac{q^{(l+1)^2/4k}}{\eta(q)^2}\left[1 + 2\sum_{n=1}^{\infty}(-1)^n q^{n(n+l+1)/2}\right]\,, \tag{3.52}$$

where we have parameterised $\sqrt{Q} = \mathfrak{q} + \mathfrak{q}^{-1}$, with $\mathfrak{q} \equiv e^{i\gamma} \equiv e^{i\pi/k}$. While the initial identification of the K_l generating functions was restricted to a few levels in [32], we have carefully checked the validity of the expansion (3.52) for a large number of levels. For K_0 for instance we have

$$K_0 = q^{-\frac{c_{\rm PF}}{24}}(1 + q^2 + 2q^3 + 4q^4 + 6q^5 + 11q^6 + \cdots)\,. \tag{3.53}$$

This has been observed on the lattice by the analysis of the first 40 eigenvalues of the transfer matrix (3.47). By considering sizes up to $N = 24$ we can see the first six levels (with multiplicities) of the spectrum generating function, as is written in equation

(3.53). For concreteness, we have focussed on the case $k = 4.2$, but other values confirm this result. Similarly, we have observed the following levels for $j = 1$:

$$K_2 = q^{\Delta_2 - \frac{c_{\rm PF}}{24}}(1 + 2q + 3q^2 + 6q^3 + 10q^4 + \cdots)\,. \tag{3.54}$$

The continuum limit is also closely related [54, 67, 68, 69] with the $SL(2,\mathbb{R})_k/U(1)$ coset model [41, 40], henceforth simply referred to as the black-hole (BH) theory because of its string-theory origins. Recall that this CFT has central charge:

$$c_{\rm BH} = 2 + \frac{6}{k-2}\,, \tag{3.55}$$

and conformal weights:

$$h_{\rm BH} = -\frac{J(J-1)}{k-2} + \frac{(n \pm wk)^2}{4k} \tag{3.56}$$

where n and w are integers. There is a continuous series of conformal weights with $J = \frac{1}{2} + is$ with $s \in \mathbb{R}^+$ and a discrete set with $\frac{1}{2} < J < \frac{k-1}{2}$, $2J \in \mathbb{N}$. The generating function of the descendants of the discrete set is given by [70, 71]:

$$\lambda^d_{J,M} = \eta(q)^{-2} q^{\frac{(J+M)^2}{k}} q^{-\frac{(J-1/2)^2}{k-2}} S_M,\ M \geq 0 \tag{3.57}$$

with $M \in \mathbb{Z}$ and where

$$S_M = \sum_{n=0}^{\infty} (-1)^n q^{\frac{n^2}{2} + \frac{n}{2}(2M+1)} \tag{3.58}$$

The discrete character $\lambda^d_{J,M}$ pertains naturally to a theory with the central charge $c_{\rm BH}$ given by (3.55) and a particular subset of the conformal weights in (3.56):

$$h_{J,M} = \frac{(J+M)^2}{k} - \frac{J(J-1)}{k-2}\,. \tag{3.59}$$

Nonetheless it is also possible to interpret it formally within a theory with central charge $c_{\rm PF}$ given by (3.49). Consider that, from equation (3.33), we only observe the central charge and conformal dimensions in the combination $\frac{c}{24} - h$. In other words, we can only directly observe the effective central charge $c_{eff} = c - 24h$. Using the correspondences:

$$\begin{aligned} J &= \frac{m+1}{2} \\ M &= \frac{l-m}{2} \end{aligned} \tag{3.60}$$

we can see that $c_{\rm PF} - 24\Delta^m_l = c_{\rm BH} - 24h_{J,M}$. In the following we shall maintain this distinction, by denoting always the weights pertaining to the black-hole theory by h, and those related the parafermionic interpretation of the AF Potts model by Δ.

The vertex representation of the AF Potts model was studied with periodic boundary conditions in [54] where both the discrete and continuous series of exponents $h_{\rm BH}$ were observed on the lattice. It was also observed in [32] that in the RSOS representation of the AF Potts model with boundary conditions such that the heights h_1 and h_{N+1} in Figure 3.16 are set to 1 and $l+1$ respectively (see [72]), the exponents are again given by 3.50 and the full generating function of the model is given by:

$$c^0_l = \sum_{n=0}^{\infty} \left(K_{l+2nk} - K_{2(n+1)k-l-2}\right) = K_l - K_{2k-l-2} + K_{l+2k} - K_{4k-l-2} + \ldots\,, \tag{3.61}$$

This expression exactly coincides with the string function of the Z_{k-2} parafermion CFT. The string function c_l^0 in (3.61) is a special case of the more general object [73]:

$$c_l^m = \frac{1}{\eta(q)^2} \sum_{\substack{n_1,n_2\in\mathbb{Z}/2 \\ n_1-n_2\in\mathbb{Z} \\ n_1\geq|n_2|,-n_1>|n_2|}} (-1)^{2n_1}\text{sign}(n_1) q^{\frac{(l+1+2n_1k)^2}{4k} - \frac{(m+2n_2(k-2))^2}{4(k-2)}} . \tag{3.62}$$

It should be clear then from the above discussion that the AF Potts model is closely related to the Euclidean Black Hole CFT as well as the Z_k parafermion CFT. Previous studies showed that the vertex version of the model produced the exponents of the Black Hole Theory whereas the RSOS version, defined for k integer, produced a subset of the exponents of the parafermionic CFT. This suggests that there should exist open boundary conditions in the AF Potts model, other than free boundary conditions, that produce the full set of parafermion exponents (3.51) and the full set of string functions (3.62). Section 3.4 will introduce new boundary conditions that achieves this. Using the same techniques discussed in section 3.2, the representation theory of the lattice algebra that describes these new boundary conditions will be utilised to derive a new identity relating the string functions (3.62) to the discrete character generating functions (3.57), shedding further light on the relationship between the Z_k parafermion CFT and the Black Hole Theory.

3.4 New boundary conditions in the antiferromagnetic Potts model

We start with the observation that the usual "blobbed" boundary conditions from section 3.1.4 (which, we recall, correspond to fixing the values of the spin in the Q-state Potts model to a subset $\{1, 2, ..., Q_1\}$ on the boundary) do not seem, in general to be conformally invariant in the critical antiferromagnetic case.[2] We have identified a whole new family of boundary conditions which are conformally invariant in the AF Potts model, but are not in the ferromagnetic one. We refer to these boundary conditions as "alt", for reasons which will become clear below.

3.4.1 The alt boundary conditions in the loop model

Instead of taking the usual blobbed boundary conditions by fixing the spins to a subset on one of the boundaries—by convention the left one—, we now fix them to two complementary, alternating subsets. In other words, we decide that Potts spins on even (say) boundary sites can only take a particular set of $Q_1 \leq Q$ values, while spins on odd boundary sites can only take values in the complementary set of $Q_2 = Q - Q_1$ values. No spin can be in both sets. As before, we can make sense of this definition for all real values of Q, Q_1 by going to the loop or vertex representation. In particular, we no longer require $0 \leq Q_1 \leq Q$. Using the same methods as section 3.1.4, the partition function of the model in the loop representation with these alternating boundary conditions is:

$$\mathcal{Z}_{\text{Potts}}^{\text{Alt}} = Q^{\frac{V}{2}} \sum_{\text{loops}} x^{|G|} Q^{\frac{\ell}{2}} \left(\frac{Q_1}{Q}\right)^{\ell_1} \left(\frac{Q_2}{Q}\right)^{\ell_2} , \tag{3.63}$$

[2] What is observed is simply that the scaled gaps, while converging to fixed (real) values for large systems as they should in a scaling theory, do not reproduce any of the features expected from a CFT. Most noticeably, they do not form conformal towers with integer-spaced scaling levels characteristic of descendent states.

where the sum is over all loops that do not touch the boundary at both even and odd sites, and ℓ_1 and ℓ_2 are the number of loops that touch the boundary at exclusively even and exclusively odd sites, respectively. This describes what we may call the partition function of an alternating boundary loop model. We eliminate the overall multiplicative factor and define:

$$\mathcal{Z}_{\text{Loop}}^{\text{Alt}} = \sum_{\text{loops}} x^{|G|} Q^{\frac{\ell-\ell_1-\ell_2}{2}} y_1^{\ell_1} y_2^{\ell_2}\,, \tag{3.64}$$

where y_1 and y_2 are the Boltzmann weights of loops that touch the boundary at exclusively even and exclusively odd sites respectively, and we define $n_0 \equiv \sqrt{Q}$ to be the weight of each of the $\ell - \ell_1 - \ell_2$ loops in the bulk (i.e. loops that do not touch any site on the left boundary). Once again the sum is over loops that do not touch the boundary at both even and odd sites. We can rewrite the foregoing expression as

$$\mathcal{Z}_{\text{Loop}}^{\text{Alt}} = \sum_{\text{loops}} x^{|G|} Q^{\frac{\ell}{2}} \left(\frac{y_1}{n_0}\right)^{\ell_1} \left(\frac{y_2}{n_0}\right)^{\ell_2}\,. \tag{3.65}$$

We can in fact use the blob algebra from section 3.1.4 to study these boundary conditions, but as we will see below, the transfer matrix is now a new function of blob algebra generators. We have $y_1 = Q_1/\sqrt{Q}$, which we parameterise as

$$y_1 = \frac{Q_1}{\sqrt{Q}} \equiv \frac{\sin(r+1)\gamma}{\sin r\gamma}\,, \tag{3.66}$$

while

$$y_2 = \frac{Q - Q_1}{\sqrt{Q}} = \sqrt{Q} - y_1 = \frac{\sin(r-1)\gamma}{\sin r\gamma}\,, \tag{3.67}$$

where we recall that we have $n_0 = \sqrt{Q} = 2\cos\gamma$. The transfer matrix T is written in terms of blob algebra generators:

$$T = t_1 t_2\,, \tag{3.68}$$

where

$$t_1 = b(e_1)(x+e_3)(x+e_5)\cdots(x+e_{2L-1})(1+xe_2)(1+xe_4)\cdots(1+xe_{2L-2}) \tag{3.69}$$

$$t_2 = (1-b)(e_1)(x+e_3)(x+e_5)\cdots(x+e_{2L-1})(1+xe_2)(1+xe_4)\cdots(1+xe_{2L-2}) \tag{3.70}$$

We stress that the new boundary condition—which we shall call "alt" in the following—is for the time being imposed on only one side of the system. Note also that under $r \to -r$, y_1 and y_2 are swapped, which corresponds simply to swapping the odd and even sites (or odd and even loops), and does not change any of the properties of the system. In what follows, we can therefore assume without loss of generality that $r \geq 0$. We can furthermore define the operator $u \equiv 1 - b$ such that b, u are orthogonal projectors:

$$\begin{aligned} b^2 &= b \\ u^2 &= u \\ bu &= ub = 0 \\ b + u &= 1 \end{aligned} \tag{3.71}$$

and we can rewrite eq. (3.70) as

$$t_2 = u(e_1)(x+e_3)(x+e_5)\cdots(x+e_{2L-1})(1+xe_2)(1+xe_4)\cdots(1+xe_{2L-2})\,. \tag{3.72}$$

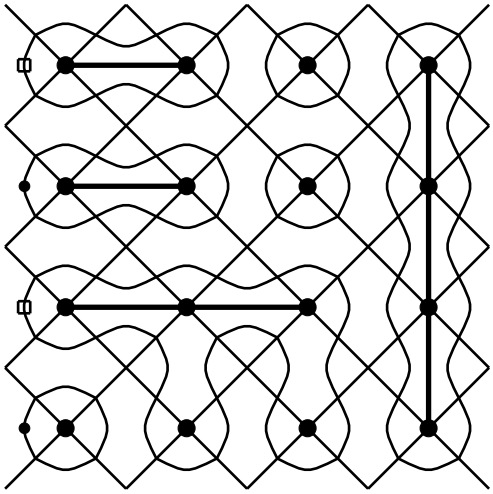


Figure 3.27: The “alternating loop model”: The “blobs" correspond to the operator b and the squares correspond to the operator $u = 1 - b$.

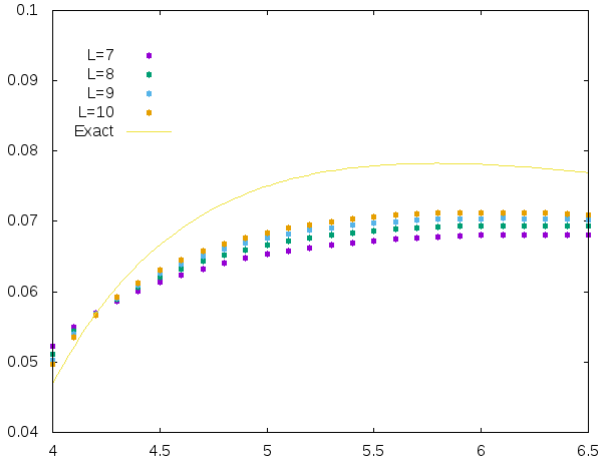


Figure 3.28: The critical exponent $\Delta_{r/2,j}$ from equation (3.79) plotted vs k, using the values $r = 2.5$ and $j = 0$. It can be seen that the finite-size values for the critical exponents converge (slowly) to the exact value.

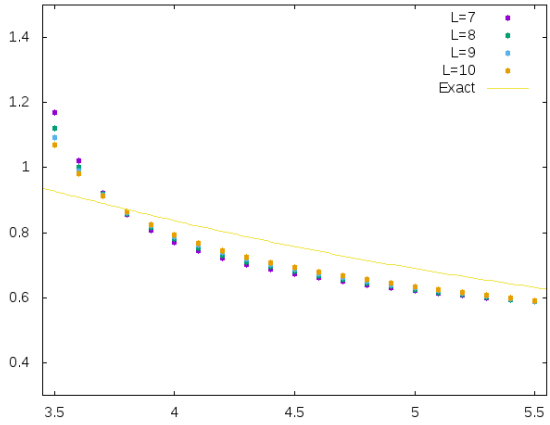


Figure 3.29: The critical exponent $\Delta_{r/2,j}$ from equation (3.79) plotted vs k, using the values $r = 2.1$ and $j = 1$ in the blob sector.

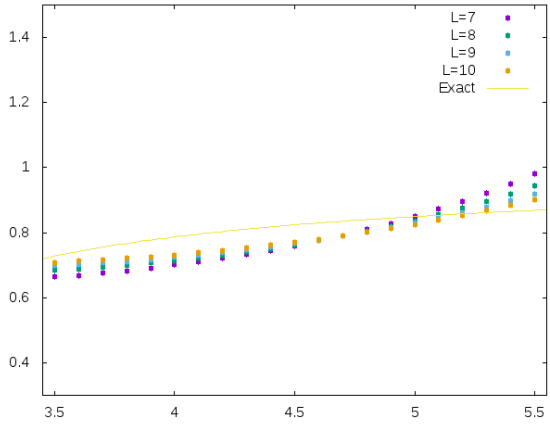


Figure 3.30: The critical exponent $\Delta_{r/2,j}$ from equation (3.79) plotted vs k, using the values $r = 2.1$ and $j = 1$ in the unblob sector.

We shall represent the operator u as a square; closed loops with a square then get the modified Boltzmann weight y_2. A configuration of the alternating loop model is shown in Figure 3.27.

Since we are dealing with a transfer matrix that is written entirely in terms of blob algebra generators, we should once again consider the blob algebra representation spaces from section 3.1.4 and in particular from Figure 3.15. Numerical studies, and the use of equations (3.33) and (3.35), show that the alt transfer matrix produces the following generating functions:

$$\mathrm{Tr}_{\mathcal{W}_j^b} q^{L_0 - c/24} \mapsto \lambda_{r,j} \tag{3.73}$$

$$\mathrm{Tr}_{\mathcal{W}_j^u} q^{L_0 - c/24} \mapsto \lambda_{k-r,j} \tag{3.74}$$

where r parameterises the blob parameter according to equations (3.66) and (3.67). The quantities $\lambda_{r,j}$ entering equations (3.73)–(3.74) are defined as

$$\lambda_{r,j} = \frac{1}{\eta(q)^2} q^{\frac{(r+2j)^2}{4k} - \frac{(r-1)^2}{4(k-2)}} S_j \,, \tag{3.75}$$

where S_j was defined in (3.58) and $\eta(q) = q^{1/24} \prod_{n=1}^{\infty}(1-q^n)$ is Dedekind's eta function. See table 3.1) for some explicit numerical results. Note that the result (3.74) follows from (3.73), since $r \to k - r$ exchanges y_1 and y_2 (using also periodicity of y_1, y_2 under $r \to r+k$), while exchanging y_1 and y_2 obviously also exchanges the roles of b and u. The quantities $\lambda_{r,j}$ are formally identical with the discrete characters of the Euclidean Black Hole theory defined in equation (3.57) when we use the correspondences in equation (3.60), which in the present notation corresponds to:

$$\begin{aligned} r &= m + 1 \\ l &= r - 1 + 2j \end{aligned} \tag{3.76}$$

and hence

$$\begin{aligned} J &= \frac{r}{2} \\ M &= j \end{aligned} \tag{3.77}$$

The correspondences in (3.77) ensure that the observed character on the lattice matches the discrete character in (3.57). In particular, we have:

$$\lambda_{r,j} \quad = \quad \lambda^d_{J,M} \tag{3.78}$$

Assuming $M \geq 0$, we then have that the leading exponent is given by:

$$\Delta_{r/2,j} = \frac{(r-1+2j)(r+1+2j)}{4k} - \frac{(r-1)^2}{4(k-2)} \tag{3.79}$$

which can be matched with the parafermion exponents Δ^m_l defined in equation (3.50) using (3.76).

Note that since we deal with systems of even length, j is integer and thus so is M. Of course the parameter r in the lattice model does not have to be integer; but since $2J \in \mathbb{N}$, it is only this case that lends itself to an interpretation in terms of discrete representations. Note, however, that even when r is an integer, $k-r$ is not an integer for k generic. The generating function in the unblobbed sector can nevertheless be interpreted in terms of $SL(2,\mathbb{R})$ as well. Indeed, for $M \leq -1$, the discrete characters are usually expressed slightly differently: [70]. [3]

$$\lambda^d_{J,M} = \eta(q)^{-2} q^{\frac{(J-|M|)^2}{k}} q^{-\frac{(J-1/2)^2}{k-2}} q^{|M|} S_{|M|}\,, \text{ for } M \leq -1\,, \tag{3.80}$$

and we find correspondingly

$$\begin{aligned} J &= \frac{r}{2}\,, \\ M &= -j\,, \\ \lambda_{k-r,j} &= \lambda^d_{J,M}\,. \end{aligned} \tag{3.81}$$

which should be compared with (3.77).

In Table 3.1 we compare the generating functions of the alternating loop model observed on the lattice with the quantites defined in equations (3.73) and (3.74). In Figures 3.28, 3.29 and 3.30 we plot the critical exponent as a function of k, and three different spin sectors: $j=0$, $j=1$ in the blob sector, and $j=1$ in the unblob sector.

Since $M = \pm j$ depending on the sector, we see that all allowed values of M in the discrete characters are observed in the lattice model. We will discuss the values of J in section 3.5. Note that the characters K_l from section 3.3 can also be expressed in terms of discrete characters. We find indeed the simple identities

$$K_l = \lambda^d_{\frac{1}{2},\frac{l}{2}} - \lambda^d_{\frac{1}{2},-\frac{l+2}{2}}\,. \tag{3.82}$$

It is interesting to consider the limit $r \to 1$. In the ferromagnetic case, the "usual" blobbed boundary conditions reduced to free boundary conditions in this limit, since both bulk and boundary loops are given the same Boltzmann weights in this case. However, we note that with the alt boundary conditions there is no way to go from them to free boundary conditions in the antiferromagnetic model by sending $r \to 1$. It turns out that sending $r \to 1$ leads to a complete change of thermodynamic properties, and is connected with normalisability issues we discuss in section 3.5.

[3] For comparison with [70] we have $\lambda^d_{J,M} = \chi^d_{-J,M+J}$. In other words, the labels j, l in this reference are given by $j = -J, l = M$.

k	Sector	r	Exponent	Generating function
4.5	$j = 0$	2	0.0667	$1 + q + 3q^2 + 6q^3 + ...$
4.5	$j = 1$ blob	2	0.733	$1 + 2q + 4q^2 + 8q^3 + ...$
4.5	$j = 1$ unblob	2	0.844	$1 + 2q + 4q^2 + 8q^3 + ...$
4.5	$j = 2$ unblob	2	2.067	$1 + 2q + 5q^2 + ...$
4.5	$j = 2$ blob	2	1.844	$1 + 2q + 5q^2 + ...$
5.1	$j = 0$	2.2	0.0664	$1 + q + 3q^2 + 6q^3 + ...$
5.1	$j = 1$ blob	2.2	0.655	$1 + 2q + 4q^2 + 8q^3 + ...$
5.1	$j = 1$ unblob	2.2	0.837	$1 + 2q + 4q^2 + 8q^3 + ...$
5.1	$j = 2$ unblob	2.2	2.066	$1 + 2q + 5q^2 + ...$
5.1	$j = 2$ blob	2.2	1.635	$1 + 2q + 5q^2 + ...$

Table 3.1: Some examples of the generating functions and critical exponents observed numerically on the lattice for two different values of k and r, in both the blobbed and the unblobbed sectors. The generating functions are written to the order to which they can be clearly observed on the lattice by diagonalising the transfer matrix for the alternating loop model. Up to this order they agree with the generating functions defined in eqs. (3.73)–(3.74).

3.4.2 The alt boundary conditions in the RSOS model

We saw in section 3.2 that the blobbed boundary conditions, described by the transfer matrix in equation (3.32), produced the generating functions of Verma modules in the continuum limit (see equations (3.40) and (3.41)). Furthermore, it was found that by going to the RSOS representation of the model, or equivalently, by constructing an irreducible representation of the blob algebra using equation (3.42) and Figure 3.25, one could derive the generating function of CFT minimal models in terms of the generating function of the Verma module. The key takeaway was that all of the properties of the representation theory of the CFT module could be observed on the finite lattice via the representation theory of the blob algebra.

In the AF model we have a new “alt" boundary condition that can also be described by the blob algebra. We can therefore perform the same analysis as the ferromagnetic model and derive an analogous expression to equation (3.43) for the AF model, this time relating the generating function obtained from the “alt version” of the RSOS model to the discrete characters in equation (3.80), the generating function obtained from the alt boundary conditions in the loop model.

The discussion in section 3.3 provides us with a hint as to what this new identity should look like, and what should be the generating function obtained from the alt boundary conditions in the RSOS model. First of all consider the form of the leading critical exponent (equation (3.50)) with free boundary conditions in the sector with $l = 2j$ through lines, and the expression in (3.51) showing that these exponents are a subset of the compact parafermion theory. Furthermore, the discussion from equation (3.59) to equation (3.60) showed that all of the parafermion critical exponents were

"contained" inside the Euclidean Black Hole discrete character when this theory was considered as one with central charge $c_{\rm PF}$. All of this suggests that we should be able to obtain all of these parafermion critical exponents via the alt boundary conditions in the RSOS model, and that we should be able to recover the string functions c_l^m defined in equation (3.62) from the RSOS model also. Section 3.4.3 will present the relevant results and discuss this in more detail.

3.4.3 Missing string functions and alt boundary conditions

Consider the expressions in equations (3.73). Since the generating functions of the loop model on the RHS are obtained by acting with a transfer matrix written in terms of blob algebra generators, we can obtain the corresponding generating function of the RSOS model for k and r integer by finding the corresponding irreducible representation of the blob algebra, exactly as in section 3.2. For clarity, the form of the irreducible representation of the blob algebra is written again here:

$$\mathcal{X}^b_{r,j} = \bigoplus_{n=0}^{\infty} \frac{\mathcal{W}^b_{j+nk}/\mathcal{W}^u_{j+r+nk}}{\mathcal{W}^b_{k-j-r+nk}/\mathcal{W}^u_{k-j+nk}} \tag{3.83}$$

The corresponding generating function of levels for the alt boundary conditions is then

$$\begin{aligned} \mathrm{Tr}_{\mathcal{X}^b_{r,j}} q^{L_0-c/24} &= \sum_{n=0}^{\infty} \left[\lambda_{m+1,\frac{l-m}{2}+nk} - \lambda_{k-m-1,\frac{l+m+2}{2}+nk} - \lambda_{m+1,\frac{2k-l-m-2}{2}+nk} + \lambda_{k-m-1,\frac{2k-l+m}{2}+nk} \right] \\ &= \sum_{p=-\infty}^{\infty} \left[\lambda^d_{\frac{m+1}{2},\frac{l-m}{2}+pk} - \lambda^d_{\frac{m+1}{2},-\frac{l+m+2}{2}+pk} \right] \end{aligned} \tag{3.84}$$

where we have used the correspondences in equation (3.77). One can verify that this is precisely the form of the string functions c_l^m. That is:

$$\mathrm{Tr}_{\mathcal{X}^b_{r,j}} q^{L_0-c/24} = c_l^m \,, \text{ for } m \le l \tag{3.85}$$

with the correspondence (3.77). As the notation indicates, this expression coincides with the string function for the Z_{k-2} parafermion theory [4] Note that since j is integer, l and m have the same parity, as required. Note also that the string functions $c_l^{-m} = c_l^m$ are invariant under $m \to -m$.

We can now study the range of values of the parameters. For $\mathfrak{q} = e^{i\pi/k}$, the simplest case is $r = 1$, for which we have to consider in fact only the TL algebra. The possible values of j are given by $j = 0, \ldots, \frac{k}{2} - 1$, so

$$l = 2j = 0, \ldots, k-2 \,. \tag{3.86}$$

For $r = 2, \ldots k-2$, we see first, from $m = r - 1$, that

$$m = 1, \ldots, k-3 \,. \tag{3.87}$$

As far as l is concerned, we have to invoke the representation theory of the blob algebra. For a given value of r, we have now the allowed values of j in the blobbed sector, $j = 0, \ldots, \frac{k-1-r}{2}$, which correspond to

$$l = r - 1 + 2j = m, \ldots, k-2 \tag{3.88}$$

[4] Sometimes string functions are defined with an extra factor $\eta(q)$, so what we denote c_l^m is referred to as $\eta(q) c_l^m$.

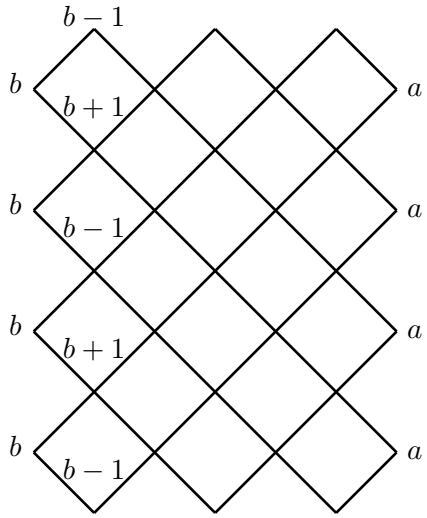


Figure 3.31: Alternating boundary conditions in the antiferromagnetic RSOS model. We will write this boundary condition as $b^{\pm}, \ldots, a$.

To get the missing values of l we need to consider the unblobbed sector. We have first the equivalent of (3.83)

$$\mathcal{X}^u_{r,j} = \bigoplus_{n=0}^{\infty} \frac{\mathcal{W}^u_{j+nk}/\mathcal{W}^u_{r-j+nk}}{\mathcal{W}^b_{k-r+j+nk}/\mathcal{W}^b_{k-j+nk}} = c^m_{2m-l}\,, \text{ for } m \leq l\,. \tag{3.89}$$

Indeed, straightforward calculation first leads to an identity similar to (3.85) but with $c^{k-2-m}_{k-2+l-2m}$, following from the transformation $r \to k-r$. Using a standard identity for string functions $c^m_l = c^{k-2-m}_{k-2-l}$ in Z_{k-2} theories [74], gives instead the string function c^m_{2m-l}. For the unblobbed sector, the allowed values of j are $j = 0, \ldots, \frac{r-1}{2}$, so $l = r-1+2j = r-1, \ldots, 2(r-1) = m, \ldots, 2m$. It follows that $2m-l = 0, \ldots m$, recovering what was missing in (3.88) to cover the whole set[5]

$$l = 0, \ldots, k-2 \tag{3.90}$$

as in (3.86). Equations (3.84) and (3.85) tell us that the alt boundary conditions in the AF Potts RSOS model should produce the string functions c^m_l in the continuum limit. We now describe what precisely "alt" means for the RSOS model.

Consider the RSOS boundary conditions on the lattice in Figure 3.31. Heights are fixed to $h_{N+1} = a$ on the right boundary, to $h_1 = b$ on the left boundary, and heights h_2 next to the left boundary alternate between $b \pm 1$ as shown. We will write this boundary condition as $b^{\pm}, \ldots, a$. It is found that the boundary condition:

$$(m+1)^{\pm}, ..., (l+1) \tag{3.91}$$

produces the string function c^m_l in the continuum limit ($m \neq 0$). Similarly, we will write $1^+, \ldots, (l+1)$ to denote the boundary condition in Figure 3.16—i.e., with a constant, non-alternating value of h_2—that produces the string function c^0_l.[6] Using this notation,

[5]Note that $l = m$ is common to both sets, since it corresponds to $j = 0$ for which there is no distinction between blobbed and unblobbed.

[6]Note that since heights are restricted to be between 1 and $k-1$ we cannot have an "alt" condition on a boundary where the boundary height is fixed as $h_1 = 1$. The superscript in $1^+, \ldots$ is actually redundant, since $h_2 = 2$ then follows from the RSOS constraint alone.

Boundary condition	Exponent	Generating function
$1^+,...,1$	0	$c_{l=0}^{m=0} = q^{h-\frac{c}{24}}(1+q^2+2q^3+\ldots)$
$1^+,...,3$	$\frac{1}{3}$	$c_{l=2}^{m=0} = q^{h-\frac{c}{24}}(1+2q+3q^2+5q^3+\ldots)$
$1^+,...,5$	1	$c_{l=4}^{m=0} = q^{h-\frac{c}{24}}(1+q+3q^2+3q^3+\ldots)$
$2^\pm$,...,2	$\frac{1}{16}$	$c_{l=1}^{m=1} = q^{h-\frac{c}{24}}(1+q+2q^2+4q^3+\ldots)$
$2^\pm$,...,4	$\frac{9}{16}$	$c_{l=3}^{m=1} = q^{h-\frac{c}{24}}(1+2q+3q^2+5q^3+\ldots)$
$3^\pm$,...,1	$\frac{3}{4}$	$c_{l=0}^{m=2} = q^{h-\frac{c}{24}}(1+q+2q^2+3q^3+\ldots)$
$3^\pm$,...,3	$\frac{1}{12}$	$c_{l=2}^{m=2} = q^{h-\frac{c}{24}}(1+q+3q^2+4q^3+\ldots)$
$3^\pm$,...,5	$\frac{3}{4}$	$c_{l=4}^{m=2} = q^{h-\frac{c}{24}}(1+q+2q^2+3q^3+\ldots)$
$4^\pm$,...,2	$\frac{9}{16}$	$c_{l=1}^{m=3} = q^{h-\frac{c}{24}}(1+2q+3q^2+5q^3+\ldots)$
$4^\pm$,...,4	$\frac{1}{16}$	$c_{l=3}^{m=3} = q^{h-\frac{c}{24}}(1+q+2q^2+4q^3+\ldots)$

Table 3.2: String functions in the $k = 6$ antiferromagnetic RSOS model. The string functions are expanded up to the terms we can clearly observe on the lattice.

Table 3.2 shows the exact correspondence between string functions and RSOS boundary conditions for the case $k = 6$. The generating functions (i.e., the string functions) are written up to the number of terms that we have observed by the numerical study of the lattice model.

3.5 Normalisability issues

The inequality $\frac{1}{2} < J < \frac{k-1}{2}$, where $2J \in \mathbb{N}$, for normalisable states in the CFT suggests that the identification of the generating function of levels in the lattice model with discrete characters must break down at some point for $r < 1$ or $r > k-1$. Where exactly it breaks down is not so clear, since $2J$ in the CFT is necessarily integer while our variable r is continuous. We find in fact that the identification breaks down for $r < r_c$ where $1 < r_c < 2$ is some critical value of r dependent on k. The same phenomenon must then happen for $r > k - r_c$, because of the $r \to k - r$ symmetry.

We find numerically that the analytical continuation of the levels contributing to the discrete character within the interval $[r_c, k-r_c]$ correspond, outside this interval, to highly excited states. In other words, there are numerous level crossings at r_c and $k-r_c$. Outside this interval, the true ground state of the theory does not follow analytically from the ground state within the interval. This is related to the behaviour of the boundary energy in equation (3.33) as will now be discussed.

Recall that to calculate the leading critical exponent from the finite-size scaling of the lattice model we use eq. (3.33), while to find the descendant states within a given sector we use eq. (3.35). It is found, however, that there are in fact two different types of states in the spectrum, with two different boundary free energies f_s in eq. (3.33). We can see from (3.33) that only states with the lower value of f_s will contribute to the low-energy spectrum in the thermodynamic limit. The values of these two boundary free energies, f_s^1 and f_s^2, however depend on r, and it is found that there exists a critical value $1 < r_c < 2$ such that they cross. Accordingly, when $r < r_c$ (or $r > k - r_c$) the

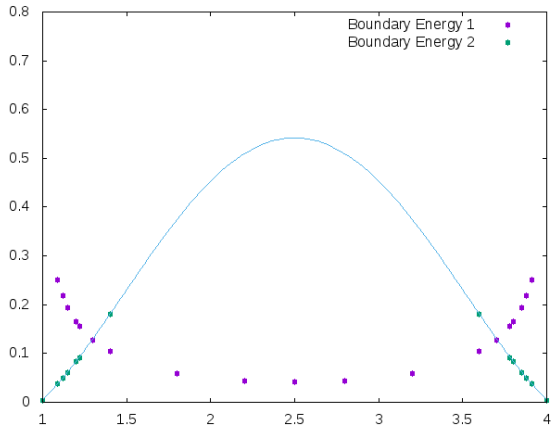


Figure 3.32: The two boundary energies f_s^1 and f_s^2 plotted vs r, for $k = 5$ in the $j = 0$ sector. The critical values of r_c are the points of intersection of the two curves.

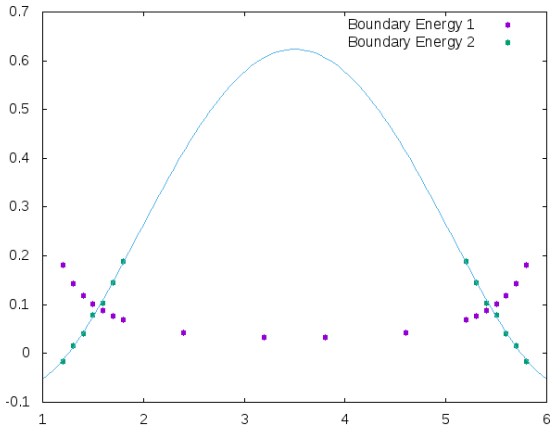


Figure 3.33: The two boundary energies f_s^1 and f_s^2 plotted vs r, for $k = 7$ in the $j = 0$ sector. The critical values of r_c are the points of intersection of the two curves.

low-energy part of the spectrum in the thermodynamic limit is no longer described by the generating functions in (3.73).

We can see this phenomenon illustrated quite clearly in Figures 3.32–3.33. When the green line is below the purple line, the $r \in [r_c, k - r_c]$ regime, the spectrum is described by equation (3.73). When the green line is above the purple line, the $r \notin [r_c, k - r_c]$ regime, the states corresponding to the green line no longer affect the low-energy part of the spectrum in the thermodynamic limit.

Certainly the states whose boundary energy is the continuation of the boundary energy within the interval do not contribute, outside the interval, to partition functions in the scaling limit. This is because the BCFT is obtained after subtracting the non-universal ground state energy f_s associated with a given boundary condition:[7] states with a higher ground-state energy are exponentially suppressed as $e^{-L(f_s' - f_s)}$ in the partition function. It is not clear what these states possibly encode from a field theoretic point of view—that is, how the low-lying excitations above the "wrong" ground state might scale. We are not sure in particular whether or not we would find the continuation of the generating functions observed for $r \in [r_c, k - r_c]$. It seems nevertheless worth pointing out that there is a known case [75] of a *bulk* model possessing a continuous parameter, which can be adjusted so as to make two different *bulk* free energies cross; and on either side of this transition both the true ground state and the "wrong" ground state obtained by analytic continuation from the other side of the transition—each together with their low-energy excitations—behave as two different fully-fledged conformal field theories. We do not wish to rule out that the present model might provide a boundary analogue of this scenario.

Note that in Figures 3.34–3.35 we see the same crossing phenomenon occurring when

[7] It is important to recall here that f_s does in general depend on the boundary condition (while it is always set equal to zero in the BCFT). The point is that, in this particular case, we have two families of states, with the same boundary conditions, and with different values of f_s.

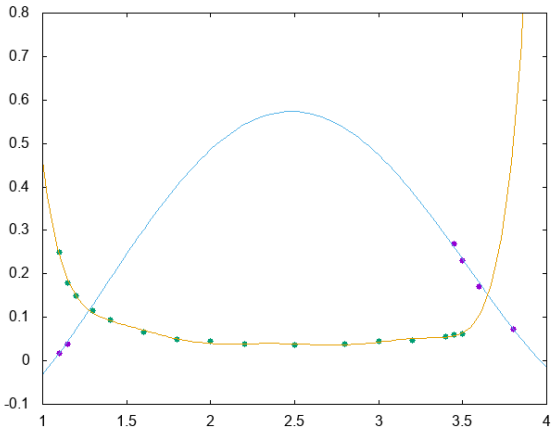


Figure 3.34: The two boundary energies f_s^1 and f_s^2 plotted vs r, for $k = 5$ in the $j = 3$ blob sector. The critical values of r_c are the points of intersection of the two curves.

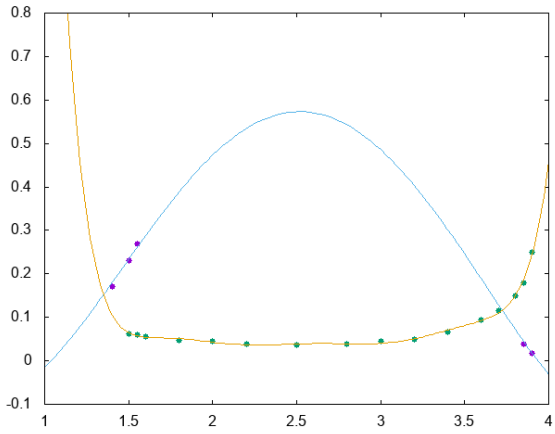


Figure 3.35: The two boundary energies f_s^1 and f_s^2 plotted vs r, for $k = 5$ in the $j = 3$ unblob sector. The critical values of r_c are the points of intersection of the two curves.

there are defect lines present in the system. In particular, Figures 3.34—3.35 illustrate this for $j = 3$. This is the scenario that we would expect from the connection between level-crossing and normalisability; the inequality $\frac{1}{2} < J < \frac{k-1}{2}$ with $2J \in \mathbb{N}$—recall the associations made in (3.81)—for normalisable states suggests that the breakdown of the correspondence between the continuum limit of the lattice model and the discrete character is independent of j and therefore should also occur for $j \neq 0$. Figures 3.34–3.35 show that this indeed the case.

3.5.1 A first-order boundary phase transition

The level crossing observed at r_c and $k - r_c$ can be interpreted as a first-order boundary phase transition, since it corresponds to a discontinuity of the derivative of the boundary free energy. Defining $f_s = -\frac{\log \mathcal{Z}}{M}$ where M is the number of sites in the vertical direction of the lattice and $\mathcal{Z}$ is the partition function defined in (3.65), an easy calculation shows that

$$\frac{\partial f_s}{\partial r} = \frac{\gamma \sin\gamma}{M \sin(r\gamma)} \left[\frac{\langle \ell_1 \rangle}{\sin((r+1)\gamma)} - \frac{\langle \ell_2 \rangle}{\sin((r-1)\gamma)} \right], \tag{3.92}$$

where $\langle \ell_1 \rangle$ and $\langle \ell_2 \rangle$ are the expectation values of the number of contractible blobbed and contractible unblobbed loops respectively. We believe that, as we cross the critical value r_c (or $k - r_c$), we go from a situation where the ground state is dominated by entropic considerations and $\langle \ell_2 \rangle$ is finite to a situation where the ground state is dominated by energy considerations and ℓ_2 is zero in the ground state.

3.6 Combining alt boundary conditions in the loop model

We now wish to consider the case where alt boundary conditions are imposed on both sides of the strip. The general situation is characterised by more parameters than previously. The parametrisation (3.66) of the alternatingly restricted number of Potts states on the boundary has to be made independently for both boundaries. Instead of r, we thus have r_1 for the left boundary and r_2 for the right boundary. The algebraic framework must be extended, so as to have blob and unblob operators—denoted b_1, b_2 and $u_1 = 1-b_1$, $u_2 = 1-b_2$ respectively—for each side. The proper algebraic framework for this situation is called the two-boundary Temperley-Lieb (2BTL) algebra [76, 56, 77]. We need to be careful with $2j > 0$ through-lines, since in this case we need to define four different sectors—denoted bb, ub, bu and uu—where the left (resp. right) label specifies whether the leftmost (resp. rightmost) through-line carries the blob or unblob operator, b_1 or u_1 (resp. b_2 or u_2).

Note that even though the lattice model allows continuous values of r_1 and r_2, the discrete character in equation (3.80) (which played the role of the generating function when "alt" was imposed on only one side of the system) is only defined for $2J \in \mathbb{N}$. From the correspondences in (3.77) and (3.81) we have then that $r \in \mathbb{N}$ also. As we shall now see, the discrete character also arises when "alt" is placed on both sides. We hence consider only the case r_1 and r_2 integer. Note that when $j = 0$ the lattice model is more subtle since loops can touch both boundaries. In what follows we instead focus only on $j > 0$.

Interestingly, in this framework there are two distinct ways to implement alt boundary conditions on both sides of the system. In Figure 3.36 the blob operator on both the left and right boundaries acts on odd-numbered rows, while the unblob operator acts on even-numbered rows on both boundaries. We call this setup "correlated boundary conditions". The alternative to this is shown in Figure 3.37. Here the blob operator acts on odd rows on the left, and on even rows on the right (and vice versa for the unblob operators). We call this setup "anti-correlated boundary conditions". In order to make sense of the continuum limit in terms of conformal field theory, we must consider correlated boundary conditions when the width of the lattice L is even and anti-correlated boundary conditions when L is odd, or anti-correlated boundary conditions when the width of the lattice L is even and correlated boundary conditions when the width of the lattice L is odd. (Note that in Figures 3.36–3.37 our conventions are such that $L = 4$).

These two ways of implementing the alt boundary conditions on both sides give rise to two different generating functions in the continuum limit. The continuum limit must include the two generating functions found, as we have explained, by treating seperately the correlated and anti-correlated boundary conditions. Redefining now $r = \min(r_1, r_2)$,[8] extensive numerical studies lead to the following conjectures in the case

[8] That is, r here has a different meaning than in the one-boundary case.

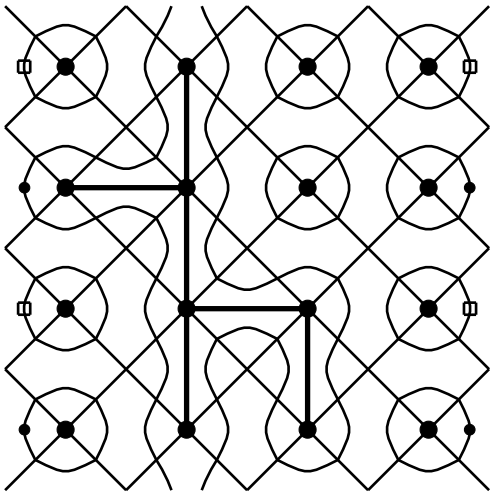


Figure 3.36: Alt on both sides: correlated boundary conditions in the bu sector with $j = 1$.

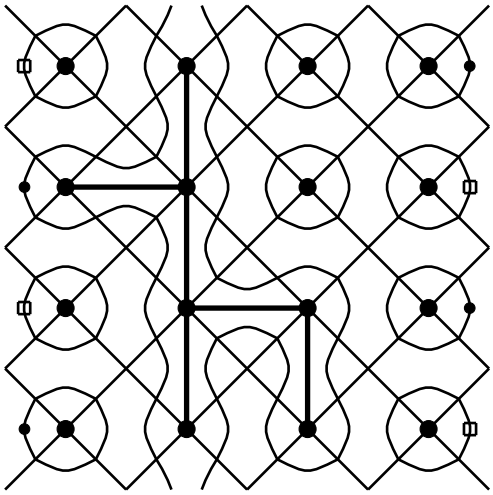


Figure 3.37: Alt on both sides: anti-correlated boundary conditions in the bu sector with $j = 1$.

r_1, r_2 integer and $j \neq 0$:

$$\mathrm{Tr}_{\mathcal{W}_j^{bb}} \mapsto \sum_{n=0}^{\infty} \lambda_{r_1+r_2-1-2nr,j+nr} + \lambda_{|r_2-r_1|+1-2nr,j+(n+1)r-1}\,, \tag{3.93}$$

$$\mathrm{Tr}_{\mathcal{W}_j^{ub}} \mapsto \sum_{n=0}^{\infty} \lambda_{-r_1+r_2-1-2nr,j+nr} + \lambda_{-r_1+r_2+1-2r(n+1),j+(n+1)r-1}\,, \tag{3.94}$$

$$\mathrm{Tr}_{\mathcal{W}_j^{bu}} \mapsto \sum_{n=0}^{\infty} \lambda_{r_1-r_2-1-2nr,j+nr} + \lambda_{r_1-r_2+1-2r(n+1),j+(n+1)r-1}\,, \tag{3.95}$$

$$\mathrm{Tr}_{\mathcal{W}_j^{uu}} \mapsto \sum_{n=0}^{\infty} \lambda_{-r_1-r_2-1-2nr,j+nr} + \lambda_{-r_1-r_2+1-2r(n+1),j+(n+1)r-1}\,. \tag{3.96}$$

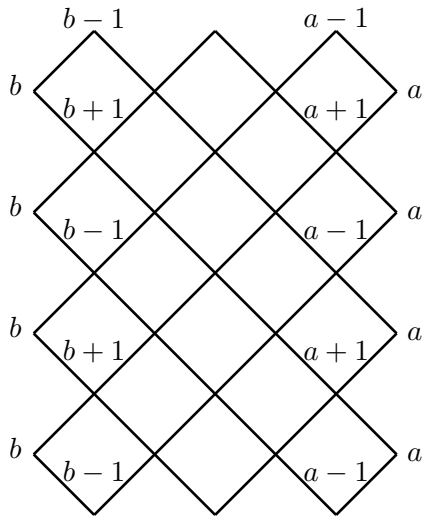


Figure 3.38: Alternating boundary conditions on both sides. We will write this boundary condition $b^{\pm}, ..., ^{\pm}a$ and refer to it as "correlated" boundary conditions.

3.7 Combining alt boundary conditions in the RSOS model

We have found that the continuum limit of the AF Potts RSOS model coincides with that of the Z_{k-2} parafermion theory and we have found an "alt" boundary condition corresponding to each of the string functions in these models. This prescription, however, was restricted to the case where the alt boundary condition is on one side only with the other side having free boundary conditions. We would expect that putting the alt boundary conditions on both sides of the lattice would correspond to the fusion of fields in the Z_{k-2} parafermion theory. As will be shown below from our numerical results, this is indeed the case.

We can however recover this result from knowledge of the generating functions produced in the continuum limit of the loop model with the alt conditions on both sides; see eqs. (3.93)–(3.96). Section 3.4.3 used the representation theory of the blob algebra to move between the AF loop model and the AF RSOS model (similarly, section 3.2 used the same procedure to move between the two ferromagnetic models). It was found that the generating function of the irreducible representation of the blob algebra created by the infinite sum in equation (3.84) produced the RSOS representation. We can use the same method for the case with the alt condition on both sides, i.e., when there are two blob operators, to calculate the generating functions in the RSOS model produced by putting the alt condition on both sides. The relevant algebra in this case is the two-boundary Temperley-Lieb (2BTL) algebra [76, 56, 77].

Section 3.7.1 will present the numerical results of the RSOS model with the alternating boundary condition on both sides. These results will be interpreted in terms of the fusion of fields in the Z_{k-2} parafermion theory. Section 3.7.2 will recover these results by studying the representation theory of the 2BTL algebra.

3.7.1 Numerics

As was the case in the loop model (see section 3.6) there are two ways to put the alt boundary condition on both sides and these two ways will give two different continuum limits. Consider the boundary conditions in Figures 3.38 and 3.39. The heights at the

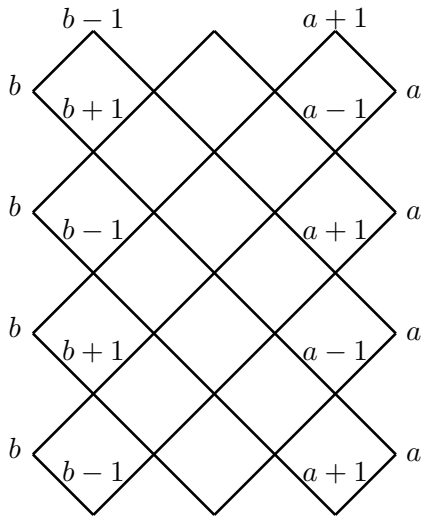


Figure 3.39: Alternating boundary conditions on both sides. We will write this boundary condition $b^{\pm}, ...,^{\mp}a$ and refer to it as "anti-correlated" boundary conditions.

boundaries are fixed to the same, constant values in the two Figures, namely $h_1 = b$ on the left boundary and $h_{N+1} = a$ on the right boundary. However, in Figure 3.38 the lattice sites with heights $h_N = a-1$ just next to the right boundary appear on the same rows as lattice sites with heights $h_2 = b - 1$ just next the left boundary. Conversely, in Figure 3.39 the heights $a - 1$ appear on the same row as $b + 1$. We will refer to these two situations as "correlated" and "anticorrelated" (alternating) boundary conditions respectively.

We will write a generic correlated boundary condition as $b^{\pm}, \ldots,^{\pm}a$ and a generic anti-correlated boundary condition as $b^{\pm}, \ldots,^{\mp}a$. We find that one can obtain two different conformally invariant continuum limits from these boundary conditions. In the first case, we must consider correlated boundary conditions when the width of the lattice L is even and anti-correlated boundary conditions when the width L is odd. The second case works the other way around: we take anti-correlated boundary conditions for L even and correlated boundary conditions for L odd. (Note that in our conventions $N = 2L = 6$ in Figures 3.38 and 3.39). The two different choices correspond to two different continuum limits. The string functions obtained from this prescription for the case $k = 6$ are shown in Table 3.3. The boundary conditions reported in the table are the boundary conditions we take for L even. The number of terms we have written in the expansion of the string function correspond to the number of terms that we can clearly observe on the lattice. We have the general result that for the correlated boundary condition:

$$(m_1 + 1)^{\pm}...^{\pm}(m_2 + 1) \tag{3.97}$$

in even sizes (and hence anti-correlated in odd sizes) the continuum limit is given by the string function $c_0^{m_1+m_2}$. Similarly, the anti-correlated boundary condition

$$(m_1 + 1)^{\pm}...^{\mp}(m_2 + 1) \tag{3.98}$$

in even sizes (and hence correlated in odd sizes) gives the string function $c_0^{m_1-m_2}$. Compare this with the parafermion fusion rules [74] for fields of the form $\phi^m_{l=0}$:

$$\phi^{m_1}_{l=0} \times \phi^{m_2}_{l=0} = \phi^{m_1+m_2}_{l=0} \tag{3.99}$$

Boundary condition	Exponent	Generating function
$2^{\pm},...,^{\pm}2$	$\frac{3}{4}$	$c_{l=0}^{m=2} = q^{h-\frac{c}{24}}(1+q+2q^2+3q^3...)$
$2^{\pm},...,^{\mp}2$	0	$c_{l=0}^{m=0} = q^{h-\frac{c}{24}}(1+q^2+2q^3...)$
$3^{\pm},...,^{\pm}3$	1	$c_{l=0}^{m=4} = q^{h-\frac{c}{24}}(1+q+3q^2+3q^4...)$
$3^{\pm},...,^{\mp}3$	0	$c_{l=0}^{m=0} = q^{h-\frac{c}{24}}(1+q^2+2q^3...)$
$2^{\pm},...,^{\pm}4$	1	$c_{l=0}^{m=4} = q^{h-\frac{c}{24}}(1+q+3q^2+3q^3...)$
$2^{\pm},...,^{\mp}4$	$\frac{3}{4}$	$c_{l=0}^{m=2} = q^{h-\frac{c}{24}}(1+q+2q^2+3q^3...)$
$4^{\pm},...,^{\pm}4$	$\frac{3}{4}$	$c_{l=0}^{m=2} = q^{h-\frac{c}{24}}(1+q+2q^2+3q^3...)$
$4^{\pm},...,^{\mp}4$	0	$c_{l=0}^{m=0} = q^{h-\frac{c}{24}}(1+q^2+2q^3...)$

Table 3.3: String functions in the $k = 6$ antiferromagnetic RSOS model with the alternating boundary condition on both sides. Note that the boundary condition written in the table corresponds to the boundary condition when L is even. When the left and right boundary conditions are "correlated" for L even then we take "anticorrelated" boundary conditions for L odd, and vice versa. The string functions are expanded up to the terms we can clearly observe on the lattice.

Clearly then, the boundary condition for L even in (3.97) corresponds to the fusion of the fields in equation (3.99) and the boundary condition in (3.98) for L even corresponds to the fusion of the fields

$$\phi_0^{m_1} \times \phi_0^{-m_2} = \phi_0^{m_1-m_2} \tag{3.100}$$

Finally, let us notice that when we put correlated and anti-correlated boundary conditions together on the same lattice (i.e., we sum the correlated and anti-correlated configurations) we will clearly get the sum of the two string functions in the continuum limit $c_0^{m_1+m_2} + c_0^{m_1-m_2}$. We can interpret this as the result of the fusion product:

$$\frac{1}{\sqrt{2}}(\phi_{l=0}^{m_1} + \phi_{l=0}^{-m_1}) \times \frac{1}{\sqrt{2}}(\phi_{l=0}^{m_2} + \phi_{l=0}^{-m_2}) \tag{3.101}$$

3.7.2 2BTL representation theory

The representation theory of the 2BTL algebra [76, 56, 77] was further studied from a conformal perspective in [63]. As was discussed in section 3.6, when there is a blob on both sides of the system there are four sectors to consider, labelled by *bb*, *ub*, *bu* and *uu*. It was found in [63] that (when $\mathfrak{q} = e^{i\pi/k}$ is a primitive root of unity) the following infinite sum corresponds to the generating function of an irreducible representation:

$$\begin{aligned}\mathcal{X}_j^{bb} = &\sum_{n_1=0} \mathcal{W}_{j+n_1k}^{bb} - \sum_{n_1=0} \mathcal{W}_{k-(r_1+r_2)+1-j+n_1k}^{bb} - \sum_{n_1=0} \mathcal{W}_{j+r_1+n_1k}^{ub} + \sum_{n_1=0} \mathcal{W}_{k-(r_2-1)-j+n_1k}^{ub} \\ &- \sum_{n_1=0} \mathcal{W}_{j+r_2+n_1k}^{bu} + \sum_{n_1=0} \mathcal{W}_{k-(r_1-1)-j+n_1k}^{bu} + \sum_{n_1=0} \mathcal{W}_{r_1+r_2+j+n_1k}^{uu} - \sum_{n_1=0} \mathcal{W}_{k+1-j+n_1k}^{uu}\,.\end{aligned} \tag{3.102}$$

We find results in agreement with equation (3.102), but we also find that the diagram of inclusions from which this infinite sum can be derived requires modification, i.e., the known 2BTL inclusion diagram does not in fact lead to equation (3.102) as was previously thought [63]. When we impose $r_1 + r_2 - 1 + 2j \leq k - 1$ and $j > 0$ we find that the inclusion diagram should instead be given by Figure 3.40. The only difference here to the diagram published in [63] is that we do not have an arrow from $\mathcal{W}^{bb}_{k+j}$ to $\mathcal{W}^{bb}_{k-(r_1+r_2-1)-j}$.

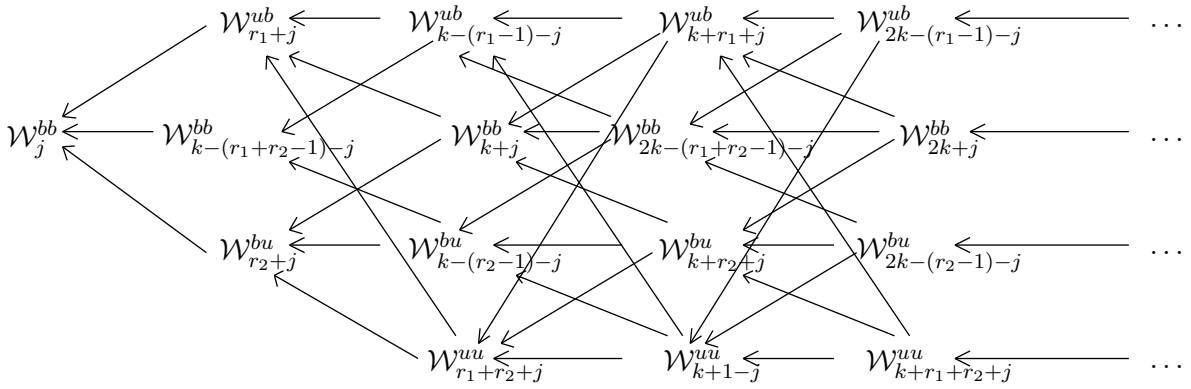


Figure 3.40: The corrected 2BTL inclusion diagram, replacing the one published in [63]. The repeated part of the diagram is such that all standard modules beyond those in the first three columns each have three out-going arrows.

We will use the expressions in eqs. (3.93)–(3.96) to calculate $\mathcal{X}^{bb}_j$, and we will show that the resulting generating function is that corresponding to the fusion of parafermion fields. We have from expressions (3.93) to (3.96):

$$\mathcal{W}^{bb}_{j+n_1k} \to \sum_{n_2=0}^{\infty} \lambda_{r_1+r_2-1-2n_2r,j+n_2r+n_1k} + \lambda_{|r_2-r_1|+1-2n_2r,j+(n_2+1)r-1+n_1k} \tag{3.103}$$

$$\mathcal{W}^{bb}_{k-(r_1+r_2)+1-j+n_1k} \to \sum_{n_2=0}^{\infty} \lambda_{r_1+r_2-1-2n_2r,k-(r_1+r_2)+1-j+n_2r+n_1k} + \lambda_{|r_2-r_1|+1-2n_2r,k-(r_1+r_2)-j+(n_2+1)r+n_1k} \tag{3.104}$$

$$\mathcal{W}^{ub}_{j+r_1+n_1k} \to \sum_{n_2=0}^{\infty} \lambda_{-r_1+r_2-1-2n_2r,j+r_1+n_2r+n_1k} + \lambda_{-r_1+r_2+1-2r(n_2+1),j+r_1+(n_2+1)r-1+n_1k} \tag{3.105}$$

$$\mathcal{W}^{ub}_{k-(r_2-1)-j+n_1k} \to \sum_{n_2=0}^{\infty} \lambda_{-r_1+r_2-1-2n_2r,k-(r_2-1)-j+n_2r+n_1k} + \lambda_{-r_1+r_2+1-2r(n_2+1),k-r_2-j+(n_2+1)r+n_1k} \tag{3.106}$$

$$\mathcal{W}^{bu}_{j+r_2+n_1k} \to \sum_{n_2=0}^{\infty} \lambda_{r_1-r_2-1-2n_2r,j+r_2+n_2r+n_1k} + \lambda_{r_1-r_2+1-2r(n_2+1),j+r_2+(n_2+1)r-1+n_1k} \tag{3.107}$$

$$\mathcal{W}^{bu}_{k-(r_1-1)-j+n_1k} \to \sum_{n_2=0}^{\infty} \lambda_{r_1-r_2-1-2n_2r,k-(r_1-1)-j+n_2r+n_1k} + \lambda_{r_1-r_2+1-2r(n_2+1),k-r_1-j+(n_2+1)r+n_1k} \tag{3.108}$$

$$\mathcal{W}^{uu}_{r_1+r_2+j+n_1k} \to \sum_{n_2=0}^{\infty} \lambda_{-r_1-r_2-1-2n_2r,j+r_1+r_2+n_2r+n_1k} + \lambda_{-r_1-r_2+1-2r(n_2+1),j+r_1+r_2+(n_2+1)r-1+n_1k} \tag{3.109}$$

$$\mathcal{W}^{uu}_{k+1-j+n_1k} \to \sum_{n_2=0}^{\infty} \lambda_{-r_1-r_2-1-2n_2r,k+1-j+n_2r+n_1k} + \lambda_{-r_1-r_2+1-2r(n_2+1),k-j+(n_2+1)r+n_1k} \tag{3.110}$$

We will consider for now the case $r_1 \leq r_2$, so that we have $r = r_1$. After taking the sum $\sum_{n_1=0}^{\infty}$ of the expression in (3.103), we can write it as:

$$\begin{aligned} &\sum_{n_1=0}^{\infty} \lambda_{r_1+r_2-1,j+n_1k} + \lambda_{-r_1+r_2+1,j+r_1-1+n_1k} \\ &+ \sum_{n_1=0}^{\infty}\sum_{n_2=0}^{\infty} \lambda_{-r_1+r_2-1-2n_2r_1,j+r_1+n_2r_1+n_1k} + \lambda_{-r_1+r_2+1-2(n_2+1)r_1,j+r_1+(n_2+1)r_1-1+n_1k}\,, \end{aligned} \tag{3.111}$$

where we see that the second term cancels the expression in eq. (3.105) entirely. Similarly, applying the same sum to the expression in (3.104) gives:

$$\begin{aligned} &\sum_{n_1=0}^{\infty} \lambda_{r_1+r_2-1,k-(r_1+r_2)+1-j+n_1k} + \lambda_{-r_1+r_2+1,k-r_2-j+n_1k} \\ &+ \sum_{n_1=0}^{\infty}\sum_{n_2=0}^{\infty} \lambda_{-r_1+r_2-1-2n_2r_1,k-(r_2-1)-j+n_1k+n_2r_1} + \lambda_{-r_1+r_2+1-2(n_2+1)r_1,k-r_2-j+n_1k+(n_2+1)r_1}\,, \end{aligned} \tag{3.112}$$

where the second term now cancels the expression in (3.106) entirely. In a similar way, we can make the same cancellations for the terms in (3.107) and (3.109) as well as (3.108) and (3.110). In the end, we are left with the terms:

$$\begin{aligned} \mathcal{X}^{bb}_j = &\sum_{n_1=0}^{\infty} \lambda_{r_1+r_2-1,j+n_1k} - \sum_{n_1=0}^{\infty} \lambda_{k-r_1-r_2+1,j+r_1+r_2-1+n_1k} \\ &- \sum_{n_1=0}^{\infty} \lambda_{r_1+r_2-1,k-r_1-r_2+1-j+n_1k} + \sum_{n_1=0}^{\infty} \lambda_{k-r_1-r_2+1,k-j+n_1k} \\ &+ \sum_{n_1=0}^{\infty} \lambda_{-r_1+r_2+1,j+r_1-1+n_1k} - \sum_{n1=0}^{\infty} \lambda_{k+r_1-r_2-1,j+r_2+n_1k} \\ &- \sum_{n_1=0}^{\infty} \lambda_{-r_1+r_2+1,k-r_2-j+n_1k} + \sum_{n1=0}^{\infty} \lambda_{k+r_1-r_2-1,k-r_1+1-j+n_1k} \end{aligned} \tag{3.113}$$

where we have dealt with the negative values of r in $\lambda_{r,j}$ by defining r modulo k. We further have the relationship

$$2j = k - r_2 - r_1 \tag{3.114}$$

when we want the loop model parameters to correspond to the RSOS model. Using equations (3.85) and (3.42), equation (3.113) then becomes

$$\mathcal{X}^{bb}_j = c^{m=r_2-r_1}_{l=k-2} + c^{m=r_1+r_2-2}_{l=k-2}\,, \tag{3.115}$$

which, after using the identities $r_1 = m_1 + 1$ and $r_2 = m_2 + 1$, yields

$$\mathcal{X}^{bb}_j = c^{m=m_2-m_1}_{l=k-2} + c^{m=m_1+m_2}_{l=k-2}\,. \tag{3.116}$$

But using the string function identities $c_l^m = c_l^{-m}$ and $c_{k-2-l}^{k-2-m} = c_l^m$, we can rewrite this as

$$\mathcal{X}_j^{bb} = c_{l=k-2}^{m=m_1-m_2} + c_{l=0}^{m=k-2-m_1-m_2}\,, \tag{3.117}$$

which, when we compare with eq. (3.101), is nothing but the fusion product

$$\frac{1}{\sqrt{2}}(\phi_{l=0}^{m_1} + \phi_{l=0}^{-m_1}) \times \frac{1}{\sqrt{2}}(\phi_{l=0}^{k-2-m_2} + \phi_{l=0}^{-k+2+m_2})\,. \tag{3.118}$$

In summary, then, we have recovered the numerical results found in section 3.7.1 from studying the representation theory of the 2BTL algebra.

3.8 Special cases: the two and three state Potts model

It is interesting to consider the results presented so far when we specialise to the well studied cases of $Q = 2$ (the Ising model) and $Q = 3$. At these two points we can consider the Potts model in its original formulation in equations (3.1) and (3.2), where the partition function is written as a sum over configurations of Potts "spins". In section 3.8.1 the alt boundary conditions will be interpreted in the language of Potts spins and the concepts of "correlated" and "anti-correlated" boundary conditions introduced in section 3.6 will be presented in the language of the $Q = 3$ state Potts model. The CFT describing the continuum limit of the model at $Q = 3$ will be reviewed and some known identities relating the string functions observed in section 3.4.2 to the generating function of a compactified free boson will be recalled. These identities will then be derived in section 3.8.2 from our lattice results; it will be shown that the $Q = 3$ AF Potts model maps exactly to the well studied six vertex model, then by using the known results pertaining to the continuum limit of the six vertex model we can write the generating function of the Potts model in terms of the six vertex model. These lattice identities become, in the continuum limit, the field theory identities relating the $\mathbb{Z}_4$ parafermionic theory to the compactified free boson.

3.8.1 The alt boundary conditions in terms of Potts spins

It is well known that the ferromagnetic $Q = 2$ state Potts model (i.e. the Ising model) is equivalent to an antiferromagnetic one in the bulk. Indeed, the mapping between these models is easily obtained by switching the sign of the couplings and flipping the spins on one sublattice at the same time. Consider the antiferromagnetic critical line:

$$e^K = -1 + \sqrt{4 - Q}\,. \tag{3.119}$$

Under the transformation $K \to -K$, equation (3.119) transforms in the following way when $Q = 2$:

$$e^K = -1 + \sqrt{2} \to e^{-K} = -1 + \sqrt{2} \tag{3.120}$$

which gives:

$$e^K = 1 + \sqrt{2} \tag{3.121}$$

which we observe corresponds to the ferromagnetic critical line from equation (3.31).

This mapping becomes more interesting in the presence of a boundary. While free boundary conditions map onto free, fixed boundary conditions map onto alt boundary

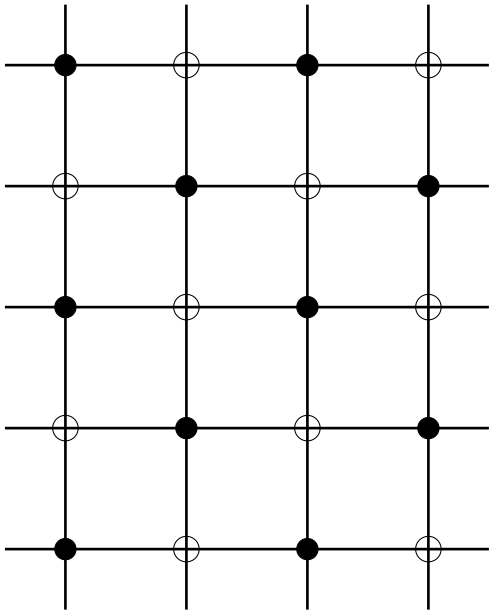


Figure 3.41: The Q-state Potts model on the square lattice. The spins live at all vertices. When we specialise to the Ising model, i.e. $Q = 4\cos^2(\frac{\pi}{4}) = 2$, the antiferromagnetic critical point can be mapped to the ferromagnetic critical point by changing the coupling constant $K \to -K$ and reversing the sign of the spins at the sites on the lattice with unfilled circles. This maps the ferromagnetic model with free boundary conditions to the antiferromagnetic model with free boundary conditions, and the ferromagnetic model with fixed boundary conditions to the antiferromagnetic model with alternating boundary conditions.

conditions (that is, alternating + and − spins on the boundary for $Q = 2$), see Figure 3.41. This suggests that the natural "equivalent" of fixed boundary conditions in the AF case is alt. Coming now to the three-state critical AF Potts model, it is also well known that it can be reformulated as a colouring problem (see the discussion in [32], for example). We see from equation (3.119) that setting $Q = 3$ sends $K \to -\infty$. Considering then the classical Potts Hamiltonian in equation (3.3), the only allowed configurations of Potts spins are those where no two neighbouring spins can be identical. This is the "colouring problem"; the partition function is given by the number of configurations that allow $Q = 3$ possible colours on each site, but no two neighbouring sites can have the same colour.

Consider now the conformal boundary conditions for the antiferromagnetic model presented in section 3.3. We discussed two types: free boundary conditions and alt boundary conditions. Free boundary conditions in the $Q = 3$ state Potts model correspond to imposing no extra constraint on the boundary spins. With alt boundary conditions, even boundary sites can take two particular values, and odd boundary sites are fixed to the remaining value (or vice versa). In the language of the colouring problem, we can fix for example all odd boundary sites to have the colour labelled by 2, and even boundary sites can take either the colours 1 or 3; see Figures 3.42 and 3.43. We see that this boundary condition automatically satisfies the colouring constraint that no neighbouring sites can have the same colour.

Note however that just as in the RSOS and loop models, there are different ways to implement the alt condition when it is applied to both the left and right boundaries at the same time. Once we fix, for example, odd boundary sites on the left to take only one colour (in Figure 3.42 this colour is 2) we have a choice between fixing odd boundary sites on the right to one specific colour or to allow odd boundary sites on the right to take two colours. If we choose the former, (i.e. odd boundary sites on both the right and left are fixed to take one colour) we refer to this as "correlated". This is the case in the right panel of Figure 3.42. If we choose the inverse, i.e., we say that odd boundary sites on the left are fixed to one specific colour but odd boundary sites on the right are allowed to take two colours (and hence *even* sites on the right boundary are fixed to the one remaining colour), we refer to this as "anti-correlated". This is the case in the left panel of Figure 3.42.

But even after we have specified "correlated" or "anti-correlated" we still have an additional choice in relation to which particular colours we choose. In Figure 3.42 the boundary site that is fixed to *one* particular value is equal to 2 on both sides. In Figure 3.43, however, this is not the case; we again have "anti-correlated" boundary conditions in the left image and correlated boundary conditions in the right image, but the fixed height on the left boundary is equal to 2 whereas on the right boundary the fixed height is equal to 3. Since everything in the colouring problem is defined modulo 3, there are only four independent cases, corresponding to those in Figures 3.42 and 3.43. We will denote these four cases by by $C^{=}$, $C^{\neq}$, $A^{=}$ and $A^{\neq}$; C and A refer to "correlated" and "anti-correlated" respectively, while the $=$ and $\neq$ signs refer to the cases where the left boundary colour that is fixed is equal (resp. not equal) to the right boundary colour that is fixed. (See Figures 3.42 and 3.43).

As we saw in sections 3.7.1 and 3.6 when considering the RSOS and loop models re-

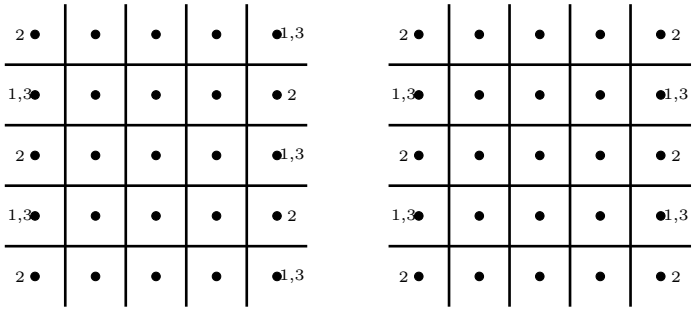


Figure 3.42: Left panel: Anti-correlated boundary condition $A^{=}$. Right panel: Correlated boundary condition $C^{=}$.

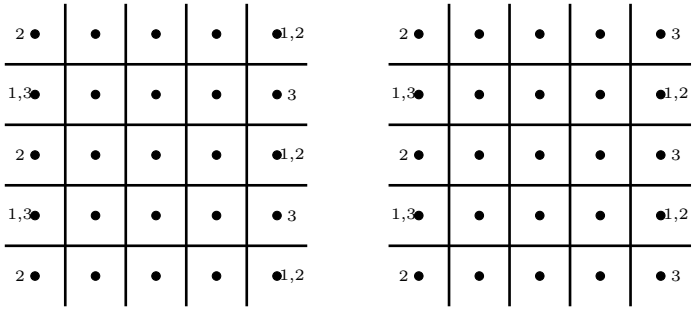


Figure 3.43: Left panel: Anti-correlated boundary condition $A^{\neq}$. Right panel: Correlated boundary condition $C^{\neq}$.

spectively, making sense of the continuum limit of the alt condition on both sides of the boundary requires much care. In particular one must consider the two different scenarios:

1. Correlated boundary conditions when the lattice width L is even and anti-correlated boundary conditions when the lattice width L is odd.

2. Anti-correlated boundary conditions when the lattice width L is even and correlated boundary conditions when the lattice width L is odd.

(Note that in our notations $L = 5$ in Figures 3.42 and 3.43). These two scenarios give two different continuum limits. The results are shown in Table 3.4.

The central charge for $Q = 3$ becomes simply $c_{\rm AF} = 1$, corresponding to a free boson (see, e.g., [78]). It is well known that the AF Potts model at this point is in fact equivalent to a compactified free boson, which is itself equivalent to the (diagonal) $\mathbb{Z}_4$ parafermionic theory. These identifications are encoded in the torus partition function

$$Z_{Q=3} = \frac{1}{\eta(q)\eta(\bar{q})} \sum_{\substack{e\in\frac{\mathbb{Z}}{3} \\ m\in 3\mathbb{Z}}} q^{\frac{1}{4}(\sqrt{3}e+\frac{m}{\sqrt{3}})^2} \bar{q}^{\frac{1}{4}(\sqrt{3}e-\frac{m}{\sqrt{3}})^2} \tag{3.122}$$

and the identity [74, 79]

$$Z_{Q=3} = \frac{1}{2}\sum_{l,m} |c_l^m|^2. \tag{3.123}$$

The expansions of the string functions c_l^m worked out in [79] are repeated here. (Our notations for c_l^m however differ from [79] by a factor of $1/\eta(q)$). Define the objects:

Boundary condition (for odd lattice size L)	Generating function
Free/Free	$c_{l=0}^{m=0} + c_{l=4}^{m=0}$
Alt/Free	$c_{l=1}^{m=1} + c_{l=3}^{m=1}$
Alt/Alt: $C^{=}$	$c_{l=0}^{m=0} + c_{l=0}^{m=4}$
Alt/Alt: $A^{=}$	$2c_{l=0}^{m=2}$
Alt/Alt: $C^{\neq}$	$c_{l=2}^{m=0}$
Alt/Alt: $A^{\neq}$	$c_{l=2}^{m=2}$

Table 3.4: Boundary conditions and their continuum limits. As explained in the text there are four independent "alt/alt" boundary conditions. The precise meaning of the labels of these four types are explained in Figures 3.42 and 3.43. The boundary conditions written above are those taken for L odd. See the main text for a discussion on the relevance of the parity of L.

$$\begin{aligned} W =& \frac{1}{\eta(q)} \sum_{k\in\mathbb{Z}} (-1)^k q^{k^2} \,, \\ W_\pm =& \frac{1}{\eta(q)} \sum_{k\in\mathbb{Z}} (\pm 1)^k q^{(k+\frac{1}{4})^2} \,, \\ Y_n(q) =& \frac{1}{\eta(q)} \sum_{k\in\mathbb{Z}} q^{3(k+\frac{n}{6})^2} \,, \text{ for } n = 0,1,2,3 \,. \end{aligned} \tag{3.124}$$

We then have:

$$\begin{aligned} c_{l=0}^{m=0} =& \frac{1}{2}(Y_0 + W) \,, & c_{l=0}^{m=2} =& \frac{1}{2} Y_3 \,, & c_{l=0}^{m=4} =& \frac{1}{2}(Y_0 - W) \,, \\ c_{l=1}^{m=1} =& \frac{1}{2}(W_+ + W_-) \,, & c_{l=1}^{m=3} =& \frac{1}{2}(W_+ - W_-) \,, & & \\ c_{l=2}^{m=0} =& Y_2 \,, & c_{l=2}^{m=2} =& Y_1 \,. & & \end{aligned} \tag{3.125}$$

3.8.2 Relationship to the six-vertex model

The relationship with the free boson corresponds, on the lattice, to the fact that the critical AF three-state Potts model is equivalent to the six-vertex model [80]. The idea is the following: pick any lattice site and choose a particular nearest neighbour. We will orient ourselves such that we are facing the nearest neighbour of interest. If this nearest neighbour has a colour with a label succeding (modulo 3) that of the site we are standing at, we will draw a left-pointing arrow between the two lattice sites.[9] If on the contrary this nearest neighbour has a colour with a label preceding (modulo 3) that of the site we are standing at, then we will assign a right-pointing arrow. There is then a one-to-one mapping between allowed configurations in the colouring problem and allowed configurations in the six-vertex model. See Figure 3.44 for an application of this mapping.

[9]Note that left and right are well-defined because we have chosen to stand facing a particular direction

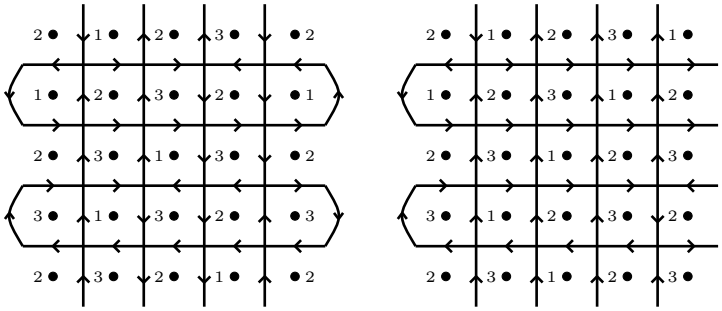


Figure 3.44: The partition function of the three-state Potts model is equal to that of the six-vertex model, where the six vertices all have the same Boltzmann weight. Each of the circles can take one of three colours (represented by 1,2 and 3) in any given configuration, and no two nearest neighbours can have the same colour. Each configuration of the three-state Potts model is mapped to the six vertex model. An example of this mapping with alt boundary conditions on both the left and right boundary is shown in the image on the left. Alt boundary conditions can be seen to correspond to reflecting boundary conditions in the six-vertex model. An example of the mapping for alt boundary conditions on the left boundary and free boundary conditions on the right boundary is shown in the Figure on the right. With free boundary conditions there is no constraint on arrows, as illustrated on the right boundary (in the Figure on the right).

We can see then that the alternating boundary conditions in the Potts model translate into "reflecting" boundary conditions in the six vertex model: arrows on the boundary are divided into pairs as shown in Figure 3.44 and each pair must include one left and one right-pointing arrow, so any outgoing arrow is reflected back into the system. Free boundary conditions for the AF Potts model correspond to free boundary conditions for the six-vertex model, meaning that arrows can freely go into or emerge from the boundary. Let us consider now the implications of this correspondence.

First recall that a vertex model can be described by a transfer matrix written as a product of R-matrices as in equation (3.18) and (3.19). Note however that equation (3.19) describes a periodic model whereas here we are interested in the open case. The R-matrix that describes the six-vertex model can be written as a function of the "spectral parameter" u which measures the anisotropy of the system, and is given by:

$$R(u) = \begin{pmatrix} \sinh(u+i\gamma) & 0 & 0 & 0 \\ 0 & \sinh(u) & \sinh(i\gamma) & 0 \\ 0 & \sinh(i\gamma) & \sinh(u) & 0 \\ 0 & 0 & 0 & \sinh(u+i\gamma) \end{pmatrix} \tag{3.126}$$

(which is the same as that in [81] when we relate the parameter η appearing in [81] to the parameter γ by $\eta = i\gamma$). Since we are dealing with open boundary conditions, we need a so-called K-matrix to take account of the Boltzmann weights of the vertices on the boundary. K matrices will be discussed in more detail in chapter 4 in the context of integrability. For now we can just see the K-matrix as a convenient tool to capture the Boltzmann weights of the boundary vertices. As discussed above and illustrated in Figure 3.44, the alt boundary condition corresponds to "reflected" boundary conditions in the six vertex model, with no extra Boltzmann weights needed. This corresponds to a K-matrix equal to the identity on both the left and the right boundary. A set of

K-matrices for the six vertex model have been previously discussed in [81], they are given by:

$$K(u) = \begin{pmatrix} \sinh(u+\xi) & 0 \\ 0 & -\sinh(u-\xi) \end{pmatrix}. \tag{3.127}$$

The connection between an open transfer matrix and a corresponding open Hamiltonian will be discussed in detail in chapter 4, but for now we will just state the result of [81] where it was shown that the Hamiltonian corresponding to the model with the K-matrices in (3.127) is given by:

$$H = -\sum_{n=1}^{N-1} (\sigma_j^x \sigma_{j+1}^x + \sigma_j^y \sigma_{j+1}^y - \cos\gamma \sigma_j^z \sigma_{j+1}^z) + \sinh i\gamma (\sigma_1^3 \coth\xi + \sigma_N^3 \coth\xi), \tag{3.128}$$

which is the XXZ Hamiltonian with some extra boundary terms. We have that for the three-state AF Potts model $\gamma = \frac{2\pi}{3}$, and for the isotropic case that we are considering $u = -\frac{i\pi}{3}$. Then setting the free parameter $\xi = \frac{i\pi}{2}$ ensures that the K-matrix in (3.127) becomes proportional to the identity, hence corresponding to the reflecting boundary conditions of Figure 3.44. With these values of the parameters the boundary term in (3.128) disappears and we are left with

$$H = -\sum_{n=1}^{N-1} (\sigma_j^x \sigma_{j+1}^x + \sigma_j^y \sigma_{j+1}^y + \frac{1}{2}\sigma_j^z \sigma_{j+1}^z). \tag{3.129}$$

The continuum limit of this Hamiltonian has been studied in [82]; comparing this work to our results in Table 3.4 allows us, as we will now show, to recover eqs. (3.125). In [82] it was found that the generating function of the spectrum of the Hamiltonian (3.128) (in the sector with spin S_z) in the continuum limit is given by

$$Z(S_z) = \frac{q^{gS_z^2}}{\eta(q)} = \frac{q^{\frac{S_z^2}{3}}}{\eta(q)}. \tag{3.130}$$

The second equality comes from the definition of g: we have $g = 1 - \frac{\gamma}{\pi}$ and $\gamma = \frac{2\pi}{3}$. Consider then the three-state AF Potts model with the boundary condition $C^=$ (defined in Figure 3.42) in odd sizes. From the relationship with the six-vertex model (Figure 3.44) we can see that this boundary condition corresponds to the spin sectors $S_z = 0, \pm 3, \pm 6, \pm 9, \ldots$ Then from (3.130) we have that the generating function of the boundary condition $C^=$ should be given by

$$\sum_{S_z \in \mathbb{Z}} Z(3S_z) = \frac{1}{\eta(q)} \sum_{S_z \in \mathbb{Z}} q^{3S_z^2}. \tag{3.131}$$

However, by comparing this to Table 3.4 we also have that the generating function arising from the boundary condition $C^=$ gives $c_{l=0}^{m=0} + c_{l=0}^{m=4}$. We can see from eqs. (3.125) that this is indeed consistent and we have

$$\frac{1}{\eta(q)} \sum_{S_z \in \mathbb{Z}} q^{3S_z^2} = Y_0 = c_{l=0}^{m=0} + c_{l=0}^{m=4}. \tag{3.132}$$

Similarly, consider the the three-state AF Potts model with the boundary condition $C^{\neq}$ (defined in Figure 3.43) in odd sizes. In this case the correspondence can be seen to

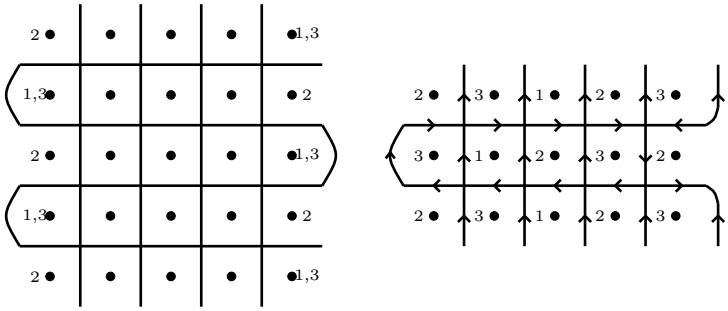


Figure 3.45: Left panel: Anti-Correlated alt boundary conditions correspond to reflecting boundary conditions in the six vertex model, but where the pairing of arrows on the left and right boundary are anti-correlated. Right panel: The Hamiltonian/Transfer Matrix that describes the vertex model acts on a chain with an extra spin that is decoupled from the rest of the system. This extra spin has the effect of adding $\pm$ to the total spin.

be with the six-vertex spin sectors: $S_z = \ldots -7, -4, -1, 2, 5, 8, \ldots\ldots$ So according to (3.130) we get for the generating function

$$\frac{1}{\eta(q)} \sum_{k\in\mathbb{Z}} q^{\frac{1}{3}(3k-2)^2}\,, \tag{3.133}$$

which when comparing with the result in table 3.4 for the generating function of this boundary condition we find:

$$c_{l=2}^{m=0} = Y_2 = \frac{1}{\eta(q)} \sum_{k\in\mathbb{Z}} q^{\frac{1}{3}(3k-2)^2} \tag{3.134}$$

which is consistent with eqs. (3.125). Eqs. (3.125) can therefore be seen as the continuum version of the equivalence between the XXZ chain with free boundary conditions and the three-state AF Potts model with alt boundary conditions.

By considering the two remaining alt/alt boundary conditions in table 3.4 (i.e. $A^{=}$ and $A^{\neq}$) we can derive two more identities appearing in (3.125). They are

$$c_{l=0}^{m=2} = \frac{1}{2} Y_3 = \frac{1}{2\eta(q)} \sum_{k\in\mathbb{Z}} q^{3(k+1/2)} \tag{3.135}$$

and

$$c_2^2 = Y_1 = \frac{1}{\eta(q)} \sum_{k\in\mathbb{Z}} q^{3(k+\frac{1}{6})^2}\,. \tag{3.136}$$

The two "anti-correlated" boundary conditions $A^{=}$ and $A^{\neq}$ correspond to half integer spin sectors of the XXZ chain. We can see this in two ways. The first way is to recall that $A^{=}$ for L odd has the same continuum limit as $C^{\neq}$ for L even. We have seen from the mapping from 3-state Potts to the XXZ chain that L even in the Potts model corresponds to an XXZ chain of *odd* length, and hence necessarily with half integer spin. In particular, one can see that $A^{=}$ produces the generating function associated with the spin sectors $S_z = \ldots -\frac{9}{2}, -\frac{3}{2}, \frac{3}{2}, \frac{9}{2} \ldots$, and $A^{\neq}$ to the sectors $S_z = \ldots -\frac{7}{2}, -\frac{1}{2}, \frac{5}{2}, \frac{11}{2} \ldots$

We can recover the same result from a different point of view. We can see from Figure 3.45 that the "anti-correlated" boundary conditions correspond to reflecting boundary

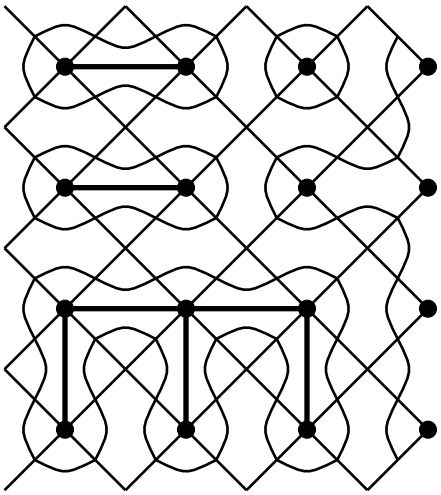


Figure 3.46: The loop model with and odd number of strands. There must be at least one defect line running through the system when N is odd. We have $N = 7$ and $j = \frac{1}{2}$ in this example. An odd number of strands in the loop model corresponds to wired boundary conditions on one boundary in the Potts model: in this Figure the wired boundary conditions are imposed on the right boundary: all Potts spins on the right boundary are identified, since they cannot be separated by any loop.

conditions in the vertex model but where the pairs of arrows on the left and right boundaries are not correlated to occur on the same rows of the lattice. We see from the right panel in Figure 3.45 that this is equivalent to a situation where the Transfer Matrix/Hamiltonian acts on a system with an extra spin that is decoupled from the system. This extra spin contributes $\pm\frac{1}{2}$ to the total spin of the system; we hence go from a system with integer spin to a system with half integer spin.

3.9 Odd number of sites and disorder operators

This chapter has so far presented results relating properties of the parafermion and black hole conformal field theories to their underlying lattice models. Section 3.4.3 showed that all of the string functions of parafermion theory could be obtained from the alt boundary conditions together with free boundary conditions. Section 3.7 showed that we could furthermore recover the fusion rules of the parafermionic conformal field theory from the lattice results. There is another important object in the parafermionic theory that we have not yet discussed in the context of these lattice studies; it was argued in [83] that the parafermionic conformal field theory should admit a field that is not accounted for by the string functions, so called C-disorder fields. We will find a lattice interpretation for this field by turning to the RSOS representation with an odd number of sites; this chapter has so far been restricted to spin chains where the number of sites $N = 2L$ was even.

The case N odd clearly requires a careful interpretation in terms of Potts spins. The correct way to implement this in terms of the Potts model is to impose "wired" boundary conditions on one side and free boundary conditions on the other. The idea of wired boundary conditions is that all of the Potts spins on one side are contracted to a single spin. This is illustrated in Figure 3.46.

It is easier to describe wired boundary conditions in the loop and RSOS version of the model. The transfer matrix now is given by:

$$T = (x + e_1) \cdots (x + e_{2L-1})(1 + xe_2) \cdots (1 + xe_{2L}) \,, \tag{3.137}$$

where the e_i are generators of the Temperley Lieb algebra in either the loop or the RSOS representation. One can then study the corresponding generating functions in exactly the same way as for the cases studied in previous sections. In particular, we make use once again of equations (3.33) and (3.35). We then find the analogous result of equation (3.52), where now j is a half integer. We have for the generating function of levels in the sector with $2j$ through lines:

$$\tilde{K}_j = Z_{\rm ND} \times \frac{1}{\eta(q)} \left(q^{k\left[\frac{1}{4} - \frac{(j+\frac{1}{2})}{k}\right]^2} - q^{k\left[\frac{1}{4} + \frac{(j+\frac{1}{2})}{k}\right]^2} \right) . \tag{3.138}$$

where

$$Z_{\rm ND} = \frac{1}{\eta(q)} \sum_{n \in \mathbb{Z}} q^{(n-\frac{1}{4})^2} \,. \tag{3.139}$$

We can give a few examples to support this result. When we fix $k = 4.2$ and analyse the first 40 eigenvalues of the loop model transfer matrix (3.137) up to size $N = 25$ we find

$$\tilde{K}_{j=\frac{1}{2}} = q^{\Delta - \frac{c}{24}} (1 + q^{\frac{1}{2}} + q + 2q^{\frac{3}{2}} + 3q^2 + 4q^{\frac{5}{2}} + 6q^3 + \ldots) \,, \tag{3.140}$$

which is consistent with eq. (3.138) up to the level written. Similarly, we have

$$\tilde{K}_{j=\frac{3}{2}} = q^{\Delta - \frac{c}{24}} (1 + q^{\frac{1}{2}} + 2q + 3q^{\frac{3}{2}} + 4q^2 + 6q^{\frac{5}{2}} + \ldots) \,. \tag{3.141}$$

Now consider the RSOS model with N odd. We consider the transfer matrix in (3.137) where the e_i now act in the RSOS representation defined in section 3.1.5. Note that moving to the RSOS representation only makes sense when k is an integer. We define the quantities:

$$\Theta_{l,2k}(q) = \sum_{n \in \mathbb{Z}} q^{k(n + \frac{m}{2k})^2} \tag{3.142}$$

Then for the RSOS model with the left boundary height set to 1 and the right boundary height set to $r = 2j + 1$, the generating functions is found to be:

$$\xi_l = \frac{Z_{ND}}{\eta(q)} \left[\Theta_{l,2k}(q) - \Theta_{2k-l,2k}(q) \right] \tag{3.143}$$

with $l = k - 2r$. It is easy to check then that

$$\xi_l = \sum_{n=0}^{\infty} \left[\tilde{K}_{j+nk} - \tilde{K}_{k-1-j+nk} \right] \tag{3.144}$$

using $r = 2j + 1$ and hence $l = k - 2 - 4j$. The quantity ξ_l is in fact the full CFT generating of the disorder field in the parafermion conformal field theory [84]. Equation (3.144) is the analogue of the relationship between the string functions and the discrete character of the black hole theory presented in section 3.4.3, where we recall that in that case the identity also corresponded, on the lattice, to a relationship between the

Boundary	k	Exponent	Generating function
1,...,2	4	0	$1+q^{\frac{1}{2}}+q^{\frac{3}{2}}+q^2+q^{\frac{5}{2}}+q^3+q^{\frac{7}{2}}+2q^4+2q^{\frac{5}{2}}+...$
1,...,2	5	$\frac{1}{40}$	$1+q^{\frac{1}{2}}+q+q^{\frac{3}{2}}+2q^2+2q^{\frac{5}{2}}+3q^3+3q^{\frac{7}{2}}+4q^4+5q^{\frac{9}{2}}+6q^5+7q^{\frac{11}{2}}+...$
1,...,4	5	$\frac{1}{8}$	$1+q+q^{\frac{3}{2}}+q^2+q^{\frac{5}{2}}+2q^3+2q^{\frac{7}{2}}+3q^4+3q^{\frac{9}{2}}+4q^5+4q^{\frac{11}{2}}+...$
1,...,2	6	$\frac{1}{16}$	$1+q^{\frac{1}{2}}+q+2q^{\frac{3}{2}}+2q^2+3q^{\frac{5}{2}}+4q^3+...$
1,...,4	6	$\frac{1}{16}$	$1+q^{\frac{1}{2}}+q+2q^{\frac{3}{2}}+2q^2+3q^{\frac{5}{2}}+4q^3+...$
1,...,2	7	$\frac{3}{28}$	$1+q^{\frac{1}{2}}+q+2q^{\frac{3}{2}}+3q^2+3q^{\frac{5}{2}}+5q^3+...$
1,...,4	7	$\frac{1}{28}$	$1+q^{\frac{1}{2}}+2q+2q^{\frac{3}{2}}+3q^2+4q^{\frac{5}{2}}+6q^3+...$
1,...,6	7	$\frac{1}{4}$	$1+q+q^{\frac{3}{2}}+2q^2+2q^{\frac{5}{2}}+3q^3+...$

Table 3.5: Generating functions in the RSOS model with an odd numbers of sites. The generating functions are written up to the number of terms that we have observed on the lattice.

loop and RSOS models.

One can observe from the lowest order term of ξ_l that the dimensions of the C-disorder fields in the Z_{k-2} theory are:

$$\Delta = \frac{k-4+(k-2-4j)^2}{16k}\,. \tag{3.145}$$

We compare the numerical results obtained from the lattice model with the CFT quantities defined in (3.144) in Table 3.5.

In conclusion, we see that the correspondence, for k integer, between RSOS restrictions of the critical antiferromagnetic Potts model and parafermions extends to the case of disorder operators for odd numbers of sites.

Chapter 4

The Bethe Ansatz

In chapter 3, numerical methods were used to find the spectrum of transfer matrices and Hamiltonians describing critical models with the goal of understanding the conformal field theories describing their continuum limits. Finding the eigenvalues is a numerically intensive procedure and hence imposes upper limits on the system sizes that we can study. Chapter 3 studied the conformal field theory describing the antiferromagnetic Potts model by using system sizes up to $N = 24$, but this will not always be a large enough lattice system for us to be able to observe certain aspects of the CFT on the lattice. This is particularly apparent when we want to use the lattice to study the non-compact aspects of a CFT for reasons that will now be outlined.

As was discussed in section 3.2, we can calculate CFT quantities (e.g. the central charge and the conformal dimensions) from a finite lattice system using finite size scaling, i.e. equations (3.33) to (3.35), leading to the observation of the corresponding CFT generating function on the lattice such as (3.40) or (3.41). It was found that using lattice sizes $N \sim 20$ was enough to observe the first few terms in these CFT generating functions. Ultimately, the reason we could do this was that, in equation (3.33), the term after the $\frac{1}{L^2}$ term was small - more precisely, it was found to be of the order $\frac{1}{L^3}$. However, this will not always be the case when we are considering the non-compact part of a CFT and we will need to study much larger systems in orde to calculate the conformal dimensions.

Compare for instance figures 4.1 and 4.2. Figure 4.1 plots the finite size gaps obtained from equation (3.35) versus $\frac{1}{L}$, calculated from the transfer matrix for the antiferromagnetic model with alternating boundary conditions defined in equation (3.68). Using quite low systems sizes we can already see that these gaps converge towards integers. It was observed that the number of states converging towards each integer is equal to what one would expect from the discrete character generating function, see equation (3.73).

However now consider figure 4.2 where the same analysis is applied to a model with a non-compact continuum limit (the data in this figure is generated from a non-compact model that will be discussed in detail chapter 6). The non-compact CFT results in the appearance of more and more states as the system size is increased, and the gaps corresponding to these states converge logarithmically to zero. This was interpreted in [54] as the appearance of a continuum of conformal dimensions on the lattice, as one would expect from a non-compact model. In particular, what this means is that

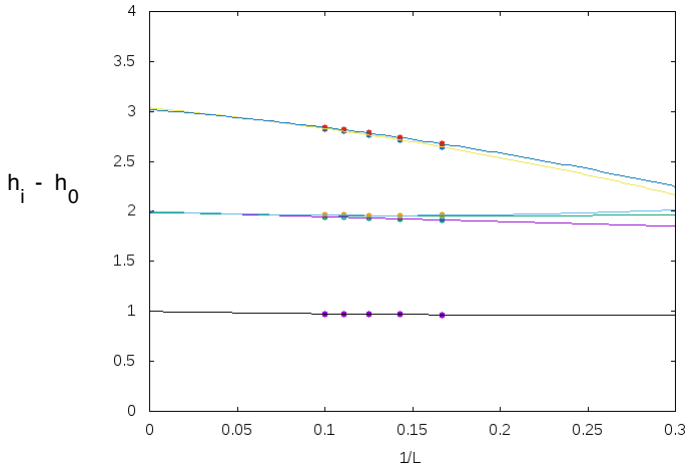


Figure 4.1: The scaling behaviour of the gaps in equation (3.35). The gaps are plotted versus $\frac{1}{L}$ and we notice their scaling behaviour can be extracted even with the low sizes considered due to the compact continuum limit.

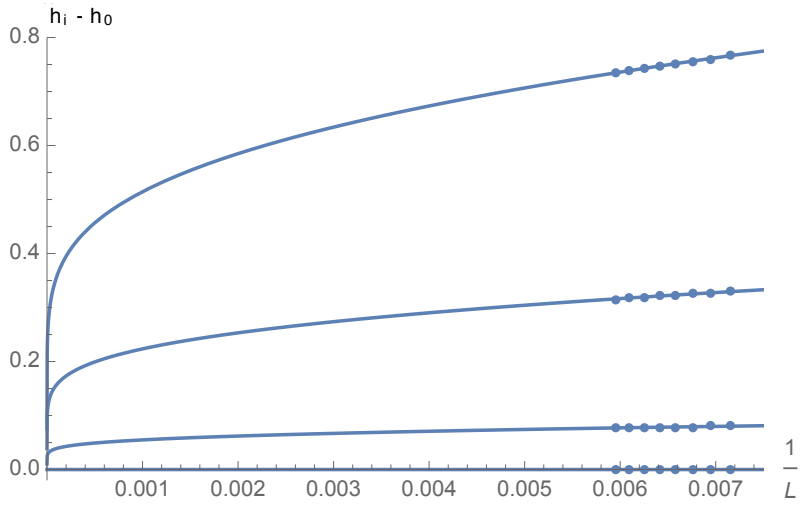


Figure 4.2: The scaling behaviour of the gaps in a non-compact model. The logarithmic corrections to the gaps necessitate the study of large systems.

the term after the $\frac{1}{L^2}$ term in equation (3.33) is no longer $\mathcal{O}(\frac{1}{L^3})$ but $\mathcal{O}(\frac{1}{L^2 \log L})$ instead.

In practical terms this means that, when logarithms are present, we need to study much larger systems in order to extract the CFT data. Directly diagonalising the transfer matrix with numerical methods [85] is no longer a viable option due to computational constraints, hence one should look for exact solutions. The goal of this chapter is to introduce some basic aspects of the Bethe Ansatz method which will be used in later chapters to find the exact solutions that we need in order to study the non-compact boundary conformal field theory that interests us.

4.1 Some general properties

We will start with a brief overview of the Bethe Ansatz in the XXX model in order to provide a general background to the topic before it is applied to more complicated models in later chapters. See [86] for a historical overview, and [87, 88] for an in-depth review. The XXX Hamiltonian with coupling J takes the following form:

$$H = \frac{J}{2} \sum_{i=1}^{L} (\sigma_i^x \sigma_{i+1}^x + \sigma_i^y \sigma_{i+1}^y + \sigma_i^z \sigma_{i+1}^z) \tag{4.1}$$

where for now periodic boundary conditions are imposed. One can in principle find the spectrum of the XXX Hamiltonian for any given size L by directly diagonalising the Hamiltonian in (4.1). However, for large L this becomes difficult for practical reasons and one would therefore hope to find a more efficient method. The Bethe Ansatz provides such a method and essentially amounts to an educated guess as to the form of the eigenstates $|\psi\rangle$ of (4.1), leading to a set constraints on the form of the eigenvalues. Since the XXX Hamiltonian is written in terms of Pauli matrices, the Hilbert space is spanned by the basis vectors $|s_1 ... s_L\rangle$ where the s_i can take the form of up spins $\uparrow$ or down spins $\downarrow$, corresponding to the eigenstates of the σ^z operator. If we consider the reference state $|0\rangle$ to be that with all up spins, then we define the state $|x_1 x_2\rangle$ as the basis state with all spins up except for the spins at positions x_1 and x_2 where the spins are flipped. Note that the XXX Hamiltonian conserves the total spin, so we can study each total spin sector separately. We will denote by n the number of spins that have been flipped with respect to the state $|0\rangle$, the state $|x_1 x_2\rangle$ referred to above therefore corresponds to $n = 2$. In principle n can range between 0 and L but we only need to consider $n \leq \frac{L}{2}$ due to the Z_2 symmetry of the Hamiltonian (4.1). Bethe's Ansatz [89] for the eigenstates of the XXX Hamiltonian in the sector with n flipped spins then takes the form:

$$|\psi\rangle_n = \sum_{1 \leq x_1 \leq ... \leq x_n \leq L} f(x_1, ..., x_n) |x_1, ..., x_n\rangle \tag{4.2}$$

with

$$f(x_1, ..., x_n) = \sum_{(p_1, ..., p_n) \in S_n} A_{p_1, ..., p_n} \prod_{i=1}^{n} e^{i k_{p_i} x_i} \tag{4.3}$$

where the sum runs over all elements of the permutation group S_n and the quantities $A_{p_1, ..., p_n}$ and k_{p_i} are yet to be determined. This Ansatz allows us to derive the following form of the energy eigenvalues:

$$E = \frac{JL}{2} + J\sum_{i=1}^{n}(2\cos k_i - 2) \tag{4.4}$$

where the momenta k_i satisfy the Bethe Ansatz equations:

$$e^{ik_jL} = (-1)^{n-1}\prod_{l\neq j}^{n}\frac{s_{l,j}}{s_{j,l}} \tag{4.5}$$

and the $s_{j,l}$ are defined as:

$$s_{j,l} = 1 - 2e^{ik_l} + e^{ik_j+ik_l} \tag{4.6}$$

In the sector with n flipped spins we have n Bethe Ansatz equations of the form (4.5) and n unknown variables k_j. Whenever one arrives at a set of Bethe Ansatz equations, an immediate question arises as to whether or not the equations are "complete", i.e. whether or not there are enough solutions to the Bethe Ansatz equations to recover all of the eigenvectors and eigenvalues of the Hamiltonian. In the example presented here one can in fact find more solutions to (4.5) than the number of eigenstates of the Hamiltonian [90]. For example, there are solutions to the Bethe Ansatz equations with coincidences of the k_i but these solutions are not "admissible" - this is related to the fact that, when $k_i = k_j$ for $i \neq j$, we see from (4.3) that the wavefunction vanishes. However the question of admissibility is a lot more subtle than is described here, see for instance [91, 92], and is an area of ongoing research [93, 94, 95].

The construction described here is referred to as the coordinate Bethe Ansatz and was the method that Bethe used in his original 1931 paper [89]. Subsequent developments [96, 97] used similar techniques to solve more complicated models and are given names such as the Algebraic Bethe Ansatz and the Analytical Bethe Ansatz to distinguish them from Bethe's original formulation. We will mainly be concerned here with the Analytical Bethe Ansatz and this will be introduced below. The main idea however remains the same: we start with a transfer matrix or a Hamiltonian and we want to reduce the problem of finding the spectrum to solving a set of Bethe Ansatz equations such as (4.5). The concept of "admissible" and "non-admissible" solutions mentioned above will still apply.

4.2 Integrability: bulk and boundary

The key object in either the algebraic or the analytical Bethe Ansatz is the R-matrix. The R-matrix is a function of the "spectral parameter" u and acts on the space $V \otimes V$ where V is a d-dimensional space. Exactly solvable models can be constructed from R-matrices that satisfy the Yang-Baxter equation [98]:

$$R_{12}(u_1 - u_2)R_{13}(u_1 - u_3)R_{23}(u_2 - u_3) = R_{23}(u_2 - u_3)R_{13}(u_1 - u_3)R_{12}(u_1 - u_2) \tag{4.7}$$

The full expressions on the LHS and RHS in (4.7) act on the space $V_1 \otimes V_2 \otimes V_3$ and the notation R_{ij} means that the R-matrix acts non-trivially on the spaces V_i and V_j and acts as the identity on the remaining space. The Yang-Baxter equation is depicted graphically in figure 4.3. We assign spectral parameters u_1, u_2 and u_3 to the three spaces depicted by the three lines and the R-matrix acts at each of the intersections of the lines. The parameter of the R-matrix is given by the difference between the left and the right spectral parameter when we consider time to be flowing upwards. When

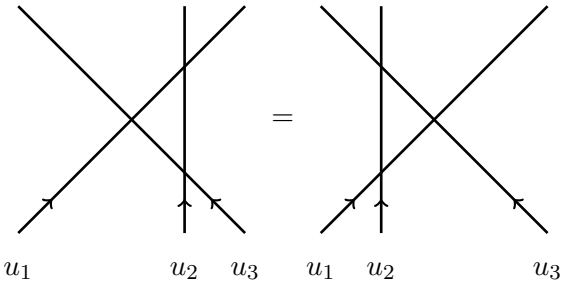


Figure 4.3: Graphical depiction of the Yang-Baxter equation. See text for explanation.

periodic boundary conditions are imposed, we can then construct a transfer matrix from the R-matrix in the following way:

$$t(u) = \mathrm{Tr}_a(R_{a1}(u)...R_{aL}(u)) \tag{4.8}$$

where a is an "auxiliary" space. Any transfer matrix of the form (4.8) with an R matrix that satisfies the Yang-Baxter equation (4.7) is integrable since it commutes with a transfer matrix with a different spectral parameter, i.e.:

$$[t(u), t(v)] = 0 \tag{4.9}$$

for all spectral parameters u and v. To construct an integrable model with open boundary conditions, however, in addition to the R-matrix that satisfies the Yang-Baxter equation we need to consider a particular $d \times d$ matrix acting at the boundary: the K-matrix. As a matter of fact, we shall need a K-matrix for both the left and right boundaries which we will denote as K^- and K^+, respectively. We require that $K^-(u)$ satisfy an analogue of the Yang-Baxter equation, the so-called boundary Yang-Baxter equation [81]:

$$R_{12}(u-v)K_1^-(u)R_{21}(u+v)K_2^-(v) = K_2^-(u)R_{12}(u+v)K_1^-(u)R_{21}(u-v) \tag{4.10}$$

so that the two-row transfer matrix

$$t(u) = \mathrm{Tr}_a\, K_a^+(u)R_{aL}(u)...R_{a1}(u)K_a^-(u)R_{1a}(u)...R_{La}(u) \tag{4.11}$$

will be integrable, i.e., satisfy $[t(u), t(v)] = 0$ for all u, v. To ensure that the right K-matrix, $K^+(u)$, satisfies the analogue of (4.10) on the right boundary we take

$$K^+(\lambda) = K^{-\mathrm{t}}(-\rho - \lambda)M\,, \tag{4.12}$$

where ρ and M are model dependent and t denotes usual matrix transposition.

4.3 The Analytical Bethe Ansatz

The idea behind the analytical Bethe Ansatz is to use the properties of the R-matrix to constrain the form of the eigenvalues $\Lambda(u)$ of the transfer matrix in (4.11). To see how this works, consider the example of the six vertex model studied in [99]. The R matrix can be written as:

$$R(u) = \begin{bmatrix} \sinh(u+\eta) & 0 & 0 & 0 \\ 0 & \sinh(u) & e^u \sinh(\eta) & 0 \\ 0 & e^{-u}\sinh(\eta) & \sinh(u) & 0 \\ 0 & 0 & 0 & \sinh(u+\eta) \end{bmatrix} \tag{4.13}$$

The six vertex model is sometimes written in terms of a parameter γ_0, the parameter η appearing in (4.13) is related to γ_0 by $\eta \equiv i\gamma_0$. One can consider the following particularly simple K^+ and K^- matrices that satisfy (4.10):

$$K^-(u) = \mathrm{Id},\ K^+(u) = M \tag{4.14}$$

where

$$M = -\begin{bmatrix} e^{\eta} & 0 \\ 0 & e^{-\eta} \end{bmatrix} \tag{4.15}$$

As is outlined in [99], one now proceeds to find the eigenvalues of the transfer matrix (4.11) using the R matrix in (4.13) and the K matrices in (4.14), by appealing to various properties that $R(u)$ and $t(u)$ must satisfy. In particular, one observes that R satisfies:

$$R_{12}(u)R_{21}(-u) = \xi(u)\mathrm{Id} \tag{4.16}$$

as well as the so-called "crossing property":

$$R_{12}(u) = V_1 R_{12}(-u-\rho)^{t_2} V_1 = V_2^{t_2} R_{12}(-u-\rho)^{t_1} V_2^{t_2} \tag{4.17}$$

where V is a "crossing matrix" that is model dependent, and in this case we have:

$$M = V^t V \tag{4.18}$$

with

$$V = \begin{bmatrix} 0 & -ie^{-\frac{\eta}{2}} \\ ie^{\frac{\eta}{2}} & 0 \end{bmatrix} \tag{4.19}$$

We furthermore have "regularity"

$$R_{12}(0) = \xi(0)^{\frac{1}{2}} P_{12} \tag{4.20}$$

as well as the commutativity property in (4.9). Combining these properties with the fact that the transfer matrix commutes with the generators of the "quantum group" $U_q(sl(2))$ leads [99] to the following form for the transfer matrix eigenvalues:

$$\Lambda(u) = \frac{\sinh(2u+2\eta)}{\sinh(2u+\eta)} \sinh^{2L}(u+\eta) \frac{Q(u-\eta)}{Q(u)} + \frac{\sinh(2u)}{\sinh(2u+\eta)} \sinh^{2L}(u) \frac{Q(u+\eta)}{Q(u)} \tag{4.21}$$

where

$$Q(u) = \prod_{k=1}^{m} \sinh(u - \lambda_k + \frac{\eta}{2}) \sinh(u + \lambda_k + \frac{\eta}{2}) \tag{4.22}$$

where m can take integer values between 0 and $\frac{L}{2}$ for L even and $\frac{L-1}{2}$ for L odd and the λ_k are the "Bethe roots". We can find the λ_k by the requirement that the residues of the poles of (4.21) all vanish, leading to the Bethe Ansatz Equations (BAE):

$$\left(\frac{\sinh(\lambda_j + \frac{\eta}{2})}{\sinh(\lambda_j - \frac{\eta}{2})} \right)^{2L} = \prod_{k \neq j}^{m} \frac{\sinh(\lambda_j - \lambda_k + \eta)}{\sinh(\lambda_j - \lambda_k - \eta)} \frac{\sinh(\lambda_j + \lambda_k + \eta)}{\sinh(\lambda_j + \lambda_k - \eta)} \tag{4.23}$$

Just as was the case for the periodic XXX model presented in section 4.1, the problem of finding the spectrum of the model of interest has been reduced to solving a set of

coupled equations which one can do using numerical methods that are less computationally expensive than direct diagonalisation. Note that the analytical Bethe Ansatz as presented here does not provide a method to calculate the eigenvectors of the transfer matrix, we can only access the eigenvalues with this method. This however is all we will need here since we will ultimately be interested in studying the CFT properties of the lattice model from finite size scaling as discussed in the introduction to this chapter. Integrable models with interesting continuum limits will be studied in later chapters using methods similar to the present analysis. The goal will remain the same: calculate the spectrum of the transfer matrix by solving a set of Bethe Ansatz equations instead of by direct diagonalisation.

4.4 The Hamiltonian Limit

We will also however be interested in the quantum Hamiltonian corresponding to a given transfer matrix. Following the construction in [81], one can define an open integrable Hamiltonian from the transfer matrix in the following way:

$$t'(0) = 2H \operatorname{Tr} K^+(0) + \operatorname{Tr} K^{+'}(0)\,, \tag{4.24}$$

which gives:

$$H = \sum_{n=1}^{L-1} H_{n,n+1} + \frac{1}{2} K_1^{-'}(0) + \frac{\operatorname{Tr}_0 K_0^+(0) H_{L0}}{\operatorname{Tr} K_0^+(0)}\,, \tag{4.25}$$

where $H_{n,n+1} = P_{n,n+1} \frac{\mathrm{d}}{\mathrm{d}\lambda} R_{n,n+1}(\lambda)|_{\lambda=0}$; the subscripts indicate on which spaces there is a non-trivial action. One can check that the Hamiltonian corresponding to the open six vertex model defined by (4.13) and (4.14) is the open XXZ Hamiltonian:

$$H = \sum_{i=1}^{L-1} (\sigma_i^x \sigma_{i+1}^x + \sigma_i^y \sigma_{i+1}^y + \cosh\eta \sigma_i^z \sigma_{i+1}^z) - \sinh\eta(\sigma_1^z - \sigma_L^z) \tag{4.26}$$

which was studied in detail in [100]. One can furthermore check from (4.21) that the energy eigenvalues are given by:

$$E = \sum_{i=1}^{m} \frac{4\sinh^2\eta}{\cosh(2\lambda_i) - \cosh(\eta)} + (L-1)\cosh\eta \tag{4.27}$$

To study the CFT using the Hamiltonian instead of the transfer matrix one can once again use the finite size scaling of the eigenvalues which have the following form:

$$E = f_0 L + f_{\mathrm{s}} - \frac{\pi v_{\mathrm{F}}(\frac{c}{24} - h)}{L} + o\left(\frac{1}{L}\right)\,, \tag{4.28}$$

where v_F is the Fermi velocity which is a model dependent quantity. In the present case of the XXZ model we have:

$$v_F = \frac{\pi \sin\gamma_0}{\gamma_0} \tag{4.29}$$

where we recall $\eta \equiv i\gamma_0$.

4.5 The CFT limit: examples

The remainder of this thesis will use equation (4.28) extensively in order to extract the CFT data from a lattice Hamiltonian in finite size. We briefly present here the well studied results of this procedure when applied to the XXZ model with a number of different boundary conditions. First of all, note that (4.28) is only valid for a model with open boundary conditions, and in the periodic case must be modified to:

$$E = f_0 L - \frac{\pi v_{\mathrm{F}}(\frac{c}{6} - 2\Delta_\phi)}{L} + o\left(\frac{1}{L}\right), \tag{4.30}$$

The CFT description of the periodic XXZ Hamiltonian, given by:

$$H = \sum_{i=1}^{L} (\sigma_i^x \sigma_{i+1}^x + \sigma_i^y \sigma_{i+1}^y + \cosh\eta \sigma_i^z \sigma_{i+1}^z) \tag{4.31}$$

was studied in [101]. The energy eigenvalues are once again given by (4.27) (but with the $L-1$ replaced by L since there is an additional interaction term in the periodic model) and the Bethe Ansatz equations given by:

$$\left(\frac{\sinh(\lambda_j - \frac{i\gamma_0}{2})}{\sinh(\lambda_j + \frac{i\gamma_0}{2})}\right)^L = -\prod_{k=1}^{m} \frac{\sinh(\lambda_j - \lambda_k - i\gamma_0)}{\sinh(\lambda_j - \lambda_k + i\gamma_0)} \tag{4.32}$$

By using (4.30), it is found [101] that, for all values of γ_0 (recall that $\eta = i\gamma_0$) the central charge is given by $c = 1$. To find a central charge that depends on γ_0, one must introduce "twisted" boundary conditions:

$$H = \sum_{i=1}^{L-1} (\sigma_i^x \sigma_{i+1}^x + \sigma_i^y \sigma_{i+1}^y + \cosh\eta \sigma_i^z \sigma_{i+1}^z) + \frac{e^{i\phi}}{2}\sigma_L^+ \sigma_1^- + \frac{e^{-i\phi}}{2}\sigma_L^- \sigma_1^+ \tag{4.33}$$

which were also studied in [101]. One can in fact calculate the thermodynamic form of the energy of the periodic model, and hence the conformal properties via equation (4.30), by using the thermodynamic Bethe Ansatz [102, 103] - also applied to the boundary case in [104].

Chapter 5

Integrable boundary conditions in the Potts model

In chapter 3 numerical methods were used to study the conformally invariant boundary conditions in the antiferromagnetic Potts model. However, an exact solution of the open model, even in the simplest case of free boundary conditions, was not considered. Chapter 4 motivated the study of exact solutions of this model and introduced the Bethe Ansatz which is the tool we will use in the present chapter to obtain the exact solutions that we are looking for.

We will do this by first recalling from section 3.1.3 that the antiferromagnetic Potts model can be reformulated as a staggered six vertex model, and that the latter model with periodic boundary conditions can be described by an integrable transfer matrix written in equation (3.19). We will then show that there is an exact mapping between the staggered six vertex model and another previously studied integrable model constructed from the twisted affine D_2^2 Lie algebra. This allows us to use some K-matrices from the D_2^2 model that satisfy the reflection equation in (4.10) to study integrable boundary conditions in the antiferromagnetic Potts model.

This chapter is structured as follows: in section 5.1 the formulation of the antiferromagnetic Potts model as a staggered six-vertex model is recalled. It is shown that there is an exact mapping between the staggered six-vertex model and the integrable model constructed from the twisted affine D_2^2 Lie algebra. In section 5.2 the model with open boundary conditions is considered. A particular K-matrix from the D_2^2 model [105, 106] is interpreted in the context of the staggered six-vertex model. In particular, it is found that the Hamiltonian of the model with the boundary conditions described by this K-matrix has a very simple interpretation in terms of generators of the Temperley-Lieb algebra. This integrable, open Hamiltonian is written in equation (5.46). The symmetry group of the chain is discussed and the additional degeneracies of the D_2^2 chain that were previously observed in [105] and [106] are interpreted using a symmetry operator written in terms of Temperley-Lieb algebra generators. In section 5.3 the Bethe Ansatz solution of the model with these boundary conditions is presented, and the critical exponents are derived analytically. Some numerical solutions to the Bethe Ansatz equations are presented and are used to show that the scaling behaviour of the chain is the same as that of the antiferromagnetic Potts model with free boundary conditions. Section 5.4 considers the model in two different representations of the Temperley-Lieb algebra and numerical results confirms that we have indeed correctly identified the underlying

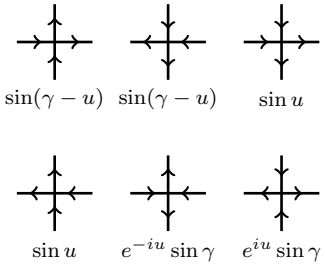


Figure 5.1: The six vertices and their Boltzmann weights.

boundary CFT.

5.1 The staggered six-vertex model and the D_2^2 model

5.1.1 Background

We recall from chapter 3 the Hamiltonian of the isotropic two-dimensional Q-state Potts model

$$\mathcal{H} = -K \sum_{\langle ij \rangle} \delta_{\sigma_i \sigma_j} , \tag{5.1}$$

where $\sigma_i = 1, 2, \ldots, Q$ and $\langle ij \rangle$ denotes the set of nearest neighbours on the square lattice. This model has been reviewed in many places [107, 32, 54]. It was shown in section 3.1 that the Potts model can be reformulated as a height, loop and vertex model where the partition functions are identical to that of the original Potts model described in terms of spins, but with different observables. It is another well-known result, reviewed in chapter 3 that when the correspondence between the Potts and the vertex model is carried out at the so-called "ferromagnetic critical point", the resulting vertex model is the celebrated "six-vertex model". Carrying out this Potts/vertex mapping at the other critical point of the Potts model, the "antiferromagnetic critical point", one obtains the "staggered six-vertex model" where the Boltzmann weights take particular values that alternate with each row/column.

Here we will show that the staggered six-vertex model is identical to an integrable model constructed from the D_2^2 affine Lie algebra. This relationship between the D_2^2 model and the staggered six vertex model was first alluded to in [108] where the spectra of the two models were shown to be identical. Here we take this result further and show that the transfer matrices of the two models can in fact be identified. This paves the way in later sections to derive new results related to the antiferromagnetic Potts model and its integrable boundary conditions. We will be particularly interested in "free" boundary conditions in the Potts model which corresponds in (5.1) to imposing no additional constraint on the Potts spins at the boundary so that the sum runs over all nearest neighbours as usual but boundary spins have fewer nearest neighbours.

5.1.2 Review of the staggered six-vertex model

The six-vertex model with no staggering was briefly discussed in section 4.3. It is defined by placing arrows on the edges of a square lattice subject to the constraint that there must be two incoming and two outgoing arrows at every vertex. The six possible vertices that satisfy this constraint are shown in Figure 5.1. Each of these vertices then

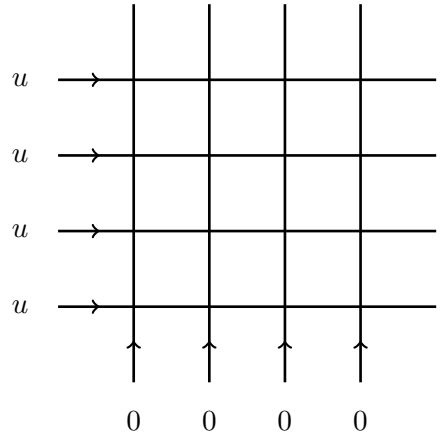


Figure 5.2: The spectral parameters on the lattice of the six-vertex model

takes a particular Boltzmann weight parameterised by the 'spectral parameter' u which controls the amount of anisotropy. The Boltzmann weights are also functions of the crossing parameter γ which appears in the Q-state Potts model as

$$\sqrt{Q} = e^{i\gamma} + e^{-i\gamma}\,. \tag{5.2}$$

We can encode the Boltzmann weights in the $\check{R}$-matrix which acts on the space

$$\{|\uparrow\uparrow\rangle, |\uparrow\downarrow\rangle, |\downarrow\uparrow\rangle, |\downarrow\downarrow\rangle\}\,. \tag{5.3}$$

The present analysis will define $\check{R}$ in the following way

$$\check{R}(u) = \begin{pmatrix} \sin(\gamma-u) & 0 & 0 & 0 \\ 0 & e^{-iu}\sin\gamma & \sin u & 0 \\ 0 & \sin u & e^{iu}\sin\gamma & 0 \\ 0 & 0 & 0 & \sin(\gamma-u) \end{pmatrix} \tag{5.4}$$

By considering $\check{R}(u)$ to act in the North-East direction, we can see that (5.4) recovers the Boltzmann weights of the vertices in (5.1). If we associate the spectral parameters u_1 and u_2 to the left and right lines as one approaches a given vertex (along the NE direction), the $\check{R}$-matrix takes the parameter $u_1 - u_2$. Note that we will henceforth refer to both the R-matrix and the $\check{R}$-matrix, the latter being the former multiplied by a permutation operator. Consider then a square lattice where the parameters u and 0 are associated to all horizontal and vertical lines, as in Figure 5.2.

The action of $\check{R}$ on the lattice in Figure 5.2 recovers the correct Boltzmann weights of the six-vertex model for all of the vertices on the lattice. With this formulation of the six-vertex model we can now generalise to the staggered six-vertex model [54, 109]. Instead of associating u and 0 to all horizontal and vertical lines, respectively, as in Figure 5.2, we will introduce a "staggering" of these parameters in both the horizontal and the vertical direction as in Figure 5.3.

This model with periodic boundary conditions was studied in detail in [54]. The staggering can be conveniently taken into account by introducing a block R-matrix as in Figure 5.4.

This new R-matrix now acts on the larger space

$$\{|\uparrow\uparrow\rangle, |\uparrow\downarrow\rangle, |\downarrow\uparrow\rangle, |\downarrow\downarrow\rangle\} \otimes \{|\uparrow\uparrow\rangle, |\uparrow\downarrow\rangle, |\downarrow\uparrow\rangle, |\downarrow\downarrow\rangle\}\,. \tag{5.5}$$

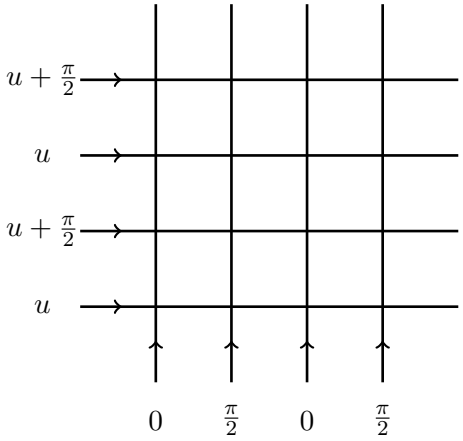


Figure 5.3: The spectral parameters on the lattice of the staggered six-vertex model .

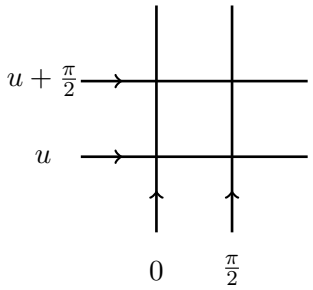


Figure 5.4: The block R-matrix.

As discussed in [54], it turns out that a convenient basis to consider is:

$$\{|\uparrow\uparrow\rangle, |0\rangle, |\bar{0}\rangle, |\downarrow\downarrow\rangle\} \otimes \{|\uparrow\uparrow\rangle, |0\rangle, |\bar{0}\rangle, |\downarrow\downarrow\rangle\}\,, \tag{5.6}$$

where

$$|0\rangle = \frac{1}{\sqrt{2\cos\gamma}}(e^{\frac{i\gamma}{2}}|\uparrow\downarrow\rangle - e^{-\frac{i\gamma}{2}}|\downarrow\uparrow\rangle)\,. \tag{5.7a}$$

$$|\bar{0}\rangle = \frac{1}{\sqrt{2\cos\gamma}}(e^{-\frac{i\gamma}{2}}|\uparrow\downarrow\rangle + e^{\frac{i\gamma}{2}}|\downarrow\uparrow\rangle)\,. \tag{5.7b}$$

In this basis there are only 38 vertices with non-zero Boltzmann weights. At each vertex, we will represent the $|\uparrow\uparrow\rangle$ state by an up or right-pointing arrow, the $|\downarrow\downarrow\rangle$ state by a down or left-pointing arrow, the $|0\rangle$ state by a thin line and the $|\bar{0}\rangle$ state by a thick line (the lines associated with $|0\rangle$ and $|\bar{0}\rangle$ carry no arrows). The 38 possible vertices are drawn in Figure 5.6. It was discussed in [54] that the R-matrix of this 38-vertex model satisfies the Yang-Baxter equation and the model was solved via Bethe Ansatz.

Sections 5.1.3 and 5.1.4 will show that the staggered six-vertex model, or equivalently the 38-vertex model, is equivalent to the integrable model constructed from the twisted affine D_2^2 Lie algebra. What we mean by 'equivalent' is the following: there is a well-defined procedure to start with a Lie algebra and find an R-matrix that satisfies the Yang-Baxter equation, and this procedure has been carried out for D_2^2 [110]. When we write this R-matrix in a particular basis we find that there are only 38 non-zero matrix components; the D_2^2 R-matrix therefore describes a 38-vertex model. It turns out then

that these matrix components are exactly those of the 38-vertex model arising from the staggered six-vertex model. [1]

5.1.3 Mapping between the two models: General strategy

Starting from a given Lie algebra, one can construct an R-matrix that satisfies the Yang-Baxter equation. This has been carried out for the twisted affine D_2^2 Lie algebra in [110]. We will show here that when written in an appropriate basis, the D_2^2 R-matrix can be identified with that of the 38-vertex model arising from the staggered six-vertex model.

The D_2^2 R-matrix is a 16×16 matrix acting on the states:

$$\{|1\rangle, |2\rangle, |3\rangle, |4\rangle\} \otimes \{|1\rangle, |2\rangle, |3\rangle, |4\rangle\} \tag{5.8}$$

where $1, 2, 3, 4$ are just labels for the four possible states that each edge in the vertex model can take. Now define

$$|\tilde{2}\rangle = \frac{1}{\sqrt{2}}(|2\rangle + |3\rangle)\,, \tag{5.9a}$$

$$|\tilde{3}\rangle = \frac{1}{\sqrt{2}}(|2\rangle - |3\rangle)\,. \tag{5.9b}$$

We are interested in calculating the D_2^2 R-matrix in the basis

$$\{|1\rangle, |\tilde{2}\rangle, |\tilde{3}\rangle, |4\rangle\} \otimes \{|1\rangle, |\tilde{2}\rangle, |\tilde{3}\rangle, |4\rangle\}\,. \tag{5.10}$$

We will do this by calculating each matrix component in the new basis term by term. The strategy is the following: first note that the D_2^2 R-matrix is written in terms of the matrices $E_{\alpha\beta} \otimes E_{\gamma\delta}$ where $E_{\alpha\beta}$ is a matrix with all components equal to zero except for the component in the α-th row and β-th column which is equal to 1, i.e.,

$$(E_{\alpha\beta})_{ij} = \delta_{i\alpha}\delta_{j\beta}\,, \tag{5.11}$$

with α,β,γ,δ taking labels $1, 2, 3$ or 4. To calculate the matrix elements in the new basis we need to expand the R-matrix in terms of matrices $E_{\tilde{\alpha}\tilde{\beta}} \otimes E_{\tilde{\gamma}\tilde{\delta}}$ where $\tilde{\alpha}, \tilde{\beta}, \tilde{\gamma}, \tilde{\delta}$ take labels 1,$\tilde{2}, \tilde{3}$ or 4 and we have

$$E_{\tilde{\alpha}\tilde{2}} = \frac{1}{\sqrt{2}}(E_{\tilde{\alpha}2} + E_{\tilde{\alpha}3})\,, \tag{5.12a}$$

$$E_{\tilde{2}\tilde{\alpha}} = \frac{1}{\sqrt{2}}(E_{2\tilde{\alpha}} + E_{3\tilde{\alpha}})\,, \tag{5.12b}$$

$$E_{\tilde{\alpha}\tilde{3}} = \frac{1}{\sqrt{2}}(E_{\tilde{\alpha}2} - E_{\tilde{\alpha}3})\,, \tag{5.12c}$$

$$E_{\tilde{3}\tilde{\alpha}} = \frac{1}{\sqrt{2}}(E_{2\tilde{\alpha}} - E_{3\tilde{\alpha}})\,. \tag{5.12d}$$

We have then, for example:

$$E_{1\tilde{2}} \otimes E_{1\tilde{2}} = \frac{1}{2}(E_{12} \otimes E_{12} + E_{12} \otimes E_{13} + E_{13} \otimes E_{12} + E_{13} \otimes E_{13})\,, \tag{5.13a}$$

$$\begin{aligned} E_{1\tilde{2}} \otimes E_{\tilde{2}\tilde{3}} = \frac{1}{2\sqrt{2}}(&E_{12} \otimes E_{22} + E_{12} \otimes E_{32} - E_{12} \otimes E_{23} - E_{12} \otimes E_{33} \\ &+ E_{13} \otimes E_{22} + E_{13} \otimes E_{32} - E_{13} \otimes E_{23} - E_{13} \otimes E_{33})\,. \end{aligned} \tag{5.13b}$$

[1] There is one subtlety that will be discussed in more detail later. Some of the matrix components of the two R-matrices differ by a sign, but this turns out to be unimportant because the full transfer matrix constructed from either R-matrix is the same.

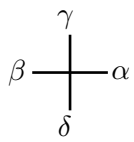


Figure 5.5: Labelling around a vertex in the D_2^2 model.

When we expand the D_2^2 R-matrix in terms of the matrices $E_{\tilde{\alpha}\tilde{\beta}} \otimes E_{\tilde{\gamma}\tilde{\delta}}$, the coefficient of each of these terms will give the Boltzmann weight of exactly one vertex. It will turn out that, in this basis, there are exactly 38 non-zero coefficients and that these coefficients are the Boltzmann weights of the 38-vertex model arising from staggered six-vertex model. The coefficient in front of the term in (5.13) will correspond to the Boltzmann weight of one of these 38 vertices, as we now discuss.

5.1.4 Deriving the Boltzmann weights

The D_2^2 R-matrix is expanded in terms of the matrices $E_{\alpha\beta} \otimes E_{\gamma\delta}$:

$$R = \sum_{\alpha\beta\gamma\delta} \omega_{\alpha\beta\gamma\delta} E_{\alpha\beta} \otimes E_{\gamma\delta} \,. \tag{5.14}$$

We then interpret $\omega_{\alpha\beta\gamma\delta}$ as the Boltzmann weight of the vertex in Figure 5.5. In particular, α is the label of the state of the right edge, β the label of the state on the left edge, γ the label of the state on the top edge and δ the label of the state on the bottom edge. We will represent these labels in the following way: associate a down or left-pointing arrow to the label 1, an up or right-pointing arrow to the label 4, a thin line to the label $\tilde{2}$ and a thick line to the label $\tilde{3}$. The coefficient ω_{1111} for example then gives the Boltzmann weight of vertex (1) in Figure 5.6, and the coefficient $\omega_{4\tilde{3}1\tilde{3}}$ gives the Boltzmann weight of vertex (13).

The explicit expression for the R-matrix of the D_2^2 model can be found in equation (3.7) of [110]. The important point for us is that this expression for the D_2^2 R-matrix is of the form (5.14) and that the weights $\omega_{\alpha\beta\gamma\delta}$ are written in terms of parameters x and k. Meanwhile, the explicit expression for the 38-vertex model can be found in section 2.3.3 of [54] and this matrix is written in terms of parameters u_0 and γ_0. The latter two parameters are related to those of the six-vertex model R-matrix (5.4) by [54]

$$u_0 = -2u \,, \tag{5.15a}$$
$$\gamma_0 = \pi - 2\gamma \,. \tag{5.15b}$$

It will turn out that the correct associations between the parameters of the two models are

$$k = -e^{-i\gamma_0} \,, \tag{5.16a}$$
$$x = e^{-iu_0} \,, \tag{5.16b}$$

so that we have

$$k = e^{2i\gamma} \,, \tag{5.17a}$$
$$x = e^{2iu} \,. \tag{5.17b}$$

With this identification, our goal is then to write the R-matrix in a new basis:

$$R = \sum_{\tilde{\alpha}\tilde{\beta}\tilde{\gamma}\tilde{\delta}} \tilde{\omega}_{\tilde{\alpha}\tilde{\beta}\tilde{\gamma}\tilde{\delta}} E_{\tilde{\alpha}\tilde{\beta}} \otimes E_{\tilde{\gamma}\tilde{\delta}} \,, \tag{5.18}$$

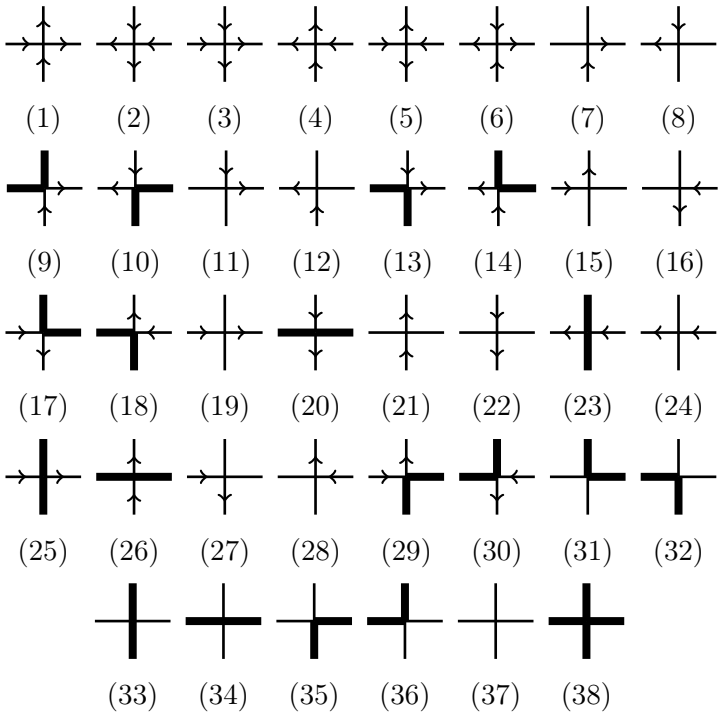


Figure 5.6: The 38 vertices of the D_2^2 model.

and to calculate the weights $\tilde{\omega}_{\tilde{\alpha}\tilde{\beta}\tilde{\gamma}\tilde{\delta}}$ in terms of the parameters u_0 and γ_0 by writing R in the form (5.18). Consider all the vertices of the 38-vertex model in Figure 5.6. There are three types of vertices to consider: vertices with four arrows (1 to 6), two arrows (7 to 30) and no arrows (31 to 38). We will study each of these three types of vertices individually.

Vertices 1 to 6

These vertices have four arrows (two in and two out). Since we associate arrows with states $|1\rangle$ and $|4\rangle$ there will be no change to the Boltzmann weights of these vertices when we change from the old basis $|1\rangle$,$|2\rangle$,$|3\rangle$,$|4\rangle$ to the new basis $|1\rangle$,$|\tilde{2}\rangle$,$|\tilde{3}\rangle$,$|4\rangle$, except for the change in parameters from x and k to u_0 and γ_0. Consider for example vertices 1 and 2. These correspond to the terms $\omega_{4444}E_{44}\otimes E_{44}$ and $\omega_{1111}E_{11}\otimes E_{11}$ in the expansion of the R-matrix. We have from [110]:

$$\omega_{1111} = \omega_{4444} = (x^2 - k^2)^2\,, \tag{5.19}$$

and we know that $\omega_{1111} = \tilde{\omega}_{1111}$ and $\omega_{4444} = \tilde{\omega}_{4444}$. Using (5.16) we then find

$$\omega_{1111} = \omega_{4444} = -4k^2x^2\sin^2(\gamma_0 - u_0)\,, \tag{5.20}$$

which is equal to the weight of these vertices in the staggered six-vertex model, up to an overall factor of $16k^2x^2$ which will turn out to be present in all terms. We can perform the same calculation for vertices 3 to 7, the results of which are shown in table 5.1. We see that when we make the associations $x = \exp(-iu_0)$ and $k = -\exp(-i\gamma_0)$, as in (5.16), all of these vertices have the same Boltzmann weight in the D_2^2 model and the staggered six-vertex model, again up to a factor of $16k^2x^2$.

Vertex	D_2^2 weight	Staggered six-vertex weight
1	$-4k^2x^2\sin^2(\gamma_0-u_0)$	$-\frac{1}{4}\sin^2(\gamma_0-u_0)$
2	$-4k^2x^2\sin^2(\gamma_0-u_0)$	$-\frac{1}{4}\sin^2(\gamma_0-u_0)$
3	$-4k^2x^2\sin^2(u_0)$	$-\frac{1}{4}\sin^2(u_0)$
4	$-4k^2x^2\sin^2(u_0)$	$-\frac{1}{4}\sin^2(u_0)$
5	$4k^2x^2e^{-2iu}\sin(\gamma_0)(\sin(u_0)-\sin(\gamma_0-u_0))$	$\frac{1}{4}e^{-2iu}\sin(\gamma_0)(\sin(u_0)-\sin(\gamma_0-u_0))$
6	$4k^2x^2e^{2iu}\sin(\gamma_0)(\sin(u_0)-\sin(\gamma_0-u_0))$	$\frac{1}{4}e^{2iu}\sin(\gamma_0)(\sin(u_0)-\sin(\gamma_0-u_0))$

Table 5.1: Correspondence between the Boltzmann weights of the D_2^2 model and the staggered six-vertex model. Vertices 1 to 6.

Vertices 7 to 30

We will now show an example of a calculation of the D_2^2 Boltzmann weight of a vertex with two arrows. Consider vertices 8 and 10, which correspond to the terms $E_{\tilde{2}1}\otimes E_{1\tilde{2}}$ and $E_{\tilde{3}1}\otimes E_{1\tilde{3}}$ in the expansion of the R-matrix. We will calculate the coefficients of these terms when we change basis from $|1\rangle,|2\rangle,|3\rangle,|4\rangle$ to $|1\rangle,|\tilde{2}\rangle,|\tilde{3}\rangle,|4\rangle$. Consider the following terms appearing in the expansion of the R-matrix in the old basis:

$$-\frac{1}{2}(k^2-1)(x^2-k^2)(x+1)x(E_{21}\otimes E_{12}+E_{31}\otimes E_{13})-\frac{1}{2}x(k^2-1)(x^2-k^2)(x-1)(E_{21}\otimes E_{13}+E_{31}\otimes E_{12})\,. \tag{5.21}$$

This can be reformulated as

$$-\frac{1}{2}(k^2-1)(x^2-k^2)x[x(E_{21}+E_{31})\otimes E_{12}+(E_{21}-E_{31})\otimes E_{12}+x(E_{21}+E_{31})\otimes E_{13}-(E_{21}-E_{31})\otimes E_{13}]\,, \tag{5.22}$$

which we can see gives:

$$-(k^2-1)(x^2-k^2)x[xE_{\tilde{2}1}\otimes E_{1\tilde{2}}+E_{\tilde{3}1}\otimes E_{1\tilde{3}}]\,. \tag{5.23}$$

After making the associations (5.16) we finally obtain

$$-4k^2x^2e^{2iu}\sin(\gamma_0-u_0)\sin(\gamma_0)[E_{\tilde{2}1}\otimes E_{1\tilde{2}}]+4k^2x^2\sin(\gamma_0-u_0)\sin(\gamma_0)[E_{\tilde{3}1}\otimes E_{1\tilde{3}}]\,. \tag{5.24}$$

The coefficients of the two terms in (5.24) give the Boltzmann weights of vertices 8 and 10 in Figure 5.6 and are compared with the Boltzmann weights of the staggered six-vertex model in table 5.2. We observe that the Boltzmann weights in the two models are equal, again up to the factor of $16k^2x^2$. In the case of vertex 10, there is a difference of sign between the two models. Vertices with a sign difference in the two models are marked with an asterisk in the last column of the table. This sign difference will turn out not to affect the transfer matrix built from the R-matrix and therefore not to have any effect on the physics. This will be explained in more detail below.

Vertices 31 to 38

This section will present the calculation of the Boltzmann weights of vertices with no arrows. These vertices are labelled 31 to 38 in Figure 5.6 and correspond to the terms $E_{\tilde{3}\tilde{2}}\otimes E_{\tilde{3}\tilde{2}}$, $E_{\tilde{2}\tilde{3}}\otimes E_{\tilde{2}\tilde{3}}$, $E_{\tilde{2}\tilde{2}}\otimes E_{\tilde{3}\tilde{3}}$, $E_{\tilde{3}\tilde{3}}\otimes E_{\tilde{2}\tilde{2}}$, $E_{\tilde{3}\tilde{2}}\otimes E_{\tilde{2}\tilde{3}}$, $E_{\tilde{2}\tilde{3}}\otimes E_{\tilde{3}\tilde{2}}$, $E_{\tilde{2}\tilde{2}}\otimes E_{\tilde{2}\tilde{2}}$, $E_{\tilde{3}\tilde{3}}\otimes E_{\tilde{3}\tilde{3}}$.

Vertex	D_2^2 weight	Staggered six-vertex weight	
7	$-4k^2x^2e^{2iu}\sin(\gamma_0-u_0)\sin(\gamma_0)$	$-\frac{1}{4}e^{2iu}\sin(\gamma_0-u_0)\sin(\gamma_0)$	
8	$-4k^2x^2e^{2iu}\sin(\gamma_0-u_0)\sin(\gamma_0)$	$-\frac{1}{4}e^{2iu}\sin(\gamma_0-u_0)\sin(\gamma_0)$	
9	$4k^2x^2\sin(\gamma_0-u_0)\sin(\gamma_0)$	$-\frac{1}{4}\sin(\gamma_0-u_0)\sin(\gamma_0)$	*
10	$4k^2x^2\sin(\gamma_0-u_0)\sin(\gamma_0)$	$-\frac{1}{4}\sin(\gamma_0-u_0)\sin(\gamma_0)$	*
11	$4k^2x^2e^{-i(\gamma-2u)}\sin(u_0)\sin(\gamma_0)$	$\frac{1}{4}e^{-i(\gamma-2u)}\sin(u_0)\sin(\gamma_0)$	
12	$4k^2x^2e^{-i(\gamma-2u)}\sin(u_0)\sin(\gamma_0)$	$\frac{1}{4}e^{-i(\gamma-2u)}\sin(u_0)\sin(\gamma_0)$	
13	$4k^2x^2e^{i\gamma}\sin(u_0)\sin(\gamma_0)$	$-\frac{1}{4}e^{i\gamma}\sin(u_0)\sin(\gamma_0)$	*
14	$4k^2x^2e^{i\gamma}\sin(u_0)\sin(\gamma_0)$	$-\frac{1}{4}e^{i\gamma}\sin(u_0)\sin(\gamma_0)$	*
15	$-4k^2x^2e^{-2iu}\sin(\gamma_0-u_0)\sin(\gamma_0)$	$-\frac{1}{4}e^{-2iu}\sin(\gamma_0-u_0)\sin(\gamma_0)$	
16	$-4k^2x^2e^{-2iu}\sin(\gamma_0-u_0)\sin(\gamma_0)$	$-\frac{1}{4}e^{-2iu}\sin(\gamma_0-u_0)\sin(\gamma_0)$	
17	$4k^2x^2e^{-i\gamma}\sin(u_0)\sin(\gamma_0)$	$-\frac{1}{4}e^{-i\gamma}\sin(u_0)\sin(\gamma_0)$	*
18	$4k^2x^2e^{-i\gamma}\sin(u_0)\sin(\gamma_0)$	$-\frac{1}{4}e^{-i\gamma}\sin(u_0)\sin(\gamma_0)$	*
19	$-4k^2x^2\sin(\gamma_0-u_0)\sin(u_0)$	$-\frac{1}{4}\sin(\gamma_0-u_0)\sin(u_0)$	
20	$-4k^2x^2\sin(\gamma_0-u_0)\sin(u_0)$	$-\frac{1}{4}\sin(\gamma_0-u_0)\sin(u_0)$	
21	$-4k^2x^2\sin(\gamma_0-u_0)\sin(u_0)$	$-\frac{1}{4}\sin(\gamma_0-u_0)\sin(u_0)$	
22	$-4k^2x^2\sin(\gamma_0-u_0)\sin(u_0)$	$-\frac{1}{4}\sin(\gamma_0-u_0)\sin(u_0)$	
23	$-4k^2x^2\sin(\gamma_0-u_0)\sin(u_0)$	$-\frac{1}{4}\sin(\gamma_0-u_0)\sin(u_0)$	
24	$-4k^2x^2\sin(\gamma_0-u_0)\sin(u_0)$	$-\frac{1}{4}\sin(\gamma_0-u_0)\sin(u_0)$	
25	$-4k^2x^2\sin(\gamma_0-u_0)\sin(u_0)$	$-\frac{1}{4}\sin(\gamma_0-u_0)\sin(u_0)$	
26	$-4k^2x^2\sin(\gamma_0-u_0)\sin(u_0)$	$-\frac{1}{4}\sin(\gamma_0-u_0)\sin(u_0)$	
27	$4k^2x^2e^{i(\gamma-2u)}\sin(u_0)\sin(\gamma_0)$	$\frac{1}{4}e^{i(\gamma-2u)}\sin(u_0)\sin(\gamma_0)$	
28	$4k^2x^2e^{i(\gamma-2u)}\sin(u_0)\sin(\gamma_0)$	$\frac{1}{4}e^{i(\gamma-2u)}\sin(u_0)\sin(\gamma_0)$	
29	$4k^2x^2\sin(\gamma_0-u_0)\sin(\gamma_0)$	$-\frac{1}{4}\sin(\gamma_0-u_0)\sin(\gamma_0)$	*
30	$4k^2x^2\sin(\gamma_0-u_0)\sin(\gamma_0)$	$-\frac{1}{4}\sin(\gamma_0-u_0)\sin(\gamma_0)$	*

Table 5.2: Correspondence between Boltzmann weights (continued). Vertices 7 to 30.

Consider the terms in the expansion of the D_2^2 R-matrix:

$$\begin{aligned}
&E_{22}\otimes E_{22}[k(x^2-1)(x^2-k^2)-\frac{1}{2}(k^2-1)(k+1)x(x+1)(x-k)]\\
+&E_{33}\otimes E_{33}[k(x^2-1)(x^2-k^2)-\frac{1}{2}(k^2-1)(k+1)x(x+1)(x-k)]\\
+&E_{22}\otimes E_{33}[k(x^2-1)(x^2-k^2)+\frac{1}{2}(k^2-1)(k+1)x(x-1)(x+k)]\\
+&E_{33}\otimes E_{22}[k(x^2-1)(x^2-k^2)+\frac{1}{2}(k^2-1)(k+1)x(x-1)(x+k)]\\
+&E_{32}\otimes E_{23}[\frac{1}{2}(k^2-1)(k-1)x(x+1)(x+k)]\\
+&E_{23}\otimes E_{32}[\frac{1}{2}(k^2-1)(k-1)x(x+1)(x+k)]\\
+&E_{32}\otimes E_{32}[-\frac{1}{2}(k^2-1)(k-1)x(x-1)(x-k)]\\
+&E_{23}\otimes E_{23}[-\frac{1}{2}(k^2-1)(k-1)x(x-1)(x-k)]\,.
\end{aligned}\tag{5.25}$$

Now use the easily verified expressions:

$$\begin{aligned}
E_{22}\otimes E_{22}+E_{33}\otimes E_{33} = {}& \tfrac{1}{2}[E_{\bar2\bar2}\otimes E_{\bar2\bar2}+E_{\bar2\bar3}\otimes E_{\bar2\bar3}+E_{\bar3\bar2}\otimes E_{\bar3\bar2}+E_{\bar2\bar3}\otimes E_{\bar3\bar2}+\\
&E_{\bar3\bar2}\otimes E_{\bar2\bar3}+E_{\bar2\bar2}\otimes E_{\bar3\bar3}+E_{\bar3\bar3}\otimes E_{\bar2\bar2}+E_{\bar3\bar3}\otimes E_{\bar3\bar3}] \quad (5.26a)\\
E_{22}\otimes E_{33}+E_{33}\otimes E_{22} = {}& \tfrac{1}{2}[E_{\bar2\bar2}\otimes E_{\bar2\bar2}-E_{\bar2\bar3}\otimes E_{\bar2\bar3}-E_{\bar3\bar2}\otimes E_{\bar3\bar2}-E_{\bar2\bar3}\otimes E_{\bar3\bar2}-\\
&E_{\bar3\bar2}\otimes E_{\bar2\bar3}+E_{\bar2\bar2}\otimes E_{\bar3\bar3}+E_{\bar3\bar3}\otimes E_{\bar2\bar2}+E_{\bar3\bar3}\otimes E_{\bar3\bar3}] \quad (5.26b)\\
E_{32}\otimes E_{23}+E_{23}\otimes E_{32} = {}& \tfrac{1}{2}[E_{\bar2\bar2}\otimes E_{\bar2\bar2}-E_{\bar2\bar3}\otimes E_{\bar2\bar3}-E_{\bar3\bar2}\otimes E_{\bar3\bar2}+E_{\bar2\bar3}\otimes E_{\bar3\bar2}+\\
&E_{\bar3\bar2}\otimes E_{\bar2\bar3}-E_{\bar2\bar2}\otimes E_{\bar3\bar3}-E_{\bar3\bar3}\otimes E_{\bar2\bar2}+E_{\bar3\bar3}\otimes E_{\bar3\bar3}] \quad (5.26c)\\
E_{32}\otimes E_{32}+E_{23}\otimes E_{23} = {}& \tfrac{1}{2}[E_{\bar2\bar2}\otimes E_{\bar2\bar2}+E_{\bar2\bar3}\otimes E_{\bar2\bar3}+E_{\bar3\bar2}\otimes E_{\bar3\bar2}-E_{\bar2\bar3}\otimes E_{\bar3\bar2}-\\
&E_{\bar3\bar2}\otimes E_{\bar2\bar3}-E_{\bar2\bar2}\otimes E_{\bar3\bar3}-E_{\bar3\bar3}\otimes E_{\bar2\bar2}+E_{\bar3\bar3}\otimes E_{\bar3\bar3}] \quad (5.26d)
\end{aligned}$$

to write the terms in (5.25) as

$$\begin{aligned}
&\frac{1}{2}\left[k(x^2-1)(x^2-k^2)-\frac{1}{2}(k^2-1)(k+1)x(x+1)(x-k)\right]\times\\
&\qquad\big(E_{\bar2\bar2}\otimes E_{\bar2\bar2}+E_{\bar2\bar3}\otimes E_{\bar2\bar3}+E_{\bar3\bar2}\otimes E_{\bar3\bar2}+E_{\bar2\bar3}\otimes E_{\bar3\bar2}+\\
&\qquad E_{\bar3\bar2}\otimes E_{\bar2\bar3}+E_{\bar2\bar2}\otimes E_{\bar3\bar3}+E_{\bar3\bar3}\otimes E_{\bar2\bar2}+E_{\bar3\bar3}\otimes E_{\bar3\bar3}\big)\\
+&\frac{1}{2}\left[k(x^2-1)(x^2-k^2)+\frac{1}{2}(k^2-1)(k+1)x(x-1)(x+k)\right]\times\\
&\qquad\big(E_{\bar2\bar2}\otimes E_{\bar2\bar2}-E_{\bar2\bar3}\otimes E_{\bar2\bar3}-E_{\bar3\bar2}\otimes E_{\bar3\bar2}-E_{\bar2\bar3}\otimes E_{\bar3\bar2}-\\
&\qquad E_{\bar3\bar2}\otimes E_{\bar2\bar3}+E_{\bar2\bar2}\otimes E_{\bar3\bar3}+E_{\bar3\bar3}\otimes E_{\bar2\bar2}+E_{\bar3\bar3}\otimes E_{\bar3\bar3}\big)\\
+&\left[\frac{1}{4}(k^2-1)(k-1)x(x+1)(x+k)\right]\times\\
&\qquad\big(E_{\bar2\bar2}\otimes E_{\bar2\bar2}-E_{\bar2\bar3}\otimes E_{\bar2\bar3}-E_{\bar3\bar2}\otimes E_{\bar3\bar2}+E_{\bar2\bar3}\otimes E_{\bar3\bar2}+\\
&\qquad E_{\bar3\bar2}\otimes E_{\bar2\bar3}-E_{\bar2\bar2}\otimes E_{\bar3\bar3}-E_{\bar3\bar3}\otimes E_{\bar2\bar2}+E_{\bar3\bar3}\otimes E_{\bar3\bar3}\big)\\
-&\left[\frac{1}{4}(k^2-1)(k-1)x(x-1)(x-k)\right]\times\\
&\qquad\big(E_{\bar2\bar2}\otimes E_{\bar2\bar2}+E_{\bar2\bar3}\otimes E_{\bar2\bar3}+E_{\bar3\bar2}\otimes E_{\bar3\bar2}-E_{\bar2\bar3}\otimes E_{\bar3\bar2}-\\
&\qquad E_{\bar3\bar2}\otimes E_{\bar2\bar3}-E_{\bar2\bar2}\otimes E_{\bar3\bar3}-E_{\bar3\bar3}\otimes E_{\bar2\bar2}+E_{\bar3\bar3}\otimes E_{\bar3\bar3}\big)\,.
\end{aligned}\tag{5.27}$$

Vertex	D_2^2 weight	Staggered six-vertex weight	
31	$4k^2x^2\sin(u_0)\sin(\gamma_0)$	$-\frac{1}{4}\sin(u_0)\sin(\gamma_0)$	*
32	$4k^2x^2\sin(u_0)\sin(\gamma_0)$	$-\frac{1}{4}\sin(u_0)\sin(\gamma_0)$	*
33	$-4k^2x^2\sin(\gamma_0-u_0)\sin(u_0)$	$-\frac{1}{4}\sin(\gamma_0-u_0)\sin(u_0)$	
34	$-4k^2x^2\sin(\gamma_0-u_0)\sin(u_0)$	$-\frac{1}{4}\sin(\gamma_0-u_0)\sin(u_0)$	
35	$4k^2x^2\sin(\gamma_0-u_0)\sin(\gamma_0)$	$-\frac{1}{4}\sin(\gamma_0-u_0)\sin(\gamma_0)$	*
36	$4k^2x^2\sin(\gamma_0-u_0)\sin(\gamma_0)$	$-\frac{1}{4}\sin(\gamma_0-u_0)\sin(\gamma_0)$	*
37	$-4k^2x^2(\sin^2(\gamma_0)+\sin(\gamma_0-u_0)\sin(u_0))$	$-\frac{1}{4}(\sin^2(\gamma_0)+\sin(\gamma_0-u_0)\sin(u_0))$	
38	$-4k^2x^2(\sin^2(\gamma_0)+\sin(\gamma_0-u_0)\sin(u_0))$	$-\frac{1}{4}(\sin^2(\gamma_0)+\sin(\gamma_0-u_0)\sin(u_0))$	

Table 5.3: Correspondence between Boltzmann weights (continued). Vertices 31 to 38.

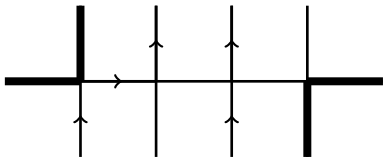


Figure 5.7: A configuration of vertices in one row generated by the action of the transfer matrix. The vertices on the far left and far right of the figure correspond to vertices (9) and (35) in Figure 5.6. The Boltzmann weights of these two vertices can be found in tables 5.1 and 5.3 respectively where we observe that both of them have a * beside them, meaning that their signs are opposite to the signs of the corresponding vertices of the staggered six vertex model. The two minus signs cancel each other out. More generally, the periodic boundary conditions ensure that there are will always be an even number of vertices with opposite signs in the two models.

We now collect coefficients of each of the terms. The coefficient of, for example, $E_{\tilde{2}\tilde{2}} \otimes E_{\tilde{2}\tilde{2}}$ reduces to $k(x^2-1)(x^2-k^2)+x^2(k^2-1)^2$ which after applying (5.16) becomes $-4k^2x^2[\sin^2(\gamma_0)-\sin(\gamma_0-u_0)\sin(u_0)]$, which is exactly the coefficient of vertex 37 in Figure 5.6 in both the D_2^2 model and the staggered six-vertex model. The results for the other coefficients are summarised in table 5.3.

Sign differences

As was briefly touched upon, there are some Boltzmann weights in the D_2^2 construction of the model that differ by a sign from the Boltzmann weights in the staggered six-vertex version of the model. These vertices have been highlighted by asterisks in the right columns of tables 5.1–5.3. From Figure 5.6 we observe that all of these vertices are such that there is one horizontal thick line and one vertical thick line. Observe then that, as well as the conservation of the direction of arrows, all vertices conserve the parity of the number of thick lines. In particular, if there is one incoming thick line there must be one outgoing thick line, and if there are two incoming thick lines there must be *either* two outgoing thick lines or no outgoing thick lines. A consequence of this is that, when periodic boundary conditions are imposed, any given configuration of vertices generated by a transfer matrix must contain an even number of these vertices with asterisks, and hence the minus signs all cancel. This is highlighted in Figure 5.7.

Figure 5.7 resolves the sign problem when studying the model with periodic boundary conditions. With open boundary conditions, however, it is not so clear that the

transfer matrices of the two models will be equal since, for a general open boundary condition, we are allowed to have odd numbers of vertices which differ by a sign in the two models. It will turn out nonetheless that the boundary conditions we are interested in also preserve the parity of the number of thick lines and the transfer matrix will ensure that we again only encounter configurations with an even number of these vertices with asterisks. This preservation of the parity of thick and thin lines turns out to be a result of a symmetry under a lattice operator denoted by C, which was first introduced in [54]. This operator is most conveniently expressed as

$$C = C_1 C_3 \cdots C_{2L-1} \tag{5.28}$$

where

$$C_i = 1 - \frac{1}{\cos\gamma} e_i \,, \tag{5.29}$$

and e_i is a generator of the Temperley-Lieb (TL) algebra [21], discussed in section 3.1.2. Both the C operator and the TL algebra will play important roles in what follows. We shall discuss this more fully below.

5.2 The open D_2^2 model

The machinery required to tackle integrable models was introduced in section 4.3. We have an R matrix that satisfies the Yang-Baxter equation (4.7) and with periodic boundary conditions this is all we need to construct the integrable transfer matrix in (4.8). For an open integrable model we need a K-matrix that satisfies the boundary version of the Yang-Baxter equation (4.10) in addition to the R-matrix. We then construct an integrable transfer matrix describing an open model using equation (4.11).

In the case that we are considering here, i.e., the D_2^2 model, the parameters ρ and M appearing in equation (4.12) are given by [105] $\rho = -\log k$ and

$$M = \mathrm{diag}(k, 1, 1, k^{-1}) \tag{5.30}$$

Here we will consider a particular K-matrix that satisfies (4.10) [106]:

$$K^-(\lambda) = \begin{bmatrix} Y_1(\lambda) & 0 & 0 & 0 \\ 0 & Y_2(\lambda) & Y_5(\lambda) & 0 \\ 0 & Y_6(\lambda) & Y_3(\lambda) & 0 \\ 0 & 0 & 0 & Y_4(\lambda) \end{bmatrix} , \tag{5.31}$$

with

$$Y_1(\lambda) = -e^{-\lambda}(e^{2\lambda} + k) \,, \tag{5.32a}$$
$$Y_4(\lambda) = -e^{3\lambda}(e^{2\lambda} + k) \,, \tag{5.32b}$$
$$Y_2(\lambda) = Y_3(\lambda) = -\frac{1}{2}(1 + e^{2\lambda})e^{\lambda}(1 + k) \,, \tag{5.32c}$$
$$Y_5(\lambda) = Y_6(\lambda) = \frac{1}{2}(e^{2\lambda} - 1)(1 - k)e^{\lambda} \,, \tag{5.32d}$$

and we recall that u and k satisfy the relations (5.16). Recall now the discussion at the end of section 5.1.4 about the particular Boltzmann weights in tables 5.1–5.3 that differed by a sign when considering the D_2^2 model and the staggered six-vertex

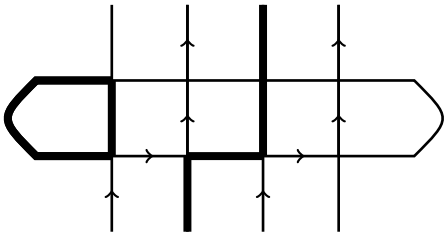


Figure 5.8: Two rows of vertices constructed from the transfer matrix. The fact that K becomes diagonal in the appropriate basis implies that the parity of the number of thick lines is conserved. This ensures that there are an even number of vertices that differ by a sign in the D_2^2 model and the staggered six-vertex model.

model. This issue was resolved by noticing that, when periodic boundary conditions are imposed, there is always an even number of these vertices and hence the transfer matrix built from either R-matrix is the same.

Now that we are considering open boundary conditions we can no longer rely on the same argument. Notice however, that in the basis defined in equation (5.6) the K-matrix in equation (5.31) becomes diagonal:

$$K^-(\lambda) \to \begin{bmatrix} Y_1(\lambda) & 0 & 0 & 0 \\ 0 & Y_2(\lambda)+Y_5(\lambda) & 0 & 0 \\ 0 & 0 & Y_2(\lambda)-Y_6(\lambda) & 0 \\ 0 & 0 & 0 & Y_4(\lambda) \end{bmatrix} \tag{5.33}$$

The K-matrix being diagonal ensures that we have conservation of both thick and thin lines at the boundary and that in any given configuration we will again have an even number of vertices that differ by a sign in the two models. See Figure 5.8 for an illustration.

The fact that the K-matrix is diagonal in this basis comes from the fact that it commutes with the C-operator defined in equation (5.29). The basis in (5.6) was in fact chosen since each of the basis vectors are eigenvectors of the C operator. The K-matrix then satisfies

$$[K, C] = 0\,. \tag{5.34}$$

This symmetry will be discussed in more detail in section 5.2.2 and it will turn out to account for the extra degeneracies observed in the spectrum of the open D_2^2 transfer matrix/Hamiltonian.

5.2.1 Hamiltonian limit

The method of constructing an integrable Hamiltonian was outlined in section 4.3, where the explicit expression of the integrable open Hamiltonian corresponding to the transfer matrix of an open model was given in equation (4.25).

Recall that the transfer matrix for the periodic case is given by (4.8) and the corresponding Hamiltonian is again obtained by taking the derivative with respect to the spectral parameter. Up to overall normalisation terms, the periodic Hamiltonian can be written [54, 111]:

$$\mathcal{H} = 2\cos\gamma \sum_{m=1}^{2L-1} e_m - (e_m e_{m+1} + e_{m+1} e_m)\,, \tag{5.35}$$

where the TL generators e_m satisfy (3.15). The open Hamiltonian in (4.25) can be similarly written as

$$\mathcal{H} = A_{\text{left}} + A_{\text{right}} + \cos\gamma(e_1 + e_{2L-1}) + 2\cos\gamma \sum_{m=2}^{2L-2} e_m - \sum_{m=1}^{2L-2} (e_m e_{m+1} + e_{m+1} e_m)\,, \quad (5.36)$$

where A_{left} and A_{right} are the boundary terms arising from the second and third terms in equation (4.25) and can be written as

$$A_{\text{left}} = \begin{pmatrix} i\sin 2\gamma & 0 & 0 & 0 \\ 0 & -\frac{\sin^2\gamma}{\cos\gamma} e^{i\gamma} & \frac{\sin^2\gamma}{\cos\gamma} & 0 \\ 0 & \frac{\sin^2\gamma}{\cos\gamma} & -\frac{\sin^2\gamma}{\cos\gamma} e^{-i\gamma} & 0 \\ 0 & 0 & 0 & -i\sin 2\gamma \end{pmatrix} \otimes \mathbb{I}^{\otimes 2L-2} \quad (5.37)$$

and

$$A_{\text{right}} = \mathbb{I}^{\otimes 2L-2} \otimes \begin{pmatrix} -i\sin 2\gamma & 0 & 0 & 0 \\ 0 & -\frac{\sin^2\gamma}{\cos\gamma} e^{i\gamma} & \frac{\sin^2\gamma}{\cos\gamma} & 0 \\ 0 & \frac{\sin^2\gamma}{\cos\gamma} & -\frac{\sin^2\gamma}{\cos\gamma} e^{-i\gamma} & 0 \\ 0 & 0 & 0 & i\sin 2\gamma \end{pmatrix} \quad (5.38)$$

after subtracting terms proportional to the identity. The usual representation of the TL generators e_i in the vertex model are given by equation (3.16), repeated here for clarity:

$$e_i = \mathbb{I}^{\otimes i-1} \otimes \begin{pmatrix} 0 & 0 & 0 & 0 \\ 0 & e^{-i\gamma} & 1 & 0 \\ 0 & 1 & e^{i\gamma} & 0 \\ 0 & 0 & 0 & 0 \end{pmatrix} \otimes \mathbb{I}^{\otimes 2L-i-1}\,, \quad (5.39)$$

but we shall need as well another representation of the TL algebra

$$\tilde{e}_i = \mathbb{I}^{\otimes i-1} \otimes \begin{pmatrix} 0 & 0 & 0 & 0 \\ 0 & e^{i\gamma} & -1 & 0 \\ 0 & -1 & e^{-i\gamma} & 0 \\ 0 & 0 & 0 & 0 \end{pmatrix} \otimes \mathbb{I}^{\otimes 2L-i-1}\,, \quad (5.40)$$

which can also be checked to satisfy (3.15). We can now write

$$A_{\text{left}} = -\frac{\sin^2\gamma}{\cos\gamma}\tilde{e}_1 + i\sin 2\gamma \left(\frac{1}{2}\sigma_1^z + \frac{1}{2}\sigma_2^z\right) \quad (5.41)$$

and

$$A_{\text{right}} = -\frac{\sin^2\gamma}{\cos\gamma}\tilde{e}_{2L-1} - i\sin 2\gamma \left(\frac{1}{2}\sigma_1^z + \frac{1}{2}\sigma_2^z\right)\,. \quad (5.42)$$

By expanding the TL generators e_i and $\tilde{e}_i$ in terms of Pauli matrices,

$$e_i = \frac{1}{2}\left[\sigma_i^x\sigma_{i+1}^x + \sigma_i^y\sigma_{i+1}^y - \cos\gamma\sigma_i^z\sigma_{i+1}^z + \cos\gamma - i\sin\gamma(\sigma_i^z - \sigma_{i+1}^z)\right]\,, \quad (5.43a)$$

$$\tilde{e}_i = \frac{1}{2}\left[-\sigma_i^x\sigma_{i+1}^x - \sigma_i^y\sigma_{i+1}^y - \cos\gamma\sigma_i^z\sigma_{i+1}^z + \cos\gamma + i\sin\gamma(\sigma_i^z - \sigma_{i+1}^z)\right]\,, \quad (5.43b)$$

we can see that the Hamiltonian (5.36) can be written entirely in terms of $\tilde{e}_i$ instead of e_i. The additional Pauli matrices in equations (5.41) and (5.42) disappear, and we get

$$\mathcal{H} = \left(\cos\gamma - \frac{\sin^2\gamma}{\cos\gamma}\right)(\tilde{e}_1 + \tilde{e}_{2L-1}) + 2\cos\gamma \sum_{m=2}^{2L-2} \tilde{e}_m - \sum_{m=1}^{2L-2} (\tilde{e}_m\tilde{e}_{m+1} + \tilde{e}_{m+1}\tilde{e}_m)\,, \quad (5.44)$$

which can be rewritten as

$$\mathcal{H} = -\frac{1}{\cos\gamma}(\tilde{e}_1 + \tilde{e}_{2L-1}) + 2\cos\gamma \sum_{m=1}^{2L-1} \tilde{e}_m - \sum_{m=1}^{2L-2} (\tilde{e}_m \tilde{e}_{m+1} + \tilde{e}_{m+1}\tilde{e}_m)\,. \tag{5.45}$$

Evidently, we can swap all of the $\tilde{e}_i \to e_i$ without changing the spectrum. Hence we get finally

$$\mathcal{H} = -\frac{1}{\cos\gamma}(e_1 + e_{2L-1}) + 2\cos\gamma \sum_{m=1}^{2L-1} e_m - \sum_{m=1}^{2L-2} (e_m e_{m+1} + e_{m+1}e_m)\,. \tag{5.46}$$

Since the Hamiltonian in (5.46) arises from a Hamiltonian of the form (4.25), it is integrable and solvable by Bethe Ansatz. We present its Bethe Ansatz solution in section 5.3.

5.2.2 Additional symmetries

It was found in [105] and [106] that the transfer matrix (4.11)—or, equivalently, the Hamiltonian (4.25)—has a particular pattern of degeneracies that suggests the open chain is invariant under the action of generators of some quantum group. The observed symmetry is very similar to what one would expect if the chain were invariant under the action of the $U_q(sl(2))$ quantum group, but in fact we have even more degeneracies than would be expected if the full symmetry group was $U_q(sl(2))$.

Consider the degeneracies of the D_2^2 chain in table 5.4 compared with those of the expected degeneracies from a chain with just $U_q(sl(2))$ symmetry. Let us first explain the notation. On the $U_q(sl(2))$ side, $[j]$ denotes the spin-$(j-1)/2$ representation dimension j, and more generally $[j]$ refers to a j-dimensional representation of the corresponding symmetry. A decomposition like $2[1] \oplus 3[3] \oplus [5]$, for example, means that there are two eigenvalues with degeneracy 1, three with degeneracy 3 and one with degeneracy 5, corresponding to a total dimension of $2 \times 1 + 3 \times 3 + 1 \times 5 = 16$.

At size $L = 2$ we see that two of the 3 times degenerate eigenvalues in the $U_q(sl(2))$ chain "become" a 6 times degenerate eigenvalue in the D_2^2 chain; the symmetry group of the D_2^2 chain is higher. At this point it is useful to recall that a D_2^2 chain of length L means that there are $N = 2L$ sites with spin $\frac{1}{2}$, since L is the number of "Potts spins" in one row of the classical Potts model defined by the Hamiltonian (5.1). The D_2^2 chain of length L therefore has a Hilbert space of dimension 2^{2L}.

We can understand the extra symmetries by studying the limit of the D_2^2 chain when $\gamma \to 0$, where it will be shown in section 5.2.3 that the chain becomes that of two decoupled open XXX chains, and that the extra symmetry comes from the permutation of these two chains. The symmetry for finite γ will be discussed in section 5.2.4.

5.2.3 The $\gamma \to 0$ limit

Consider the Hamiltonian in (5.46) in the limit $\gamma \to 0$:

$$\mathcal{H} = (e_1 + e_{2L-1}) + 2\sum_{m=2}^{2L-2} e_m - \sum_{m=1}^{2L-2} (e_m e_{m+1} + e_{m+1}e_m)\,. \tag{5.47}$$

Using the expression in (5.43), this becomes

$$\mathcal{H} = -\frac{1}{2}\sum_{i=1}^{L-1}(\sigma_{2i-1}^x\sigma_{2i+1}^x + \sigma_{2i-1}^y\sigma_{2i+1}^y + \sigma_{2i-1}^z\sigma_{2i+1}^z) - \frac{1}{2}\sum_{i=1}^{L-1}(\sigma_{2i}^x\sigma_{2i+2}^x + \sigma_{2i}^y\sigma_{2i+2}^y + \sigma_{2i}^z\sigma_{2i+2}^z) \tag{5.48}$$

L	$U_q(sl(2))$	D_2^2
2	$2[1] \oplus 3[3] \oplus [5]$	$2[1] \oplus [3] \oplus [5] \oplus [6]$
3	$5[1] \oplus 9[3] \oplus 5[5] \oplus [7]$	$3[1] \oplus [2] \oplus 3[3] \oplus [5] \oplus 3[6] \oplus [7] \oplus 2[10]$
4	$14[1] \oplus 28[3] \oplus 20[5] \oplus 7[7] \oplus [9]$	$6[1] \oplus 4[3] \oplus 4[2] \oplus 4[5] \oplus 12[6] \oplus 1[7] \oplus [9] \oplus 8[10] \oplus 3[14]$

Table 5.4: The degeneracies of the D_2^2 spin chain of length $N = 2L$ compared with those of the $U_q(sl(2))$ chain.

Eigenvalue	Eigenspace	Decomposition	Degeneracy
$2\lambda_1$	$\|1\rangle \otimes \|1\rangle$	$\|1\rangle$	1
$2\lambda_3$	$\|3\rangle \otimes \|3\rangle$	$\|5\rangle \oplus \|3\rangle \oplus \|1\rangle$	9
$\lambda_1 + \lambda_3$	$\|1\rangle \otimes \|3\rangle \oplus \|3\rangle \otimes \|1\rangle$	$\|6\rangle$	6

Table 5.5: Analysis of the spectrum of the D_2^2 chain for $L = 2$, in the limit $\gamma \to 0$.

up to terms proportional to the identity. The Hamiltonian in (5.48) is the sum of two decoupled open XXX chains of length L. (A similar observation was made for the periodic model in [54].) Note that for the XXX chain, a chain of length L means that the Hamiltonian acts on L spin $\frac{1}{2}$ sites, unlike the D_2^2 chain where a chain of length L means that the Hamiltonian acts on $2L$ spin-$\frac{1}{2}$ sites. This is most easily understood when considering equation (5.48), where we observed that the D_2^2 chain becomes equivalent to two XXX chains.

Consider first the case $L = 2$. The $sl(2)$ symmetry of each individual XXX Hamiltonian is such that there are two eigenvalues, one non-degenerate and one three times degenerate. The eigenvectors of each Hamiltonian are the so-called singlet and triplet states which we will denote by $|1\rangle$ and $|3\rangle$ respectively. We will denote the corresponding eigenvalues by λ_1 and λ_3. Now consider the Hamiltonian obtained by summing the two XXX Hamiltonians. The situation is summarised in table 5.5. There are clearly three distinct eigenvalues given by $2\lambda_1$, $2\lambda_3$ and $\lambda_1 + \lambda_3$ with the degeneracies 1, 9 and 6 respectively. The eigenvectors of the full Hamiltonian are the tensor products of the eigenvectors of the two individual XXX Hamiltonians. The eigenspace of dimension 9 comes about from the tensor product of the two spaces of dimension 3. We can decompose this tensor product into a direct sum of spaces $|5\rangle$, $|3\rangle$ and $|1\rangle$. Note that this is just the usual tensor product of two spin-1 spaces into the spaces with spin 2, 1 and 0. The eigenspace with dimension 6 is more subtle. The eigenvalue $\lambda_1 + \lambda_3$ corresponds to placing the eigenvector $|1\rangle$ on one XXX chain and the eigenvector $|3\rangle$ on the other. Clearly, we can swap the two chains to obtain another eigenvector with the same eigenvalue. This results then in an eigenspace of dimension 6.

5.2.4 Non-zero γ

In the $\gamma \to 0$ limit the even-dimensional eigenspaces of the Hamiltonian were understood to be the result of the permutation symmetry of the two XXX chains. This symmetry exists on top of the $sl(2)$ symmetry. When $\gamma \neq 0$, the $sl(2)$ symmetry is replaced by

Eigenvalue	Eigenspace	Decomposition	Degeneracy
$2\lambda_1^a$	$\|1^a\rangle \otimes \|1^a\rangle$	$\|1\rangle$	1
$\lambda_1^a + \lambda_1^b$	$\|1^a\rangle \otimes \|1^b\rangle \oplus \|1^b\rangle \otimes \|1^a\rangle$	$\|2\rangle$	2
$\lambda_1^a + \lambda_3^a$	$\|1^a\rangle \otimes \|3^a\rangle \oplus \|3^a\rangle \otimes \|1^a\rangle$	$\|6\rangle$	6
$\lambda_1^a + \lambda_3^b$	$\|1^a\rangle \otimes \|3^b\rangle \oplus \|3^b\rangle \otimes \|1^a\rangle$	$\|6\rangle$	6
$\lambda_1^a + \lambda_3^c$	$\|1^a\rangle \otimes \|3^c\rangle \oplus \|3^c\rangle \otimes \|1^a\rangle$	$\|6\rangle$	6
$\lambda_1^a + \lambda_5$	$\|1^a\rangle \otimes \|5\rangle \oplus \|5\rangle \otimes \|1^a\rangle$	$\|10\rangle$	5
$2\lambda_1^b$	$\|1^b\rangle \otimes \|1^b\rangle$	$\|1\rangle$	1
$\lambda_1^b + \lambda_3^a$	$\|1^b\rangle \otimes \|3^a\rangle \oplus \|3^a\rangle \otimes \|1^b\rangle$	$\|6\rangle$	6
$\lambda_1^b + \lambda_3^b$	$\|1^b\rangle \otimes \|3^b\rangle \oplus \|3^b\rangle \otimes \|1^b\rangle$	$\|6\rangle$	6
$\lambda_1^b + \lambda_3^c$	$\|1^b\rangle \otimes \|3^c\rangle \oplus \|3^c\rangle \otimes \|1^b\rangle$	$\|6\rangle$	6
$\lambda_1^b + \lambda_5$	$\|1^b\rangle \otimes \|5\rangle \oplus \|5\rangle \otimes \|1^b\rangle$	$\|10\rangle$	5
$2\lambda_3^a$	$\|3^a\rangle \otimes \|3^a\rangle$	$\|5\rangle \oplus \|3\rangle \oplus \|1\rangle$	9
$\lambda_3^a + \lambda_3^b$	$\|3^a\rangle \otimes \|3^b\rangle \oplus \|3^b\rangle \otimes \|3^a\rangle$	$\|10\rangle \oplus \|6\rangle \oplus \|2\rangle$	18
$\lambda_3^a + \lambda_3^c$	$\|3^a\rangle \otimes \|3^c\rangle \oplus \|3^c\rangle \otimes \|3^a\rangle$	$\|10\rangle \oplus \|6\rangle \oplus \|2\rangle$	18
$\lambda_3^a + \lambda_5$	$\|3^a\rangle \otimes \|5\rangle \oplus \|5\rangle \otimes \|3^a\rangle$	$\|14\rangle \oplus \|10\rangle \oplus \|6\rangle$	30
$2\lambda_3^b$	$\|3^b\rangle \otimes \|3^b\rangle$	$\|5\rangle \oplus \|3\rangle \oplus \|1\rangle$	9
$\lambda_3^b + \lambda_3^c$	$\|3^b\rangle \otimes \|3^c\rangle \oplus \|3^c\rangle \otimes \|3^b\rangle$	$\|10\rangle \oplus \|6\rangle \oplus \|2\rangle$	18
$\lambda_3^b + \lambda_5$	$\|3^b\rangle \otimes \|5\rangle \oplus \|5\rangle \otimes \|3^b\rangle$	$\|14\rangle \oplus \|10\rangle \oplus \|6\rangle$	30
$2\lambda_3^c$	$\|3^c\rangle \otimes \|3^c\rangle$	$\|5\rangle \oplus \|3\rangle \oplus \|1\rangle$	9
$\lambda_3^c + \lambda_5$	$\|3^c\rangle \otimes \|5\rangle \oplus \|5\rangle \otimes \|3^c\rangle$	$\|14\rangle \oplus \|10\rangle \oplus \|6\rangle$	30
$2\lambda_5$	$\|5\rangle \otimes \|5\rangle$	$\|9\rangle \oplus \|7\rangle \oplus \|5\rangle \oplus \|3\rangle \oplus \|1\rangle$	25

Table 5.6: Spectrum of the D_2^2 chain with $L = 4$, in the limit $\gamma \to 0$.

$U_q(sl(2))$ and the permutation symmetry is replaced by a symmetry under the action of the operator C as will now be discussed.

First observe that the eigenvalues of C are all ± 1. Then, since $[H, C] = 0$, any eigenspace of H is invariant under the action of C. The even degeneracies in the eigenvalues come from the coupling of two eigenspaces of C, with eigenvalues ± 1 respectively, under the action of H. Consider for example two linearly independent eigenvectors of H, $|\psi_1\rangle$ and $|\psi_2\rangle$, with the same energy eigenvalue. We therefore have that $|\psi_3\rangle \equiv |\psi_1\rangle + |\psi_2\rangle$ and $|\psi_4\rangle \equiv |\psi_1\rangle - |\psi_2\rangle$ are eigenstates of H. If it is the case that $|\psi_1\rangle$ has eigenvalue 1 under the action of C but $|\psi_2\rangle$ has eigenvalue -1, then $C|\psi_3\rangle = |\psi_4\rangle$ and $C|\psi_4\rangle = |\psi_3\rangle$.

One can indeed check that the even degeneracies of H come from linear combinations of eigenvectors of C with eigenvalues 1 *and* -1 and that all of the odd dimensional spaces are linear combinations of eigenvectors of C with eigenvalues that are *either* 1 *or* -1. We have checked this fact for sizes up to $L = 4$, and we conjecture it to hold true in general.

5.3 The Bethe Ansatz solution

The advantage of having an open boundary condition that stems from a solution to the boundary Yang-Baxter equation (4.10) is that the model should admit an exact solution. In particular, the Bethe Ansatz equations corresponding to the K-matrix defined in (5.31)–(5.32) have been found in [105] and [106], using the analytic Bethe Ansatz method presented in section 4.3. When the additive and multiplicative normalisation constants of the Hamiltonian are defined as in (5.46), the Bethe Ansatz solution tells us that the energy eigenvalues are given by

$$E_{D_2^2} = \sum_{j=1}^{m} \frac{2\sin^2(2\gamma)}{\cosh 2\lambda_j - \cos 2\gamma}\,, \tag{5.49}$$

where the λ_j are solutions to the Bethe Ansatz equations (BAE)

$$\left[\frac{\sinh(\lambda_j + i\gamma)}{\sinh(\lambda_j - i\gamma)}\right]^{2L} = \prod_{k=1, k\neq j}^{m} \frac{\sinh\left(\frac{\lambda_j}{2} - \frac{\lambda_k}{2} + i\gamma\right)}{\sinh\left(\frac{\lambda_j}{2} - \frac{\lambda_k}{2} - i\gamma\right)} \frac{\sinh\left(\frac{\lambda_j}{2} + \frac{\lambda_k}{2} + i\gamma\right)}{\sinh\left(\frac{\lambda_j}{2} + \frac{\lambda_k}{2} - i\gamma\right)}\,. \tag{5.50}$$

We once again study the finite size scaling of the energy eigenvalues using equation (4.28), repeated here for clarity:

$$E = f_0 L + f_{\mathrm{s}} - \frac{\pi v_{\mathrm{F}}(\frac{c}{24} - h)}{L} + o\left(\frac{1}{L}\right)\,, \tag{5.51}$$

where L is the system size, c is the central charge, h is the conformal dimension of the primary field corresponding to the eigenvalue under consideration, f_0 is the bulk energy density and f_{s} is the surface energy. The Fermi velocity v_{F} for the present model was calculated in [54] and is given by

$$v_{\mathrm{F}} = \frac{2\pi \sin(\pi - 2\gamma)}{\pi - 2\gamma}\,. \tag{5.52}$$

It is found that, in the continuum limit, the generating function of levels is

$$\mathcal{Z} = \sum_{m=0}^{\infty} (2m+1) Z_m \,, \tag{5.53}$$

where Z_m is the generating function corresponding to the antiferromagnetic Potts model with free boundary conditions, given in [32] as

$$Z_m = \frac{q^{h_m - \frac{c}{24}}}{\eta^2(q)} \left(1 + 2 \left[\sum_{j=1}^{\infty} q^{2m^2+m(2j+1)} - \sum_{j=0}^{\infty} q^{2(m+\frac{1}{2})^2+(m+\frac{1}{2})(2j+1)} \right] \right) , \tag{5.54}$$

where

$$h_m = \frac{m(m+1)}{k} \,, \tag{5.55}$$

with $m \in \mathbb{Z}$ and $\gamma = \frac{\pi}{k}$. Moreover, $\eta(q)$ is the Dedekind eta function, and q denotes the modular parameter. The central charge c is given by

$$c = 2 - \frac{6}{k} \,. \tag{5.56}$$

These values for the central charge (5.56) and critical exponents (5.55) will be derived analytically in section 5.3.1 by mapping some of the solutions to (5.50) to solutions of the Bethe Ansatz equations of the open XXZ Hamiltonian with some particular boundary conditions. Section 5.3.2 will then consider solutions to (5.50) that do not correspond to solutions of any XXZ Bethe Ansatz equations. Some examples of these other solutions to (5.50) will be presented and the scaling behaviour of the eigenvalues corresponding to these solutions will be shown to reproduce the first few terms in (5.54). In section 5.4, the generating function defined in (5.54) will be observed by direct diagonalisation of the Hamiltonian for a range of values of γ.

5.3.1 The XXZ subset

Even number of Bethe roots

Consider solutions to the BAE (5.50) of the form

$$\lambda_j^0 = \alpha_j^0 + i\frac{\pi}{2} \,, \tag{5.57a}$$

$$\lambda_j^1 = \alpha_j^1 - i\frac{\pi}{2} \,, \tag{5.57b}$$

so that (5.50) becomes

$$\begin{aligned} \left[\frac{\cosh(\alpha_j^0 + i\gamma)}{\cosh(\alpha_j^0 - i\gamma)} \right]^{2L} = & \prod_{k=1, k\neq j}^{\frac{m}{2}} \frac{\sinh(\frac{\alpha_j^0}{2} - \frac{\alpha_k^0}{2} + i\gamma)}{\sinh(\frac{\alpha_j^0}{2} - \frac{\alpha_k^0}{2} - i\gamma)} \frac{\cosh(\frac{\alpha_j^0}{2} + \frac{\alpha_k^0}{2} + i\gamma)}{\cosh(\frac{\alpha_j^0}{2} + \frac{\alpha_k^0}{2} - i\gamma)} \\ & \prod_{k=1}^{\frac{m}{2}} \frac{\cosh(\frac{\alpha_j^0}{2} - \frac{\alpha_k^1}{2} + i\gamma)}{\cosh(\frac{\alpha_j^0}{2} - \frac{\alpha_k^1}{2} - i\gamma)} \frac{\sinh(\frac{\alpha_j^0}{2} + \frac{\alpha_k^1}{2} + i\gamma)}{\sinh(\frac{\alpha_j^0}{2} + \frac{\alpha_k^1}{2} - i\gamma)} \,, \end{aligned} \tag{5.58}$$

while the α_j^1 can be seen to satisfy a similar equation. Taking the subset of solutions where

$$\alpha_k^0 = \alpha_k^1 \equiv \alpha_k \,, \tag{5.59}$$

equation (5.58) becomes

$$\left[\frac{\cosh(\alpha_j+i\gamma)}{\cosh(\alpha_j-i\gamma)}\right]^{2L}\frac{\sinh(\alpha_j-i\gamma)}{\sinh(\alpha_j+i\gamma)}=\prod_{k=1,k\neq j}^{\frac{m}{2}}\frac{\sinh(\alpha_j-\alpha_k+2i\gamma)}{\sinh(\alpha_j-\alpha_k-2i\gamma)}\frac{\sinh(\alpha_j+\alpha_k+2i\gamma)}{\sinh(\alpha_j+\alpha_k-2i\gamma)}\,. \tag{5.60}$$

Consider now the open XXZ Hamiltonian with boundary fields H and H':

$$\mathcal{H}_{\rm XXZ}=-\frac{1}{2}\left[\sum_{i=1}^{L-1}(\sigma_i^x\sigma_{i+1}^x+\sigma_i^y\sigma_{i+1}^y-\cos\gamma_0\,\sigma_i^z\sigma_{i+1}^z)+H\sigma_1^z+H'\sigma_L^z\right]. \tag{5.61}$$

It was shown in [82] that the eigenvalues of $\mathcal{H}_{\rm XXZ}$ are given by

$$E=-\sum_{k=1}^{m'}\frac{2\sin^2\gamma_0}{\cosh 2\mu_k-\cos\gamma_0}+\frac{1}{2}(L-1)\cos\gamma_0+\text{boundary terms}\,. \tag{5.62}$$

The second term and the boundary terms in (5.62) are not important here, since we are interested in looking at the CFT properties in the thermodynamic limit which we can calculate from the terms proportional to $\frac{1}{N}$. The m' Bethe roots μ_k in (5.62) are given by the solutions to the BAE

$$\left(\frac{\sinh(\mu_j+i\frac{\gamma_0}{2})}{\sinh(\mu_j-i\frac{\gamma_0}{2})}\right)^{2L}\frac{\sinh(\mu_j+i\Lambda)}{\sinh(\mu_j-i\Lambda)}\frac{\sinh(\mu_j+i\Lambda')}{\sinh(\mu_j-i\Lambda')}=\prod_{k\neq j}^{m'}\frac{\sinh(\mu_j-\mu_k+i\gamma_0)}{\sinh(\mu_j-\mu_k-i\gamma_0)}\frac{\sinh(\mu_j+\mu_k+i\gamma_0)}{\sinh(\mu_j+\mu_k-i\gamma_0)}\,, \tag{5.63}$$

where the parameters Λ,Λ' are defined in terms of the boundary parameters H,H' as

$$e^{2i\Lambda}=\frac{H-\Delta-e^{i\gamma_0}}{(H-\Delta)e^{i\gamma_0}-1} \tag{5.64}$$

and similarly for Λ'. Compare the energies in equations (5.62) and (5.49) and set $\gamma_0=\pi-2\gamma$ as in (5.15). We then have that

$$E_{D_2^2}=-\sum_{k=1}^{m}\frac{2\sin^2\gamma_0}{\cosh 2\alpha_k-\cos\gamma_0}\,, \tag{5.65}$$

where the α_k were defined in equation (5.57) and subject to (5.59). Observe that the form of the energy in equation (5.65) is precisely the same as the energy of the XXZ chain in equation (5.62) if we have $\alpha_k=\mu_k$, up to the boundary and bulk terms that will only contribute to the $\mathcal{O}(1)$ and $\mathcal{O}(N)$ terms which we are not interested in here. We can ensure that $\alpha_k=\mu_k$ by comparing (5.63) with (5.60) and setting

$$m = 2m'\,, \tag{5.66a}$$
$$\Lambda = \frac{\pi}{2}-\frac{\gamma_0}{2}\,, \tag{5.66b}$$
$$\Lambda' = 0\,, \tag{5.66c}$$

which ensures that the solutions to (5.63) are identical with the solutions of (5.60) and hence

$$E_{D_2^2}=2E_{\rm XXZ}\,. \tag{5.67}$$

Now we can use the known scaling behaviour of the open XXZ chain to study the scaling behaviour of some states in the D_2^2 chain, namely the subset of states satisfying (5.59). We have from [82] that, for general Λ, Λ', the effective central charge of the lowest-energy state the XXZ chain (corresponding to the critical exponent h) with total magnetisation S is given by

$$c_{\text{eff}} = 1 - \frac{6}{1-\frac{\gamma_0}{\pi}} \left(1 - \frac{\gamma_0 + \Lambda + \Lambda' - 2\pi S(1-\frac{\gamma_0}{\pi})}{\pi}\right)^2 . \tag{5.68}$$

Using then the fact [112] that the Fermi velocity v_0 of the XXZ model is given by $\frac{v_{\text{F}}}{2}$ where v_{F} is defined in (5.52), and using also (5.15), (5.66) and (5.67), and setting $\gamma = \frac{\pi}{k}$, we obtain that the effective central charge $\tilde{c}_{\text{eff}}$ of a state in the D_2^2 model is

$$\tilde{c}_{\text{eff}} = 2c_{\text{eff}} = 2 - \frac{6}{k}(1+4S)^2 . \tag{5.69}$$

From the bulk central charge of the staggered six-vertex model [32] given in (5.56) and the relationship between the critical exponent h and the effective central charge

$$h = \frac{c - \tilde{c}_{\text{eff}}}{24} , \tag{5.70}$$

we can obtain

$$h = -\frac{1}{4k} + \frac{1}{4k}(1+4S)^2 = \frac{2S(2S+1)}{k} . \tag{5.71}$$

Setting now $l = 2S$ we have:

$$h = h_l \equiv \frac{l(l+1)}{k} , \tag{5.72}$$

with l an even integer. The critical exponents of the antiferromagnetic Potts model with free boundary conditions are actually given by (5.72) for all l integer [107], but the analysis here only recovered the exponents for l even, since we only considered an even number of Bethe roots m. We will now consider solutions to the Bethe Ansatz equations with an odd number of Bethe roots and will recover the exponents (5.72) for l odd.

Odd number of Bethe roots

The analysis in the preceding section considered solutions with an even number of Bethe roots and hence recovered the critical exponents of the antiferromagnetic Potts model in equation (5.72) corresponding to even sectors of magnetisation. We will now consider an odd number of Bethe roots and derive the critical exponents (5.72) for l odd. Consider solutions to the Bethe Ansatz equations in (5.50) of the form in (5.57) but with one additional root, $\lambda_0^0 = i\frac{\pi}{2}$. We now have one more root of the form λ_j^0 than roots of the form λ_j^1, and this additional root has vanishing real part. We can go through the same analysis that led to (5.60) for the m even case, finding now

$$\left[\frac{\cosh(\alpha_j + i\gamma)}{\cosh(\alpha_j - i\gamma)}\right]^{2L} \frac{\sinh(\alpha_j - 2i\gamma)}{\sinh(\alpha_j + 2i\gamma)} \frac{\sinh(\alpha - i\gamma)}{\sinh(\alpha + i\gamma)} = \prod_{k=1, k\neq j}^{\frac{m-1}{2}} \frac{\sinh(\alpha_j - \alpha_k + 2i\gamma)}{\sinh(\alpha_j - \alpha_k - 2i\gamma)} \frac{\sinh(\alpha_j + \alpha_k + 2i\gamma)}{\sinh(\alpha_j + \alpha_k - 2i\gamma)} \tag{5.73}$$

when m is odd. Now compare the Bethe Ansatz equations in (5.73) to the XXZ Bethe Ansatz equations in (5.63). When we set

$$\begin{aligned} m-1 &= 2m', && \text{(5.74a)} \\ \Lambda &= \frac{\pi}{2} - \frac{\gamma_0}{2}, && \text{(5.74b)} \\ \Lambda' &= \pi - \gamma_0, && \text{(5.74c)} \end{aligned}$$

applying again (5.15), then the solutions α_j to (5.73) will be the same as the solutions to (5.63) and we will once again have that the energy of the D_2^2 chain is equal to twice that of the XXZ chain as in (5.67). Using (5.68) with the Λ, Λ' taking values in (5.74) we find

$$\tilde{c}_{\text{eff}} = 2c_{\text{eff}} = 2 - \frac{6}{k}(4S-1)^2 . \tag{5.75}$$

Now using (5.70) we finally obtain

$$h = \frac{2S(2S-1)}{k}, \tag{5.76}$$

which is equivalent to (5.72) for $l = 2S-1$.

5.3.2 Other solutions of Bethe Ansatz equations

We have so far managed to use the Bethe Ansatz solution to derive the critical exponents (5.72) and central charge (5.56) which provides a lot of evidence that the particular boundary conditions under consideration are in the same universality class as the antiferromagnetic Potts model with free boundary conditions. In order to be sure of this, however, we need to check that the full spectrum of the model is consistent with the generating function (5.54). In other words, we have so far only confirmed that the first term in the expansion of Z_m in (5.54) is consistent with the critical exponents (5.72) derived in section 5.3.1, but we need to study the excited states in the chain to compare with the other terms. We will do this by finding solutions to the Bethe Ansatz equations (5.50) that are not of the form (5.57).

We shall present some solutions for the test case $\gamma = \frac{\pi}{5}$ and show that the results are indeed consistent with (5.54). Section 5.4 will then show by direct diagonalisation for a range of values of γ that (5.54) is indeed the correct generating function of levels for the spin chain. We will consider separately the cases with total magnetisation n equal to two, one and zero. Note that in our notation m is the number of Bethe roots in any given solution to the Bethe Ansatz equations (5.50). Solutions with $m = L$ roots correspond to states in the zero magnetisation sector and more generally, when we define:

$$m = L - n, \tag{5.77}$$

the solutions with m Bethe roots correspond to states with magnetisation n.

The $n = 2$ sector

The Bethe Ansatz equations (5.50) are more easily handled when cast in logarithmic form:

$$2L \log\left(\frac{\sinh(i\gamma+\lambda_j)}{\sinh(i\gamma-\lambda_j)}\right) = 2i\pi I_j + \sum_{k=1,k\neq j}^{m}\left[\log\left(\frac{\sinh(i\gamma+\frac{1}{2}(\lambda_j-\lambda_k)}{\sinh(i\gamma-\frac{1}{2}(\lambda_j-\lambda_k)}\right) + \log\left(\frac{\sinh(i\gamma+\frac{1}{2}(\lambda_j+\lambda_k))}{\sinh(i\gamma-\frac{1}{2}(\lambda_j+\lambda_k))}\right)\right], \tag{5.78}$$

where the I_j are integers introduced as a result of the periodicity of the logarithms. Now consider solutions of the form (5.57). Equations (5.78) become

$$\begin{aligned} 2L\log\left(\frac{\cosh(i\gamma+\alpha_j^0)}{\cosh(i\gamma-\alpha_j^0)}\right) &= 2i\pi I_j^0 + \sum_{k=1,k\neq j}^{m^0}\log\left(\frac{\sinh(i\gamma+\frac{1}{2}(\alpha_j^0-\alpha_k^0)}{\sinh(i\gamma-\frac{1}{2}(\alpha_j^0-\alpha_k^0)}\right) \\ &+ \sum_{k=1,k\neq j}^{m^0}\log\left(\frac{\cosh(i\gamma+\frac{1}{2}(\alpha_j^0+\alpha_k^0)}{\cosh(i\gamma-\frac{1}{2}(\alpha_j^0+\alpha_k^0)}\right) + \sum_{k=1}^{m^1}\log\left(\frac{\cosh(i\gamma+\frac{1}{2}(\alpha_j^0-\alpha_k^1)}{\cosh(i\gamma-\frac{1}{2}(\alpha_j^0-\alpha_k^1)}\right) \\ &+ \sum_{k=1}^{m^1}\log\left(\frac{\sinh(i\gamma+\frac{1}{2}(\alpha_j^0+\alpha_k^1)}{\sinh(i\gamma-\frac{1}{2}(\alpha_j^0+\alpha_k^1)}\right), \end{aligned} \tag{5.79}$$

where m^0 and m^1 are the number of roots of the form λ_j^0 and λ_j^1 respectively. Note that the Bethe numbers I_j^0 now take half-integer values when m^0+m^1 is even, and integer values when m^0+m^1 is odd. An equation similar to (5.79) holds for the α_j^1 roots and the Bethe numbers in that case are written as I_j^1. It is convenient to define the functions

$$k(\lambda) = -i\log\left(\frac{\cosh(i\gamma+\lambda)}{\cosh(i\gamma-\lambda)}\right), \tag{5.80a}$$

$$\theta^0(\lambda) = -i\log\left(\frac{\sinh(i\gamma+\frac{\lambda}{2})}{\sinh(i\gamma-\frac{\lambda}{2})}\right), \tag{5.80b}$$

$$\theta^1(\lambda) = -i\log\left(\frac{\cosh(i\gamma+\frac{\lambda}{2})}{\cosh(i\gamma-\frac{\lambda}{2})}\right). \tag{5.80c}$$

Equations (5.79) then become

$$\begin{aligned} 2Lk(\alpha_j^0) = 2\pi I_j^0 &+ \theta^0\left(\frac{1}{2}(\alpha_j^0-\alpha_k^0)\right) + \theta^1\left(\frac{1}{2}(\alpha_j^0+\alpha_k^0)\right) \\ &+ \theta^1\left(\frac{1}{2}(\alpha_j^0-\alpha_k^1)\right) + \theta^0\left(\frac{1}{2}(\alpha_j^0+\alpha_k^1)\right) \end{aligned} \tag{5.81a}$$

and

$$\begin{aligned} 2Lk(\alpha_j^1) = 2\pi I_j^1 &+ \theta^1\left(\frac{1}{2}(\alpha_j^1-\alpha_k^0)\right) + \theta^0\left(\frac{1}{2}(\alpha_j^1+\alpha_k^0)\right) \\ &+ \theta^0\left(\frac{1}{2}(\alpha_j^1-\alpha_k^1)\right) + \theta^1\left(\frac{1}{2}(\alpha_j^1+\alpha_k^1)\right). \end{aligned} \tag{5.81b}$$

It is found that the following configuration of Bethe numbers

$$I_j^0 = j-\frac{1}{2}, \tag{5.82a}$$

$$I_j^1 = j-\frac{1}{2} \tag{5.82b}$$

leads to a unique solution of (5.81) corresponding to the lowest-energy state in the particular magnetisation sector under investigation. These are the states that result in the critical exponents (5.72).

This section will consider the magnetisation sector $n=2$, so that there are a total of $m=L-2$ Bethe roots, and the structure of the Bethe roots corresponding to excited states that are presented here are valid for $\gamma=\frac{\pi}{5}$. To create an excited state in this

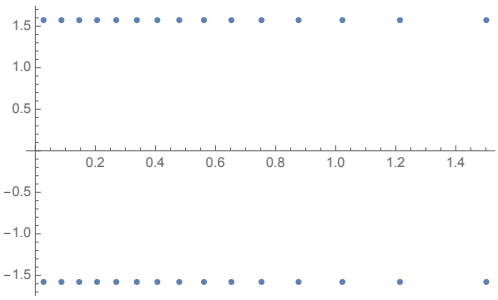


Figure 5.9: Bethe roots for $L = 32$ corresponding to the lowest-energy state in the $n = 2$ sector with $\gamma = \frac{\pi}{5}$.

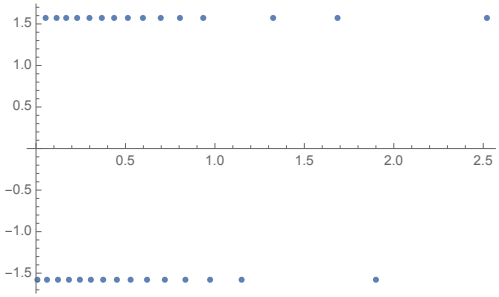


Figure 5.10: Bethe roots for $L = 32$ corresponding to an excited state in the $n = 2$ sector with $\gamma = \frac{\pi}{5}$. The Bethe numbers on the two lines are shifted by $n^0 = 3$ and $n^1 = 1$ respectively.

sector and for this particular value of γ we can shift some of the Bethe numbers in (5.82) to the right. In particular, if the lowest-energy state with the configuration in (5.82) corresponds to a critical exponent h, then if we shift the largest n^0 Bethe numbers in the set I_j^0 by 1, and if we shift the largest n^1 Bethe numbers in the set I_j^1 by 1, then we will find a solution to the Bethe Ansatz equations in (5.81a) and (5.81b) that results in a descendent state with critical exponent $h + n^0 + n^1$.

Consider the following example: take $L = 8$ and the following configuration of Bethe numbers:

$$\begin{aligned} I_1^0 = \frac{1}{2},\ I_2^0 &= \frac{5}{2},\ I_3^0 = \frac{7}{2}\,, \\ I_1^1 = \frac{1}{2},\ I_2^0 &= \frac{3}{2},\ I_3^0 = \frac{7}{2}\,. \end{aligned} \tag{5.83}$$

These Bethe numbers correspond to a total shift of $n^0+n^1 = 2+1 = 3$, hence we expect that in the thermodynamic limit a state of this form corresponds to a critical exponent $h_2 + 3$ where h_2 is the critical exponent in (5.72) with $l = 2$. Observe then that for a given gap of $n^0 + n^1$ there are $n^0 + n^1 + 1$ ways to realise this gap, since after fixing $n^0 + n^1$ there are $n^0 + n^1 + 1$ possible values of n^0 which in turn fixes n^1. Examples of solutions of this form are shown in Figures 5.9–5.10.

There are solutions to (5.50), however, that do not have the form (5.57). An example of a solution of this kind is shown in Figure 5.11, where there is one root with zero imaginary part, one with zero real part, and all of the other roots have imaginary parts that lie close to $\pm\frac{\pi}{2}$ and are complex conjugates of each other. By studying the scaling behaviour of the state in Figure 5.11 we observe that it corresponds to a critical exponent $h_l + 2$ with h_l given by (5.72) with $l = 2$. Using the solutions presented, in addition to the fact that we can always create a new solution to (5.50) by shifting all Bethe roots by $+i\pi$, we can reconstruct the first three terms of Z_2 in (5.54) for $\gamma = \frac{\pi}{5}$.

The $n = 1$ sector

We will now consider an example of solutions to (5.50) in the $n = 1$ sector, i.e. with $m = L - 1$ Bethe roots, again at the particular point $\gamma = \frac{\pi}{5}$. As is the case for all sectors, the solution corresponding to the lowest-energy state is of the form (5.57). An

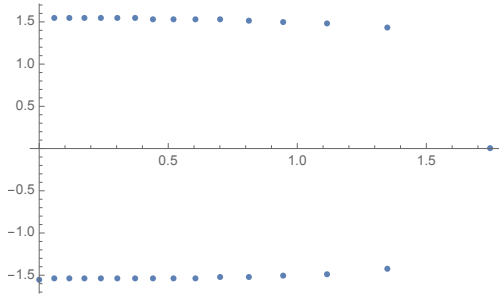


Figure 5.11: Bethe roots for $L = 32$. A solution to the BAE in the $n = 2$ sector with $\gamma = \frac{\pi}{5}$.

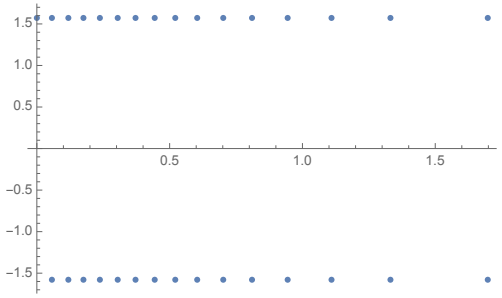


Figure 5.12: Bethe roots for $L = 32$. Lowest-energy state in the $n = 1$ sector with $\gamma = \frac{\pi}{5}$.

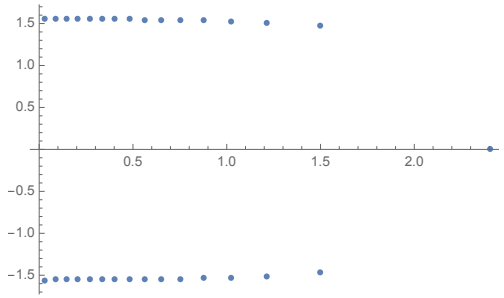


Figure 5.13: Bethe roots for $L = 32$. First excited state in the $n = 1$ sector with $\gamma = \frac{\pi}{5}$.

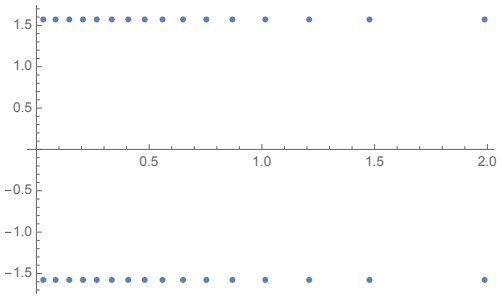


Figure 5.14: Bethe roots for $L = 32$. Ground state in the $n = 0$ sector with $\gamma = \frac{\pi}{5}$.

example of such a solution is shown in Figure 5.12. Since there is an odd number of Bethe roots in the $n = 1$ sector, the analysis of section 5.3.1 applies and the critical exponent corresponding to the lowest-energy state is given by (5.72) with $l = 1$. The solution corresponding to the first excited state in this sector is shown in Figure (5.13). This solution has one Bethe root with zero imaginary part and all of the other roots have imaginary parts that lie close to $\frac{\pi}{2}$ and are complex conjugates of each other. The critical exponent corresponding to this state is given by h_1+1 and is therefore consistent with the form of Z_1 in (5.54).

The $n = 0$ sector

There are $m = L$ roots in the magnetisation $n = 0$ sector. The ground state is of the form (5.57) and a solution for $L = 32$ and $\gamma = \frac{\pi}{5}$ is shown in Figure 5.14. In the thermodynamic limit, a state of this form corresponds to a critical exponent $h = 0$, corresponding to $l = 0$ in equation (5.72). The first excited state is of the form shown in Figure 5.15, where we observe that all but two of the roots are on the lines with imaginary part $\frac{\pi}{2}$ and the remaining two roots have imaginary parts 0 and π. All of the roots come in pairs differing by $\pm i\pi$. This state results in a critical exponent $h = 2$ in the continuum limit, corresponding to the first term of Z_0 in (5.54). The next excited state is of the form shown in Figure 5.16. There is one root with zero imaginary part, one with imaginary part equal to π, and all of the other roots come in complex conjugate pairs with imaginary parts very close to $\pm\frac{\pi}{2}$. This state results in a critical exponent

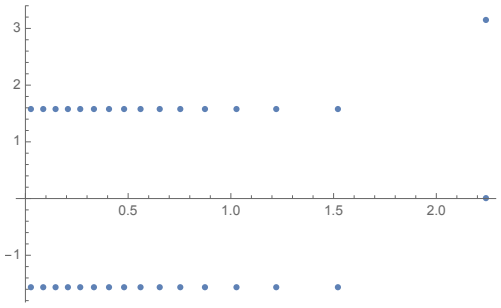


Figure 5.15: Bethe roots for $L = 32$. First excited state in the $n = 0$ sector with $\gamma = \frac{\pi}{5}$.

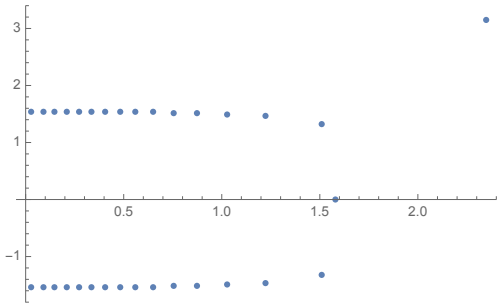


Figure 5.16: Bethe roots for $L = 32$. Second excited state in the $n = 0$ sector with $\gamma = \frac{\pi}{5}$.

$h = 3$ and corresponds to the next term (5.54).

5.4 Other Temperley-Lieb representations

We have until now been considering the Hamiltonian in (5.46) with the e_m defined in terms of Pauli matrices by (5.43). This is known as the vertex-model representation of the TL algebra (3.15), but there are others representations that we can consider. We will consider the loop representation of the TL algebra in section 5.4.1, and the RSOS representation in section 5.4.2.

5.4.1 Loop representation

The loop representation of the TL algebra was introduced in section 3.1.2. We can study the Hamiltonian in (5.46) with this loop representation of e_i. By studying the scaling behaviour of the eigenvalues of the Hamiltonian it is found that the generating function in the continuum limit, in the sector with $2j$ through lines, is given by Z_j, defined in (5.54). The full generating function is then given by

$$\mathcal{Z} = \sum_{m=0}^{\infty} Z_m \,, \tag{5.84}$$

which, when compared to (5.53), is seen to be the same as the generating function in the vertex representation, except that there is a restriction to the highest-weight states of the quantum group symmetry $U_q(sl(2))$. It is also worth pointing out that the Bethe Ansatz has previously been applied to other loop models [113, 114].

5.4.2 RSOS representation

RSOS models were discussed in section 3.1.5 and the RSOS representation of the TL algebra was defined in equation (3.28) and Figure 3.18. It was found in [32] that the generating function of the antiferromagnetic Potts model with free boundary conditions in the RSOS representation is given by the string functions c_l^0, i.e. the generating function of levels in the Z_{k-2} parafermion CFT. The general form of the string functions

c_l^m are given by [73]:

$$c_l^m = \frac{1}{\eta(q)^2} \sum_{\substack{n_1,n_2\in\mathbb{Z}/2 \\ n_1-n_2\in\mathbb{Z} \\ n_1\geq|n_2|,-n_1>|n_2|}} (-1)^{2n_1}\mathrm{sign}(n_1) q^{\frac{(l+1+2n_1k)^2}{4k}-\frac{(m+2n_2(k-2))^2}{4(k-2)}}, \tag{5.85}$$

and $l = |h_{N+1}-h_1|$ is the difference between the heights on the left and right boundaries. We observe the same generating function in the continuum limit when we take the RSOS representation of the TL algebra in the Hamiltonian (5.46), once again using finite size scaling.

Chapter 6

A Non-Compact Boundary Conformal Field Theory

Previous chapters have used a combination of techniques to study the open antiferromagnetic Potts model in its various formulations as a loop model, a vertex model and an RSOS model. In particular, chapter 3 used a combination of algebraic and numerical techniques to study the underlying boundary CFT of the model with the new boundary conditions that were presented there. Chapter 5 found an exact mapping between the vertex formulation of the antiferromagnetic Potts model and the integrable D_2^2 model, and hence used the Bethe Ansatz to study the continuum limit in that case. We recall now the discussion from the introduction to chapter 4, and in particular Figures 4.1 and 4.2, where the use of Bethe Ansatz techniques was motivated by their potential to study very large lattices and hence be used to understand models with a non-compact continuum limit. However, the boundary conditions that were so far studied using the Bethe Ansatz did not produce a non-compact continuum limit and were instead described by the generating function in equation (5.54) which clearly generates a discrete spectrum - and therefore corresponds to a *compact* boundary CFT.

In this chapter we will consider a different D_2^2 K-matrix that we will show produces a non-compact continuum limit. We will start with the same strategy as was used in chapter 5, i.e. take advantage of the mapping between the AF Potts model and the D_2^2 model by interpreting a D_2^2 K matrix in the language of the Potts model and its vertex formulation. We will show that the Hamiltonian of the model with this new K-matrix also has a very convenient form in terms of the Temperley-Lieb algebra, see equation (6.9). Furthermore, we show that this K-matrix has a simple interpretation in the language of the transfer matrix, see equation (6.22).

The fact that the D_2^2 K-matrix that we will consider here satisfies the boundary Yang-Baxter equation introduced in section 4.3 means that the D_2^2 model is integrable with these boundary conditions. However, a complete Bethe Ansatz solution has, until now, been lacking. We present here an exact solution of the model with these boundary conditions which allows us to study the continuum limit and show that it is indeed described by a non-compact boundary CFT.

This chapter is structured as follows: in section 6.1 the K-matrix under consideration is introduced and its corresponding Hamiltonian in terms of Temperley-Lieb algebra generators is derived. A construction to move between the geometry of integrable models

and the geometry most natural in the context of AF Potts and of loop models is reviewed and applied to the present case, allowing us to derive a loop model interpretation of the new boundary conditions, this key result is given in equation (6.22). Section 6.2 derives the complete exact solution of the model and section 6.3 studies the properties of the CFT describing the continuum limit. Finally in section 6.4 it is shown that there is a renormalisation group flow between the boundary conditions presented in this chapter and those of chapter 5, giving rise to a renormalisation group flow from a non-compact boundary CFT to a compact one.

6.1 New Boundary Conditions

Let us start by writing the K-matrix that was first presented in [115]. We have:

$$K^-(\lambda) = \frac{1}{\sinh(\lambda+\eta)} \begin{pmatrix} -\sinh(\lambda-\eta) & 0 & 0 & 0 \\ 0 & \cosh\lambda\sinh\eta & -\sinh\lambda\cosh\eta & 0 \\ 0 & -\sinh\lambda\cosh\eta & \cosh\lambda\sinh\eta & 0 \\ 0 & 0 & 0 & -\sinh(\lambda-\eta) \end{pmatrix} \tag{6.1}$$

where the correspondence with our previous notation (defined in section 5.1.4) is:

$$\begin{aligned} \lambda &= 2iu \\ \eta &= i\gamma \end{aligned} \tag{6.2}$$

We take K^- to act on the left boundary. As always, we also need a K^+ matrix for the right boundary and we take:

$$K^+(\lambda) = K^-(-\lambda+2\eta)^t M \tag{6.3}$$

where M is defined in equation (5.30).

6.1.1 The Hamiltonian limit

To calculate the Hamiltonian corresponding to the K-matrix in (6.1) we can no longer use the usual definition in equations (4.24) and (4.25) because we have $\operatorname{Tr} K_0^+(0) = 0$. We must therefore define the Hamiltonian as the *second* derivative of the transfer matrix which gives [116]:

$$\begin{aligned} \mathcal{H} = \frac{t''(0)}{4(T+2A)} = \sum_{j=1}^{L-1} \mathcal{H}_{j,j+1} + \frac{1}{2}K^{-\prime}(0) \\ + \frac{1}{2(T+2A)}(\operatorname{Tr}_0(K_0^+(0))G_{L0} + 2\operatorname{Tr}_0(K_0^{+\prime}(0)H_{L0}) + \operatorname{Tr}(K_0^+(0)H_{L0}^2)) \end{aligned} \tag{6.4}$$

where the quantities A, T and G are defined by:

$$\begin{aligned} \operatorname{Tr}_0 K_0^+(0)H_{L0} &= A\mathbb{1} \\ T &= \operatorname{Tr} K^{+\prime}(0) \\ G_{j,j+1} &= \mathcal{P}_{j,j+1}\frac{d^2R_{j,j+1}(u=0)}{du^2} \end{aligned} \tag{6.5}$$

The general form of the open Hamiltonian was written in (5.36) and is repeated here:

$$\mathcal{H} = A_{\text{left}} + A_{\text{right}} + \cos\gamma(e_1 + e_{2L-1}) + 2\cos\gamma \sum_{m=2}^{2L-2} e_m - \sum_{m=1}^{2L-2} (e_m e_{m+1} + e_{m+1} e_m)\,, \quad (6.6)$$

The terms A_{left} and A_{right} correspond to the second and third terms in (6.4). The K-matrix in (6.1) is written in the basis in (5.8), but to understand its Temperley Lieb interpretation we need to write it in the basis in (5.5). After this basis change, and up to constants proportional to the identity we find for A_{left} and A_{right}:

$$A_{\text{left}} = \cos\gamma \begin{pmatrix} 0 & 0 & 0 & 0 \\ 0 & e^{-i\gamma} & 1 & 0 \\ 0 & 1 & e^{i\gamma} & 0 \\ 0 & 0 & 0 & 0 \end{pmatrix} \otimes \mathbb{I}^{\otimes 2L-2} \quad (6.7)$$

and

$$A_{\text{right}} = \mathbb{I}^{\otimes 2L-2} \otimes \cos\gamma \begin{pmatrix} 0 & 0 & 0 & 0 \\ 0 & e^{-i\gamma} & 1 & 0 \\ 0 & 1 & e^{i\gamma} & 0 \\ 0 & 0 & 0 & 0 \end{pmatrix} \quad (6.8)$$

So the total Hamiltonian in (6.6) becomes:

$$\mathcal{H} = 2\cos\gamma \sum_{j=1}^{2L-1} e_j - \sum_{j=1}^{2L-2} (e_j e_{j+1} + e_{j+1} e_j) \quad (6.9)$$

We remark that (6.9) is an extraordinarily simple result - let us take a moment to compare it to the periodic model. The Hamiltonian of the periodic model is defined as:

$$\mathcal{H}_{periodic} \equiv \frac{1}{2}\sin 2\gamma \sum_{n=1}^{L} \frac{dR_{n,n+1}}{du} = \sum_{m=1}^{2L} (2\cos\gamma e_m - (e_m e_{m+1} + e_{m+1} e_m)) \quad (6.10)$$

We see then that (6.9) is in some sense a very natural open Hamiltonian since we can obtain it just by changing the limits in the sum in the final expression in (6.10). However, if we tried to do this by defining an open model in the following way:

$$\mathcal{H}_{open} \equiv \frac{1}{2}\sin 2\gamma \sum_{n=1}^{L-1} \frac{dR_{n,n+1}}{du} = \cos\gamma(e_1 + e_{2L-1} + 2\sum_{m=2}^{2L-2} e_m) - \sum_{m=1}^{2L-2} (e_m e_{m+1} + e_{m+1} e_m) \quad (6.11)$$

we see that the result is a Hamiltonian with different coefficients for the e_1 and e_{2L-1} terms. This is the Hamiltonian we would get from setting the K matrices equal to the identity, (however the identity operator does not satisfy the boundary Yang Baxter equation and hence is not an integrable boundary condition). By comparing with 6.9, we see that the K-matrix in (6.1) ensures that all the e_i terms get the same coefficients.

6.1.2 Geometry change

The two open integrable models that we have so far considered are described by a transfer matrix of the form in equation (4.11). The diagrammatic form of this transfer matrix is shown in Figure (5.8), and similarly in Figure 6.1. Notice however that this geometry is quite different from the open vertex model of Figure 3.9 and 3.10. In particular, the vertices in Figure 3.10 are rotated by 45^o with respect to the vertices in

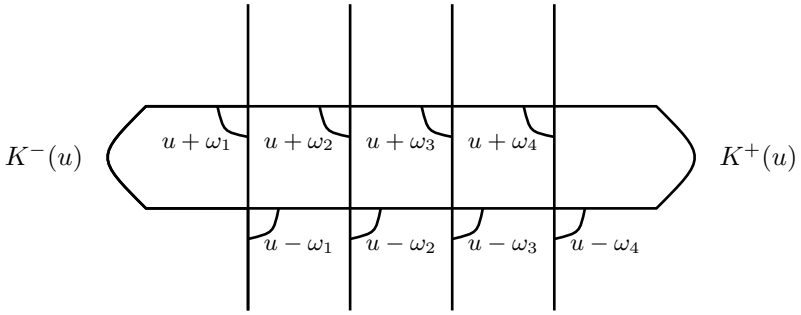


Figure 6.1: The geometrical interpretation of the transfer matrix in equation (6.12)

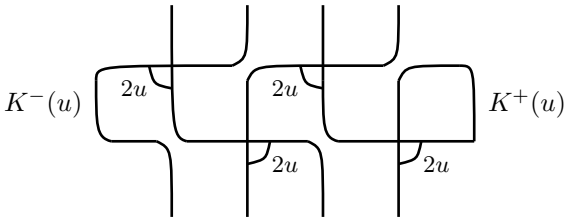


Figure 6.2: The geometrical interpretation of the transfer matrix in (6.12) when the parameters ω_j are given by equation (6.13).

Figure (6.1), which means that the way we implement the boundary condition in each model must be quite different. From the discussion in section 3.1.1, it becomes clear that the geometry of Figure 3.9 is the most natural one in which to study the Potts model and its loop model formulation with open boundary conditions, since in this case the conformal boundary conditions have a simple lattice interpretation. To study these models using the tools of integrability however we require the model to be defined on the lattice of Figure 6.1. Fortunately, it was discussed in [117, 118] that one can transform an integrable model defined on the lattice in Figure 6.1 into one defined on the lattice of Figure 3.9, where the boundary conditions have a more natural interpretation and the model remains solvable by Bethe Ansatz. This procedure will be reviewed in the next section, and the K-matrix in equation (6.1) will have a simple interpretation in terms of a boundary condition on the lattice in Figure 3.10.

6.1.3 The Transfer Matrix

The open integrable transfer matrix of equation (4.11) can in fact be generalised to include inhomogeneous spectral parameters on each line, meaning that the spectral parameter is altered by parameters ω_i at each vertex while leaving the model solvable by Bethe Ansatz. The form of the transfer matrix of a model with these altered spectral

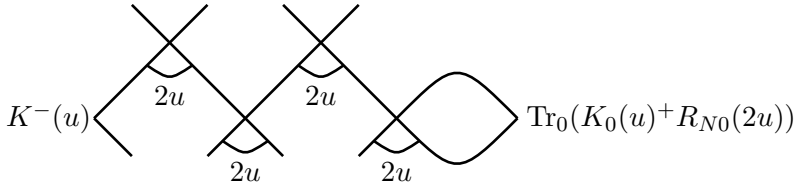


Figure 6.3: A rearrangement of the lattice in Figure 6.2 - the two lattices are topologically equivalent and correspond to the same transfer matrix.

parameters is:

$$t(u) = \mathrm{Tr}_a\, K_a^+(u) R_{aL}(u+\omega_L)...R_{a1}(u+\omega_1) K_a^-(u) R_{1a}(u-\omega_1)...R_{La}(u-\omega_L) \quad (6.12)$$

The graphical depiction of this transfer matrix is shown in Figure 6.1. Now the main idea of this construction is to choose the parameters ω_i in such a way as to make the transfer matrix proportional to one describing the model on the rotated lattice of interest. Consider the following choice of the parameters ω_j:

$$\omega_j = (-1)^{j+1} u \quad (6.13)$$

Since the R-matrix is proportional to the permutation operator when its argument is zero, (or equivalently, the $\check{R}$-matrix is proportional to the identity operator: $\check{R}(0) = \mathbb{1}$), this choice of the ω_i transforms Figure 6.1 into 6.2. It can be easily seen then that Figure 6.2 can be redrawn as Figure 6.3, which is the vertex model defined on lattice that we are interested in, i.e. the lattice of Figure 3.9. The Boltzmann weight of the vertices in the bulk are now captured by the R-matrix with spectral parameter $2u$, the Boltzmann weights arising from interaction with the left boundary is captured by $K^-(u)$, and Boltzmann weights from interactions with the right boundary are described by $\mathrm{Tr}_0(K_0(\frac{u}{2})^+ R_{N0}(u))$.

Let's now see how this works for the present K-matrix under study, i.e. that of equation (6.1). Firstly we must consider a technical point. Recall from chapter 5 that the D_2^2 R-matrix was equivalent to the block R-matrix from the staggered six vertex model in Figure 5.4. If we apply the construction just outlined to this block R-matrix and the corresponding K-matrix, the lattice that we end up with is shown in Figure 6.4, where the dotted lines are where the vertices live, and the full lines are the tiles surrounding these vertices, just as in Figure 3.9. Recall now from equation (3.18) the form of the block R-matrix in terms of Temperley-Lieb operators, repeated here for clarity:

$$R_{i,i+1} = (x + e_{2i})(1 + x e_{2i-1})(1 + x e_{2i+1})(x + e_{2i}) \quad (6.14)$$

The full lattice model and its Boltzmann weights then is that shown in Figure 6.5, where each term of the form $1 + x e_i$ or $x + e_i$ corresponds to one of the vertices comprised of dotted lines in Figure 6.4.

Recall from section 3.1.1 that the isotropic point of the model is the point at which the parameter x is the same on both even and odd tiles in Figure 6.5, corresponding to the equality of horizontal and vertical couplings in the original formulation of the classical Potts model (equation (3.1)). The general form of x in terms of the spectral parameter u is given by [37]:

$$x(u) = \frac{\sin u}{\sin(\gamma - u)} \quad (6.15)$$

It is easily verified [37] that the value of the spectral parameter u_0 that corresponds to the isotropic point is given by:

$$u_0 = \frac{\gamma}{2} + \frac{\pi}{4} \quad (6.16)$$

As can be seen from Figures 6.2, 6.3 and 6.5, we must consider the K-matrix on the left boundary with half the spectral parameter of the bulk. The next task then is to calculate $K^-\left(\frac{u_0}{2}\right)$ and interpret it as a physical boundary condition. Equation (6.1) gives:

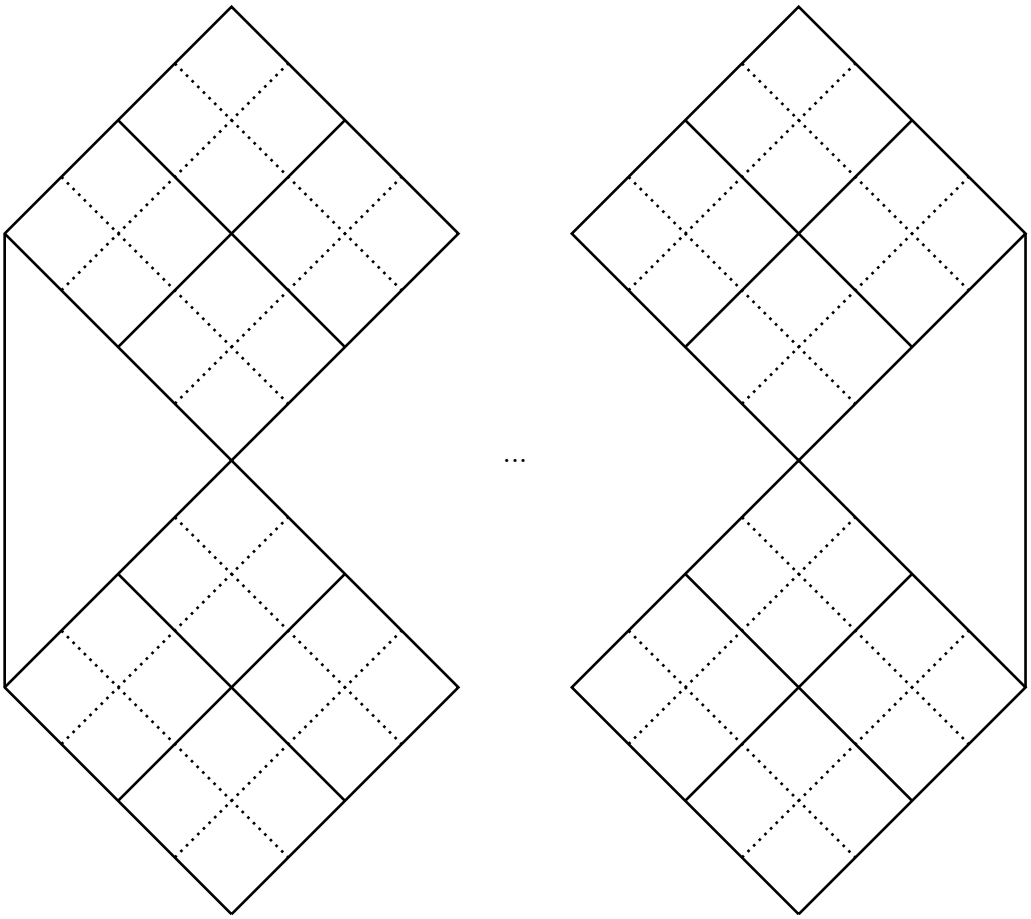


Figure 6.4: The lattice from Figure 6.3 but when with a block R-matrix such as that in Figure 5.4. The dotted lines in the Figure are the edges of the vertex model. The full lines in this Figure are just the tiles that surround these vertices.

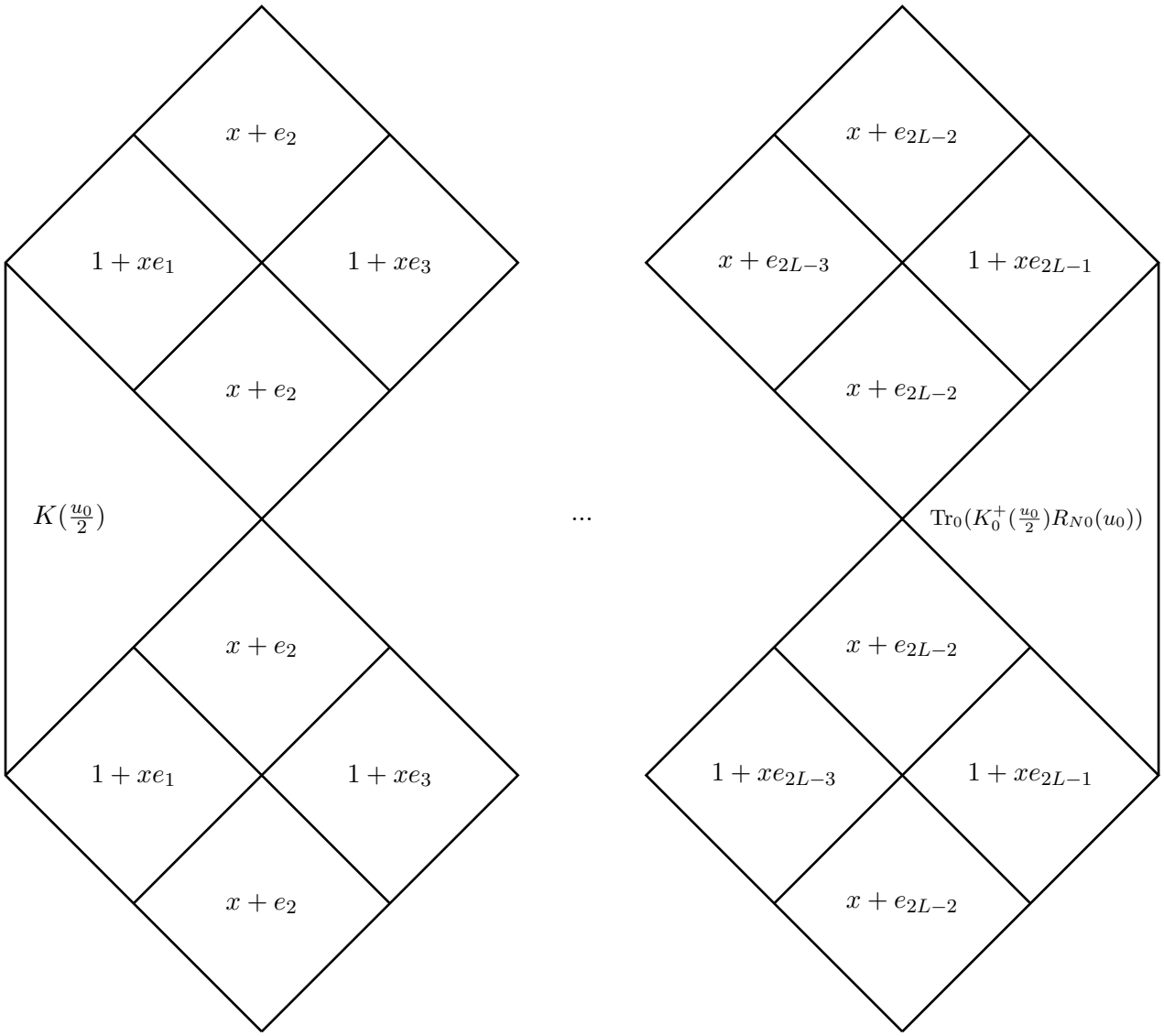


Figure 6.5: The lattice from Figure 6.4 with the action of the R-matrix and K-matrix written in place of the vertices.

$$K^-\left(\frac{u_0}{2}\right) = \begin{pmatrix} \frac{\sin\frac{\gamma}{2}-\cos\frac{\gamma}{2}}{\sin\frac{3\gamma}{2}+\cos\frac{3\gamma}{2}} & 0 & 0 & 0 \\ 0 & \frac{\sin\gamma(\cos\frac{\gamma}{2}-\sin\frac{\gamma}{2})}{\sin\frac{3\gamma}{2}+\cos\frac{3\gamma}{2}} & \frac{-\cos\gamma(\sin\frac{\gamma}{2}+\cos\frac{\gamma}{2})}{\sin\frac{3\gamma}{2}+\cos\frac{3\gamma}{2}} & 0 \\ 0 & \frac{-\cos\gamma(\sin\frac{\gamma}{2}+\cos\frac{\gamma}{2})}{\sin\frac{3\gamma}{2}+\cos\frac{3\gamma}{2}} & \frac{\sin\gamma(\cos\frac{\gamma}{2}-\sin\frac{\gamma}{2})}{\sin\frac{3\gamma}{2}+\cos\frac{3\gamma}{2}} & 0 \\ 0 & 0 & 0 & \frac{\sin\frac{\gamma}{2}-\cos\frac{\gamma}{2}}{\sin\frac{3\gamma}{2}+\cos\frac{3\gamma}{2}} \end{pmatrix} \tag{6.17}$$

This K-matrix is written in the basis of (5.8) so to understand it in terms of the vertex model we must write $K^-\left(\frac{u_0}{2}\right)$ in the basis of (5.5). After doing so, we finally arrive at:

$$K^-\left(\frac{u_0}{2}\right) \propto \left(\frac{\sin\frac{\gamma}{2}-\cos\frac{\gamma}{2}}{\sin\frac{\gamma}{2}+\cos\frac{\gamma}{2}}\right)\mathbb{I} + e_1 \tag{6.18}$$

We furthermore have from equation (6.15) and (6.16) that the isotropic value of x is given by:

$$x(u_0) = \frac{\sin\frac{\gamma}{2}+\cos\frac{\gamma}{2}}{\sin\frac{\gamma}{2}-\cos\frac{\gamma}{2}} \tag{6.19}$$

and hence:

$$K^-\left(\frac{u_0}{2}\right) \propto \mathbb{I} + xe_1 \tag{6.20}$$

A similar calculation for the right boundary leads to:

$$\mathrm{Tr}_0(K_0^+\left(\frac{u_0}{2}\right)R_{L0}(u_0)) \propto \mathbb{I} + xe_{2L-1} \tag{6.21}$$

To arrive at the result in (6.21) one must be careful with the form of the R-matrix used. Recall from section 5.1.4 that the R matrix of the D_2^2 model differed from that of the staggered six vertex model by some minus signs of certain matrix components. The result in (6.21) is only valid for the D_2^2 R-matrix.

These two results allow us to write the full transfer matrix corresponding to Figure 6.5 as:

$$T = (1+xe_1)\cdots(1+xe_{2L-1})(x+e_2)\cdots(x+e_{2L-2})\,, \tag{6.22}$$

Compare this with the transfer matrix corresponding to free boundary conditions in the AF Potts model considered in equation (3.47) in section 3.3. We observe that the transfer matrix in 6.22 is obtained from (3.47) by the transformation $x \to \frac{1}{x}$, up to an irrelevant overall constant term. The transformation $x \to \frac{1}{x}$ is the duality transformation discussed in section 3.1. We have therefore shown that the boundary condition defined by the K-matrix in equation (6.1) is equivalent to the *dual* of free boundary conditions in the antiferromagnetic Potts model.

6.2 Finding an Exact Solution

The preceding sections have shown that the K-matrix in equation (6.1) has a very clean and convenient interpretation in the Hamiltonian formulation - see equation (6.9) - as well as the transfer matrix formuation - see equation (6.22). However an exact solution of the model with these boundary conditions has, until now, been lacking. (Note that this is unlike the boundary conditions from equation (5.31) where the solutions

to the Bethe Ansatz equations were studied in [119]). In [120] the authors presented a set of Bethe Ansatz equations that successfully accounted for a significant part of the spectrum of the model with the boundary conditions in (6.1), but many states in the spectrum could not be accounted for by this Bethe Ansatz solution. We present here a slight modification to the Bethe Ansatz solution of [120] which accounts for all of the states in the spectrum.

We start with a brief review of the partial solution presented in [120], where the goal was to calculate the eigenvalues $\Lambda(u)$ of the transfer matrix of equation (4.11) with the K-matrices given in (6.1). We have:

$$\Lambda(u) = \phi(u)\lambda(u) \tag{6.23}$$

where

$$\phi(u) = \frac{\sinh(u)\sinh(u-2\eta)}{\sinh(u+\eta)\sinh(u-3\eta)} \tag{6.24}$$

and

$$\lambda(u) = Z_1(u) + Z_2(u) + Z_3(u) + Z_4(u) \tag{6.25}$$

where $Z_1(u)$, $Z_2(u)$, $Z_3(u)$ and $Z_4(u)$ are defined as follows:

$$Z_1(u) = a(u)\frac{Q(u+\eta)Q(u+\eta+i\pi)}{Q(u-\eta)Q(u-\eta+i\pi)}\prod_{k=1}^{L} 16\sinh^{4L}(u-2\eta) \tag{6.26}$$

$$Z_2(u) = b(u)\frac{Q(u-3\eta)Q(u+\eta+i\pi)}{Q(u-\eta)Q(u-\eta+i\pi)}\prod_{k=1}^{L} 16\sinh^{2L}(u-2\eta)\sinh^{2L}(u) \tag{6.27}$$

$$Z_3(u) = b(-u+2\eta)\frac{Q(u+\eta)Q(u-3\eta+i\pi)}{Q(u-\eta)Q(u-\eta+i\pi)}\prod_{k=1}^{L} 16\sinh^{2L}(u-2\eta)\sinh^{2L}(u) \tag{6.28}$$

$$Z_4(u) = a(-u+2\eta)\frac{Q(u-3\eta)Q(u-3\eta+i\pi)}{Q(u-\eta)Q(u-\eta+i\pi)}\prod_{k=1}^{L} 16\sinh^{4L}(u) \tag{6.29}$$

where we have:

$$a(u) = \frac{\cosh^2(u-2\eta)}{\cosh(u-\eta)} \tag{6.30}$$

$$b(u) = \frac{\cosh(u)\cosh(u-2\eta)}{\cosh^2(u-\eta)} \tag{6.31}$$

$$Q(u) = \prod_{j=1}^{m}\sinh(\frac{1}{2}(u-u_j))\sinh(\frac{1}{2}(u+u_j)) \tag{6.32}$$

where the u_j are the Bethe roots that can be found in the usual way by requiring that the residues of the poles of $\Lambda(u)$ all cancel, leading to the following set of Bethe Ansatz equations

$$\left(\frac{\sinh(u_j+\eta)}{\sinh(u_j-\eta)}\right)^{2L} = \frac{\sinh(u_j+\eta)}{\sinh(u_j-\eta)}\frac{\cosh(u_j-\eta)}{\cosh(u_j+\eta)}\prod_{k\neq j}^{m}\frac{\sinh(\frac{1}{2}(u_j-u_k)+\eta)}{\sinh(\frac{1}{2}(u_j-u_k)-\eta)}\frac{\sinh(\frac{1}{2}(u_j+u_k)+\eta)}{\sinh(\frac{1}{2}(u_j+u_k)-\eta)} \tag{6.33}$$

As was discussed in detail in [120], this Bethe Ansatz solution is *not* complete. In fact it is found that all eigenvalues with even degeneracy are not accounted for, but all of the eigenvalues with odd degeneracy are. Furthermore, these states with odd degeneracies correspond to an even number m of Bethe roots u_j that come in pairs $\{u_j, u_j + i\pi\}$, with $j = 1, ..., \frac{m}{2}$. The Bethe Ansatz equations for roots of this form are simplified to the following set:

$$\left(\frac{\sinh(u_j+\eta)}{\sinh(u_j-\eta)}\right)^{2L} = \frac{\sinh(u_j+\eta)}{\sinh(u_j-\eta)} \prod_{k\neq j}^{\frac{m}{2}} \frac{\sinh(u_j-u_k+2\eta)}{\sinh(u_j-u_k-2\eta)} \frac{\sinh(u_j+u_k+2\eta)}{\sinh(u_j+u_k-2\eta)} \quad (6.34)$$

We will present in section (6.2.1) a new solution that accounts for the missing states but whose set of Bethe Ansatz equations also reduces to (6.34) for states that come in pairs $\{u_j, u_j + i\pi\}$.

6.2.1 The complete solution

The complete solution can be obtained by turning to the McCoy method [121] - a procedure used to obtain the Bethe roots corresponding to a particular eigenvalue. Note that to do this we normally need to know the general form of the eigenvalues in advance, which notably we do not know here. However, as we will see this method will prove fruitful regardless.

The first step of the McCoy method is to pick a particular value u_0 of the spectral parameter and to calculate numerically the eigenvectors of the transfer matrix at this point. Now recall that an integrable transfer matrix satisfies $[t(u), t(v)] = 0$ for all spectral parameters u and v, and hence the eigenvectors of the transfer matrix are invariant under a change of spectral parameter. Defining the variable $x \equiv e^u$, one can therefore now find a polynomial expression in x for any eigenvalue $\Lambda(u)$, by acting with the transfer matrix $t(u)$ on the corresponding eigenvector. Next one returns to the general expression of the eigenvalue in terms of the Q-function, in the case of interest this expression is given by equations (6.23) to (6.32). Using the polynomial expression of Λ in terms of x, one can solve equations (6.23) to (6.32) to obtain a polynomial expression in x for Q. Finally, one finds the roots x_j of the polynomial $Q(x)$ which gives the Bethe roots u_j via $x_j \equiv e^{u_j}$.

Let us apply this procedure to the present case where a complete Bethe Ansatz solution is missing. In terms of the variables x and x_j (where we recall that $x \equiv e^u$ and $x_j \equiv e^{u_j}$), the quantity Q becomes:

$$Q(x) = \prod_{k=1}^{m} \frac{1}{4}(x - x^{-1} - x_k - x_k^{-1}) = \sum_{k=-m}^{m} a_k x^k \quad (6.35)$$

for some coefficients a_k that depend on the Bethe roots u_j. The expression in (6.32) clearly satisfies $Q(u) = Q(-u)$, which now in polynomial form corresponds to $Q(x) = Q(x^{-1})$, meaning that $a_k = a_{-k}$. Applying the McCoy method to one of the states with odd degeneracy that can be obtained by the previous incomplete solution, we find that the corresponding Q-polynomial does indeed satisfy the property $a_k = a_{-k}$.

However, when we apply the McCoy method to one of the states that is *not* obtained by the partial solution in equations (6.23) to (6.32), we find that Q is given by a polynomial

with coefficients a_k that satisfy $a_k = (-1)^k a_{-k}$. One observes that the expression in (6.32) cannot satisfy this property and must be modified to:

$$Q(u) = \prod_{j=1}^{m} \sinh(\frac{1}{2}(u - u_j)) \cosh(\frac{1}{2}(u + u_j)) \tag{6.36}$$

We find that changing the form of $Q(u)$ from equation (6.32) to (6.36) while keeping equations (6.23) to (6.31) leads to a complete Bethe Ansatz solution that accounts for all of the eigenvalues. The new Bethe Ansatz equations, obtained by requiring that the residues of the poles of $\Lambda(u)$ all cancel, are now given by:

$$\left(\frac{\sinh(u_j + \eta)}{\sinh(u_j - \eta)}\right)^{2L} = \prod_{k \neq j}^{m} \frac{\sinh(\frac{1}{2}(u_j - u_k) + \eta)}{\sinh(\frac{1}{2}(u_j - u_k) - \eta)} \frac{\cosh(\frac{1}{2}(u_j + u_k) + \eta)}{\cosh(\frac{1}{2}(u_j + u_k) - \eta)} \tag{6.37}$$

There are a few important remarks to be made on this complete solution. Firstly, note that the subset of equations that satisfy $\{u_j, u_j + i\pi\}$ still satisfy (6.34), since the equations in (6.37) reduce to (6.34) for Bethe roots u_j of this form. Our redefinition of $Q(u)$ in (6.36) therefore leaves unaffected the states that had been previously accounted for with the original partial solution in [120].

Secondly, observe that the new set of Bethe Ansatz equations do not obey the symmetry $u_j \to -u_j$ but instead $u_j \to \pi - u_j$. This appears to be related to the fact that, as we will see in (6.2.2), the model with these boundary conditions maps to the XXX model with *periodic* boundary conditions in the $\gamma \to 0$ limit; the "admissible solutions" (recall the discussion at the end of section 4.1) to the Bethe Ansatz equations of the periodic XXX model allow for vanishing Bethe roots u_j [94], whereas the open XXX model does not [95].

Finally, recall from equation (6.4) that the Hamiltonian corresponding to the transfer matrix is, in this case, given by the second derivative of the transfer matrix. From equation (6.23) we observe then that the energy eigenvalues are given by:

$$E \propto \Lambda''(0) = \phi'(0)\lambda'(0) \tag{6.38}$$

which leads to

$$E_{D_2^2} = \sum_{j=1}^{m} \frac{2\sin^2(2\gamma)}{\cosh 2u_j - \cos 2\gamma} \tag{6.39}$$

which we observe is exactly the same form as the eigenvalues in (5.49). Our exact solution therefore tells us that the eigenvalues of the Hamiltonian defined in (6.9) are given by (6.39) where the u_j satisfy (6.37).

6.2.2 Correspondence with the XXX model

It is enlightening to study the present model in the limit $\gamma \to 0$. Recall that the Hamiltonian in (5.46) was studied in this limit in section 5.2.3 where it was shown to be equivalent to two decoupled open XXX chains. We will show here that the Hamiltonian in (6.9) becomes equivalent to a *periodic* XXX Hamiltonian in the limit $\gamma \to 0$.

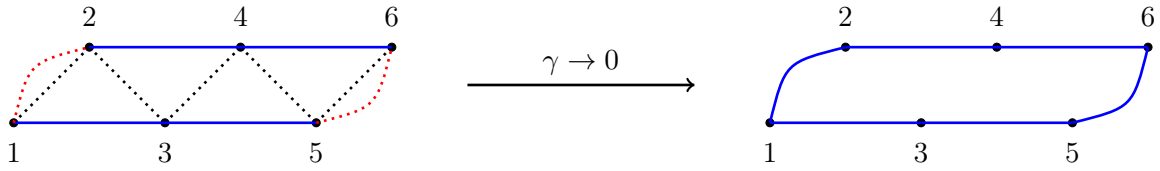


Figure 6.6: The graphical interpretation of the terms in the Hamiltonian in (6.40) for a chain of length $2L = 6$ are shown in the figure on the left. The nearest neighbour interaction is represented by the dotted black line, the XXX next to nearest neighbour interaction is represented by the solid blue line and the boundary interactions are represented by the dotted red line between sites 1 and 2 and between sites 5 and 6. The three site interaction is not represented here. The figure on the right shows the interactions in the limit $\gamma \to 0$, where one observes that the Hamiltonian becomes equivalent to a periodic XXX Hamiltonian.

Consider the Hamiltonian in (6.9) written in terms of Pauli matrices:

$$\begin{aligned}
\mathcal{H} = &-\frac{1}{2}\sum_{i=1}^{L-1}(\sigma^x_{2i-1}\sigma^x_{2i+1}+\sigma^y_{2i-1}\sigma^y_{2i+1}+\sigma^z_{2i-1}\sigma^z_{2i+1})-\frac{1}{2}\sum_{i=1}^{L-1}(\sigma^x_{2i}\sigma^x_{2i+2}+\sigma^y_{2i}\sigma^y_{2i+2}+\sigma^z_{2i}\sigma^z_{2i+2})\\
&-\frac{1}{2}i\sin\gamma\sum_{i=3}^{2L}(\sigma^z_i(\sigma^x_{i-1}\sigma^x_{i-2}+\sigma^y_{i-1}\sigma^y_{i-2})-\sigma^z_{i-2}(\sigma^x_{i-1}\sigma^x_i+\sigma^y_{i-1}\sigma^y_i))\\
&+\frac{1}{2}\sin^2\gamma\sum_{i=1}^{2L-2}(\sigma^z_i\sigma^z_{i+1}+\sigma^z_{i+1}\sigma^z_{i+2})\\
&-\frac{1}{2}i\sin\gamma\cos\gamma(\sigma^z_1+\sigma^z_2-\sigma^z_{2L-1}-\sigma^z_{2L})+\frac{1}{2}\cos\gamma(\sigma^x_1\sigma^x_2+\sigma^y_1\sigma^y_2+\sigma^x_{2L-1}\sigma^x_{2L}+\sigma^y_{2L-1}\sigma^y_{2L})\\
&-\frac{1}{2}\cos^2\gamma(\sigma^z_1\sigma^z_2+\sigma^z_{2L-1}\sigma^z_{2L})-i\sin\gamma\cos\gamma(\sigma^z_1-\sigma^z_{2L})
\end{aligned} \tag{6.40}$$

where we have used the identity in (5.43). We notice that there are four types of terms in (6.40): the first line is an XXX interaction between next to nearest neighbours, the second line is a three site interaction, the third line is a nearest neighbour interaction and the last two lines are the boundary terms. All of these interactions, except for the three site interaction, are represented graphically for a chain of length $2L = 6$ in the diagram on the left hand side of Figure 6.6. When we take the limit $\gamma \to 0$, the only non-vanishing terms are the next to nearest neighbour XXX interaction (the first line of (6.40)) and a contribution from the boundary terms (the last two lines of (6.40)) so that the Hamiltonian becomes:

$$\begin{aligned}
\mathcal{H} = &-\frac{1}{2}\sum_{i=1}^{L-1}(\sigma^x_{2i}\sigma^x_{2i+2}+\sigma^y_{2i}\sigma^y_{2i+2}+\sigma^z_{2i}\sigma^z_{2i+2}+\sigma^x_{2i-1}\sigma^x_{2i+1}+\sigma^y_{2i-1}\sigma^y_{2i+1}+\sigma^z_{2i-1}\sigma^z_{2i+1})\\
&+\frac{1}{2}(\sigma^x_1\sigma^x_2+\sigma^y_1\sigma^y_2-\sigma^z_1\sigma^z_2)\\
&+\frac{1}{2}(\sigma^x_{2L-1}\sigma^x_{2L}+\sigma^y_{2L-1}\sigma^y_{2L}-\sigma^z_{2L-1}\sigma^z_{2L})
\end{aligned} \tag{6.41}$$

This Hamiltonian is represented graphically in the diagram on the right hand side of Figure 6.6. The term on the first line of (6.41) corresponds to two decoupled open XXX chains, the second term and third terms introduce an interaction between the two

chains to make a periodic chain. We observe that the signs of the $\sigma^x\sigma^x + \sigma^y\sigma^y$ terms on the second and third lines of (6.41) are opposite to the signs of the corresponding terms in the first line. However, it is easily verified that one can always change the sign of an **even** number of $\sigma^x\sigma^x + \sigma^y\sigma^y$ terms without changing the spectrum of the XXX Hamiltonian. Doing so for the two boundary terms results in exactly the XXX Hamiltonian. We have therefore shown that the spectrum of (6.9) as $\gamma \to 0$ is identical to that of the periodic XXX chain, as is illustrated in Figure 6.6.

Let us now consider this result in the context of the exact solution of the model presented in section 6.2.1. Firstly, let's write the periodic XXX Hamiltonian from equation (6.41) in the much cleaner form:

$$H = -\frac{1}{2}\sum_{i=1}^{2L}(\sigma_i^x\sigma_{i+1}^x + \sigma_i^y\sigma_{i+1}^y + \sigma_i^z\sigma_{i+1}^z) \tag{6.42}$$

The Bethe Ansatz solution of this Hamiltonian was already studied in section 4.1. We will write this solution in a slightly different and more convenient form for our purposes. The eigenvalues of (6.42) are given by:

$$E = \sum_{k=1}^{m}\frac{4}{\lambda_k^2+1} \tag{6.43}$$

where the Bethe roots λ_k satisfy the following set of Bethe Ansatz equations:

$$\left(\frac{\lambda_j+i}{\lambda_j-i}\right)^{2L} = \prod_{k\neq j}^{m}\left(\frac{\lambda_j-\lambda_k+2i}{\lambda_j-\lambda_k-2i}\right) \tag{6.44}$$

and where m is the number of Bethe roots in any given solution. Now compare this to the Bethe Ansatz solution of the D_2^2 chain presented in section 6.2.1. Consider the eigenvalues of the D_2^2 chain in equation (6.39) when we rescale the Bethe roots $u_j \to \gamma u_j$. The energies in (6.39) now become:

$$E = \sum_{k=1}^{m}\frac{4}{u_k^2+1} \tag{6.45}$$

in the limit $\gamma \to 0$, which we see is identical to (6.43) for $u_k = \lambda_k$. Now let's consider how the D_2^2 Bethe Ansatz equations look in the limit $\gamma \to 0$. Let us first consider the simplest case of roots that come in pairs $\{u_j, u_j + i\pi\}$, which we recall satisfy the simplified Bethe Ansatz equations in (6.34). Recalling that $\eta \equiv i\gamma$, we have that the equations in (6.34) become:

$$\left(\frac{u_j+i}{u_j-i}\right)^{2L} = \left(\frac{u_j+i}{u_j-i}\right)\prod_{k\neq j}^{\frac{m}{2}}\left(\frac{(u_j-u_k+2i)(u_j+u_k+2i)}{(u_j-u_k-2i)(u_j+u_k-2i)}\right) \tag{6.46}$$

as $\gamma \to 0$. Now take a solution to the XXX BAE in (6.44) with Bethe roots λ_j that are symmetric about 0, i.e. the roots come in pairs $\{\lambda_j, -\lambda_j\}$. For roots of this form, the equations in (6.44) are identical to (6.46) for $u_k = \lambda_k$. This is consistent with the discussion surrounding equation (6.40) and Figure 6.6 showing that the D_2^2 chain in (6.9) becomes a periodic XXX chain.

Now let's return to the original partial solution, with Bethe Ansatz equation in (6.34), to see where it breaks down for states that do not come in pairs $\{u_j, u_j + i\pi\}$. The simplest example of roots that are not of this form are a set with an odd number of roots with one vanishing root, say $u_1 = 0$, with all of the other roots coming in pairs $\{u_j, u_j + i\pi\}$. The Bethe Ansatz equations in (6.33) for roots of this form become:

$$\left(\frac{\sinh(u_j+\eta)}{\sinh(u_j-\eta)}\right)^{2L} = \frac{\sinh(u_j+\eta)}{\sinh(u_j-\eta)}\left(\prod_{k\neq j}^{\frac{m}{2}} \frac{\sinh(u_j-u_k+2\eta)}{\sinh(u_j-u_k-2\eta)}\frac{\sinh(u_j+u_k+2\eta)}{\sinh(u_j+u_k-2\eta)}\right) \times \left(\frac{\sinh(\frac{1}{2}u_j+\eta)}{\sinh(\frac{1}{2}u_j-\eta)}\right)^2 \tag{6.47}$$

which in the limit $\gamma \to 0$ become:

$$\left(\frac{u_j+i}{u_j-i}\right)^{2L} = \left(\frac{u_j+i}{u_j-i}\right)\left(\frac{u_j+2i}{u_j-2i}\right)^2 \prod_{k\neq j}^{\frac{m}{2}} \left(\frac{(u_j-u_k+2i)(u_j+u_k+2i)}{(u_j-u_k-2i)(u_j+u_k-2i)}\right) \tag{6.48}$$

We would like to compare these Bethe Ansatz equations to the Bethe Ansatz equations in (6.44) for the periodic XXX model. In analogy with the previous case, we should consider solutions to (6.44) with one root $\lambda_1 = 0$ and all other roots coming in pairs $\{\lambda_j, -\lambda_j\}$. For roots of this form, the equations in (6.44) become:

$$\left(\frac{\lambda_j+i}{\lambda_j-i}\right)^{2L} = \left(\frac{\lambda_j+i}{\lambda_j-i}\right)\left(\frac{\lambda_j+2i}{\lambda_j-2i}\right) \prod_{k\neq j}^{\frac{m}{2}} \left(\frac{(\lambda_j-\lambda_k+2i)(\lambda_j+\lambda_k+2i)}{(\lambda_j-\lambda_k-2i)(\lambda_j+\lambda_k-2i)}\right) \tag{6.49}$$

Comparing (6.49) with (6.48) one observes that when $\lambda_j = u_j$ the two sets of equations differ as a result of the square on the second factor on the right hand side of (6.48). One can use this result to guess the form of the correct Bethe Ansatz equations in (6.37) that were obtained in section 6.2.1 by turning to the McCoy method. One starts with the observation that the square in the second factor in (6.48) comes from the two sinh terms in the product in equation (6.33). To get rid of this square one changes one of these sinh terms to a cosh, whose leading order term vanishes in the $\gamma \to 0$ limit. Then to ensure that the new equations still reduce to (6.34) for roots that come in pairs $\{u_j, u_j + i\pi\}$, one must remove the terms outside of the product in (6.33), and one is left with the new Bethe Ansatz equations in (6.37).

6.3 The Continuum Limit

Previous sections in this chapter have presented various results relating to the boundary conditions in (6.1) on a finite lattice. We will now consider the description of the model in terms of boundary conformal field theory when we take the continuum limit. In particular, we will be interested in calculating the generating function of scaling levels corresponding to the transfer matrix in (6.22), or equivalently, the Hamiltonian in (6.9). As usual, we will use finite size scaling to do this - equation (5.51) will be made use of in the Hamiltonian formulation, whereas equation (3.33) will be made use of in the transfer matrix formulation. Note that the Fermi velocity v_F appearing in (5.51) is once again given by (5.52) since it does not depend on the boundary conditions. Since the Hamiltonian (6.9) and transfer matrix (6.22) are written entirely in terms of Temperley Lieb algebra generators e_i we can consider both the RSOS representation and the

loop representation, as was done in sections 5.4.1 and 5.4.2 for the boundary conditions presented in (5.31).

We will start with the loop representation in section 6.3.1 where we observe a continuous spectrum which, as discussed in the introduction to this chapter, corresponds to a non-compact boundary CFT. It will be shown in section 6.3.5 that the states in the loop model that form this continuum disappear when we restrict to the RSOS representation, and that the generating function of scaling levels in this case is given by a combination of string functions.

Section 6.4 will then consider a more general Hamiltonian that includes the Hamiltonians in (6.9) and (5.46) as special cases. It will be shown that there is a boundary renormalisation group flow from the Hamiltonian (6.9) to (5.46), which in the language of CFT corresponds to a renormalisation group flow from a non-compact theory to a compact one.

6.3.1 The Loop model

We will consider here the transfer matrix in (6.22), or equivalently the Hamiltonian in (6.9) but now with the e_i in the loop representation defined in Figures 3.5 and 3.8. The boundary CFT describing the continuum limit in the loop representation has some quite fascinating properties - most notably the appearance of a continuum of critical exponents, a phenomenon that had until now only been observed in the bulk spectrum.

We start with the observation that the central charge is observed to be given by:

$$c = 2 - \frac{6}{k} \tag{6.50}$$

but that, as we shall see below, for certain values of k the leading exponent h is *negative*, leading to an effective central charge $c_{eff} = c - 24h$ that is *greater* than c. Using the formalism introduced in section 3.1.2 and in particular Figure 3.5, we will consider separately each of the sectors with $2j$ through lines. In each of these sectors we observe both a discrete and a continuous set of critical exponents. Let's first consider the continuous set. We observe the continuum to begin at:

$$h = \frac{l(l+2)}{4k} \tag{6.51}$$

with l given by:

$$l = k - 2j - 2 \tag{6.52}$$

Note that (6.52) means that for certain values of k the exponent in (6.51) can be negative. In particular, when k is an odd integer we can have $l = -1$, corresponding to $2j = k - 1$. The appearance of a continuum on the lattice is identified by the logarithmic convergence of exponents to the value in (6.51), as $L \to \infty$ we observe an infinite number of these states. This was briefly discussed in the introduction to chapter 4 and in particular the text surrounding Figure 4.2 which we repeat in Figure 6.7 for clarity. Let's consider these results in the context of the black hole theory discussed in section 3.3. First, let's recall the central charge c_{BH} in (3.55) and the critical exponent h_{BH} in (3.56, repeated here:

$$h_{\rm BH} = -\frac{J(J-1)}{k-2} + \frac{(n \pm wk)^2}{4k} \tag{6.53}$$

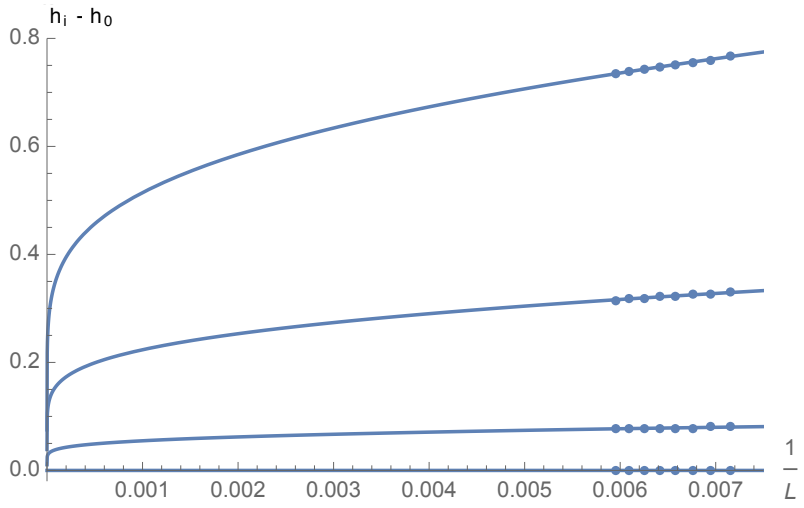


Figure 6.7: The scaling behaviour of the gaps generated from the Hamiltonian in (6.9) with $\gamma = \frac{\pi}{4}$, in the sector $2j = 4$. We observe that the gaps converge logarithmically to $h = 0$ as we expect from equations (6.51) and (6.52), and that an infinite number of such states appear in the limit $L \to \infty$.

The continuous spectrum in the black hole theory is obtained by setting:

$$J = \frac{1}{2} + is \tag{6.54}$$

for s positive. In section 3.3 the parafermion CFT with central charge was related to the black hole CFT by equating:

$$c_{PF} - 24\Delta_{PF} = c_{BH} - 24h_{BH} \tag{6.55}$$

where Δ_{PF} is a critical exponent in the parafermion theory and c_{PF} is given in (6.50). Combining equations (6.53), (6.54) and (6.55) we get:

$$\Delta_{PF} = \frac{(n \pm wk - 1)(n \pm wk + 1)}{4k} + \frac{s^2}{k-2} \equiv \frac{l(l+2)}{4k} + \frac{s^2}{k-2} \tag{6.56}$$

where:

$$l = n \pm wk - 1 \tag{6.57}$$

We see that (6.56) is consistent with our earlier observation that the loop model produces a continuum of critical exponents beginning at (6.51) - combining equations (6.52) and (6.57) leads to $n = -1$ and $w = 1$. We observe that the effective central charge $c_{eff} = c - 24h$ is given by $c_{eff} = c = 2 - \frac{6}{k}$ for k an even integer and $c_{eff} = 2$ for k an odd integer. The general case is plotted in Figure 6.8 and is given by

$$c_{eff} = 2 - 24\frac{(\text{frac}\left(\frac{k}{2}\right) - \frac{1}{2})^2}{k} \tag{6.58}$$

which is consistent with (6.51) and (6.52).

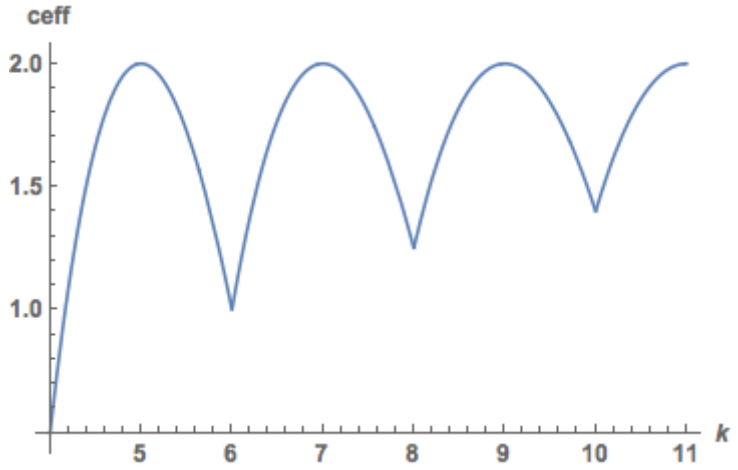


Figure 6.8: The effective central charge as a function of k. For k an odd integer we have $c_{eff} = 2$, for k and even integer we have $c_{eff} = 2 - \frac{6}{k}$

6.3.2 Back to the Bethe Ansatz

It is worthwhile discussing in more detail the states on the lattice that lead to the continuum in the field theory, particularly in the context of the Bethe Ansatz solution from section 6.2.1. The appearance of a continuous spectrum in the periodic model, studied in [54], could be understood in terms of a particular class of solutions to the Bethe Ansatz equations:

$$\left(\frac{\sinh(u_j+\eta)}{\sinh(u_j-\eta)}\right)^L = -\prod_{k\neq j}^{m} \frac{\sinh(\frac{1}{2}(u_j-u_k)+\eta)}{\sinh(\frac{1}{2}(u_j-u_k)-\eta)} \tag{6.59}$$

A subset of the solutions to these equations have the following form:

$$\begin{aligned} u_j^0 &= \alpha_j^+ + i\frac{\pi}{2} \\ u_j^1 &= \alpha_j^- - i\frac{\pi}{2} \end{aligned} \tag{6.60}$$

with $\alpha_j^{\pm}$ real. States in the continuum arise from solutions of the form (6.60) with different numbers of u_j^0 roots and u_j^1 roots. Let's denote the number of u_j^0 roots as m^+ and the number of u_j^1 roots as m^-. Then define:

$$\begin{aligned} m^+ &= \frac{L}{2} - n^+ \\ m^- &= \frac{L}{2} - n^- \end{aligned} \tag{6.61}$$

In the bulk, the continuum states converge logarithmically to the "floor states" h_0 as:

$$h = h_0 + K(\gamma, L)(n^+ - n^-)^2 \tag{6.62}$$

where $K(\gamma, L) \to 0$ as $L \to \infty$. Figure 6.9 shows an example of a configuration of Bethe roots with $n^+ \neq n^-$, therefore corresponding to a continuum state.

We saw in chapter 5 that we do not observe a continuum with the boundary conditions studied in that case and we can understand this in the following way. The Bethe Ansatz equations from chapter 5:

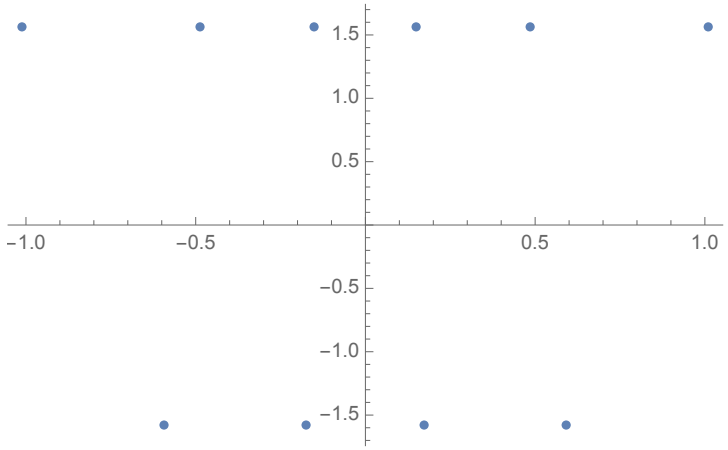


Figure 6.9: An example of a solution to the bulk BAE that leads to a continuum state. This example corresponds to $L = 12$, $n^+ = 0$ and $n^- = 2$.

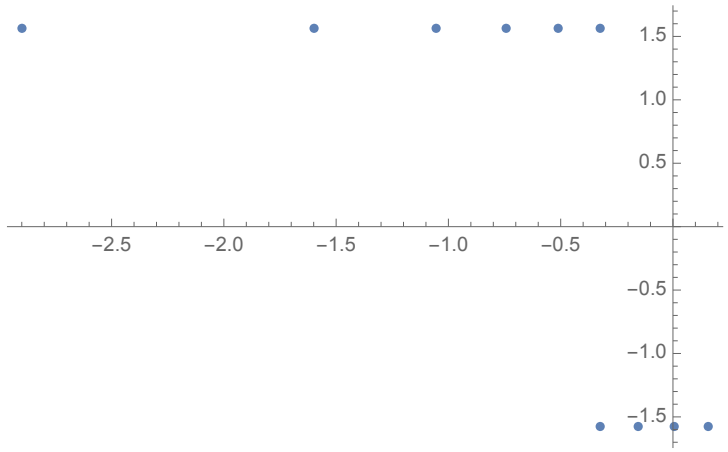


Figure 6.10: An example of a solution to the type 2 boundary BAE that *does not* lead to a continuum state, unlike the bulk case. This example corresponds to $L = 12$, $n^+ = 0$ and $n^- = 2$.

$$\left(\frac{\sinh(u_j+\eta)}{\sinh(u_j-\eta)}\right)^{2L} = \prod_{k\neq j}^{m} \frac{\sinh(\frac{1}{2}(u_j-u_k)+\eta)}{\sinh(\frac{1}{2}(u_j-u_k)-\eta)} \frac{\sinh(\frac{1}{2}(u_j+u_k)+\eta)}{\sinh(\frac{1}{2}(u_j+u_k)-\eta)} \tag{6.63}$$

also permit solutions of the form in (6.60), and one such solution is shown in figure 6.10. This solution satisfies $n^+ \neq n^-$ but does not correspond to a continuum state, unlike the bulk case. The reason is that, with these boundary conditions, if we multiply any number of Bethe roots u_k by a sign then the equations in (6.63) will still be satisfied and the energy will not change. By using this symmetry under $u_k \to -u_k$ we can therefore transform any solution to (6.63) with $n^+ \neq n^-$ into one with $n^+ = n^-$ and hence the $K(\gamma, L)$ term in (6.62) will not play a role. More precisely, the symmetry $u_k \to -u_k$ allows us to transform any u_j^0 root into a u_j^1 root, meaning that only $n = n^+ + n^-$ is a meaningful quantity for solutions to (6.63) whereas n^+ and n^- have no physical meaning individually. Compare this to the Bethe Ansatz equations in (6.37) where we no longer have the symmetry $u_k \to -u_k$, but instead we have symmetry under $u_k \to -u_k + i\pi$. The symmetry $u_k \to -u_k + i\pi$ does not affect n^+ or n^- and therefore

equation (6.62) can be applied to the Bethe Ansatz equations in (6.37), and we hence observe a continuum of exponents.

6.3.3 Discrete States

There are states in the spectrum which do not correspond to the continuum states of equations (6.51) and (6.52) but to discrete states. Let us first consider the case with k an integer where we observe that the exponents are given by the parafermion exponents of equation (3.51) with l and m integer. We conjecture that the full loop model generating function of scaling levels in the sector with $2j = l$ defect lines is given by:

$$\mathcal{Z}_l = \sum_{m=-k+3}^{k-2} \mathrm{Tr}_{\tilde{F}_{lm}} q^{L_0 - \frac{c}{24}} \tag{6.64}$$

with

$$\mathrm{Tr}_{\tilde{F}_{lm}} q^{L_0 - c/24} = \frac{q^{\frac{(l+1)^2}{4k} - \frac{m^2}{4(k-2)}}}{\eta(q)^2} \left[\sum_{n=0}^{\infty} (-1)^n q^{\frac{n^2}{2} + \frac{n(l+1-m)}{2}} + \sum_{n=1}^{\infty} (-1)^n q^{\frac{n^2}{2} + \frac{n(l+1+m)}{2}} \right] \tag{6.65}$$

for l and m with the same parity, and we define $\mathrm{Tr}_{\tilde{F}_{lm}} q^{L_0 - c/24} = 0$ for l and m of opposite parity. Consider now the case for $k \notin \mathbb{Z}$. There is no change to the discussion of the continuous spectrum in section 6.3.1 for $k \notin \mathbb{Z}$. However, we must take care with the discrete part, since it is not clear how (6.64) will "disintegrate" for $k \notin \mathbb{Z}$. It turns out that there are two distinct parts to the discrete spectrum: a part with l integer and independent of k and with $m = 0$, and a part where l and m depend continuously on k. The exponents of the "k independent part" are given by (6.51) with $l = 0, 2, 4, 6, ...$ and the exponents of the "k dependent part" are given by:

$$h = \frac{l(l+2)}{4k} - \frac{m^2}{4(k-2)} \tag{6.66}$$

with $l = k - 2n$ and $m = k - 2n'$ with n, n' positive integers and $n, n' \leq \frac{k+1}{2}$. It is not yet clear to us how to interpret the generating function of scaling levels in (6.64) for $k \notin \mathbb{Z}$ since k in that case is necessarily integer - we leave this as an open question for now.

6.3.4 XXZ Subset

Recall from section 5.3.1 that there was a subset of solutions to the Bethe Ansatz equations under consideration in that case that corresponded to the solution to a set of Bethe Ansatz equations for the XXZ model with particular boundary conditions. The XXZ boundary Bethe Ansatz equations from (5.63) are repeated here:

$$\left(\frac{\sinh(\lambda_j + i\frac{\gamma_0}{2})}{\sinh(\lambda_j - i\frac{\gamma_0}{2})} \right)^{2L} \frac{\sinh(\lambda_j + i\Lambda)}{\sinh(\lambda_j - i\Lambda)} \frac{\sinh(\lambda_j + i\Lambda')}{\sinh(\lambda_j - i\Lambda')} = \prod_{k \neq j}^{m} \frac{\sinh(\lambda_j - \lambda_k + i\gamma_0)}{\sinh(\lambda_j - \lambda_k - i\gamma_0)} \frac{\sinh(\lambda_j + \lambda_k + i\gamma_0)}{\sinh(\lambda_j + \lambda_k - i\gamma_0)} \tag{6.67}$$

Now consider the BAE in (6.34), corresponding to the BAE in (6.37) when the solutions come in pairs $\{u_j, u_j + i\pi\}$. Now as in section 5.3.1 we set $\gamma_0 = \pi - 2\gamma$ (where $\eta = i\gamma$)

and consider solutions of the form $u_j = \alpha_j - i\frac{\pi}{2}$. The equations (6.34) become:

$$\left(\frac{\sinh(\alpha_j + i\frac{\gamma_0}{2})}{\sinh(\alpha_j - i\frac{\gamma_0}{2})}\right)^{2L} \frac{\sinh(\alpha_j - i\frac{\gamma_0}{2})}{\sinh(\alpha_j + i\frac{\gamma_0}{2})} = -\prod_{k\neq j}^{m} \frac{\sinh(\alpha_j - \alpha_k + i\gamma_0)}{\sinh(\alpha_j - \alpha_k - i\gamma_0)} \frac{\sinh(\alpha_j + \alpha_k + i\gamma_0)}{\sinh(\alpha_j + \alpha_k - i\gamma_0)} \tag{6.68}$$

Setting $\Lambda = -\frac{\gamma_0}{2}$ and $\Lambda' = \frac{3\pi}{2}$ we have that the solutions α_j to (6.68) are also solutions to (6.67), i.e. we have $\lambda_j = \alpha_j$. Now proceeding exactly as in section 5.3.1, we write the energy in (6.39) in terms of α_j and γ_0 to find:

$$E_{D_2^2} = -\sum_{j=1}^{m} \frac{2\sin^2\gamma_0}{\cosh 2\alpha_j - \cos\gamma_0} \tag{6.69}$$

which is the energy of the XXZ chain:

$$E_{\text{XXZ}} = \sum_{j=1}^{m} \frac{-2\sin^2\gamma_0}{\cosh 2\lambda_j - \cos\gamma_0} \tag{6.70}$$

when $\alpha_j = \lambda_j$. Since the solutions to the D_2^2 BAE admit twice as many roots as the XXZ chain, the final result is in fact:

$$E_{D_2^2} = 2E_{XXZ} \tag{6.71}$$

Recall from equation (6.8) that the effective central charge of the open XXZ chain for generic Λ, Λ' is given by:

$$c_{\text{eff}} = 1 - \frac{6}{1-\frac{\gamma_0}{\pi}}\left(1 - \frac{\gamma_0 + \Lambda + \Lambda' - 2\pi S(1-\frac{\gamma_0}{\pi})}{\pi}\right)^2. \tag{6.72}$$

where S is the total magnetisation of the chain in a given sector. We have $\gamma_0 = \pi - 2\gamma$, $\gamma = \frac{\pi}{k}$, $\Lambda = -\frac{\gamma_0}{2}$ and $\Lambda' = \frac{3\pi}{2}$, which gives us:

$$c_{eff} = 1 - \frac{3}{k}(1 - k + 4S)^2 \tag{6.73}$$

When considering the D_2^2 chain however, we must multiply the effective central charge in (6.73) by 2 to get for the D_2^2 chain:

$$c_{eff} = 2 - \frac{6}{k}(1 - k + 4S)^2 \tag{6.74}$$

We must take a lot of care when using (6.74) however. Since the D_2^2 chain contains a lot more states than the XXZ chain, there is no guarantee that the state scaling with c_{eff} in equation (6.74) is the ground state of the D_2^2 system. Consider for example the cases $k = 5$ and $k = 7$. For $k = 5$ the ground state of the system occurs in the $S = 1$ sector and we recover the numerical result $c_{eff} = 2$, which in this case does indeed correspond to equation (6.74). For $k = 7$ however, the ground state of the D_2^2 system does not correspond to a solution to the XXZ equations in (6.68). In this case then, the lowest energy state that scales with (6.74) will be an excited state of the D_2^2 chain. Note that as we increase k, the first (i.e. lowest energy) state that scales like (6.74) appears in higher and higher magnetisation sectors S.

6.3.5 RSOS model

We first recall the discussion of the RSOS models from section 3.1.5. In particular, we will take the RSOS representation of the Temperley Lieb algebra generators e_i, written explicitly in (3.28), and insert this expression into the Hamiltonian in (6.9). We will fix the left most RSOS height to 1 and the right most height to $l+1$. We will write this boundary condition as:

$$1, ..., l+1 \tag{6.75}$$

We once again observe the parafermion central charge in equation (6.50) and the parafermion exponents from equation (3.51). Furthermore, we find that the full generating function is given by particular combinations of the string functions, whose definition was given in (5.85). More specifically, for k an odd integer (recall: $\gamma = \frac{\pi}{k}$), it is found that the boundary condition in (6.75) produces a generating function $\mathcal{Z}$ given by the following combination of string functions:

$$\mathcal{Z} = c_l^{m=0} + 2 \sum_{\substack{n=2 \\ n \ even}}^{k-3} c_l^{m=n} \tag{6.76}$$

while for k an even integer we get:

$$\mathcal{Z} = c_l^{m=0} + 2 \sum_{\substack{n=2 \\ n \ even}}^{k-4} c_l^{m=n} + c_l^{m=k-2} \tag{6.77}$$

Table 6.1 presents explicit examples of this correspondence for $k = 4, 5, 6, 7$. Recalling the definition $c_l^m = 0$ when m and l do not have the same parity, and the identity $c_l^{-m} = c_l^m$. Equations (6.76) and (6.77) can then be seen to reduce to:

$$\mathcal{Z} = \sum_{m=-k+3}^{k-2} c_l^m \tag{6.78}$$

Now let's recall the connection between the generating function of scaling levels in the loop model and in the RSOS model. For the AF Potts model with free boundary conditions, we had equation (3.61), repeated here:

$$c_l^0 = \sum_{n=0}^{\infty} \left(K_{l+2nk} - K_{2(n+1)k-l-2} \right) = K_l - K_{2k-l-2} + K_{l+2k} - K_{4k-l-2} + \dots , \tag{6.79}$$

where K_l is the generating function of the loop model - defined in (3.52) - and where the correspondence with the loop model is $l = 2j$. For the states that correspond to the continuum in the loop model to disappear in the RSOS model we need them to appear in different sectors of l so that these states cancel in (6.79). From (6.79) we see that a continuum state in the sector with $2j$ through lines in (6.51) must also appear in the sector with $2k - 2j - 2$ through lines. This is consistent with the discussion of the critical exponents in section 6.3.1: from the right hand side of (6.52), we can see that the exponent h in (6.51) is invariant under: $2j \to 2k - 2j - 2$ and we indeed observe that these cancellations do in fact appear as degeneracies in the loop model spectrum. The string functions, defined in (5.85), can in fact be written as:

$$c_l^m = \sum_{n=0}^{\infty} \mathrm{Tr}_{\tilde{F}_{l+2nk,m}} q^{L_0 - \frac{c}{24}} - \mathrm{Tr}_{\tilde{F}_{2k-l-2+2nk,m}} q^{L_0 - \frac{c}{24}} \tag{6.80}$$

where $\mathrm{Tr}_{\tilde{F}_{l+2nk,m}}$ was defined in (6.65). We must be able to relate the generating function of *discrete* scaling levels in (6.64) to the combination of string functions in (6.78) observed in the RSOS model by summing the $\mathcal{Z}_m$ in the same way that we sum the K_l in (6.79). Indeed, from (6.80) we have:

$$\sum_{m=-k+3}^{k-2} c_l^m = \sum_{n=0}^{\infty} \left(\mathcal{Z}_{l+2nk} - \mathcal{Z}_{2(n+1)k-l-2} \right) \tag{6.81}$$

which is precisely the relation one would expect to hold from considering the correspondence between the loop and RSOS models.

Boundary Condition	k	Generating Function
1,...,1	4	$c_{l=0}^{m=0} + c_{l=0}^{m=2}$
1,...,1	5	$c_{l=0}^{m=0} + 2c_{l=0}^{m=2}$
1,...,1	6	$c_{l=0}^{m=0} + 2c_{l=0}^{m=2} + c_{l=0}^{m=4}$
1,...,1	7	$c_{l=0}^{m=0} + 2c_{l=0}^{m=2} + 2c_{l=0}^{m=4}$
1,...,3	4	$c_{l=2}^{m=0} + c_{l=2}^{m=2}$
1,...,3	5	$c_{l=2}^{m=0} + 2c_{l=2}^{m=2}$
1,...,3	6	$c_{l=2}^{m=0} + 2c_{l=2}^{m=2} + c_{l=2}^{m=4}$
1,...,3	7	$c_{l=2}^{m=0} + 2c_{l=2}^{m=2} + 2c_{l=2}^{m=4}$
1,...,5	6	$c_{l=4}^{m=0} + 2c_{l=4}^{m=2} + c_{l=4}^{m=4}$
1,...,5	7	$c_{l=4}^{m=0} + 2c_{l=4}^{m=2} + 2c_{l=4}^{m=4}$

Table 6.1: The continuum limit of the RSOS model.

6.4 A Boundary RG Flow

Let us now consider the following Hamiltonian:

$$\mathcal{H} = \alpha(e_1 + e_{2L-1}) + 2\cos\gamma \sum_{m=1}^{2L-1} e_m - \sum_{m=1}^{2L-2} (e_m e_{m+1} + e_{m+1} e_m) \tag{6.82}$$

where α is a free boundary parameter. Observe that by setting $\alpha = 0$ we get back the Hamiltonian in (6.9) and by setting $\alpha = -\frac{1}{\cos\gamma}$ we get back the Hamiltonian in (5.46). Both of these cases admitted a Bethe Ansatz solution in sections 6.2.1 and 5.3 respectively. The continuum limit of the case $\alpha = 0$ was found to be described by a non-compact boundary CFT, discussed in section 6.3.1 and the case $\alpha = -\frac{1}{\cos\gamma}$ was found to be described by a compact boundary CFT, discussed in section 5.4.1. It is interesting then to consider the continuum limit when α varies continuously between the two exactly solvable points $\alpha = 0$ and $\alpha = -\frac{1}{\cos\gamma}$.

The result of such an investigation is summarised in Figure 6.11. The points $\alpha = 0$ and $\alpha = -\frac{1}{\cos\gamma}$ are found to be fixed points under RG, with $\alpha = 0$ a repulsive fixed point

and $\alpha = -\frac{1}{\cos\gamma}$ an attractive fixed point. Some numerical results show this RG flow explicitly in Figures 6.12 and 6.13 for the loop model and RSOS model respectively. To understand these figures one must first recall the discussion of finite size scaling for models described by Hamiltonians in section 5.3 and in particular equation (5.51). In both figures we have $\frac{1}{L}$ on the x-axis and on the y-axis we have the first gap, i.e. $h_1 - h_0$, where h_1 and h_0 are the numerical approximations to the conformal dimensions appearing on the right hand side of (5.51) for the first excited state and the ground state respectively of the Hamiltonian. In Figure (6.12) the black curve corresponds to $\alpha = 0$ and, as expected from the discussion in section 6.3.1, the gap converges logarithmically to zero. The red curve corresponds to $\alpha = -\frac{1}{\cos\gamma}$ and, as expected from the discussion in section 5.4.1, this gap to converges nicely to 1. Now let's take the blue curve which corresponds to a slight perturbation away from $\alpha = 0$. We observe that, for low sizes, the numerical approximation to $h_1 - h_0$ is very close to the result for $\alpha = 0$, but that in the limit $\frac{1}{L} \to 0$ the curve converges towards 1, thus showing that $\alpha = 0$ is a repulsive fixed point and that $\alpha = -\frac{1}{\cos\gamma}$ is an attractive fixed point - the interpretation is that of a lattice realisation of an RG flow away from a non-compact boundary conformal field theory towards a compact one. The same analysis for the RSOS model is presented in Figure 6.13.

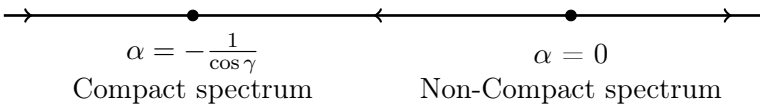


Figure 6.11: RG flow from the Hamiltonian in (6.9) to the Hamiltonian in (5.46), which result in a compact and a non-compact continuum limit respectively.

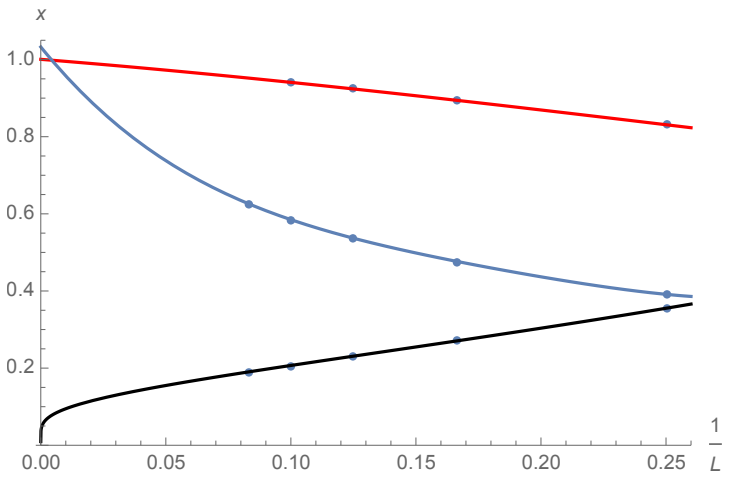


Figure 6.12: The convergence of the first gap in the loop model in the sector with $2j = 2$ through lines, with $\gamma = \frac{\pi}{4}$. The black line corresponds to $\alpha = 0$ in (6.82), the red line corresponds to $\alpha = -\frac{1}{\cos\gamma} = -1.41$, and the blue line corresponds to $\alpha = -0.46$. From section 5.4.1, we expect the first gap for $\alpha = -\frac{1}{\cos\gamma} = -1.41$ to converge to 1, as observed. Similarly, from section 6.3.1 we expect the first gap for $\alpha = 0$ to converge logarithmically to 0, as observed. Finally, we observe that when we perturb α slightly away from 0 the model flows under RG to $\alpha = -\frac{1}{\cos\gamma}$.

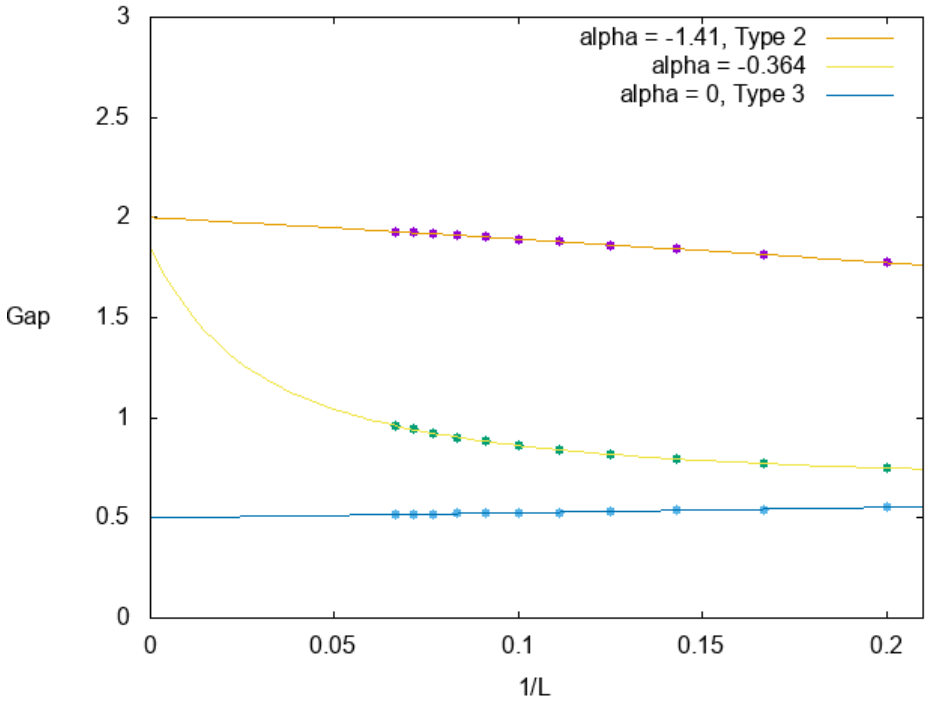


Figure 6.13: The blue line corresponds to the case $\alpha = 0$. As expected, we see that the first gap over the ground state converges to $h = \frac{1}{2}$ since in this case the full generating function is given by the sum of the two string functions $c_{l=0}^{m=0} + c_{l=0}^{m=2}$. The orange line corresponds to the case $\alpha = -\frac{1}{\cos\gamma}$. As expected, we see that the first gap over the ground state converges to $h = 2$ since the generating function in this case is given only by the string function $c_{l=0}^{m=0}$. The yellow line corresponds to a perturbation of α away from zero, (in the figure we take $\alpha = -0.364$). We see that in this case the gap also converges to 2, but it converges much more slowly than the case $\alpha = -\frac{1}{\cos\gamma}$. We can interpret this as an RG flow away from the non-compact theory with $\alpha = 0$, to the compact theory with $\alpha = -\frac{1}{\cos\gamma}$.

Chapter 7

Discussion

There are a number of directions that the research presented in this thesis can be taken in. Before discussing this, we briefly recall the original results that were presented in each chapter.

In chapter 3 the open antiferromagnetic Potts model was considered. A previous conjecture - equation (3.52) for the generating function of scaling levels for the model with free boundary conditions was confirmed numerically - equations (3.53) and (3.54). New conformally invariant boundary conditions for the AF Potts model were presented in section 3.4 and it was shown that these boundary could be described in terms of the blob algebra - equation (3.68), and that the generating function of scaling levels in this case is given by the discrete character of the Black Hole CFT - equations (3.73) and (3.74). The same boundary conditions were considered in the RSOS model and found to produce the string functions from the parafermion CFT in the continuum limit. The representation theory of the blob algebra - equation (3.83) - was then used to derive a new identity between the string functions and the discrete character - equation (3.85). Other aspects of the Black Hole and parafermion theories were then considered, such as the issue of normalisable states (section 3.5) and fusion (section 3.6). In particular, the parafermion fusion rules were derived analytically from the representation theory of the Two Boundary Temperely Lieb algebra (section 3.7.2). The "alt" boundary conditions were interpreted in the context of the three state Potts model in section 3.8 and used to show that a set of previously found identities - equation (3.125) - could be seen as the continuum version of the equivalence between the XXZ spin chain with free boundary conditions and the three-state AF Potts model with "alt" boundary conditions. In section 3.9 it was shown that the disorder operators arising in the parafermion theory could be observed on the lattice.

Chapter 5 then used the tools from integrability to tackle related problems. It was shown in section 5.1 that there is an exact mapping between the the vertex formulation of the antiferromagnetic Potts model - the staggered six vertex model - and an integrable model constructed from the twisted affine D_2^2 Lie algebra. One of the known K-matrices of the D_2^2 model was then considered in section 5.2 and shown to result in a Hamiltonian written entirely in terms of Temperely Lieb algebra generators - equation (5.46) - and that this Hamiltonian becomes that of two decoupled XXX chains in a particular limit (section 5.2.3). The Bethe Ansatz solution of the model was then used to study the continuum limit in section 5.3 and it was shown analytically that the critical exponents of the model were precisely those of the AF Potts model with free boundary

conditions. The loop and RSOS formulation of the model with these boundary conditions were then considered in section 5.4 and the results confirmed that the boundary conditions arising from the D_2^2 K-matrix are indeed in the same universality class as free boundary conditions in the AF Potts model.

Chapter 6 studied a different set of D_2^2 boundary conditions, and showed that this case also admitted a very simple interpretation in terms of Temperley Lieb algebra generators - see equation (6.9). By assigning *inhomogeneous* values of the spectral parameter in a very specific way - see Figure 6.2 - it was shown that the model on the rectangular geometry of Figure 6.1 could be transformed into the same model with a "diagonal" geometry - see Figure 6.3 - and that the transfer matrix in this case is given by the *dual* AF Potts model with free boundary conditions - see equation (6.22). A complete Bethe Ansatz solution of the model was then presented in section 6.2, where it was also shown that the open model becomes the *periodic* XXX model in a particular limit. The Bethe Ansatz solution was used to show that the continuum limit is described by a non-compact boundary CFT closely related to the continuous part of the Black Hole theory. A conjecture for the discrete part was presented in equation (6.64) and the generating function of scaling levels in the RSOS model was found in section 6.3.5. Finally, in section 6.4 it was shown that the boundary conditions of chapter 6 flow under RG to the boundary conditions of chapter 5, corresponding to an RG flow from a non-compact boundary CFT to a compact one.

There are a number of questions raised by these results. Let's first turn our attention to the RG flow observed in section 6.4. It would be interesting to find the operator driving this flow. A previous study [122] also observed a boundary RG flow in a different context, and used numerical methods to find the operator driving it. A detailed study applying the same methods to the present case should shed light on this problem. In [58], the *ferromagnetic* $Q = 3$ state Potts model was studied and the boundary RG flows were classified. One of these flows was generated by a boundary magnetic field operator and we tentatively note a close analogy with our case. More work is required however to understand the case for general Q.

It was mentioned in section 6.3.3 that the conjecture (6.64) for the generating function of discrete states needs to be re-interpreted or modified for the case $k \notin \mathbb{Z}$. This question will be addressed in an upcoming work.

In chapter 5 it was shown that the K-matrix in (5.31) corresponds to a boundary condition in the same universality class as free boundary conditions in the AF Potts model. However, we did not manage to show in finite size that the two boundary conditions are equivalent. It would be interesting to find a geometrical interpretation of this K-matrix, as was done successfully for the case considered in section 6.1, as this would shed light on why we observe free boundary conditions in the continuum limit.

The two K-matrices considered in chapters 5 and 6 correspond to the two fixed points in Figure 6.11. It is possible that there exist other fixed points along this line that we have not yet found. Indeed, additional K-matrices for the D_2^2 model were found in [115] - it is conceivable that these correspond to additional fixed points along the flow in Figure 6.11. Further study is required to find a complete classification of the boundary phase diagram.

Finally, returning to chapter 6, it would be interesting to interpret further the transfer matrix found in equation (6.22). In its current form it is easily interpreted as "the dual of free boundary conditions" but this analysis could be taken further; the dual of free boundary conditions is fixed boundary conditions - where the Potts spins are constrained to take only one value on the boundary - this suggests a return to "blobbed" boundary conditions from section 3.1.4. It was remarked in section 3.4 that the general blobbed boundary condition in the antiferromagnetic model seemed not to correspond to a conformal boundary condition - but it remains possible that a *specific* blobbed boundary condition, i.e. a particular value of r for each γ in (3.23), could yield a conformal boundary condition in the antiferromagnetic model. These observations warrant further study.

Appendix A

Résumé

Il est bien connu depuis plusieurs décennies que les limites continues des modèles sur réseau qui passent par une transition de phase du deuxième ordre sont décrites par des théories des champs conformes (CFTs). Le modèle d'Ising à son point critique est un exemple bien étudié - sa limite continue étant décrite par des fermions libres. En outre, il existe des modèles sur réseau qui s'appellent les modèles RSOS qui deviennent, dans la limite continue, les "modéles minimaux" de CFT, y compris le modèle d'Ising. Tous ces exemples, et la plupart des exemples qui ont déjà été étudiés, sont des exemples des modèles sur réseau "compacts" car le nombre de degrés de liberté est fini. Il n'est donc pas surprenant que les théories des champs conformes qui les décrivent sont aussi compactes - dont la signification pour les CFTs est que leur spectres soient discrets.

Cependant, il existe certains CFTs dites "non-compactes" avec des spectres continus - une propriété identifiée par l'observation d'un continuum d'exposants critiques dans le formalisme de la mécanique statistique, et par l'observation d'un continuum de dimensions conformes dans le formalisme de la CFT. Ces théories sont parfois intéressantes, comme par exemple la CFT qui décrit le "Integer Quantum Hall Effect" à son point critique, et aussi la "Théorie Conforme Euclidienne" dont le nom vient de son origine en théorie des cordes. Il n'est pas difficile de trouver des modèles sur réseau non-compacts qui deviennent ces CFTs dans la limite continue, mais très difficiles de les étudier en pratique en raison de leur nombre infini de degrés de liberté. Cependant, un résultat surprenant est qu'il existe des modèles sur réseau compacts mais dont leurs limites continues sont non-compactes - un fait qui nous permit d'étudier les CFTs non-compactes avec les outils venant des études sur réseau.

On se concentre particulièrement sur le modèle de Potts au point critique antiferromagnétique, dont le nom vient du signe devant la constante de couplage à ce point critique. Il est bien connu que ce modèle peut être reformulé comme un modèle de six vertex décalé - et que ce modèle de vertex avec des conditions aux bords périodique est décrit par la Théorie Conforme Euclidienne. Le problème cependant, est que jusqu'à présent on ne savait pas formuler cette CFT intéressante sur un réseau avec des conditions aux bords ouvertes. Il serait utile de savoir comment s'y prendre parce que les CFTs ouvertes sont manifestement plus simple que des CFTs venant des modèles sur réseaux périodique. La raison est

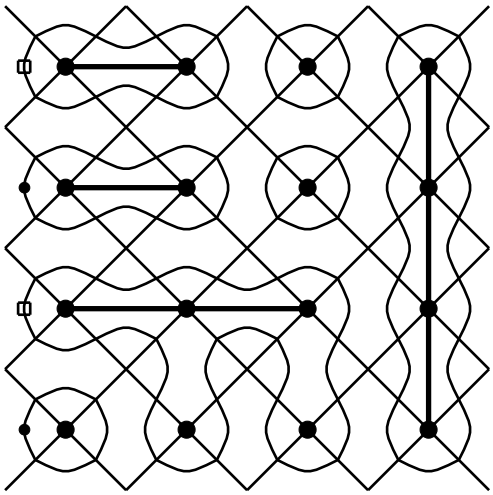


Figure A.1: L'interprétation graphique des conditions aux bords décrites par la matrice de transfert de l'équation A.1.

que l'algèbre de la symétrie d'une CFT ouverte n'est donné que par une copie de l'algèbre Virasoro, mais celle du cas périodique est donné par deux copies. En termes plus concret: l'espace d'Hilbert d'une CFT ouverte n'est généré que par une copie de l'algèbre Virasoro et parfois, si les conditions aux bords sont suffisamment bien choisies, cette espace d'Hilbert n'est donné que par un état primaire et tous ces descendants - un fait qui nous permettre d'isoler et d'étudier une partie à la fois d'une CFT compliquée.

Donc, le but de cette thèse était de trouver des conditions aux bords pour le modèle de Potts au point critique antiferromagnétique, telles que la limite continue soit décrite par une CFT ouverte non-compacte. Pour ce faire, on a utilisé trois méthodes.

La premiére méthode utilise des algèbres sur réseau - l'algèbre Temperley-Lieb et l'algèbre Blob - dont les résultats sont présentés au chapitre 3. Le point de départ de cette analyse est la présentation des nouvelles conditions aux bords conformes pour le modèle de Potts antiferromagnétique pour lesquelles la matrice de transfert peut être écrite en termes des générateurs de l'algèbre blob. Cette matrice de transfer est:

$$T = t_1 t_2 \,, \tag{A.1}$$

avec

$$t_1 = b(e_1)(x+e_3)(x+e_5)\cdots(x+e_{2L-1})(1+xe_2)(1+xe_4)\cdots(1+xe_{2L-2}) \tag{A.2}$$

$$t_2 = (1-b)(e_1)(x+e_3)(x+e_5)\cdots(x+e_{2L-1})(1+xe_2)(1+xe_4)\cdots(1+xe_{2L-2}) \tag{A.3}$$

où x est lié à la constante de couplage du modèle de Potts, définie au chapitre 3, et où e_i et b sont les générateurs de l'algèbre Blob, aussi définie au chapitre 3. L'interprétation graphique de ces conditions aux bords est illustrée dans la figure A.1.

Ces conditions aux bords produisent, dans la limite continue, le caractère discret de la "Théorie Conforme Euclidienne" - la partie compacte d'une CFT non-compacte. En utilisant la théorie des représentations de l'algèbre Temperley-Lieb et Blob, on a trouvé des relations entre ce caractère discret et des fonctions des cordes d'une théorie conforme parafermionique. Même si ces résultats sont intéressants, ils ne nous fournissent pas un spectre continu qui indiquerait que la CFT est non-compacte - qui nous motive d'essayer une autre méthode de trouver une telle CFT.

Le deuxième méthode utilise des outils venant d'intégrabilité - l'Ansatz de Bethe en particulier - dont les resultats sont présentés au chapitre 5. Motivé par le potentiel d'appliquer ces outils, on montre qu'il existe une correspondence exacte entre le modèle de Potts antiferromagnétique, et en particulier sa description comme modèle de vertex décalé, et une modèle integrable construit depuis l'algèbre D_2^2. Ce résultat nous permet d'utiliser les conditions aux bords intégrables pour ce modèle D_2^2 et de les interpréter dans la formalisme du modèle de Potts afin qu'on puisse étudier une autre CFT ouverte. Les premiers conditions aux bords intégrable qu'on considère nous fournissent un Hamiltonian très simple qu'on peut écrire en termes des générateurs de l'algèbre Temperley Lieb:

$$\mathcal{H} = -\frac{1}{\cos\gamma}(e_1 + e_{2L-1}) + 2\cos\gamma \sum_{m=1}^{2L-1} e_m - \sum_{m=1}^{2L-2}(e_m e_{m+1} + e_{m+1}e_m)\,. \qquad \text{(A.4)}$$

Le fait que ces conditions aux bords sont intégrables nous permet de les étudier avec la solution exacte venant de l'Ansatz de Bethe, qui rendent possible l'étude de la limite continue. Cependant, la CFT en ce cas là est aussi compacte - on observe un spectre discret. Ce spectre est celle du modèle de Potts antiferromagnétique avec des conditions aux bords libres - donc on a trouvé une solution exacte de ce modèle mais des conditions aux bords qui produisent une limite continue non-compacte nous manquent toujours.

Donc, on essaie une troisième méthode d'atteindre le but originale - de construire des conditions aux bords ouvertes pour un modèle compact sur réseau telles que la limite continue soit une CFT ouverte non-compacte. Ce méthode utilise des outils d'intégrabilité encore, mais il se concentre sur les conditions aux bords intégrables pour lequel une solution exacte n'existe pas. Les résultats sont présentés au chapitre 6. En utilisant les outils de la première method, i.e. l'algèbre sur réseau, on a réussi de trouver une solution exacte pour un de ces cas, et d'écrire un Hamiltonian et une matrice de transfert en termes de générateurs de l'algèbre Temperley Lieb qui permet une interprétation simple en termes des modèles de boucles. Cette fois-ci, l'Hamiltonian est:

$$\mathcal{H} = 2\cos\gamma \sum_{j=1}^{2L-1} e_j - \sum_{j=1}^{2L-2}(e_j e_{j+1} + e_{j+1}e_j) \qquad \text{(A.5)}$$

La solution exacte nous permet d'étudier la limite continue et ce cas nous fournissent un spectre continue, et par conséquence, une CFT ouverte non-compacte. En outre, ce spectre continu est interprété dans la formalisme de la Théorie Con-

forme Euclidienne.

Finalement, le fait que les Hamiltonians qui ont été trouvés avec le deuxième et le troisième méthode peuvent être écrits en termes des générateurs de l'algèbre Temperley Lieb ouvre la voie pour des autres questions importantes. En particulier, ils nous suggèrent qu'un Hamiltonian plus général pourrait avoir des propriétés intéressant en terme de la théorie du champ. En étudiant cet Hamiltonian, on trouve qu'il y a un flot de la group de renormalisation de la CFT ouverte non-compacte de méthode 3 vers la CFT ouverte compacte de méthode 2, présentée au chapitre 5.

Bibliography

[1] S. Ribault. Conformal field theory on the plane. *arXiv preprint arXiv:1406.4290*, 2014.

[2] A. M. Polyakov. Conformal symmetry of critical fluctuations. *JETP Lett.*, 12:538–541, 1970.

[3] K. G. Wilson. The renormalization group and critical phenomena. *Reviews of Modern Physics*, 55(3):583, 1983.

[4] P. Di Francesco, P. Mathieu, and D. Senechal. *Conformal Field Theory*. Graduate Texts in Contemporary Physics. Springer-Verlag, New York, 1997.

[5] A. A. Belavin, A. M. Polyakov, and A. B. Zamolodchikov. Infinite conformal symmetry of critical fluctuations in two dimensions. *Journal of Statistical Physics*, 34(5-6):763–774, 1984.

[6] A.M. Gainutdinov, J.L. Jacobsen, N. Read, H. Saleur, and R. Vasseur. Logarithmic conformal field theory: a lattice approach. *Journal of Physics A: Mathematical and Theoretical*, 46(49):494012, 2013.

[7] R. Vasseur, J. L. Jacobsen, and H. Saleur. Logarithmic observables in critical percolation. *Journal of Statistical Mechanics: Theory and Experiment*, 2012(07):L07001, 2012.

[8] R. Vasseur. *Indecomposability in field theory and applications to disordered systems and geometrical problems*. PhD thesis, 2013. Thèse de doctorat dirigée par Saleur, Hubert Physique Théorique Paris 6 2013.

[9] J. Cardy. Logarithmic conformal field theories as limits of ordinary CFTs and some physical applications. *Journal of Physics A: Mathematical and Theoretical*, 46(49):494001, 2013.

[10] J. Cardy. *Scaling and renormalization in statistical physics*, volume 5. Cambridge university press, 1996.

[11] D. Poland, S. Rychkov, and A. Vichi. The conformal bootstrap: Theory, numerical techniques, and applications. *Reviews of Modern Physics*, 91(1):015002, 2019.

[12] S. El-Showk, M. Paulos, D. Poland, S. Rychkov, D. Simmons-Duffin, and A. Vichi. Conformal field theories in fractional dimensions. *Physical review letters*, 112(14):141601, 2014.

[13] S. Migliaccio and S. Ribault. The analytic bootstrap equations of non-diagonal two-dimensional CFT. *Journal of High Energy Physics*, 2018(5):169, 2018.

[14] S. El-Showk, M. F. Paulos, D. Poland, S. Rychkov, D. Simmons-Duffin, and A. Vichi. Solving the 3D Ising model with the conformal bootstrap. *Physical Review D*, 86(2):025022, 2012.

[15] S. El-Showk, M. F. Paulos, D. Poland, S. Rychkov, D. Simmons-Duffin, and A. Vichi. Solving the 3d Ising Model with the Conformal Bootstrap II. - Minimization and Precise Critial Exponents. *Journal of Statistical Physics*, 157(4-5):869–914, 2014.

[16] B. Huckestein. Scaling theory of the integer quantum Hall effect. *Reviews of Modern Physics*, 67(2):357, 1995.

[17] M. R. Zirnbauer. Conformal field theory of the integer quantum Hall plateau transition. *arXiv preprint hep-th/9905054*, 1999.

[18] J. L. Cardy. Conformal invariance and universality in finite-size scaling. *Journal of Physics A: Mathematical and General*, 17(7):L385, 1984.

[19] H.W.J. Blöte, J. L. Cardy, and M.P. Nightingale. Conformal invariance, the central charge, and universal finite-size amplitudes at criticality. *Physical Review Letters*, 56(7):742, 1986.

[20] J. Cardy. *Finite-size scaling*. Elsevier, 2012.

[21] H. N. V. Temperley and Elliot H. Lieb. Relations between the 'percolation' and 'colouring' problem and other graph-theoretical problems associated with regular planar lattices: some exact results for the 'percolation' problem. *Proc. Roy. Soc. London*, 322:251, 1971.

[22] V. Pasquier and H. Saleur. Common Structures Between Finite Systems and Conformal Field Theories Through Quantum Groups. *Nuclear Physics*, B330:523–556, 1990.

[23] W.M. Koo and H. Saleur. Representations of the Virasoro algebra from lattice models. *Nuclear Physics B*, 426(3):459 – 504, 1994.

[24] P. P. Martin and D. Woodcock. On the structure of the blob algebra. *Journal of Algebra*, 225(2):957–988, 2000.

[25] J. Belletête, A. M. Gainutdinov, J. L. Jacobsen, H. Saleur, and R. Vasseur. On the correspondence between boundary and bulk lattice models and (logarithmic) conformal field theories. *Journal of Physics A: Mathematical and Theoretical*, 50(48):484002, 2017.

[26] M. Henkel. *Conformal invariance and critical phenomena*. Springer Science & Business Media, 2013.

[27] J. Cardy. Boundary conformal field theory. *arXiv preprint hep-th/0411189*, 2004.

[28] J. Cardy. Conformal field theory and statistical mechanics. *Exact methods in low-dimensional statistical physics and quantum computing*, pages 65–98, 2008.

[29] J. L. Cardy. Conformal invariance and surface critical behavior. *Nuclear Physics B*, 240(4):514–532, 1984.

[30] L. Onsager. Crystal statistics. I. A two-dimensional model with an order-disorder transition. *Physical Review*, 65(3-4):117, 1944.

[31] J. L. Cardy. Effect of boundary conditions on the operator content of two-dimensional conformally invariant theories. *Nuclear Physics B*, 275(2):200–218, 1986.

[32] H. Saleur. The antiferromagnetic Potts model in two dimensions: Berker-Kadanoff phase, antiferromagnetic transition, and the role of Beraha numbers. *Nuclear Physics B*, 360(2):219 – 263, 1991.

[33] J.L. Jacobsen. Conformal field theory applied to loop models, in Polygons, Polyominoes and Polycubes. *(Lecture Notes in Physics),Guttman A.L. ed.*, 775, 2009.

[34] R.S.K. Mong, D. J. Clarke, J. Alicea, N. H. Lindner, and P. Fendley. Parafermionic conformal field theory on the lattice. *Journal of Physics A: Mathematical and Theoretical*, 47(45):452001, 2014.

[35] R. Kedem. Thermodynamics of the 3-state Potts Spin chain. *Journal of statistical physics*, 71(5-6):903–921, 1993.

[36] R.J. Baxter. Critical Antiferromagnetic Square-Lattice Potts Model. *Proceedings of the Royal Society of London Series A*, 383(1784):43–54, Sep 1982.

[37] J. L. Jacobsen and H. Saleur. The antiferromagnetic transition for the square-lattice Potts model. *Nuclear Physics B*, 743(3):207 – 248, 2006.

[38] M P Nightingale and M Schick. Three-state square lattice Potts antiferromagnet. *Journal of Physics A: Mathematical and General*, 15(1):L39–L42, jan 1982.

[39] Jian-Sheng Wang, R. H. Swendsen, and R. Kotecký. Antiferromagnetic Potts models. *Physical Review Letters*, 63:109–112, Jul 1989.

[40] R. Dijkgraaf, H. L. Verlinde, and E. P. Verlinde. String propagation in a black hole geometry. *Nuclear Physics B*, 371:269–314, 1992.

[41] E. Witten. String theory and black holes. *Physical Review D*, 44:314–324, Jul 1991.

[42] P. Goddard, A. Kent, and D. Olive. Unitary representations of the Virasoro and super-Virasoro algebras. *Communications in Mathematical Physics*, 103(1):105–119, 1986.

[43] E. Vernier, J. L. Jacobsen, and H. Saleur. Non compact continuum limit of two coupled Potts models. *Journal of Statistical Mechanics: Theory and Experiment*, 2014(10):P10003, oct 2014.

[44] E. Vernier, J. L. Jacobsen, and H. Saleur. Non compact conformal field theory and the Izergin–Korepin model in regime III. *Journal of Physics A: Mathematical and Theoretical*, 47(28):285202, 2014.

[45] R. Couvreur, E. Vernier, J. L. Jacobsen, and H. Saleur. On truncations of the Chalker-Coddington model. *Nuclear Physics B*, 941:507 – 559, 2019.

[46] E. Vernier, J. L. Jacobsen, and H. Saleur. A new look at the collapse of two-dimensional polymers. *Journal of Statistical Mechanics: Theory and Experiment*, 2015(9):P09001, 2015.

[47] V.B. Petkova and J. Zuber. BCFT: from the boundary to the bulk. *arXiv preprint hep-th/0009219*, 2000.

[48] V. B. Petkova and J. Zuber. Conformal Boundary Conditions and what they teach us. In *Non-perturbative QFT Methods and Their Applications*, pages 1–35. World Scientific, 2001.

[49] J. L. Cardy. Boundary conditions, fusion rules and the Verlinde formula. *Nuclear Physics B*, 324(3):581–596, 1989.

[50] V. A. Fateev and A. B. Zamolodchikov. Parafermionic Currents in the Two-Dimensional Conformal Quantum Field Theory and Selfdual Critical Points in Z(n) Invariant Statistical Systems. *Sov. Phys. JETP*, 62:215–225, 1985. [Zh. Eksp. Teor. Fiz.89,380(1985)].

[51] R. J. Baxter. Potts model at the critical temperature. *Journal of Physics C: Solid State Physics*, 6(23):L445–L448, nov 1973.

[52] C.M. Fortuin and P.W. Kasteleyn. On the random-cluster model: I. Introduction and relation to other models. *Physica*, 57(4):536 – 564, 1972.

[53] R. J. Baxter, S. B. Kelland, and F. Y. Wu. Equivalence of the Potts model or Whitney polynomial with an ice-type model. *Journal of Physics A: Mathematical and General*, 9(3):397–406, mar 1976.

[54] Y. Ikhlef, J. L. Jacobsen, and H. Saleur. A staggered six-vertex model with non-compact continuum limit. *Nuclear Physics B*, 789(3):483 – 524, 2008.

[55] P. Martin and H. Saleur. The Blob algebra and the periodic Temperley-Lieb algebra. *Lett. Math. Phys.*, 30:189, 1994.

[56] J. L. Jacobsen and H. Saleur. Combinatorial aspects of boundary loop models. *Journal of Statistical Mechanics: Theory and Experiment*, 2008(01):P01021, jan 2008.

[57] J. L. Jacobsen and H. Saleur. Conformal boundary loop models. *Nuclear Physics*, B788:137–166, 2008.

[58] I. Affleck, M. Oshikawa, and H. Saleur. Boundary critical phenomena in the three-state Potts model. *Journal of Physics A: Mathematical and General*, 31(28):5827–5842, jul 1998.

[59] V. Pasquier. Two-dimensional critical systems labelled by Dynkin diagrams. *Nuclear Physics B*, 285:162 – 172, 1987.

[60] V. Pasquier. Lattice derivation of modular invariant partition functions on the torus. *Journal of Physics A: Mathematical and General*, 20(18):L1229, 1987.

[61] V. Pasquier. Operator content of the ADE lattice models. *Journal of Physics A: Mathematical and General*, 20(16):5707, 1987.

[62] G. E. Andrews, R. J. Baxter, and P. J. Forrester. Eight vertex SOS model and generalized Rogers-Ramanujan type identities. *Journal of Statistical Physics*, 35:193–266, 1984.

[63] J. Dubail. *Boundary conditions in some non-unitary conformal field theories.* Theses, Université Paris Sud - Paris XI, September 2010.

[64] A. M. Gainutdinov, J. L. Jacobsen, H. Saleur, and R. Vasseur. A physical approach to the classification of indecomposable Virasoro representations from the blob algebra. *Nuclear Physics B*, 873(3):614 – 681, 2013.

[65] S. Caracciolo, J. L. Jacobsen, H. Saleur, A. D. Sokal, and A. Sportiello. Fermionic field theory for trees and forests. *Physical Review Letters*, 93:080601, 2004.

[66] J. L. Jacobsen and H. Saleur. The Arboreal gas and the supersphere sigma model. *Nuclear Physics*, B716:439–461, 2005.

[67] Y. Ikhlef, J. L. Jacobsen, and H. Saleur. Integrable Spin Chain for the $\mathrm{SL}(2,R)/\mathbf{U}(1)$ Black Hole Sigma Model. *Physical Review Letters*, 108:081601, Feb 2012.

[68] C. Candu and Y. Ikhlef. Nonlinear integral equations for the $SL(2,\mathbb{R})/U(1)$ black hole sigma model. *Journal of Physics A: Mathematical and Theoretical*, 46(41):415401, sep 2013.

[69] V.V. Bazhanov, G.A. Kotousov, S.M Koval, and L.L. Lukyanov. On the scaling behaviour of the alternating spin chain. *Journal of High Energy Physics*, 87, 2019.

[70] S. Ribault and V. Schomerus. Branes in the 2D black hole. *Journal of High Energy Physics*, 2004(02):019–019, feb 2004.

[71] D. Israel, A. Pakman, and J. Troost. Extended SL(2,R) / U(1) characters, or modular properties of a simple nonrational conformal field theory. *Journal of High Energy Physics*, 04:043, 2004.

[72] V. Pasquier. Etiology of IRF Models. *Commun. Math. Phys.*, 118:355, 1988.

[73] T. Jayaraman, K.S. Narain, and M.H. Sarmadi. $SU(2)_k$ WZW and Z_k parafermion models on the torus. *Nuclear Physics B*, 343(2):418–449, 1990.

[74] D. Gepner and Z. Qiu. Modular Invariant Partition Functions for Parafermionic Field Theories. *Nuclear Physics*, B285:423, 1987.

[75] E. Vernier, J. L. Jacobsen, and J. Salas. Q-colourings of the triangular lattice: Exact exponents and conformal field theory. *Journal of Physics*, A49(17):174004, 2016.

[76] J. de Gier and A. Nichols. The two-boundary Temperley–Lieb algebra. *Journal of Algebra*, 321(4):1132 – 1167, 2009.

[77] J. Dubail, J. L. Jacobsen, and H. Saleur. Conformal two-boundary loop model on the annulus. *Nuclear Physics*, B813:430–459, 2009.

[78] J. L. Cardy, J. L. Jacobsen, and A. D. Sokal. Unusual corrections to scaling in the 3 state Potts antiferromagnet on a square lattice. *Journal of Statistical Physics*, 105:25–47, 2001.

[79] S Yang. $Z(4)$ X $Z(4)$ Symmetry and Parafermion Operators in the Selfdual Critical Ashkin-teller Model. *Nuclear Physics*, B285:639–650, 1987.

[80] R.J. Baxter. Exactly solved models in statistical mechanics. *Academic Press, London*, B285, 1982.

[81] E. K. Sklyanin. Boundary conditions for integrable quantum systems. *Journal of Physics A: Mathematical and General*, 21(10):2375–2389, may 1988.

[82] H. Saleur and M. Bauer. On Some Relations Between Local Height Probabilities and Conformal Invariance. *Nuclear Physics*, B320:591–624, 1989.

[83] A. B. Zamolodchikov and V. A. Fateev. Disorder Fields in Two-Dimensional Conformal Quantum Field Theory and N=2 Extended Supersymmetry. *Sov. Phys. JETP*, 63:913–919, 1986. [Zh. Eksp. Teor. Fiz.90,1553(1986)].

[84] F. Ravanini and S. Yang. C Disorder Fields and Twist Partition Functions in Parafermionic Conformal Field Theories. *Nuclear Physics*, B295:262–276, 1988.

[85] F.M. Gomes and D.C. Sorensen. Arpack++—An object-oriented version of Arpack eigenvalue package, 2000.

[86] M. T. Batchelor et al. The Bethe ansatz after 75 years. 2007.

[87] M. Karabach, G. Müller, H. Gould, and J. Tobochnik. Introduction to the Bethe ansatz I. *Computers in Physics*, 11(1):36–43, 1997.

[88] M. Karbach, K. Hu, and G. Müller. Introduction to the Bethe ansatz II. *Computers in Physics*, 12(6):565–573, 1998.

[89] H. Bethe. Zur theorie der metalle. *Zeitschrift für Physik*, 71(3-4):205–226, 1931.

[90] W. Hao, R. I. Nepomechie, and A. J. Sommese. Completeness of solutions of Bethe's equations. *Physical Review E*, 88(5):052113, 2013.

[91] R. I. Nepomechie and C. Wang. Algebraic Bethe ansatz for singular solutions. *Journal of Physics A*, 46:325002, 2013.

[92] L. Avdeev and A. Vladimirov. Exceptional solutions to the Bethe ansatz equations. *Theor. Math. Phys.*, 69:2, 05 1987.

[93] C. Marboe and D. Volin. Fast analytic solver of rational Bethe equations. *Journal of Physics A*, 50(20):204002, 2017.

[94] E. Granet and J. L. Jacobsen. On zero-remainder conditions in the Bethe ansatz. *Journal of High Energy Physics*, 03:178, 2020.

[95] Z. Bajnok, E. Granet, J. L. Jacobsen, and R. I. Nepomechie. On Generalized Q-systems. *Journal of High Energy Physics*, 03:177, 2020.

[96] E. K. Sklyanin, L. A. Takhtadzhyan, and L. D. Faddeev. Quantum inverse problem method. I. *Teoreticheskaya i Matematicheskaya Fizika*, 40(2):194–220, 1979.

[97] E. K. Sklyanin. Quantum version of the method of inverse scattering problem. *Journal of Soviet Mathematics*, 19(5):1546–1596, 1982.

[98] M. Jimbo. *Yang-Baxter equation in integrable systems*, volume 10. World Scientific, 1990.

[99] L. Mezincescu and R. I. Nepomechie. Analytical Bethe Ansatz for quantum-algebra-invariant spin chains. *Nuclear Physics B*, 372(3):597 – 621, 1992.

[100] A. M. Gainutdinov and R. I. Nepomechie. Algebraic Bethe ansatz for the quantum group invariant open XXZ chain at roots of unity. *Nuclear Physics B*, 909:796–839, 2016.

[101] F. C. Alcaraz, M. N. Barber, and M. T. Batchelor. Conformal invariance, the XXZ chain and the operator content of two-dimensional critical systems. *Annals of Physics*, 182(2):280–343, 1988.

[102] H.J. De Vega and F. Woynarovich. Method for calculating finite size corrections in Bethe ansatz systems: Heisenberg chain and six-vertex model. *Nuclear Physics B*, 251:439–456, 1985.

[103] C.J. Hamer. Finite-size corrections for ground states of the XXZ Heisenberg chain. *Journal of Physics A: Mathematical and General*, 19(16):3335, 1986.

[104] C.J. Hamer, G.R.W. Quispel, and M.T. Batchelor. Conformal anomaly and surface energy for Potts and Ashkin-Teller quantum chains. *Journal of Physics A: Mathematical and General*, 20(16):5677, 1987.

[105] M.J. Martins and X.-W. Guan. Integrability of the D_n^2 vertex models with open boundary. *Nuclear Physics B*, 583(3):721 – 738, 2000.

[106] R. I. Nepomechie, R. A. Pimenta, and A. L. Retore. The integrable quantum group invariant $A_{2n-1}^{(2)}$ and $D_{n+1}^{(2)}$ open spin chains. *Nuclear Physics B*, 924:86–127, 2017.

[107] N. F. Robertson, J. L. Jacobsen, and H. Saleur. Conformally invariant boundary conditions in the antiferromagnetic Potts model and the $SL(2,\mathbb{R})/U(1)$ sigma model. *Journal of High Energy Physics*, 10:254, 2019.

[108] H. Frahm and M. J. Martins. Phase diagram of an integrable alternating $U_q[sl(2|1)]$ superspin chain. *Nuclear Physics B*, 862(2):504 – 552, 2012.

[109] Y. Ikhlef, J. L. Jacobsen, and H. Saleur. The staggered vertex model and its applications. *Journal of Physics A: Mathematical and Theoretical*, 43(22):225201, 2010.

[110] M. Jimbo. Quantum R matrix for the generalized Toda system. *Communications in Mathematical Physics*, 102(4):537 – 547, 1986.

[111] Y. Ikhlef, J. L. Jacobsen, and H. Saleur. A Temperley-Lieb quantum chain with two- and three-site interactions. *Journal of Physics A: Mathematical and Theoretical*, 42(29):292002, jul 2009.

[112] F. C. Alcaraz, M. N. Barber, M. T. Batchelor, R. J. Baxter, and G. R. W. Quispel. Surface exponents of the quantum XXZ, Ashkin-Teller and Potts models. *Journal of Physics A: Mathematical and General*, 20(18):6397–6409, dec 1987.

[113] A. Nichols, V. Rittenberg, and J. De Gier. One-boundary Temperley–Lieb algebras in the XXZ and loop models. *Journal of Statistical Mechanics: Theory and Experiment*, 2005(03):P03003, 2005.

[114] J. De Gier and P. Pyatov. Bethe ansatz for the Temperley–Lieb loop model with open boundaries. *Journal of Statistical Mechanics: Theory and Experiment*, 2004(03):P002, 2004.

[115] R. I Nepomechie and R. A. Pimenta. New K-matrices with quantum group symmetry. *Journal of Physics A: Mathematical and Theoretical*, 51(39):39LT02, 2018.

[116] R. Cuerno and A. González-Ruiz. Free Fermionic Elliptic Reflection Matrices and Quantum Group Invariance. *Journal of Physics A General Physics*, 26, 04 1993.

[117] C Destri and H.J. De Vega. Bethe ansatz and quantum groups: the light-cone lattice approach (I). Six vertex and SOS models. *Nuclear Physics B*, 374(3):692–719, 1992.

[118] C. M. Yung and M. T. Batchelor. Integrable vertex and loop models on the square lattice with open boundaries via reflection matrices. 1994.

[119] N. F. Robertson, M. Pawelkiewicz, J. L. Jacobsen, and H. Saleur. Integrable boundary conditions in the antiferromagnetic Potts model. *Journal of High Energy Physics*, 2020(2003.03261):1–35, 2020.

[120] R. I. Nepomechie, R. A. Pimenta, and A. L. Retore. Towards the solution of an integrable D_2^2 spin chain. *Journal of Physics A: Mathematical and Theoretical*, 52(43):434004, 2019.

[121] K. Fabricius and B. M. McCoy. Bethe's equation is incomplete for the XXZ model at roots of unity. *Journal of Statistical Physics*, 103(5-6):647–678, 2001.

[122] J. Dubail, J. L. Jacobsen, and H. Saleur. Conformal boundary conditions in the critical O(n) model and dilute loop models. *Nuclear physics B*, 827(3):457–502, 2010.

université PARIS-SACLAY

ÉCOLE DOCTORALE
Physique en l'Île-de-France (PIF)

Titre: Théorie des champs conformes non-compactes et modèles sur réseau - le cas ouvert

Mots clés: Théorie conforme des champs, Ansatz de Bethe, Modèle de Potts

Résumé: Il est bien connu depuis plusieurs décennies que la limite continue des modèles sur réseau qui passent par une transition de phase du deuxième ordre sont décrits par des théories des champs conformes (CFTs). Cette thèse concerne des modèles sur réseau avec des conditions aux bords ouvertes et leur descriptions par les théories des champs conformes ouvertes. On s'intéresse particulièrement aux modèles pour lesquels la description en tant que CFT a des propriétés exotiques, comme par exemple le fait d'être "non-compact" - une propriété identifiée par l'observation d'un continuum d'exposants critiques dans le formalisme de la mécanique statistique, et par l'observation d'un continuum de dimensions conformes dans le formalisme de la CFT. On utilise des outils venant de l'integrabilité et de l'Ansatz de Bethe ainsi que des outils numériques comme la diagonalisation exacte afin de relier les descriptions des modèles sur réseau avec des descriptions en termes de théories des champs. On se concentre particulièrement sur le modèle de Potts au point critique antiferromagnétique, dont le nom vient du signe devant la constante de couplage à ce point critique. Le point de départ de cette analyse est la présentation des nouvelles conditions aux bords conformes qui produisent, dans la limite continue, le caractère discret de la "Théorie conforme euclidienne" sur le réseau. En étudiant la théorie des représentations des algèbres sur le réseau on trouve une identité reliant le caractère discret aux fonctions des cordes d'une théorie conforme parafermionique. Motivé par la potentiel d'appliquer les outils d'integrabilité, on montre qu'il existe une correspondence exacte entre le modèle de Potts antiferromagnétique, et en particulier sa description comme modele de vertex décalé, et un modèle integrable construit depuis l'algèbre D_2^2. Ce résultat ouvre la voie pour une solution exacte du modèle avec deux conditions aux bords conformes et qui permet une interprétation simple en termes des modèles de boucles. La limite continue d'un de ces conditions à bord est non-compacte, et on observe un flot du groupe de renormalisation de la CFT ouverte non-compacte vers la CFT ouverte compacte.

Title: Non-compact conformal field theory and lattice models - the open case

Keywords: Conformal field theory, Bethe Ansatz, Potts model

Abstract: It is well known that lattice systems undergoing second-order phase transitions are described by Conformal Field Theories (CFTs) in the continuum limit. This thesis revolves around the study of open critical lattice models and their descriptions in the continuum limit by boundary CFTs, and is particularly concerned with models whose CFT descriptions have certain exotic properties such as being non-compact, a property identified by the appearance of a continuum of critical exponents in the language of statistical mechanics, and by the appearance of a continuum of conformal dimensions in the language of CFT. Tools from integrability such as the Bethe Ansatz, as well as numerical techniques such as exact diagonalisation are used to move between the lattice and field theory descriptions of the models under consideration. Particular focus is applied to the Potts model at its antiferromagnetic critical point, so-called due to the sign of the coupling constant at this critical point. A starting point in the analysis presented here is that new conformal boundary conditions in the antiferromagnetic Potts model are found and are shown to result in the appearance of the discrete character of the Euclidean Black Hole CFT on the lattice. Further study involving the lattice algebra representation theory results in an identity relating this discrete character to the string functions from the parafermion CFT. Motivated by the potential to apply the tools of integrability, the antiferromagnetic Potts model - and in particular its description as a staggered vertex model - is shown to map exactly to an integrable model constructed from the so-called D_2^2 algebra. This paves the way for an exact solution of the antiferromagnetic Potts model with two independent conformally invariant boundary conditions, both of which have convenient interpretations when the problem is formulated as a loop model. The continuum limit of the model with one of these boundary conditions is found to be non-compact, and a boundary renormalisation group flow is observed from a non-compact boundary CFT to a compact one.

Université Paris-Saclay
Espace Technologique / Immeuble Discovery
Route de l'Orme aux Merisiers RD 128 / 91190 Saint-Aubin, France